Doctoral thesis

Identification and monitoring of structures, controls, and evolution dynamics of hydrothermal systems and associated alteration through high-resolution remote sensing and in situ analysis

by

Daniel Müller

Cumulative dissertation submitted in fulfillment of the requirements
for the degree of "Doctor rerum naturalium" (Dr. rer. nat)
in the scientific field "Remote Sensing"

Institute of Geosciences - Faculty of Science
University of Potsdam

1st Supervisor: Prof. Thomas R. Walter
2nd Supervisor: Prof. Valentin R. Troll
Mentor: Dr. Kevin Fleming

Published online on the
Publication Server of the University of Potsdam:
https://doi.org/10.25932/publishup-62668
https://nbn-resolving.org/urn:nbn:de:kobv:517-opus4-626683

Declaration of Originality

I declare that this thesis is the product of my own work. All assistance received in preparing this thesis and the sources used have been acknowledged. This thesis has not been submitted to any other university.

Potsdam, 10.08.2023 Signature:

Abstract

Volcanic hydrothermal systems are an integral part of most volcanoes and typically involve a heat source, adequate fluid supply, and fracture or pore systems through which the fluids can circulate within the volcanic edifice. Associated with this are subtle but powerful processes that can significantly influence the evolution of volcanic activity or the stability of the near-surface volcanic system through mechanical weakening, permeability reduction, and sealing of the affected volcanic rock. These processes are well constrained for rock samples by laboratory analyses but are still difficult to extrapolate and evaluate at the scale of an entire volcano. Advances in unmanned aircraft systems (UAS), sensor technology, and photogrammetric processing routines now allow us to image volcanic surfaces at the centimeter scale and thus study volcanic hydrothermal systems in great detail. This thesis aims to explore the potential of UAS approaches for studying the structures, processes, and dynamics of volcanic hydrothermal systems but also to develop methodological approaches to uncover secondary information hidden in the data, capable of indicating spatiotemporal dynamics or potentially critical developments associated with hydrothermal alteration. To accomplish this, the thesis describes the investigation of two near-surface volcanic hydrothermal systems, the El Tatio geyser field in Chile and the fumarole field of La Fossa di Vulcano (Italy), both of which are among the best-studied sites of their kind. Through image analysis, statistical, and spatial analyses we have been able to provide the most detailed structural images of both study sites to date, with new insights into the driving forces of such systems but also revealing new potential controls, which are summarized in conceptual site-specific models. Furthermore, the thesis explores methodological remote sensing approaches to detect, classify and constrain hydrothermal alteration and surface degassing from UAS-derived data, evaluated them by mineralogical and chemical ground-truthing, and compares the alteration pattern with the present-day degassing activity. A significant contribution of the often neglected diffuse degassing activity to the total amount of degassing is revealed and constrains secondary processes and dynamics associated with hydrothermal alteration that lead to potentially critical developments like surface sealing. The results and methods used provide new approaches for alteration research, for the monitoring of degassing and alteration effects, and for thermal monitoring of fumarole fields, with the potential to be incorporated into volcano monitoring routines.

Zusammenfassung

Vulkanische Hydrothermalsysteme sind ein integraler Bestandteil vieler Vulkane und erfordern allgemein eine ausreichende Wärmequelle, eine ausreichende Flüssigkeitszufuhr und Kluft- oder Porensysteme, durch die Flüssigkeiten zirkulieren können. Damit verbunden sind subtile, aber wirksame Prozesse, welche die Entwicklung der vulkanischen Aktivität oder die Stabilität des oberflächennahen Vulkansystems durch mechanische Schwächung, Verringerung der Durchlässigkeit und Versiegelung des betroffenen vulkanischen Gesteins erheblich beeinflussen können. Solche Prozesse sind für Gesteinsproben durch Laboranalysen gut definiert, aber es ist immer noch schwierig sie auf der Skala eines ganzen Vulkans zu bewerten. Fortschritte bei unbemannten Flugsystemen (UAS), Sensortechnologie und photogrammetrischen Prozessierungs-routinen ermöglichen es uns heute, Vulkanoberflächen im Zentimeterbereich abzubilden und damit vulkanische Hydrothermalsysteme sehr detailliert zu untersuchen. Ziel dieser Arbeit ist es, deren Potenzial für die Untersuchung der Strukturen, Prozesse und Dynamik solcher Systeme zu erforschen, aber auch methodische Ansätze zu finden, um in den Daten verborgene Sekundärinformationen zu analysieren, die auf raum-zeitliche Dynamiken oder potenziell kritische Entwicklungen im Zusammenhang mit hydrothermaler Alteration hinweisen können. Wir haben zwei oberflächennahe vulkanische hydrothermale Systeme analysiert, das Geysirfeld von El Tatio in Chile und das Fumarolenfeld von La Fossa di Vulcano in Italien, die beide zu den am besten untersuchten Systemen ihrer Art gehören. Durch Bildanalyse, statistische und räumliche Analysen konnten wir das bisher detaillierteste Abbild des strukturellen Aufbaus beider Standorte erstellen, neue Einblicke in die oft faszinierende Systematik solcher Systeme geben, aber auch neue potenzielle Kontrollfaktoren aufzeigen. Die Ergebnisse werden in konzeptionellen Modellen zusammengefasst. Darüber hinaus haben wir methodische Ansätze der Fernerkundung zur Erkennung, Klassifizierung und räumlichen Eingrenzung hydrothermaler Alteration aus UAS-Daten untersucht, durch mineralogisches und chemisches „Ground-Truthing“ bewertet und die Alterationsmuster mit der aktuellen Entgasungsaktivität verglichen. Wir zeigen dass die oft nicht berücksichtigte diffuse Aktivität einen signifikanten Beitrag zur Gesamtaktivität liefert, aber auch Bereiche in denen sekundäre Prozesse hydrothermaler Alteration scheinbar zu potenziell kritischen Entwicklungen wie Oberflächenversiegelung führen. Die Ergebnisse und die verwendeten Methoden bieten neue Ansätze für die Alterationsforschung, für die Überwachung von Entgasungs- und Alterationseffekten und für die thermische Überwachung

von Fumarolenfeldern, und haben Potential in Vulkanüberwachungsroutinen integriert zu werden.

Acknowledgments

Working on volcanoes is a unique experience, and witnessing the creative power of a volcanic eruption cannot be described in words. I have been fortunate to have had the opportunity to study volcanoes and witness their fascinating dynamics over the past years, and I am grateful to all the people who have accompanied, guided, and supported me during this time and who have participated in the realization of this work. First and foremost I would like to thank Prof. Thomas R. Walter for his never ending commitment, without which none of this would have been possible, for his guidance and support, but also for the freedom to develop and pursue ideas. I would like to thank Prof. Valentin Troll for his guidance and support which I greatly appreciate. Further, I would like to thank all my co-authors and colleagues for their contribution and fruitful discussions and their company and friendship during the last years. I would like to acknowledge GFZ Potsdam, University of Potsdam and INGV Palermo for their support, and DAAD for providing a research grant without which parts of the study could not have been realized. Finally, I want to thank my family, especially my parents, for their continued unconditional support throughout my entire academic career.

Table of Contents

List of Figures

Chapter 1

Chapter 2

Chapter 3

Chapter 4

List of Appendices

Appendix Chapter 2

Appendix Chapter 3

Appendix Chapter 4

Chapter 1

Introduction and thesis organization

1.1 Background

There are ~1400 active volcanoes on land worldwide (Siebert et al., 2015), and human society has always been closely related to its neighboring volcanoes. They are commonly associated with beautiful landscapes, closely linked to human culture and history, are part of our myths as places of ancient gods (Thomaidis et al., 2021), and settlers have benefited from the fertile soils (Neall, 2009) that produce fruits, vegetables, grapes and wines, or from the heat from the underground that feeds thermal springs and baths. However, volcanoes are also associated with recurrent catastrophic events and devastation for those living nearby, and have historically been one of the greatest threats. The sources of volcanic hazards are as complex as the volcanoes themselves. Erupting volcanoes threaten nearby settlements with pyroclastic density currents (PDCs), or lava flows (Branca et al., 2017), and can trigger lahars or glacial floods (Carrivick and Tweed, 2019). Emitted gases can poison vegetation and livestock (Thordarsson and Self, 2003), and ash can affect distal areas, burying fields and infrastructures beneath, as seen in historical eruptions in the Campanian Plain (Rosi et al., 1999; Doronzo et al., 2022).

Today, many such large-scale events are predictable by changes identified in geophysical, geochemical, or other geological parameters. The inflow of magma into shallow reservoirs or the lateral propagation of dykes can be detected, often weeks before an eruption occurs by deformation or seismic unrest that precedes the actual event (e.g. Sigmundsson et al., 2015). Melt accumulations can be tracked and monitored even at depths of tens of kilometers (Hensch et al., 2019) and deformation of volcanic buildings or instability of volcanic flanks can be tracked by satellite and from the ground (Acocella, 2021). But still, to date, catastrophic events happen without our previous notice, or in unexpected dimensions. The eruption of Hunga Tonga in 2022, the White Island incident in 2019, and the cascading events that led to the complete destruction of Anak Krakatau (Walter et al., 2019) are just a few recent examples that demonstrate our still limited understanding of volcanic systems and their dynamics.

Most of these catastrophic events are triggered by large-scale magmatic events, which typically show precursory signs of ongoing activity. However, there are other processes and dynamics that are more subtle, but not less powerful. One such aspect of processes and dynamics with a potentially large impact on the volcanic system is volcanic hydrothermal fluid circulation and the associated alteration of volcanic rocks.

1.2 Hydrothermal systems and related processes

Volcanic hydrothermal systems are an integral part of many volcanoes and typically depend on three conditions: an adequate heat source, adequate fluid supply, and fracture or pore systems through which the fluids can circulate. At the surface, they can produce phenomena like geysers, hot springs, mud ponds, or fumaroles, often clustered in larger provinces of hydrothermal activity such as Yellowstone National Park, the geyser fields of Sol de Manana or El Tatio, or the degassing and fumarole fields of Solfatara di Pozzuoli, Nisyros, or Vulcano. Such surface manifestations of hydrothermal venting- or degassing sites have been studied extensively, because they often provide the most direct window to a deeper source of a magmatic or magmatic-hydrothermal system, and may indicate volcanic unrest (Kern et al., 2022), the general conditions of a melt body (Giggenbach, 1996), the interaction of magmatic and hydrothermal fluids (Inguaggiato et al., 2022), or deeper processes of steam separation or chemical mixing with groundwater or hydrothermal layers (Chiodini et al., 1995; Nucchio et al., 1999). Chemical studies have been particularly useful in resolving details of deeper hydrothermal systems, however, the study of hydrothermal systems is important for other reasons as well. Associated with hydrothermal systems are subtle but powerful processes that can significantly influence the evolution of volcanic activity or the stability of the volcanic building. Circulating hydrothermal fluids or propagating gases form strong acids in solution with condensing water vapor and affect the involved rock masses by mineral dissolution, leaching, or remineralization, processes summarized under the term hydrothermal alteration (Pirajno, 2009).

The importance of studying structures, alteration processes, and dynamics of volcanic hydrothermal systems may have been underestimated for a long time. While early studies of hydrothermal systems mainly focused on the identification of ore or mineral deposits (e.g. Di Tommaso and Rubinstein, 2007), more recent studies have shown that alteration effects can have a significant influence on the stability of a volcanic building. Mechanical tests, for instance, applied to hydrothermally altered rock have shown significant mechanical weakening (e.g. Julia et al., 2014; Heap et al., 2019; Darmawan et al., 2022), usually due to mineral dissolution and reprecipitation, which can further lead to permeability changes and in some cases even seal off gas pathways (e.g. Heap et al., 2019; Gertisser et al., 2023). Alteration at volcanic domes, for instance, has been identified as a point of structural weakening (Darmawan et al., 2018) and Heap et al. (2019) showed that acid-sulfate alteration can reduce the permeability of a dome by 4 orders of magnitude, possibly leading to internal pressurization

within the dome and eventually even triggering explosions. Heinicke et al. (2009) suggest hydrothermal alteration to be the trigger for seismic activity in fault zones where the weakening facilitates shear failure propagation, and Rosas-Carbajal et al. (2016) link the collapse of some stratovolcano edifices to mechanical weakening and pore fluid pressurization. These rather dramatic effects are well constrained for rock samples by laboratory analyses but are not easy to constrain and extrapolate to the scale of a volcanic building.

It may be related to the complexity of these hazardous natural systems, that we still often have limited knowledge of the structures, processes, and dynamics associated, but also to the scales at which these processes occur, or to the scales at which we are able to detect them. Although hydrothermal alteration occurs on potentially large spatial scales, the chemical and physical processes operate on microscales, e.g. on the scale of minerals or crystals. Chemical weathering or pore space reduction by alteration or mineral precipitation are not processes that give clear and strong signals at the surface, such as deformation due to magmatic intrusions would do and are therefore generally more difficult to detect. These processes also occur on different time scales. Furthermore, most alteration activity occurs below the surface but we can usually only observe the surface part of hydrothermal systems.

At the surface, such processes and dynamics may express themselves by the localized formation or extinction of vents, the opening or closing of fluid or gas pathways (Harris et al., 2000), but also by spatial and temporal changes in the evolving extent of a surface system, or in specific structural arrangements of vents or activity clusters. Such dynamics could not be tracked for a long time due to limited detection thresholds associated with the often coarse satellite data.

1.3 UAS-based remote sensing

Due to the hazardous nature and the large number of sites, volcanoes have been elaborated using different remote sensing techniques. The thesis is mainly working with data acquired by unoccupied aircraft systems (UAS), equipped with lightweight but high-quality camera sensors. Thanks to their user-friendly and cost-effective application, UASs have been a game changer in volcano remote sensing. For the first time, a scientist can acquire aerial data as desired and, if necessary, reach remote and inaccessible target locations, independently of the complex and expensive flight campaign planning typically required for airborne surveys, or safety issues for ground surveys, allowing the data acquisition even during volcanic crises or eruptions (James et al., 2020). The data provided by modern UASs and sensor systems are of

high quality and resolution, covering optical, thermal, multi- or even hyperspectral remote sensing (James et al., 2020). With the freedom to choose the flight altitude (according to the respective law at target locations), data can be obtained with desired ground resolution from centimeters to decimeters, which is at least an order of magnitude higher than modern high-resolution optical satellite data and much higher than satellite-based thermal data. The ability to image volcanic surfaces at the centimeter scale provides the opportunity to study the surface portions of hydrothermal systems in great detail (Darmawan et al., 2022), and to detect and monitor structures, processes, and dynamics associated that were previously invisible.

1.4 Aims of the thesis

The thesis has two general objectives. Objective 1 is to analyze volcanic hydrothermal systems for their surface structural makeup, to identify potential controls, but also to reveal processes and dynamics that indicate important processes of a temporal evolution or secondary processes associated with discharge or venting activity, and to synthesize results in developing new conceptual models that contribute to a better understanding of such systems.

Objective 2 is to evaluate and develop the ability of UAS-derived high-resolution data to improve our knowledge of volcanic hydrothermal systems. This includes the acquisition, processing, and analysis of UAS-derived data for structural studies but also finding methodological approaches to uncover and evaluate secondary information more hidden in the data, e.g. by analyzing vent topologies or vent arrangements, clustering, peculiarities in distributions, or characteristics of surface manifestations. This objective also includes identifying indicators for subtle and hidden processes and dynamics that may be particularly relevant, such as hydrothermal alteration effects for instance, by merging different sensor systems or approaches. The key to a better understanding of the processes and dynamics of hydrothermal systems is a detailed understanding of the structures, which is why the primary research questions are:

- What can we learn from high-resolution studies about specific structural arrangements, their controls, and process dynamics of volcanic hydrothermal systems and how much do these insights contribute to the existing state of knowledge for the respective system?

One of the most relevant topics in volcanology in recent years associated with hydrothermal activity is hydrothermal alteration, which is why further research questions focus on hydrothermal alteration.

- How can we detect and track degassing and hydrothermal alteration effects of volcanic degassing systems?

- How can UAS-based studies contribute to the monitoring of degassing and alteration processes at volcanic degassing systems?

To answer these questions we analyzed two systems, a fluid-dominated system, the El Tatio geyser field in Chile, and a volcanic degassing system, the fumarole field of La Fossa cone on Vulcano Island (Italy).

1.5 Organization of the thesis

The organization of the thesis is as follows. First, I will briefly introduce some of the methods and analytical approaches used. Then I will provide a brief summary of the research chapters, followed by the actual research Chapters 2-4, each including a peer-reviewed research paper. In Chapter 5, I will discuss the original research questions considering the total of the manuscripts but also highlight particularly interesting findings or important insights that contribute to the current state of knowledge in the respective study area. Other contributions are mentioned in the publication list and briefly in Chapter 9, but are not further considered and discussed here.

1.6 Methods

A brief description of the approaches and methods applied to realize our studies and answer the posed research questions is given below. UAS-based image acquisition provides key advantages for studying volcanic hydrothermal systems by allowing the acquisition of data sets with resolutions at centimeter scales. However, low flight altitudes and high resolution come at the cost of limited ground coverage per acquisition, a common trade-off in remote sensing

systems. Here, advances in the field of photogrammetric processing provided the second game changer, Structure from Motion (SfM) processing.

1.6.1 Photogrammetry and Structure from Motion (SfM) processing

The term photogrammetry covers a number of remote sensing or non-contact methods for determining the 3-dimensional positions or shapes of objects from a pair or series of photographs. The original term photogrammetry was first published in 1867, soon after the invention of photography, and had the original meaning of measuring in pictures. Photogrammetry soon found wide applications in terrestrial photogrammetry, but also in aerial photogrammetry from airplanes or later from satellites (Luhmann, 2004).

SfM is the most recent method in the field of photogrammetry and has its origin in the field of computer vision (e.g. Spetsakis and Aloimonos, 1991, Szeliski and Kang, 1994). It allows the 3-dimensional generation of surfaces or objects from a series of overlapping photographs and the production of high-resolution data products, such as orthomosaic and digital elevation models. Compared to previous photogrammetric methods, the knowledge of the absolute position of the acquisition system during each acquisition is not a first-order requirement, as positions are estimated from changing pixel patterns that are recognizable in multiple images during sensor motion (Figure 1.1A). Under the condition of a constant focal length and known system internal image geometries, camera positions can be estimated during the acquisitions (Westoby et al., 2012). The removal of the condition to know the exact acquisition positions gives a high degree of freedom for acquisition systems and increases the range of potential applications, even though SfM acquisition systems, like UAS, nowadays usually provide geotags (coordinates for the respective acquisitions) in metadata files, which facilitates and definitely improves the processing results. Even RTK (Real Time Kinematic) systems are finding applications, resulting in within-model errors of only a few centimeters (Kalacska et al., 2020). SfM is now the most widely used photogrammetric approach. It is an easy-to-use technique and existing software solutions (e.g. Agisoft, 2016) provide efficient workflows. In addition to the ease of use, SfM provides other important benefits.

It allows the generation of 3D structures from 2D photographs (Westoby et al., 2012), similar to other photogrammetric techniques, but provides 3D models with a high point density. Applications in volcanology include monitoring of deformation and growing volcanic domes

(Darmawan et al., 2018; Zorn et al., 2020), morphological evolution (Ai et al., 2023), or the monitoring of unstable flanks (Gracchi et al., 2022), for instance.

The second major advantage of SfM is that it allows merging the high resolution of single close-up images to mosaics composed of hundreds or thousands of images, eventually representing volcanic surfaces with coverage of square kilometers at simultaneously high resolutions of centimeters. Such data opens up possibilities for insights into the structures and dynamics of natural systems at levels of detail that were unprecedented before.

1.6.2 Image and geospatial analysis

The resulting raster data sets from SfM processing often contain tens of millions of pixels, and require appropriate image analysis techniques in order to extract relevant information and explore the data quantitatively and in-depth. Unlike satellite remote sensing, such approaches are often not yet available as established workflows and need to be developed by combining image analysis and spatial analysis techniques to reveal the information stored in the data.

Image analysis is by definition "the extraction of meaningful information from an image". Accessing or even quantifying this meaningful information from aerial images of volcanic surfaces can be challenging. In this study 3 types of images are used (Figure 1.1B), which are orthomosaic (orthorectified true-color representations with 3 8-bit bands in Red-Green-Blue color coding), digital elevation models (single-band images that provide a single elevation value per pixel), and thermal infrared mosaic (a single-band image with a 16-bit value representing the radiation value measured at the sensor). Each of these image types contains, in addition to the primary information, hidden secondary information that needs to be revealed (Figure 1.1C).

Information extraction and quantitative use of single-band images are comparably easy and usually only require the detection of thresholds representing the data of interest. Thermal anomalies, for instance, can be extracted based on a lower temperature threshold value and then quantitatively compared to other anomaly units. High-temperature pixels can be extracted, converted to vector data now providing coordinates for each data point, and then analyzed spatially (Yuill, 1971; Hahsler et al., 2016), statistically, or for their topological relationship to local geologic structures.

However, analyzing RGB data from volcanoes can be challenging. Volcanoes, by their nature, tend to be poorly colored, mostly grayish, with slight shifts towards yellowish or reddish. If we

imagine a photograph of a volcano not as an image, but as a three-dimensional space of red, green, and blue values, a volcano might look something like Figure 1.2.

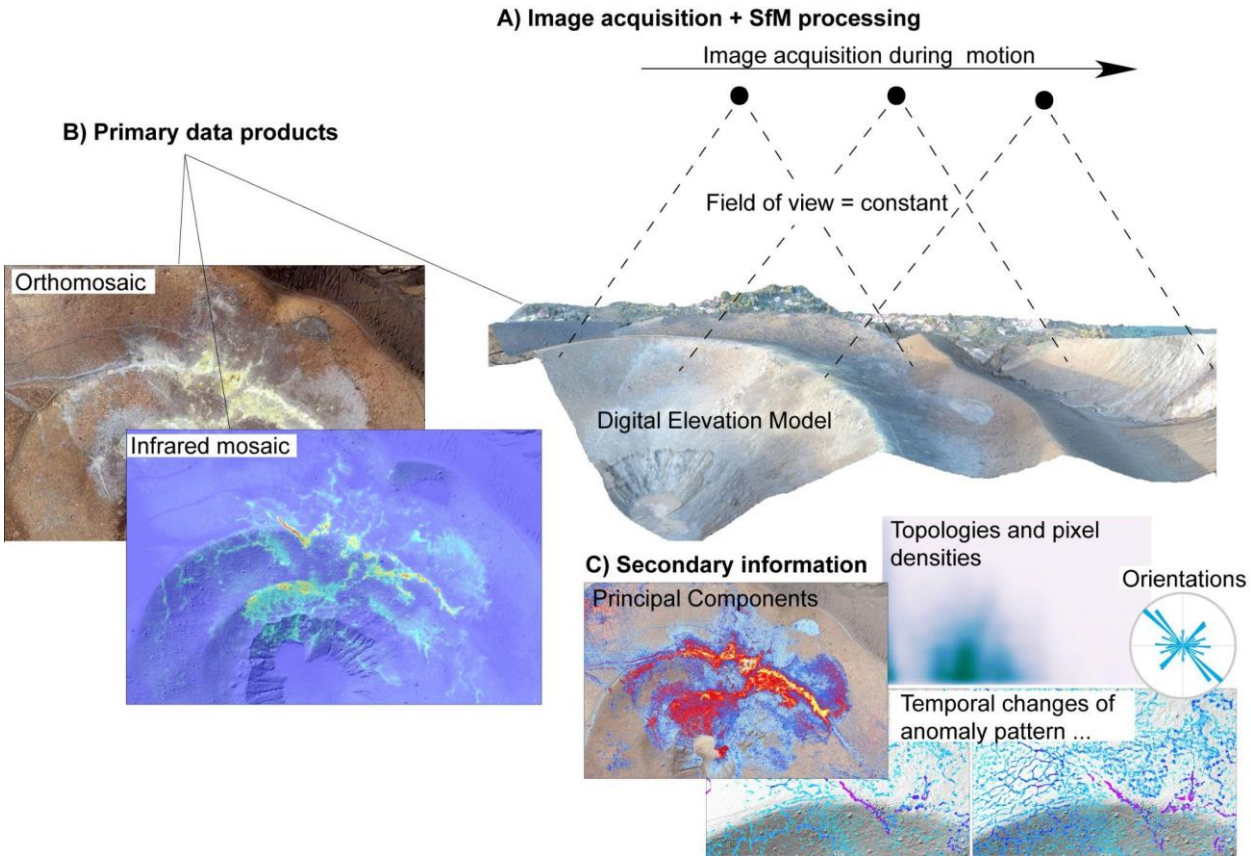

Figure 1.1 A) Sketch of the SfM acquisition procedure. Images are acquired during motion with the requirement of a constant focal length and sufficient overlap in the acquisitions. Black dots depict image acquisition positions, and dashed lines depict the field of view. B) Primary data products of the SfM approach are orthomosaic, digital elevation model, and infrared mosaic. C) In addition to the primary information, each image contains secondary information, such as virtual channels from band ratios or principal components, but also topologies, orientations, density distributions, temporal changes of anomaly patterns, or other geometric, geographic, or other quantitative information to name a few.

The narrow elongated cluster (Figure 1.2A) visually illustrates the poor color range and associated poor interpretability as we are not using much of the available image color space and data clusters along the main axis (black [0 0 0] - white [255 255 255]). Furthermore, the information of the RGB bands is correlated, making any analysis a 3-dimensional problem. Therefore approaches need to be found that are capable of exploring the information hidden in a data set, extracting it, and making it usable for quantitative or structural analysis.

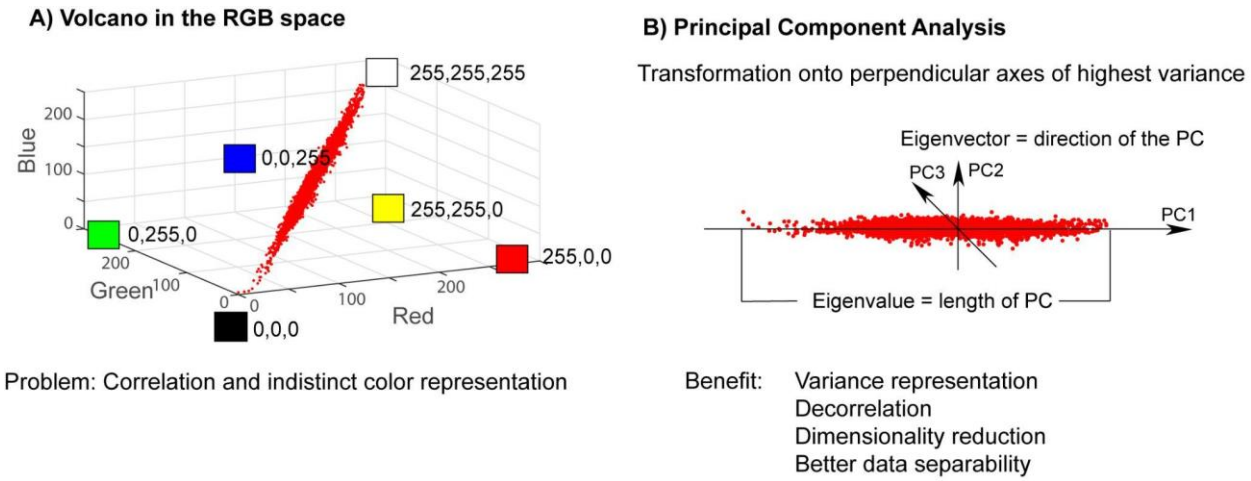

Figure 1.2 One example of an image analysis approach is Principal Component Analysis. A) The representation of color values of a volcano in the RGB space (Red, Green, Blue) is often a narrow elongated cluster along the black-to-white axis. B) Principal component data transformation onto the perpendicular axes of highest variance results in a variance representation, decorrelation of RGB bands, a dimensionality reduction, and therefore better data separability.

Within this thesis, a variety of approaches were employed. However, especially Principal Component Analysis (PCA), a method widely applied in satellite remote sensing (e.g. Loughlin, 1991) proved particularly useful for the analysis of volcanic surfaces. This is due to the principles of PCA (Lillesand et al., 2015), which transforms the original data onto its perpendicular axes of the highest variance, resulting in a decorrelation of the initial RGB bands and providing a "variance" representation (Figure 1.2B), but also due to the shape and orientation of a volcanic RGB cluster along the axis black to white. Consequently resulting from the geometrical laws of PCA, the Principal Components 2 and 3 will point towards colored end members like red, yellow, green, or blue or mixed members out of them. In the case of volcanoes with degassing systems and alteration effects, a dominance of yellow or reddish pixels next to the dominantly grayish surface is likely and can therefore be potentially well constrained by PCA. Due to the decorrelation of the RGB bands, PCA further provides good data separability, allowing the extraction of data fractions of interest, which can then be further and more sensitively analyzed by image analysis techniques, or also spatially by converting the extracted raster data into vectors with coordinates and attributes. By combining image analysis, raster, and vector operations, and geospatial or statistical analysis tools, secondary information can be revealed that goes far beyond the original image data. This secondary information is actually stored in the original images but obscured and not directly

accessible. In other words, one can turn pixels, their topologies, clusters, or orientations, but also colors into concrete numbers that can be used to access and quantify effects observed in the data.

1.6.3 Ground-truthing, mineralogical, and bulk chemical composition

Part of our studies required ground-truthing, as the detection and analysis of hydrothermal alteration from UAS-derived RGB data is not yet an established approach. We provide ground truthing to verify our findings through mineralogical analysis of representative rock samples obtained by X-ray diffraction (XRD) method and Rietveld refinement, and by analysis of the bulk-chemical composition obtained by X-ray fluorescence (XRF).

X-ray powder diffraction (XRD)

X-ray diffraction uses X-rays generated in a sealed tube under a vacuum. A filament inside the tube emits electrons, when an electric current is applied, which are then accelerated by a high voltage within the tube and strike a target, usually copper, where the impact produces additional X-rays. These X-rays are directed onto a grained powder sample, diffracted, and measured by a detector (Dulong and Jackson, 1997). This X-ray diffraction can be used to measure distances between atoms according to Bragg's Law (Epp, 2016), which then represents a distinct set of d-spacings, the characteristic fingerprint of materials. Quantitative phase analysis was performed using the Rietveld refinement method (Westphal et al., 2009), providing mineral compositions. X-ray diffraction and Rietveld refinement in this study, plus subsequent interpretation of the results were performed by Andreas Karlsson (Swedish Museum of Natural History) and Prof. Valentin Troll (University of Uppsala).

X-ray fluorescence (XRF)

XRF is a technique used to determine the elemental composition of a sample. In an XRF analyzer, a sample is irradiated and excited by a primary strong X-ray source leading to the displacement of electrons on the inner orbital shells of an atom. To retain stability, an electron from an outer orbital shell drops to the lower energy state of the inner shell, thereby emitting an element-specific amount of energy in the form of secondary X-rays (Oyedotun, 2018). This process is termed fluorescence. The emitted secondary X-rays are amplified and analyzed by a detector providing information about the elemental composition of the respective sample. The XRF analysis was performed by Dr. Jessica Stammeier (GFZ Potsdam) following the procedure outlined by Beckhoff et al. (2007).

1.6.4 Surface degassing

Many of the techniques described above address surface structures that are a consequence of long-term processes, such as the observed alteration patterns for instance. So they show a combination of effects of present activity but also previous activity. This is especially interesting as it might indicate the effects of spatiotemporal changes and dynamics of the system, but the present-day component has to be distinguished. We did that by analyzing the thermal structure, but also by analysis and comparison with the present-day surface degassing patterns, obtained from a measurement campaign following an accumulation chamber approach (Chiodini et al., 1998), utilizing a simplified accumulation chamber connected to a handheld multigas instrument measuring CO_2, H_2S, and SO_2 simultaneously. A detailed description of the measurement procedure can be found in Appendix A.4.2. The analysis of the thermal structure and of spatial variabilities of certain gas species was especially beneficial in order to explain some of the observed effects and to highlight processes associated with degassing of especially acidic gas species.

1.7 Short summaries of research chapters

The research is presented in 3 chapters, each of which includes a peer-reviewed publication that addresses the research questions posed. Minor modifications were made to accommodate formatting differences. Chapters 2 to 4 are first-author publications, of which chapters 3 and 4 are related and build upon each other. A brief summary of chapters 2-4 is provided below.

Summary Chapter 2: Distribution, structural and hydrological control of the hot springs and geysers of El Tatio, Chile, revealed by optical and thermal infrared drone surveying

This work addresses the first research questions and examines the structural makeup of the El Tatio hydrothermal system and potential controls. We used Structure from Motion processing of airborne optical and infrared imagery of El Tatio (Chile), one of the largest geyser fields in the world, to create a high-resolution database of orthomosaic, digital elevation model, and infrared mosaic. From these, we identified objects associated with hydrothermal activity, stored them in a mapping database, assigned them unique attributes, and classified them into object types. We then analyzed their distributions and topologies and placed them in the context of local geologic structures. We show that hydrothermal vents cluster into at least 5 spatially

distinct groups, each with specific vent arrangements and discharge characteristics. An analysis of vent arrangements revealed a dominance of two azimuthal directions and a preferred orientation of vents along lineaments or intersecting lineaments. The general location and orientation of vent clusters are consistent with an earlier described fault, but observations at more local scales suggest a more complex setting. Local-scale vent arrangements are likely influenced by a preexisting fracture network, as evidenced by a fracture pattern in a bedrock formation at the northern boundary of El Tatio, that resembles the same two preferred azimuthal directions. In addition to structural controls, We propose additional hydrological controls that influence the dominance of certain vent types in certain areas. With this work, we provide a detailed picture of the structural arrangement of the El Tatio hydrothermal system, show new insights into the controls of vent arrangements and discharge peculiarities, and also provide evidence for temporal effects such as local large-scale silica precipitation and vent evolution dynamics.

Author contributions:
Daniel Müller is the lead author and is responsible for writing, and editing the manuscript, as well as handling the peer-review and publication process, contributing to over 70% of the paper. Daniel Müller is also responsible for all processing and analysis of remote sensing data. The co-authors contributed as follows: Thomas R. Walter provided all funding, acquired the data, and supervised and supported the writing of the manuscript. Martin Zimmer and Gabriel Gonzalez supported this project due to their long-term engagement in Chile and supported the writing of the manuscript.

This chapter and the corresponding supplementary material have been published in Elsevier - Journal of Volcanology and Geothermal Research:

Müller, D., Walter, T. R., Zimmer, M., & Gonzalez, G. (2022). Distribution, structural and hydrological control of the hot springs and geysers of El Tatio, Chile, revealed by optical and thermal infrared drone surveying. Journal of Volcanology and Geothermal Research, 432, 107696. https://doi.org/10.1016/j.jvolgeores.2022.107696

Summary Chapter 3: Surveying fumarole sites and hydrothermal alteration by unoccupied aircraft systems (UAS) at the La Fossa cone, Vulcano Island (Italy)

This work explores the potential of drone-based remote sensing data to investigate volcanic degassing systems with particular focus on hydrothermal alteration. It has a methodological

and volcanological focus. We used SfM processing to generate a high-resolution orthomosaic image and a thermal infrared mosaic from our airborne data, which then served as a database for the analysis. Unlike satellite remote sensing, there are often no established workflows available for the further analysis of drone-derived data, so approaches for information extraction from drone-derived orthomosaics need to be developed. We applied Principal Component Analysis on the original orthomosaic, a data transformation along the perpendicular axes of the highest variance of the initial RGB bands, resulting in an RGB decorrelation and providing a variance representation of the initial image data. This allowed us to identify areas affected by volcanic degassing and associated hydrothermal alteration effects. Local variability within the as altered identified regions apparently represents alteration gradients. We identified several spatially distinct regions, analyzed their spectral characteristics, and found that they cluster into 3 surface types, outlining a specific structural makeup of the fumarole field. The improved data separability associated with PCA (due to RGB decorrelation) allowed us to extract data portions of interest and perform more sensitive image and spatial analyses. We extracted thermal anomalies and sulfur deposits, vectorized them, and performed geospatial analysis taking into account the local crater topography. Thermal anomalies and sulfur deposits show systematic changes in azimuth orientation in the center of the fumarole field, accompanied by higher distribution densities of classified sulfur pixels and systematic color shifts that may indicate compositional, temperature or path effects of the emitted gases. This study demonstrated an efficient way to investigate poorly colorized high-resolution RGB data of volcanic degassing systems and provide several new insights into the structural setup of the La Fossa fumarole field and degassing and alteration pattern.

Author contributions:

Daniel Müller is the lead author and responsible for the conceptualizing, writing, and editing of the manuscript, as well as for handling the peer-review and publishing process, contributing to over 70% of the paper. Daniel Müller is also responsible for the acquisition and processing of data, the development of methodological approaches and workflows for quantitative image analysis and interpretation, as well as the creation of the figures.

The co-authors contributed as follows: Stefan Bredemeyer acquired data in the field, supported the writing, and reviewed the manuscript. Edgar Zorn acquired some of the drone-based image data and reviewed the manuscript. Erica De Paolo acquired data in the field and reviewed the manuscript. Thomas R. Walter supervised the project and the writing of the manuscript. All

authors contributed to the writing and editing of the manuscript, and have read and agreed to the published version.

This chapter and the corresponding supplementary material have been published in Elsevier - Journal of Volcanology and Geothermal Research:

Müller, D., Bredemeyer, S., Zorn, E., De Paolo, E., & Walter, T. R. (2021). Surveying fumarole sites and hydrothermal alteration by unoccupied aircraft systems (UAS) at the La Fossa cone, Vulcano Island (Italy). Journal of Volcanology and Geothermal Research, 413, 107208. https://doi.org/10.1016/j.jvolgeores.2021.107208

Summary Chapter 4: Anatomy of a fumarole field; drone remote sensing and petrological approaches reveal the degassing and alteration structure at La Fossa cone, Vulcano Island, Italy

This work is a follow-up study to Müller et al. (2021), and focuses on resolving the detailed anatomy of the La Fossa fumarole field and constraining the influence of hydrothermal alteration. It consists of three approaches. In a remote sensing study, similar to Müller et al. (2021), We investigated the detailed degassing and alteration structure, based on anomaly detection in UAS-based high-resolution thermal and optical data. We resolved the general pattern of hydrothermal alteration and identified hydrothermal alteration gradients and major diffuse active units that, next to the actual fumarole sites, contribute significantly to the total activity.

To provide ground-truthing for our remote sensing results, we performed mineralogical and geochemical analyses of representative rock samples. This way we could prove that the observed anomalies are meaningful, link remote sensing and in situ processes, explain the driving forces for the observed anomaly pattern and also validate the methodological approach. The comparison of the revealed alteration structure with the present-day thermal structure and diffuse degassing pattern allowed us to distinguish the present-day activity pattern from prior activity, assess the state of essential units of the degassing system, and highlight areas of increased diffuse degassing activity, but also areas where we observed potentially critical evolution, such as surface sealing. The presented combination of methods is an efficient and comprehensive approach to investigating volcanic degassing systems. This work provides the, to date, most detailed picture of the anatomy of the La Fossa fumarole field and has implications for further alteration research and volcano monitoring.

Author contributions: Daniel Müller is the leading author and responsible for the conceptualizing, writing, and editing of the manuscript as well as for handling the peer-review and publishing process, contributing to over 60% of the paper. Daniel Müller is also responsible for the acquisition and processing of remote sensing data, the collection of samples, and the gas measurement campaign. The co-authors contributed as follows: Thomas R. Walter provided funding and instruments, supported the conceptualization, and supervised the writing. Valentin R. Troll supported the conceptualization, initiated and interpreted XRD analysis, and supervised the writing. Jessica Stammeier performed an XRF analysis and supported the writing. Andreas Karlsson performed an XRD analysis and supported the writing. Erica De Paolo collected data and samples, supported most of the fieldwork, and supported the writing. Antonino Fabio Pisciotta supported fieldwork and on-the-ground logistics, acquired data, and supported the writing. Martin Zimmer supported the gas measurement campaign and supported the writing. Benjamin De Jarnatt supported the fieldwork and writing of this manuscript.

This chapter and the corresponding supplementary material have been published in EGU - Solid Earth, currently in a preprint version open for public review and discussion.

Müller, D., Walter, T. R., Troll, V. R., Stammeier, J., Karlsson, A., De Paolo, E., ... & De Jarnatt, B. (2023). Anatomy of a fumarole field; drone remote sensing and petrological approaches reveal the degassing and alteration structure at La Fossa cone, Vulcano Island, Italy. *EGUsphere*, *2023*, 1-45. https://doi.org/10.5194/egusphere-2023-1692

Chapter 2

Distribution, structural and hydrological control of the hot springs and geysers of El Tatio, Chile, revealed by optical and thermal infrared drone surveying

Daniel Müller (1), Thomas R. Walter (1), Martin Zimmer (1), Gabriel Gonzalez (2)
Correspondence daniemue@gmx.de

(1) GFZ German Research Center for Geosciences, Telegrafenberg, 14473 Potsdam, Germany
(2) CIGIDEN, National Research Center for Integrated Natural Disaster Management, Departamento de Ciencias Geológicas, Universidad Católica del Norte, Antofagasta, Chile

This article was published in:
Journal of Volcanology and Geothermal Research, Vol. 432, Müller, D., Walter, T.R., Zimmer, M., & Gonzalez, G., Distribution, structural and hydrological control of the hot springs and geysers of El Tatio, Chile, revealed by optical and thermal infrared drone surveying, 107696, Copyright Elsevier (2022)

Abstract

Boiling mud ponds, hot springs, and geysers are the scenic surface expression of rising thermal fluids, often emerging in clusters. The details on the spatial appearance and structural control of such geothermal objects as well as on the variability of their locations are rarely investigated, however. Here we use Unmanned Aerial Systems (UAS) to acquire close-range optical and thermal infrared data over the El Tatio geothermal field (Chile), one of the largest geyser fields in the world. From high-resolution aerial images, processed using the Structure from Motion (SfM) method, we compute spatial image data at 1.5 to 14.5 cm resolution for a ~ 2 km^2 area. We identify 1863 objects related to geothermal activity, providing an unprecedented catalog of the geothermal area. Out of these, 148 were classified as topography objects (e.g. cone geysers), 415 showed signs of fluid discharge, and 1091 were characterized by a thermal signature exceeding background temperatures. The geothermal objects were further analyzed regarding their spatial distribution and clustering, suggesting a high degree of organization in 5 main groups on a broader scale, and clustering in specific vent arrangements resembling two main orientations on a smaller scale. The 5 zones show significant differences considering their

orientation, types of geothermal objects located within, but also their eruptive characteristics, and thermal energy release. We discuss these, considering the structural setup and hydrological setting of the El Tatio geothermal field. Over 90% of the mapped geothermal objects are located within a 100 m distance to an estimated trend line oriented NE-SW. We thus hypothesize a possible structural arrangement controlling the location and activity of geothermal objects at El Tatio with important implications for other geothermal areas worldwide.

2.1 Introduction

Geothermal fields develop spectacular features at the surface that are commonly associated with temperature anomalies, hot gas and fluid discharge, remineralization, and silica deposition relevant for exploitation (Ruff and Farmer, 2016). One of the most scenic surface expressions is geysers with explosively and episodically erupting water fountains. In some places, those geysers erupt 30 m or higher jets of water and steam. Geysers can be regarded as geothermal piercing points that tend to develop in groups and in association with a variety of hydrothermal surface manifestations like thermal springs and boiling mud pools (Rinehart, 2011). The study of the location, distribution, and phenomenology of these geothermal objects, may allow us to infer the fluid pathways at depth and in the shallow crustal structure (Hurwitz and Manga, 2017). To assess their appearance and distribution, remote sensing techniques have been particularly useful (Neale et al., 2009).

Satellite missions such as LANDSAT Thematic Mapper, ASTER, and MODIS provide data with a resolution of several meters and allow a general overview of geothermal regions and deposition mapping on a broader scale (Rowan et al., 2003; Di Tommaso and Rubinstein, 2007; Carranza and Hale, 2002; and others). However, small-scale geothermal objects, such as boiling mud ponds, hot springs, and geysers, are often decimeter-scale only and remain invisible due to the coarse resolution of the satellite sensor. High-resolution optical satellites (Pleiades, Quickbird) and airborne photogrammetry may exceed the 1-m resolution scale, and provide much more detailed, three-dimensional point cloud data that can be used for morphometric and structural analysis (James et al., 2020). Studies at geothermal fields ideally are complemented by temperature field studies. Airborne thermal infrared (TIR) analysis realized by a forward-looking infrared (FLIR) camera over the Yellowstone geothermal area revealed a structural control of hot sites, pools, and thermal springs (Neale et al., 2016). Unmanned Aerial Systems (UAS) allow a centimeter-scale analysis of the morphology or

structural setup of geothermal fields, such as the Haukadalur geothermal field in Iceland (Walter et al., 2020) or the fumarole field of the La Fossa cone, Vulcano island (Müller et al., 2021).

Repeated airborne measurements could identify the spatio-temporal changes of geothermal objects, e.g. disappearing, migrating, or establishing new manifestations, underlining that also geothermal changes follow trends of preexisting structures like fractures and faults (Neale et al., 2016; Friedman, 2007). However, in many geothermal fields, the details about the structural geology are hidden beneath younger deposits and are difficult to map out directly. However, the detailed study of the distribution, clustering, and alignment of boiling mud ponds, hot springs, and geysers may allow indirect mapping of a hidden structural architecture. This was demonstrated at Yellowstone National Park, where airborne TIR measurements could reveal a fracture-dominated hydrothermal system that is arranged in an N-S direction, in agreement with the structural architecture (Dzurisin et al., 2012; Chang et al., 2007; Neale et al., 2016).

The activity of boiling mud ponds, hot springs, and geysers is thought to be controlled by intrinsic and extrinsic factors. Intrinsic factors are, amongst others, the geometry of holes and craters at the surface, the width and path of the water-filled conduit, the depth and dimension of reservoirs, and the mixing of different fluid phases. For instance, the path and conduit geometry affect the water-column temperature (Walter et al., 2020). The width, temperature, and depth of the conduit control eruption intervals (Hurwitz and Manga, 2017), and the depth of a reservoir or bubble trap controls the height of eruptions (Reed et al., 2021), as well as recharge and the periodicity of eruptions (Eibl et al., 2021). Extrinsic factors are the external modulation of the appearance, style, and frequency of the bursts occurring at boiling mud ponds, hot springs, and geysers, and may involve hydro-meteorological factors (Hurwitz and Manga, 2017), triggered by tectonic earthquakes (Manga and Brodsky, 2006) and volcanic unrest (Neale et al., 2016). To better understand the location and appearance of boiling mud ponds, hot springs, and geysers, and the hidden structural architecture along which they form, a detailed and high-resolution mapping and geospatial analysis of geothermal objects are important.

Here we explore the geothermal objects of El Tatio, which is the third-largest geyser field in the world after Yellowstone National Park (USA) and the Valley of Geysers (Kamchatka). The El Tatio geothermal field has dimensions ideally suited for UAS, hosting many different objects in proximity. We describe data collected during past years' field works, where our UAS were equipped with both high-resolution optical and FLIR radiometric cameras, respectively,

to map extinct and active thermal spots and geysers in unprecedented levels of detail.

2.2 Study area

The El Tatio geothermal field is located in the western cordillera of the Central Andes Volcanic Zone (CVZ) around 22°33′ S and 68°00′ W, close to Calama. Located at an altitude of >4200 m, El Tatio and the neighboring Sol De Manana are the highest elevated geothermal fields known. The El Tatio geothermal field contains >80 active geysers, uncounted hot springs, mud ponds, fumaroles, and mud volcanoes (Glennon and Pfaff, 2003) that are also an important tourist attraction due to the widespread steaming and thermal sites (Fig. 2.1).

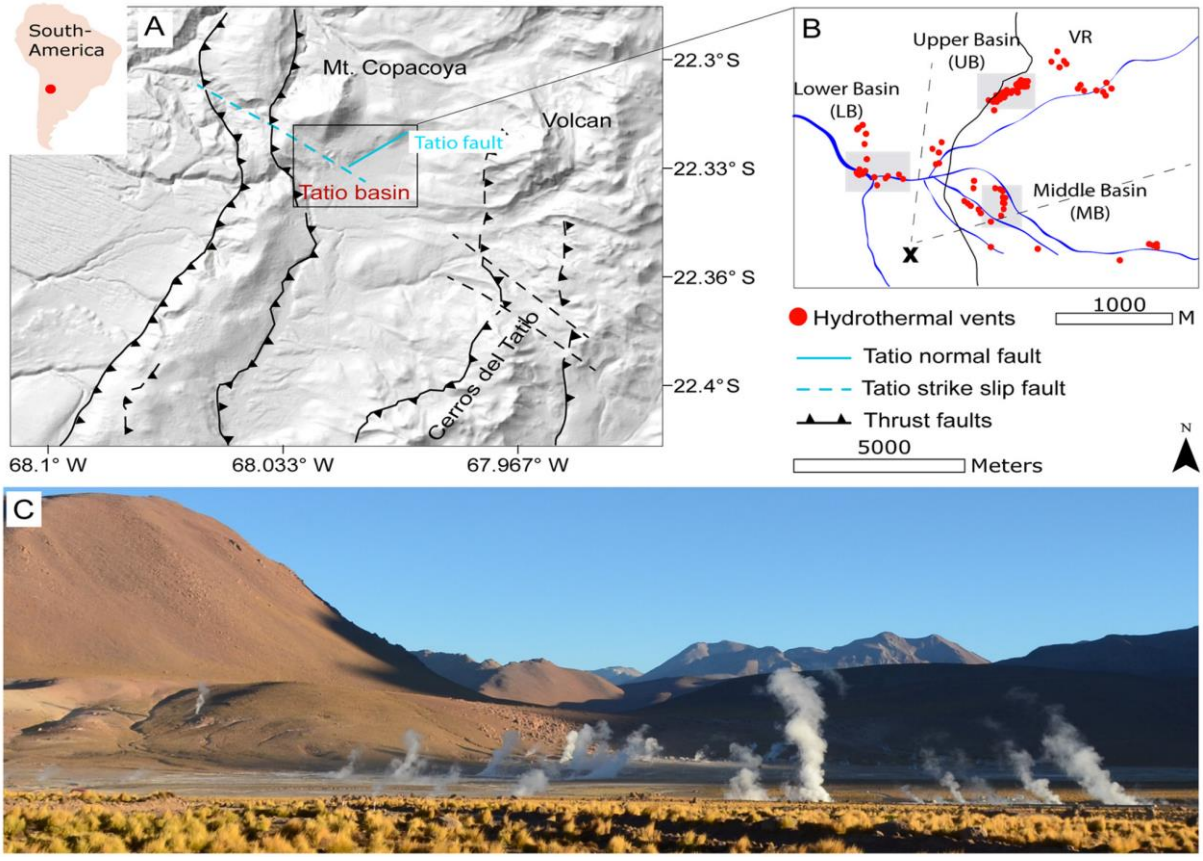

Fig. 2.1 (A) El Tatio geothermal field with simplified geological and tectonic map (after Lucchi et al., 2009), showing the El Tatio basin embedded in the broader geologic context of a compressive regime. Blue lines indicate two local faults relevant to El Tatio. The inset shows the location in Chile. (B) The spatial arrangement of hydrothermal surface manifestations (after Glennon and Pfaff, 2003). (C) Photograph showing the steaming grounds and locations of hot springs and geysers in the upper basin, seen from the southwest. The acquisition position and view angle are marked in Fig. 2.1B by an X and dashed lines.

The geothermal activity of El Tatio is closely associated with volcanism developed as result of the subduction of the Nazca oceanic plate beneath the South American continental plate, where major magmatic intrusions and eruptions produced a province of enormous volcanic deposits ranging from 21˚S to 24˚S, called the Altiplano–Puna Volcanic Complex (De Silva, 1989). Several major tephra and ignimbrite eruptions during the past millions of years created the Altiplano Puna Volcanic Complex with calderas exceeding 10 km in diameter (Zandt et al., 2003). The region is intensely faulted, as documented by the Serrania de Tucle–Loma Lucero horst in the West, and aligned volcanic centers in the East. N-S-oriented thrust faults in the east and west of the El Tatio geothermal field indicate an *E*-W compressive regime (Lucchi et al., 2009). Today the El Tatio geothermal field is located in a NE-SW elongated tectonic graben, filled by up to 2000 m thick ignimbrites and tephra, overlain by glacial sediments (Procesi, 2014), forming a basin of 6 km in length and 4 km in width. Two main fault structures are dominant in the El Tatio basin (Fig. 2.1), a NE-SW striking fault referred to as the Tatio fault, and a SE-NW striking left lateral transverse fault that intersects at the western edge of the El Tatio geothermal area (Lahsen, 1976; Lucchi et al., 2009; Montecinos-Cuadros et al., 2021). These faults are natural boundaries, nowadays relevant for the subterranean pathways of the geothermally heated waters aggravating the lateral flow, as well as for the rise and expulsion of geothermal waters at the surface (Lucchi et al., 2009; Montecinos-Cuadros et al., 2021).

The El Tatio geothermal system is fed by geothermal water that originates from precipitation in the higher Andes, *E*-SE of El Tatio (Giggenbach, 1978; Healy and Hochstein, 1973; Zandt et al., 2003; Munoz-Saez et al., 2018). It is heated by contact within the Laguna Colorada complex ~20 km east of El Tatio, transported through permeable layers, and enters the Tatio basin in the southeast (Lahsen, 1976). Isotopic studies prove this model and propose a residence time of over 60 years until the waters discharge in the Tatio basin (Cortecci et al., 2005; Munoz-Saez et al., 2018). At depth, the waters are migrating laterally along the regional slope and ascent at fractures aligned NE-SW and SE-NW (Fernandez-Turiel et al., 2005). Two aquifers of thermal waters were identified, a shallow and colder aquifer (<250 m and ~ 160 °C) and a deeper aquifer (>800 m and ~ 260 °C) of which the deeper aquifer is assumed to be the dominant main aquifer (Lahsen, 1976; Healy and Hochstein, 1973; Giggenbach, 1978). Recent studies based on electrical resistivity provide a detailed image of the shallow structure of the Tatio basin, showing a persistent shallow (<60 m) high conductivity layer and the presence of an impermeable geological barrier controlling fluid flow (Montecinos-Cuadros et al., 2021).

El Tatio can be subdivided into 3 pronounced regions, the upper basin (UB) hosting the

majority of active geysers, the middle basin (MB), and the lower basin (LB) (Lahsen, 1976). The UB is bound to the east by the Vega Rinconada (VR), a wetland densely populated with surficial ponds and boiling mud ponds. Geothermal activity is densely concentrated in these three regions and covers an area of about 10 km^2 (Fernandez-Turiel et al., 2005). But geothermal objects can be found over a larger area of 30 km^2 (Healy and Hochstein, 1973; Lahsen, 1976; Glennon and Pfaff, 2003). For a detailed summary of the region, we refer to Lahsen (1976).

The geothermal manifestations of El Tatio are active as long as 27 ka (Munoz-Saez et al., 2020), which is an extended period of emission of high-chloride waters (Giggenbach, 1978) and led to the built-up of large sinter cones, mounds, and terraces. A detailed analysis of the sinter accumulation history suggests that some of the sinter mounds have been active for over ten thousand years (Wilmeth et al., 2020).

El Tatio has been studied for ~100 years now (Tocchi, 1923), with extensive examinations realized in the 1960-70ties (Lahsen, 1976) to investigate the potential of El Tatio to be used for geothermal exploration (Procesi, 2014). El Tatio has been studied with a focus on geothermal resource exploitation for instance in the United Nations Development Program (CORFO/UNDP) (Armbrust et al., 1974; Cusicanqui, 1975; Lahsen, 1976; Giggenbach, 1978). The last detailed mapping approach was realized using traditional ground-truthing, where approximately 80 active geysers were counted, plus an unspecified number of boiling mud ponds, hot springs, and remnants of earlier activity (Glennon and Pfaff, 2003). Individual geysers have recently been studied by modern geophysical methods, revealing episodic deformation associated with the eruptions and rather complex conduit structures in the first few meters beneath the ground (Munoz-Saez et al., 2015). However, a systematic investigation of the distribution of the boiling mud ponds, hot springs, and geysers as well as relation to sinter expressions of extinct geysers and a structural control was not performed yet. El Tatio is considered not only one of the largest but also one of the least studied major geothermal fields on Earth (Fernandez-Turiel et al., 2005).

In this work, by precise drone-based mapping and geospatial analysis of the distribution and types of hydrothermal features, their structural control and possible evolution will be elaborated for the first time.

2.3 Data and methods

2.3.1 Drone data collection

The field studies in El Tatio were realized during the Southern Hemisphere summer period (November to February) in the period 2014–2020. The aim of this work is the geospatial mapping, and the generation of a data inventory that can be used to statistically analyze locations, clustering, and alignments of geothermal objects. To this aim, we acquired drone-based optical and infrared image data of the central El Tatio geothermal field, referred to as the upper basin (UB). The UB is an elongated NE-SW trending area of densely clustered boiling mud ponds, and hot springs, and hosting the majority of geysers documented in the greater El Tatio geothermal field (Glennon and Pfaff, 2003; Munoz-Saez et al., 2018).

For the acquisition of our close-range aerial photogrammetric data, we performed overflights by utilizing different UAS equipped with both optical and thermal infrared (TIR) camera systems. These multiple surveys guaranteed the complete photogrammetry coverage of the high-altitude region (above 4200 m). Optical data was acquired in 2014, 2016, and in 2020. The 2014 survey was realized with a helium-filled balloon, and the 2016 and 2020 surveys with commercially available drones manufactured by DJI, respectively. By combining the data, we could realize a complete optical, three-dimensional, and thermal infrared geospatial analysis of the UB. The data was analyzed statistically, a temporal change analysis was beyond the scope of the present manuscript, however. Following the data processing and the creation of an inventory database, we were able for the first time to produce a detailed description of the spatial distributions of hydrothermal objects, their appearance, and the possible structural arrangement.

In 2014, the image acquisition was performed using a 3 m^3 helium-filled balloon-kite (Helikite, manufactured by Allsop Helikites Inc., UK), equipped with a Ricoh GR mounted in nadir view under the kite. The Ricoh GR camera has a high-quality optical 16.9-megapixel CMOS Sensor (APS-C 23.6 × 15.8 mm). With its fixed 14 mm focal length and 16.9 MP resolution, it provides the highest quality images of all our surveys. For the acquisition, the Helikite was attached by a rope to a person walking in loops on the ground, and flight altitudes from 50 to 120 m above ground were realized. The acquisition rate was set to one image per 10 s. The data is of high quality and resolution but due to the poor ability of flight path control, images are often acquired oblique and do not completely cover the upper basin.

Mapping campaigns of the following years were performed by manually controlled quadcopter-UAS. The steady evolution of copter-based UAS during recent years now provides

easy-to-use and efficient tools for mapping campaigns, equipped with high-quality camera systems, permanent GPS tracking, and flight path control in the live view mode. Modern Quadcopter-UAS are capable of flying at high altitudes of over 5000 m, but at the cost of increased energy consumption, decreasing the flight times significantly to approximately 15 min. In 2016, the data acquisition was performed using a DJI Matrice 100 quadcopter, a mid-sized copter able to carry a payload of ~1.5 kg at 4200 m altitude. The drone was equipped with a 12 MP Zenmuse X3 camera, recording optical images at an acquisition rate of 0.5 Hz. The 2020 survey was merely aimed to obtain additional ground-truthing and collect ground control points. Optical overflights in 2020 were performed using a DJI Phantom 4 Pro, equipped with a 20 MP optical camera and 1" CMOS sensor. The acquisition rate was set to 0.5 Hz.

All optical overflights were performed during the daytime, from noon to afternoon, when the atmosphere was clear and the visible steaming activity of the geysers was low. The image data were acquired in nadir mode and geotagged by GPS, providing an approximate acquisition position and altitude in the image metadata. To improve the localization and referencing of the different data sets, additional Ground Control Points (GCPs) were acquired at marker flags, 0.25 × 0.25 m in size, and at natural markers, such as boulders, holes, or man-made structures. GCPs were measured by dual-frequency DGPS (Differential Global Positioning System). We used the GCPs and point cloud referencing to transfer the maps and final data into accurate and matching geolocation.

The thermal infrared (TIR) data was acquired in 2016 by using a Flir Tau 2 camera, which is a fully radiometric camera sensor with a 9 mm lens and a resolution of 640 × 512 pixels. The camera was mounted to the drone by a 3D-printed camera mount in a nadir view position to the ground. The Flir Tau 2 images are stored in a Teax Thermal Capture data logger at an interval of 8 Hz. The Flir camera sensor operates in the 7.5–13 μm thermal infrared band and was set to a calibrated temperature range of − 40 to 120 °C (high gain mode). This was considered a sufficient temperature range to cover the expected thermal expressions at El Tatio. The camera and data logger are powered by an external lithium-polymer battery, and an external GPS mouse provides the recorded images with geotags.

Infrared flights were realized before sunrise (between 3 and 5 a.m.) to minimize distortions like irregular surface heating due to solar radiation, and exclusively map radiation emitted by the hydrothermal system. Further, the low outdoor temperatures (commonly − 10 to 0 °C) are beneficial to obtain the highest temperature contrasts and allow the mapping of low-

temperature anomalies. Temperatures obtained by thermal remote sensing are considered apparent temperatures and are affected by pixel size to vent ratios, radiative properties (emissivity) of the measured object, but also to hydro-meteorological conditions, and water vapor or steam plumes, which may largely affect the results (Ball and Pinkerton, 2006). Therefore, the apparent temperatures, especially in natural environments, are typically lower than direct in situ temperature measurements. To account for these effects, we considered a mean emissivity of the ground of 0.95 and a transmissivity of 0.7, which is in accordance with many previous studies (Stevenson and Varley, 2008; Spampinato et al., 2011). Due to the low distance to ground flights, and the low humidity of the air at the high latitude of El Tatio, atmospheric distortions are considered to be negligible. An overview of the acquired data sets, including acquisition and processing parameters can be found in Table 2.1. All collected drone data was locally stored and then analyzed using the Structure-from-Motion approach described below.

Table 2.1: Overview of the processed data sets 1–4, respective flight altitudes, camera systems used, images used for the processing, number of data points in the dense point cloud and resulting pixel resolution, the area covered, and point density in points/m². The point density of the processed dense point clouds ranges from 423 data points per m² to 11 points per m², resulting in resolutions from 1.5 cm/pixel to 29 cm/pixel. Feature detection thresholds of the different data sets increase or decrease accordingly.

Data set	Data type	Flight altitude (m)	Camera system	Images processed	Dense cloud (m points)	Resolution cm/pixel	Area (km²)	Point density (p/m²)
1	**2014 Mosaic**	50	Ricoh GR	532	68.3.	1.5	0.16	423
1	**2014 DEM**	50	Ricoh GR	532	68.3	4.9	0.16	423
2	**2016 Mosaic**	370	Matrice 100	101	29.0	14.5	2.09	12
2	**2016 DEM**	370	Matrice 100	101	29.0	29	2.09	12
3	**2020 Mosaic**	250	Phantom 4 Pro	397	94.8	6.4	1.36	60
3	**2020 DEM**	250	Phantom 4 Pro	397	94.8	12.8	1.36	60
4	**2016 TIR**	100	Teax TC 2	1308	10.6	15.1	1.01	11

2.3.2 Structure-from-Motion (SfM)

The Structure-from-Motion approach allows for generating data sets from a series of photographs, reproducing surfaces in 3 dimensions, and merging the high resolution of single photographs to cover larger areas. To do so, all image data were inspected, quality checked, and preselected. Images out of focus were removed, and regions with insufficient data were omitted. We considered only high-quality images, assuring an overlap of about 70%, for processing. The software used is the Structure-from-Motion commercial software package Agisoft Metashape Professional Edition (vs. 1.6.0). We loaded the data into individual data chunks, then performed a coarse alignment and dense cloud reconstruction in high resolution. In the following step, we generated a textural dataset, a digital elevation model, and built the orthomosaic. The geolocation of the data was realized by both, in-built GPS geo-tagging of the drones, and by the use of 24 ground control points measured with a dual frequency GNSS receiver, which we processed independently, and defined as reference markers in each chunk of the SfM processing. As a result of the SfM processing, we obtain high-resolution orthomosaic maps, digital elevation models (DEM), and thermal infrared-mosaic (TIR) in GeoTIFF format (Fig. 2.2).

From our aerial data, four data sets were created (Table 2.1). The aim of these data sets in here is to generate a high-resolution database (examples are provided in Fig. 2.3) to be used for structural and geomorphological studies, where especially the combination of optical data, elevation data, and thermal signature is beneficial. Details of the data sets processed are as follows.

Data set 1 (2014) has the best quality in terms of resolution and detail but covers only the central part of the upper basin. It was created from 532 images, acquired with the Ricoh GR camera mounted under a balloon-kite. The low flight altitude of 50–120 m combined with the 16.9 MP CMOS sensor of the Ricoh GR DSLR camera provides us a data set of a very high data point density of 423 points per square meter (68,349,514 data points covering an area of 162,619 m^2). The eventually resulting pixel resolution is 0.015 m for the orthomosaic and 0.05 m for the DEM.

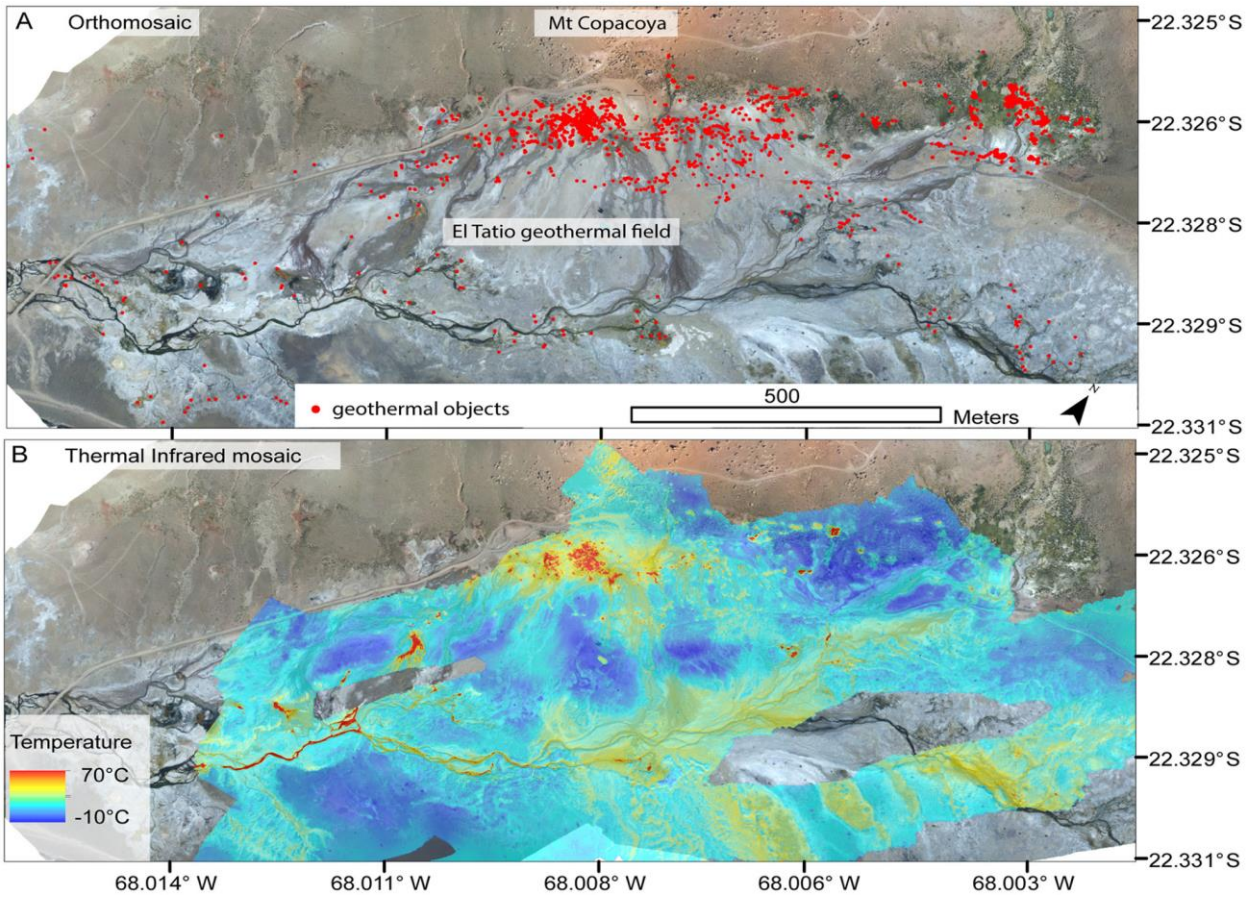

Fig. 2.2 Data set overview showing the El Tatio geothermal field as orthomosaic (A) and thermal infrared mosaic (B). The red dots in A mark the mapped geothermal object inventory derived from drone data (this work).

Data set 2 and 3 were taken from higher altitude overflights and covered the whole upper basin but at the cost of a lower pixel resolution. Data set 2 (2016) was processed from 101 images, acquired at a flight altitude of ~350 m by a DJI Matrice 100. With 29,021,800 points covering an area of 2.09 km^2, this data set has a point density of only 12 pixels per square meter (3% of the point density of the Ricoh data set) and a pixel resolution of 0.15 m for the orthomosaic and 0.3 m for the DEM. Data set 3 was processed from 397 images acquired at a flight altitude of 250 m by a Phantom 4 Pro quadcopter with a 20 MP camera. With 94,811,839 points on 1.36 km^2, this data set has a point density of 60.8 points per square meter, resulting in a pixel resolution of 0.06 m for the orthomosaic and 0.13 m for the DEM. All optical data sets were processed in high resolution in Agisoft Metashape. Where possible, we use the higher quality data set respectively for the analysis.

The thermal infrared (TIR) data was inspected and preprocessed in Thermoviewer (Version 2.0 and 3.0). A radiometric correction was applied assuming the emissivity of 0.95. A selection

of 1308 thermal images was exported in 16-bit grayscale TIFF format and further processed in Agisoft Metashape. The resulting thermal infrared mosaic (data set 4) covers an area of 1.01 km^2 at a resolution of 0.15 m. Details of the data sets used in this study are provided in Table 2.1. The presented data sets were used to investigate and catalog El Tatio's geothermal surface manifestations, as described in the following.

2.3.3 Geothermal object-mapping

2.3.3.1 Inventory

A geothermal object mapping was realized based on the optical orthomosaic maps, the DEM, and a thermal-infrared mosaic (TIR). The data covers the central and eastern sectors of the El Tatio valley, referred to as the upper basin (UB). Our data now allows for a comprehensive study of the number, location, types, and distribution of objects related to geothermal activity. Typical geothermal objects are cone geysers, geysers erupting from flat sinter slabs or fractures, sinter mounds, hot springs, pools with sinter rims, mud ponds, or natural springs. Those were identified either based on their optical appearance from the orthomosaic, their topography (relative elevation above the surrounding ground e.g. cone geysers or sinter slabs) in the DEM, or their thermal signature in the infrared mosaic. A selection of common geothermal objects and their appearances in our data sets is shown in Fig. 2.3. The manually digitized geothermal objects were stored in an ArcMap geodatabase (vs. 10.2.1) and were further specified by basic attributes like temperature signal, signs of discharge, topography, the existence of microbial mats (Dunckel et al., 2009), and a possible type of object was inferred. All objects are provided with precise coordinates, which allow us a detailed analysis of their geospatial relationships like topological relationships, density distribution, clustering, vent alignments, or azimuthal orientation of aligned objects or object clusters.

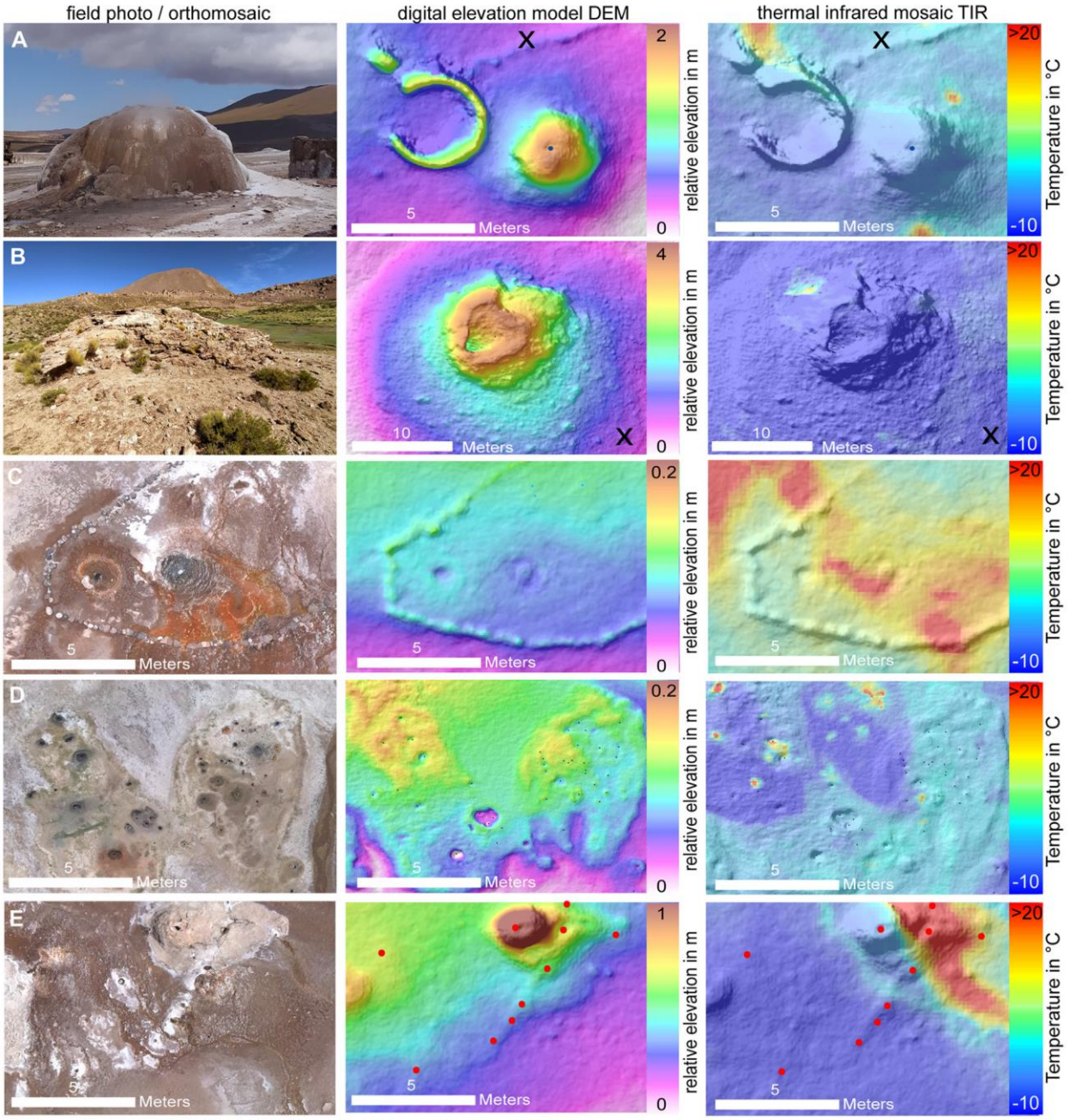

Fig. 2.3 Examples of geothermal objects and their appearance in our data are shown as field photos or orthomosaic (left), digital elevation model (center), or thermal infrared mosaic (right). Objects shown are an active cone geyser (row A), an extinct sinter mound (row B), a series of hot springs or pool geysers (row C), a series of mud ponds (row D), and a combination of a sinter slab and vents arranged along a lineament or fracture (row E). The rough viewpoints for field photos in rows A and B are marked by an X. Potential vents in row E are marked by a red dot for better visibility. The large elliptic form in row C is made artificially by boulders aligned.

2.3.3.2 Cluster analysis

A cluster analysis, applying the density-based cluster algorithm DBSCAN in R (Ester et al., 1996; Hahsler et al., 2019), was performed on the classified (topography, water discharge, temperature signal) mapped geothermal objects. To this aim, we were using a minimum point number of 4, and varying search distances (3, 5, 10, 20, 50, and 100 m). In the case of elongated-shaped clusters, cluster azimuths were calculated by linear regression through the coordinates of all points. The cluster analysis allowed testing if geothermal objects are arranged in a clustered or aligned fashion. We then test if the local Tatio fault (Lahsen, 1976), see also Fig. 2.1, is in agreement with the locations and clusters of the objects. We note that the DBSCAN cluster algorithm is appropriate to detect the general orientation of point clusters, but the radial search distance cannot resolve anisotropic orientations like lineaments. For that reason, in the case that vent clusters are apparently arranged along lineaments or intersecting lineaments, a manual lineament mapping was additionally performed.

2.3.4 Volumetric analysis

Discharge of hydrothermal fluids is associated with the precipitation of minerals and sinter deposition. To analyze these effects throughout the El Tatio basin, sinter volumes were calculated. The calculation is based on the elevation difference of the 2020 DEM to an artificial plane, a Mean-DEM, calculated from the same data set as the average of the elevation information over a certain area. For the calculation of the Mean-DEM, a kernel with a width of 390 cells equal to 50 m, and 1953 cells equal to 250 m was used. This range enables us to better locate hydrothermal features over various scales, ranging from single sinter cones to larger sinter complexes and eventually plateaus covering thousands of square meters. From this differential DEM (dDEM) a relative elevation contour map (5 cm interval) was calculated and the outlines for single objects were identified. Due to the large number of contours created from the dDEM, we reduced the file size by omitting all contours with a length below 5 m. From this dataset, volumes were calculated for the main body of prominent single objects, and their basements, but also larger sinter complexes. We note that this dDEM analysis can only help to identify those geothermal objects that are topographically expressed. For the distinction of these sinter bodies to the surrounding, the lowest contour of an approximately circular shape was chosen in accordance with the information of a slope map. In case the zero contour line was not appropriate, another contour line was picked, and the height was corrected. The Mean-

DEM was clipped by these contours and the raster cell values were multiplied by the cell area, providing a volume per cell, and eventually summarized within the respective object outlines providing a volume per object or object cluster.

2.3.5 Thermal infrared analysis

The thermal radiative power was used to characterize the thermal emission of single vents and areas, and as a relative discharge estimate for comparison. Based on our 16-bit grayscale thermal infrared mosaic, we calculated an apparent temperature map by

$$Tp\ (in\ K) = grayvalue * 0.04 \quad (1)$$

The calculated pixel temperature is representing the remotely sensed temperature (also termed apparent or brightness temperature). To be able to spatially separate single eruptive units from others, we defined the 0 °C isotherms as the lower boundary and extracted the raster data at $T > 0$ °C. We calculated the radiative power by applying the modified Boltzmann Law.

$$Q = e * b * A * (Tp^4 - To^4) \quad (2)$$

The emissivity (e) was assumed to be 0.95, the Boltzmann constant (b) is 5.670737×10^{-8} $Wm^{-2}K^4$, the area of a pixel (A) is 0.024 m^2. *Tp* is the pixel temperature and *To* is the average background temperature (calculated mean of all pixels <0 °C, based on 37 Mio pixels) of − 12 °C. The background temperature accounts for radiation of 6.01 W/pixel or 250.57 W/m^2. In the results, we indicate the values for both, the total radiation and the background corrected radiation (then written in brackets). To calculate thermal emissions for large single vents, or active regions, pixels forming a spatial eruptive unit were summed within the 0 °C isotherms.

2.4 Results

2.4.1 Geothermal mapping and spatial distribution of hydrothermal objects

The generated data sets allow a detailed overview of the geyser field, its expression, topography, and thermal anomalies. The photogrammetric orthomosaics cover an area of up to 2.09 km^2. For the different orthomosaic data sets, we obtain a ground resolution ranging from 1.5 to 14.5 cm. The highest resolution is obtained at the region of the highest geyser activity at the northern boundary of the Tatio basin. The same data sets were also used to generate three-

dimensional point clouds, and from that digital elevation models (DEM) with a ground resolution of 4.9–29 cm. In addition, the thermal infrared data was processed in the same way but additionally provides thermal gradient analysis, at a resolution of 15 cm. Those four data sets were used to identify and classify geothermal objects. We mapped and cataloged 1863 objects related to geothermal activity (Fig. 2.2A and 2.4). This catalog represents a variety of object types of geothermal surface manifestations. We observed cone geysers, geysers erupting from fractures or pools, natural springs (low temperature), hot springs, mud ponds, sinter mounds, pools, or sinter rims, but also highly altered-, crater-perforated-, or steaming grounds. Field inspections could help to attribute common types of geothermal objects. In order to sort the dataset, the 1863 objects were grouped based on their dominant attributes into (i) topography objects (Obj_dem), (ii) water-discharging objects (Obj_h20), and (iii) thermal anomalies (Obj_therm).

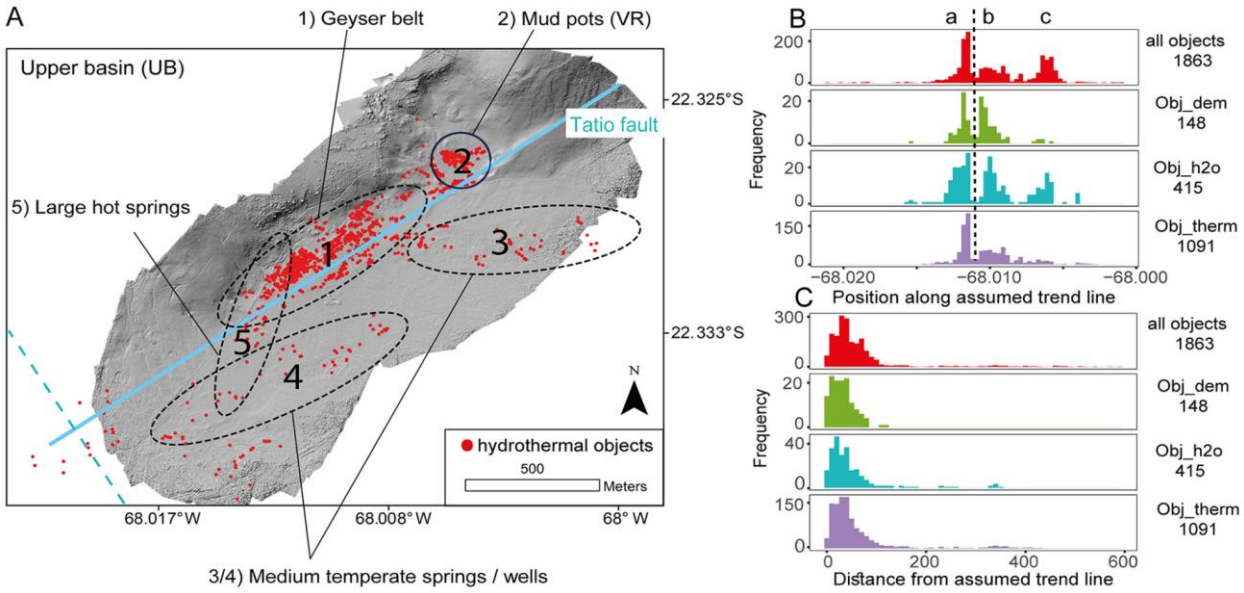

Fig. 2.4 Overview of the distribution of mapped geothermal objects in El Tatio. (A) Positions of objects related to geothermal activity are denoted by a red dot and cluster in 5 groups. The blue line indicates the estimated position of a local fault, referred to as the Tatio fault in the following. The dashed line indicates the approximate location of a second fault dominant in El Tatio (Lucchi et al., 2009). (B) The distribution density of the mapped objects along the local trend shows several distribution maxima but also activity gaps. (C) The distribution of the mapped objects normal to the estimated local trend line shows the majority of vents located in a narrow belt.

The topographic expression of the objects (Obj_dem) was identified from the DEM and the dDEM, which is the topography difference to the averaged elevation data (Mean-DEM). We consider the shape and relative elevation of objects above the surrounding ground. Obj_dem

comprises objects with evolved sinter bodies like cones, mounds, rims, or sinter terraces. Of the mapped objects, 148 were classified as Obj_dem, ranging in size from a sub-m^2 scale to large objects covering tens of m^2 and relative elevations up to >3 m. The largest of those, an inactive sinter mound, has a surface area of 108 m^2. As a criterion for the shape of sinter objects, we consider the height-width ratio. We analyzed 144 objects, of which only 16 have a height-width ratio above 0.2. Cone geysers typically range from h/w 0.25 to >1.

Out of all objects, 415 were showing signs of fluid discharge during the acquisition (Obj_h2o). Discharge is identified either from the orthomosaic or the TIR-mosaic.

The thermal anomalies (Obj_therm) are all objects identified based on thermal signature with temperatures exceeding the background temperature of − 12 °C. They represent the largest group by both number and area. Out of the 1863 objects, 1091 were identified based on their thermal signature. Their sizes range from pixel size to large complexes of thousands of m^2.

Mapped objects can display more than one of the classification characteristics. Objects that show no signs of activity like fluid discharge or a thermal anomaly might be considered inactive, or still active but in a temporary quiescent period. Cone geysers, in particular, tend to be free of any thermal anomaly during the quiescent periods, although in many cases they are still active. The large quantity of over 1863 mapped objects allows us to identify 5 spatially distinct groups (groups 1–5 in Fig. 2.4). The majority of the mapped geothermal objects are aligned along a NE-SW trending zone, especially group 1, herein referred to as a geyser belt. This zone is delimited towards the north by the topography of Mount Copacoya. The NE-SW alignment of the geyser belt is corresponding to the estimated location and orientation of a local fault (blue line in Fig. 2.4A, referred to as Tatio fault in the following) described earlier by Lahsen (1976).

To further evaluate the geometric relation between geothermal objects and the alleged Tatio fault, the positions of all identified objects were compared with respect to an assumed NE-SW trend line (Fig. 2.4B/C). In the direction along this trend line, we can identify several maxima of object density (Fig. 2.4B). The most expressed bimodal maximum representing group 1 is located between 68.013° and 68.008° W, hosting the majority of all objects (peaks a and b in Fig. 2.4B). Both density peaks are separated by an apparent geothermal gap at 68.0115° W, especially considering Obj_dem and water Obj_h2o. The third maximum represents objects of Group 2 and follows to the east (-68.0075° W to -68.005° W), separated by another activity gap from Group 1. Considering geothermal objects identified in the thermal data only (Obj_therm), we observe a distinct maximum of the number of objects at peak a.

Quantitatively, peak a represents the majority of mapped objects with 94% of Obj_dem, 72% of Obj-h2o, and 60% of Obj_therm.

Counting the number of objects as a function of the normal distance to the inferred NE-SW trend line, we found the majority of the mapped objects located in the vicinity of the trend line (Fig. 2.4C). In numbers, 90.5% of all mapped objects, 98.5% of Obj_dem, 91% of Obj_h2o, and 89.5% of Obj_therm are located within a 100 m distance. The distribution of the geothermal objects therefore follows the NE-SW oriented Tatio fault but rather points to more than a single fault plane. A closer look suggests that the geothermal object analysis reveals the presence of 3 or more linear zones that are oriented parallel to the Tatio fault trend, at some 80–250 m distance. Other groups appear subparallel (group 4) or oblique (groups 3, 5) to the main trend (Fig. 2.4). They are apparently less densely populated, which is supported by field observations. However, the data resolution and therewith feature detection threshold in this study is varying. The highest data resolution was obtained in areas coincident with groups 1 and 2. The absolute point density of mapped objects therefore might be influenced by this varying resolution.

2.4.2 Object group composition and characteristics of hydrothermal expressions

Each of the defined groups 1–5 shows distinct characteristics considering the location, elevation, but also object types, composition, and eruptive characteristics. Their typical appearance in the orthomosaic is illustrated in the photo pane in Fig. 2.5. The groups can be described as follows.

(a) Group 1 (Figs. 2.4 and 2.5A-C) is an elongated, densely clustered zone of 200 m in width (NW-SE) and 800 m in length (NE-SW), hosting the majority of the mapped objects in general and geysers in specific. Therefore, it is referred to as a geyser belt in the following. The geyser belt resembles the northern boundary of the El Tatio basin. We observe fluid discharge and the formation of geyser cones, sinter aprons, mounds, pools with rims, or large sinter terraces. The area is free of vegetation. Some pools and flow channels appear in bright orange-brown tints, indicating the existence of extensive microbial mats associated with high water temperatures, studied previously (Dunckel et al., 2009). An area of altered, highly perforated ground hosting hundreds of small holes/craters (A1 in Fig. 2.6), but with only minor discharge, is located in the western part of this group. A more detailed analysis of cone geysers and sinter deposits will follow in Sections 4.3 and 4.4.

(b) Group 2 (Figs. 2.4 and 2.5D-F) is located on the northeastern edge of El Tatio. It is composed of a high number of mud ponds and colored mud ponds that exclusively accumulate in this northeastern part. The surrounding ground appears perforated and apparently altered, hosting numerous water-filled pools/holes arranged in several distinct clusters. The largest ten of those have a surface area of >5 m^2 and the largest five range from 31 m^2 to 164 m^2. These objects are special as they represent rare locations with surface water reservoirs in El Tatio. The environmental conditions for vegetation seem less harsh and the widespread vegetation is indicating a sufficient freshwater supply. Vegetation is absent only in the central part, suggesting the existence of geysers or high-chloride water vents that are otherwise rare in this area. One prominent vent couple is dominating the area, an active one that formed a flat but widespread basement, and the largest (by volume, ~1500 m^3 including the broad basement) extinct sinter mound (Fig. 2.5F and S5 in Fig. 2.6). Group 2 is not covered by our thermal data, but the numerous mud ponds prove a hydrothermal influence. However, this area with its widespread vegetation is significantly different from the active areas further west.

(c) Group 3 (Figs. 2.4 and 2.5G-I) is located in the southeastern part of the Tatio basin. It consists of several vent clusters, which together resemble an elongated belt of 800 m in length and ~ 120 m in width, oriented N89°, obliquely intersecting the geyser belt. Group 3 is dominated by vents with evolved flow channels, instead of splash areas, indicating rather steady discharge conditions. Therefore, they might be considered rather natural or thermal hot springs. Water temperatures in this group are generally lower compared to group 1. But intermediate temperatures of up to 30 °C prove a geothermal influence. Several hydrothermal rims striking in a northwest direction are located in the southeastern part of group 3. They show only minor thermal anomalies and discharge but pronounced lineament-shaped white sinter mineralization.

(d) Group 4 (Figs. 2.4 and 2.5J-L) shows a similar extent and object composition to group 3. It is oriented N64°, subparallel to the geyser belt, with vents arranged in several vent clusters that together form a belt of ~130 m in width and ~ 950 m in length. Group 4 bounds the Tatio basin to the south. The eastern part of group 4 is characterized by medium-temperature springs. At the intersection with group 5, large hot springs become the dominating feature, and water temperatures, as well as discharge volume, seem to increase (see chapters 4.5 and 4.6).

(e) Group 5 (Figs. 2.4 and 2.5M-O) is located in the lower southwestern part of the Tatio basin. With an SSW-NNE strike direction, it intersects groups 1 and 4 in an oblique manner. The dominant features are few, but large hot springs, discharging apparently high volumes of hot

water. A sufficient supply of high-tempered waters is also indicated by the existence of large areas of bright orange colorization, which are likely high-temperature microbial mats described earlier (Dunckel et al., 2009). Discharge particularities of groups 1–5 will be addressed in more detail in chapters 2.4.5 and 2.4.6.

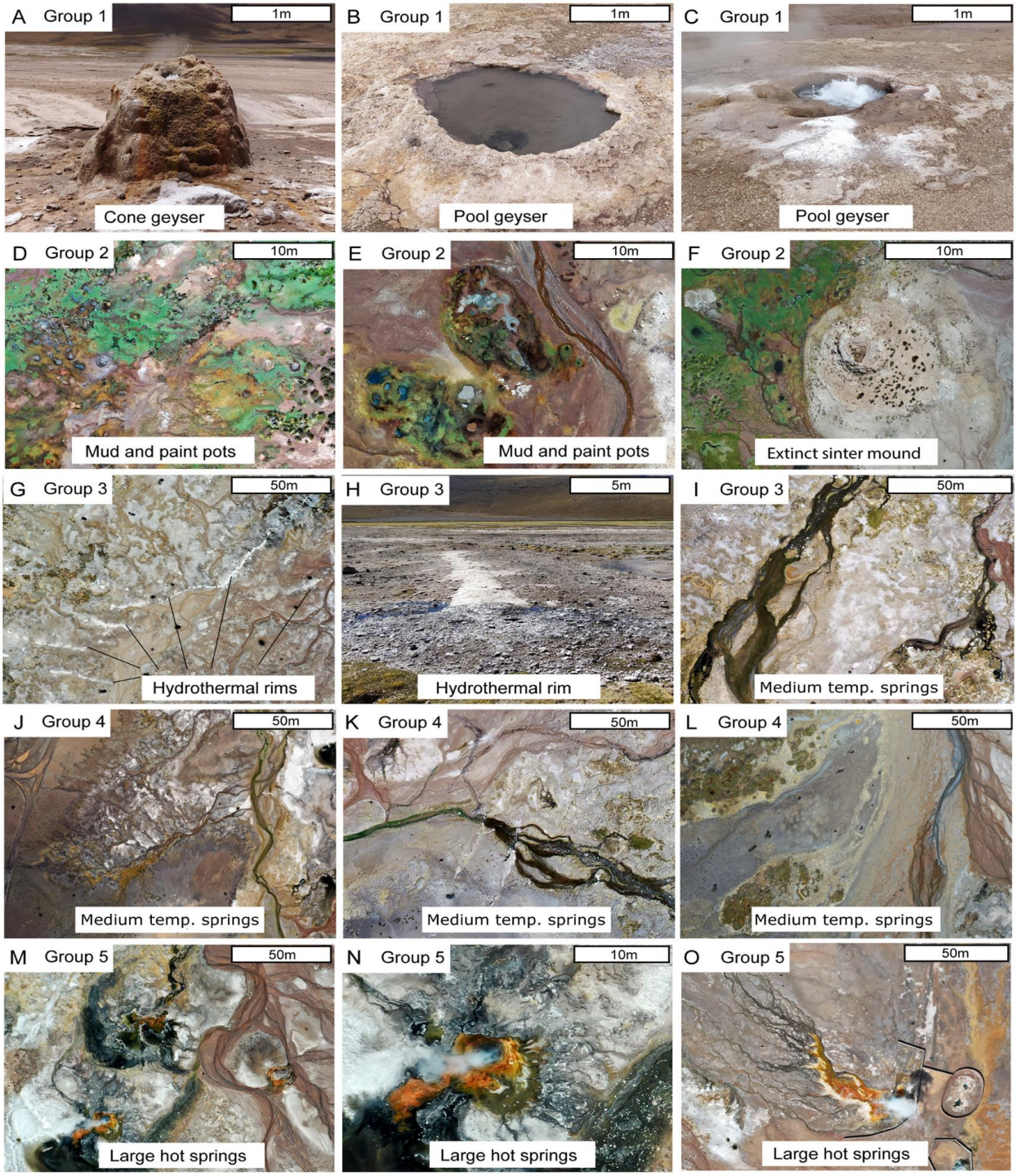

Fig. 2.5 Close-up views and characteristic geothermal object compositions of groups 1–5. (A-C) Group 1: Cone and pool geysers, (D-F) Group 2: Mud and paint ponds and environmental conditions allowing widespread vegetation, (G-I) Group 3: Hydrothermal rims, wetlands, and

medium temperature springs, (J-L) Group 4: Wetlands and medium temperature springs, (M-O) Group 5: Large hot springs.

2.4.3 Topography and morphology of the upper basin

Erupting hydrothermal fluids contain high mineral contents and lead to the deposition of hydrothermal minerals. Considering the long-term activity of El Tatio, two deposition phenomena contribute to the recent appearance. The more obvious is the formation of large geyser cones, sinter terraces, or mounds, that might grow to enormous sizes and represent the most prominent objects in El Tatio (chapter 4.4.1). But besides, a subtle process producing far higher volumes occurs. Clusters of vents are typically building rather flat sinter slabs, merging their runoff systems to sinter complexes and eventually forming sinter plateaus. Those can be hardly identified by eye due to their broad extent, often covering thousands of m². We were able to reveal these plateaus indicating zones of apparently high sinter deposition in a relative elevation map, based on the subtraction of a Mean-DEM (250-m kernel) from the original DEM (Fig. 2.6).

The largest of those plateaus is coincident with the area of the highest mapped object density, the geyser belt or group 1 (main plateau in Fig. 2.6). It is a half-circle-shaped area of increased elevation with a radius of ~250 m, covering an area of >100,000 m². It elevates up to 7 m above the surrounding ground with multiple zones of higher relative elevation (A1, A2, B, C in Fig. 2. 6). Intersected by an N-S oriented morphological structure through the main plateau, it splits into a western and eastern part (A1, A2 in Fig. 2.6). Both parts are associated with a larger number of vents, merging their runoff systems to complex larger sinter slabs. Area A1 is dominated by geysers erupting from rather flat sinter slabs, fractures, or small craters in the ground. The most prominent, but flat-shaped geyser is X4 (labeled T25 after Glennon and Pfaff, 2003), which created a set of sinter terraces extending to a distance of 20 m and 85 m away from the vent respectively (X4 in Fig. 2.6).

Area A2 bears similarities to A1, but differs from it by a higher number of cone geysers and sinter mounds that are well defined in our topographic data set (chapter 4.4.1). Large sinter mounds occur mainly on the northeastern edge (B, C, and VR in Fig. 2.6) of the main plateau. They are mostly inactive and without any thermal expression, possibly indicating previous stages of hydrothermal activity at the northern boundary of the El Tatio basin. S5, the largest observed sinter mound is bounding the occurrence of geysers and sinter mounds to the east,

followed by an area almost exclusively hosting mud ponds and pools, the Vega Rinconada (VR in Fig. 2.6).

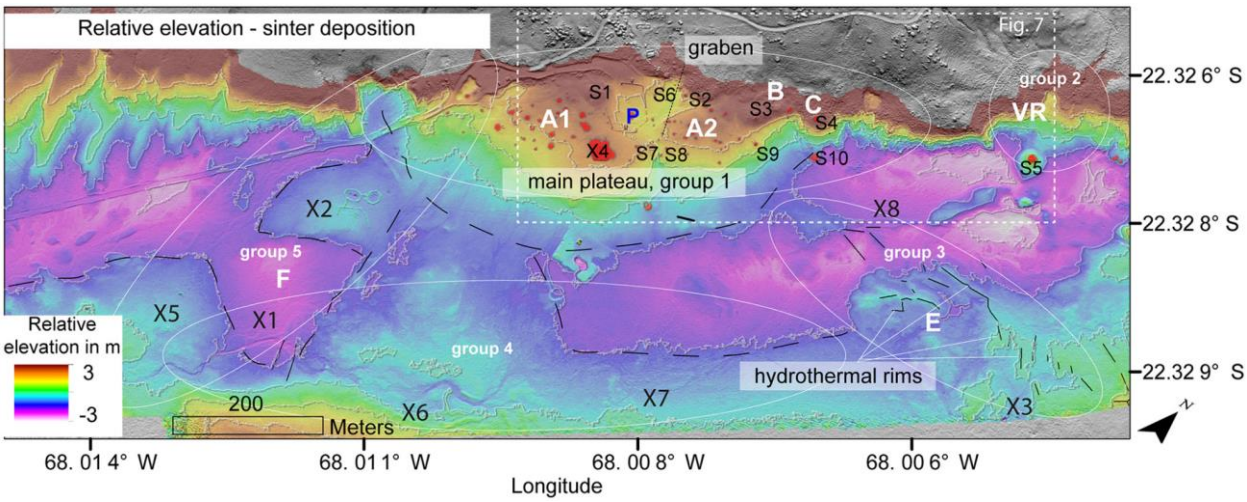

Fig. 2.6 Overview of the topography of the upper basin. The relative elevation map highlights the formation of plateaus and large sinter bodies due to mineral deposition. The highest elevation above the surrounding ground is observed coincident with the geyser belt (or group 1 respectively), especially at pronounced spots along the northern rim of the Tatio basin (A1, A2, B and C). The largest geyser observed is X4. A series of large cone geysers and extinct sinter mounds (S1 – S10) is located in the eastern section of the main plateau and the northeastern edge of the upper basin. Several smaller plateaus, outlined by black dashed lines, are apparently associated with single large hot springs (X2, X5). Black solid lines depict hydrothermal rims, which appear as bright lineament-shaped sinter rims with increased ground temperatures. The white dashed line depicts the outline of Fig. 2.7.

The southeastern part (E in Fig. 2.6) of El Tatio is characterized by a series of hydrothermal and topographic ridges that are aligned in a sub-parallel orientation. The hydrothermal ridges are particularly well expressed in our photogrammetric data, as they are on average 7–15 m wide and extend over tens to hundreds of meters in length. They are capped with a white silicate crust and show signs of small discharge and a slight thermal signal only. The average height of these surface encrustations is below 0.5 m, and the average diameter is 2–5 m. Although the elevation is only minor, it can be well distinguished from the surrounding ground in our relative elevation map. The sum of all hydrothermal ridges merges into a well-defined plateau. The southern boundary of the El Tatio basin is elevated with respect to the center of the basin and highlights the general graben-like structure of the El Tatio basin.

Other plateaus that are apparently associated with single large hot springs, suggesting mineral depositions on a broader scale, could be revealed in the southern and southwestern parts. At location X2 (Fig. 2.6) a large thermal spring is located in the center of a flat sinter plateau

covering an area of ~17,000 m², suggesting the origin of this plateau to be related to this thermal spring. Other plateaus (X5, X6 in Fig. 2.6) are located more to the SE and SW, of which X5 is also apparently related to a single large hot spring. They will be addressed in detail in chapters 2.4.5 and 2.4.6.

In summary, the geomorphological analysis reveals volumes of sinter terraces and cones, indicating that the highest rates of sinter deposition are associated with the plateau hosting region A1 and A2 followed by several smaller plateaus associated with large hot springs (X2, X5 in Fig. 2.6). The largest single objects hence accumulate in the northeastern part of the El Tatio basin with extinct single geyser cones and sinter mounds of extraordinary size (see chapter 2.4.1).

2.4.4 Object group segmentation and vent alignments

2.4.4.1 Cone geyser and sinter mound segments

Cone geysers and sinter mounds are rare but the most prominent objects in El Tatio. Our data shows that the inactive mounds reach heights of up to 3 m, whereas the currently active cones typically range from 1 to 1.5 m height above the ground. Cones and mounds are characterized by very steep topography, with a height-to-width ratio of 0.25 to >1. Some are resting on much larger flat basements. We observed 10 big cone geysers and sinter mounds, 5 active and 5 inactive ones (S1-S10 in Figs. 2.6 and 2.7), associated with Groups 1 and 2. Ideally-shaped cone geysers and large sinter mounds appear almost exclusively in the eastern part of group 1. Our geospatial data reveals that most of these are aligned along two lineaments, highlighted by the lines L1 and L2 in Fig. 2.7.

The lineament L1 is a 470 m long, N63° trending line, resembling the northern boundary of activity in the Tatio basin. L1 hosts large, mostly extinct geyser cones and sinter mounds. They are well aligned with a normal offset of fewer than 5 m to L1. Only S3 (Fig. 2.7), a cone geyser resting on a large sinter pile that is still showing minor activity, is located with an offset of 13 m towards the south of L1. The objects depicted here are of extraordinary size and shape.

The largest sinter mound (S5 in Figs. 2.6 and 2.7) has a dimension of 13 × 13 m and an estimated volume of 266 m^3. Including its 45 × 45 m basement, its volume sums up to 1500 m^3. The sinter mound is extinct and about ten times larger than the recent active geyser cones. A second particularly large sinter mound is the neighboring S4 with dimensions of ~7 × 9 m and an estimated volume of 117 m^3, resting on a basement with ~60 m diameter. The southern

part of this basement is pierced by several large circular mounds and depressions, with diameters of up to 20 m. Those are strongly corroded and therefore almost invisible to the naked eye in the field. Although the geologic and structural origin of lineament L1 is unclear, our data suggests it has major relevance for the formation of cone geysers and sinter mounds on the northern boundary of the Tatio basin. With a larger southward distance to L1, we find a general trend of increasing object density and decreasing object size. All current activity occurs south of L1.

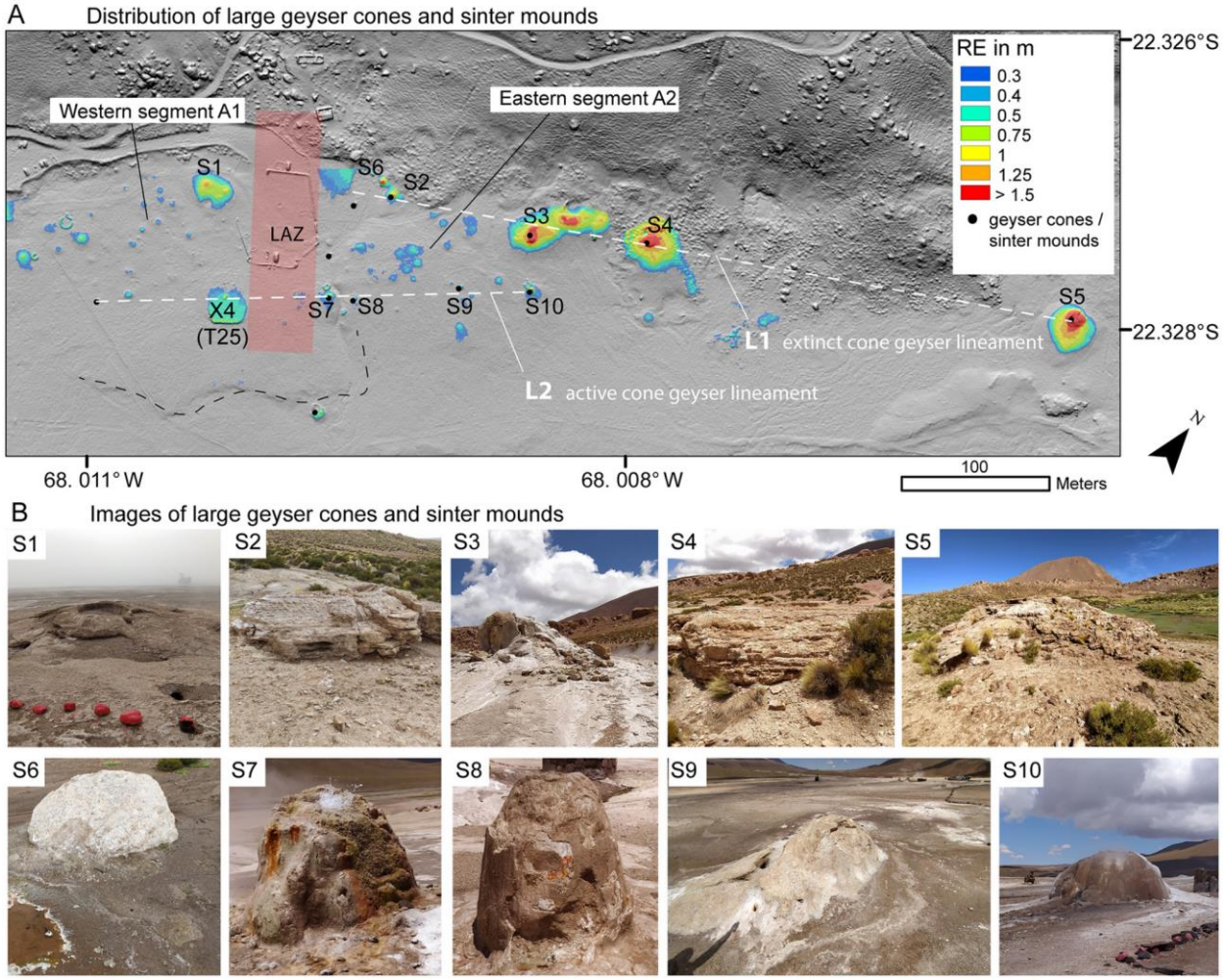

Fig. 2.7 Overview of prominent geyser cones and sinter mounds. (A) Cone geysers and large sinter mounds are aligned along lineaments L1 and L2. L1 represents a section of large extinct sinter mounds and extinct geyser cones. Volumes for single objects are extraordinary along this northern lineament ranging up to 1500 m^3 (S5). Active cone geysers are aligned along a second lineament L2, together with the most prominent geyser X4 (T25 after Glennon and Pfaff, 2003) and other smaller but distinct sinter mounds in the west. Objects are color-coded by their relative elevation above the surrounding ground (RE in m). (B) Close-ups of prominent geyser cones and sinter mounds.

Using the same approach of linearly connecting prominent geysers, a second lineament (L2) is

traceable for 295 m length, striking N52.5°, located in the central and eastern part of group 1. L2 is connecting 4 large active cone geysers (S7–10 Fig. 2.7) as well as other geysers that build up sinter slabs of heights >1 m, west of the intersecting graben structure, X4 geyser (labeled T25 after Glennon and Pfaff, 2003) for instance. The distance of objects for this imaginary line is commonly only <4 m. In contrast to Lineament L1, the majority of eruptive activity occurs north of L2. Both lineaments are roughly subparallel to the Tatio fault, with a lateral offset of ~50 m to each other and slightly different azimuths. L2 defines the southern boundary of the recent activity of the geyser belt. Although the alignment of past and present geysers is well documented, a structural link is debatable and further discussed in the discussion section below. A higher number of smaller sinter mounds or sinter slabs is located in the vicinity (see colored patches in Fig. 2.7), especially associated with group 1, whereby they are largely bound to north and south by the above-mentioned segments L1 and L2. Some 20 of such objects can be found in each of the western and eastern parts (A1, A2 in Fig. 2.6). They typically elevate up to a maximum of 0.6 m.

2.4.4.2 Activity along lineaments

Next to the general orientation of the elongated groups 1–5 or the alignment of prominent cone geysers and sinter mounds along linear trends, we also observed clustering and particular vent arrangements on a local scale (Fig. 2.8).

To carry out a more detailed, systematic analysis of the spatial distribution and orientations of objects or object clusters, the mapped objects, grouped into Obj_dem, Obj_h2o, and Obj_therm were clustered based on their spatial location by applying the density-based cluster algorithm DBSCAN. The majority of the identified object clusters are rather elongated and directed and follow a geometric order. Vent arrangements often resemble lineaments or intersecting lineaments. The DBSCAN algorithm is searching radially and cannot resolve anisotropy in the near field.

Therefore, all clusters were analyzed for these specific vent arrangements, and in necessary cases, a manual lineament mapping was carried out. Azimuths for all lineaments were calculated and are shown in Fig. 2.8, together with representative examples showing multiple elongated vents, small-scaled pools, and craters located along two lineaments, intersecting at an angle of 58°. This is a typical vent setup. We found a clear dominance of two orientations N*E*-SW and E-W (Fig. 2.8B). This indicates that the activity and formation of vents are

preferably appearing along a predefined pattern, which might resemble fractures, fracture networks, or joints.

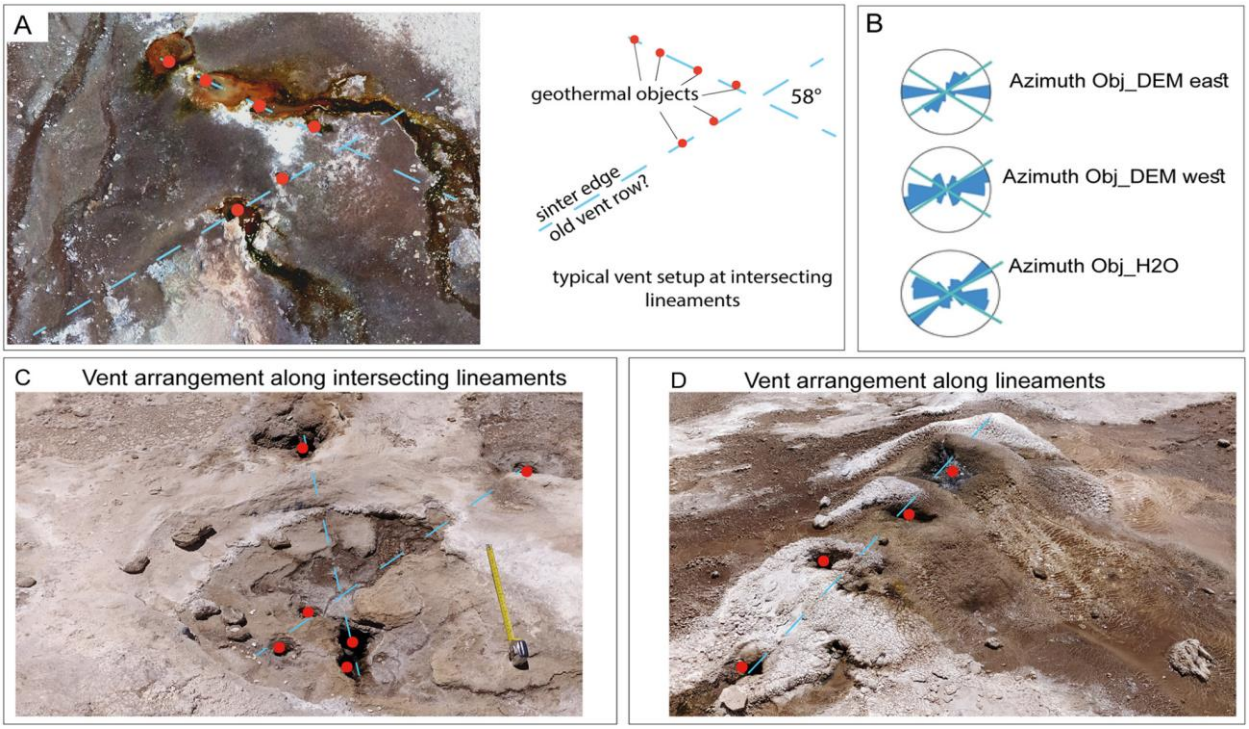

Fig. 2.8 Overview of the azimuthal orientation of active segments observed in El Tatio. (A) Example for vent arrangements along lineaments or intersecting lineaments. The Figure shows an arrangement of pools, elongated pools, and small sinter cones along two lineaments intersecting at 58◦. (B) The rose plots show the orientation of all mapped lineaments, weighted based on the respective lineament length. (C/D) More examples of vent alignments along lineaments or intersecting lineaments.

2.4.5 Location and orientation of thermal anomalies and discharging vents

Geothermal waters from geysers or hot springs are punctually expelled and form either splash areas surrounding the respective geyser vent, or channelized more or less evolved runoff systems. Our photogrammetric data helps to better identify locations of water-discharging vents, especially when combining both the optical and infrared data (Fig. 2.9). From this, we could identify 415 discharging objects clustered in the mentioned groups 1–5, representing a broad variety of types of vents, ranging from episodically erupting geysers to steadily discharging or artesian natural or hot springs. Splash areas are mainly observed in the geyser belt (group 1), while vents of groups 3–5 are characterized by extensive flow channels. In our infrared mosaic, active vents appear as a hotspot with high temperatures in the center and

decreasing temperature values in the outer parts.

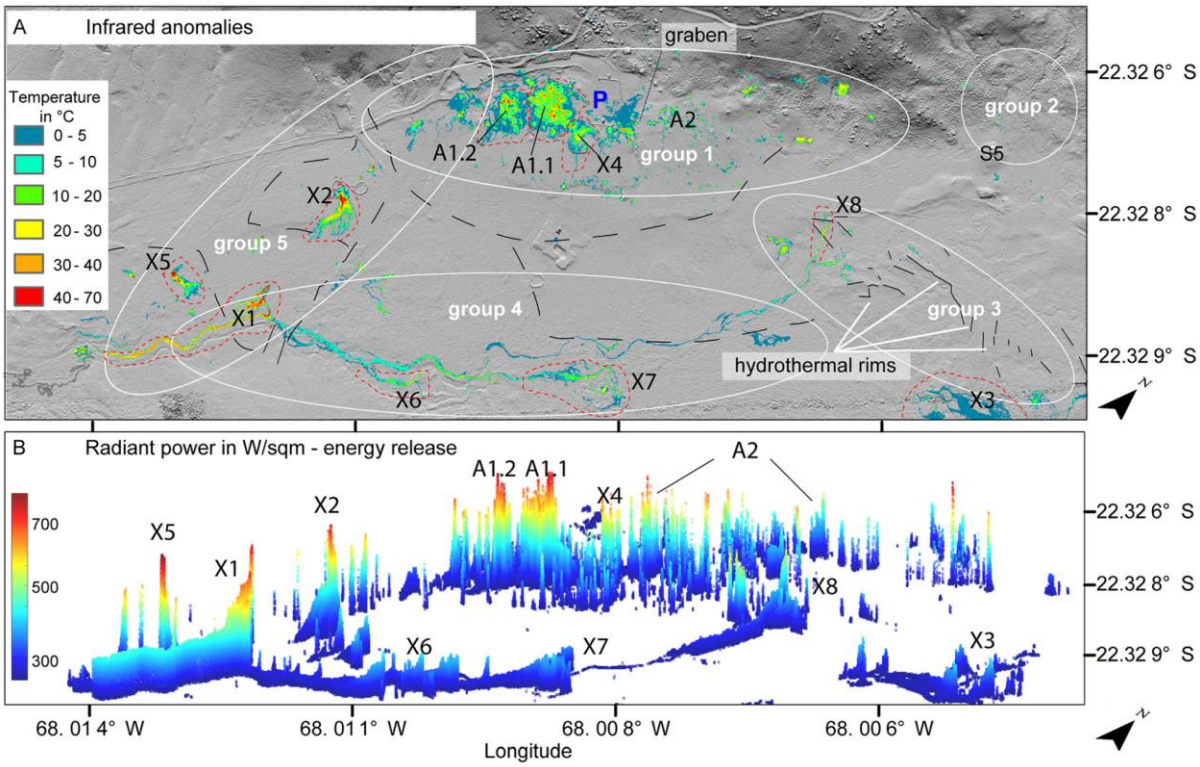

Fig. 2.9 (A) A temperature map shows the temperature distribution equivalent to discharge in the Tatio basin. High-temperature pixels are associated with clusters A1.1, A1.2, and A2 in the geyser belt, the large hot springs of group 5, and medium temperature springs of groups 3 and 4. (B) Energy release of active regions and single vents in a 3D scatterplot. The plot shows the same extent as the maps above just rotated for a 3D representation. Single vents in the southwestern area show high thermal outputs and can be related to large volumes of erupted hot water.

The majority of discharging vents or vents with a thermal signature are coincident with the elongated group 1, in the vicinity and in azimuth with the local dominating trend (Fig. 2.9). Distinct clusters of high-temperature pixels suggest a separation of vents of group 1 into areas A1.1, A1.2 (west of the morphological structure/graben), and A2 (east of the morphological structure). For clusters A1.1 and A1.2, the vent density is so high that single vents can hardly be spatially constrained in the TIR data. Therefore, we consider those as vent complexes. The vent density and general thermal output in A2 are lower. Group 2 is in line with Group 1 located further east, but was only sparsely covered by our infrared data. Frequencies of high-temperature pixels, temperatures, and thermal emission for groups 3 and 4 are generally lower than observed for groups 1 or 5, for instance. This indicates differences in the thermal regime between the northern and western sections with higher maximum temperatures and the

southern and eastern sections of the upper basin with lower maximum temperatures. This is better illustrated in Fig. 2.10, a simplified temperature plot with 3 temperature classes 20–50 °C, 50–60 °C, and > 60 °C.

High apparent pixel temperatures of over 60 °C occur in two confined zones, either coincident with groups 1 and 2 in the vicinity of the assumed Tatio trend line within a normal distance of below 100 m, or in group 5 (Fig. 2.10).

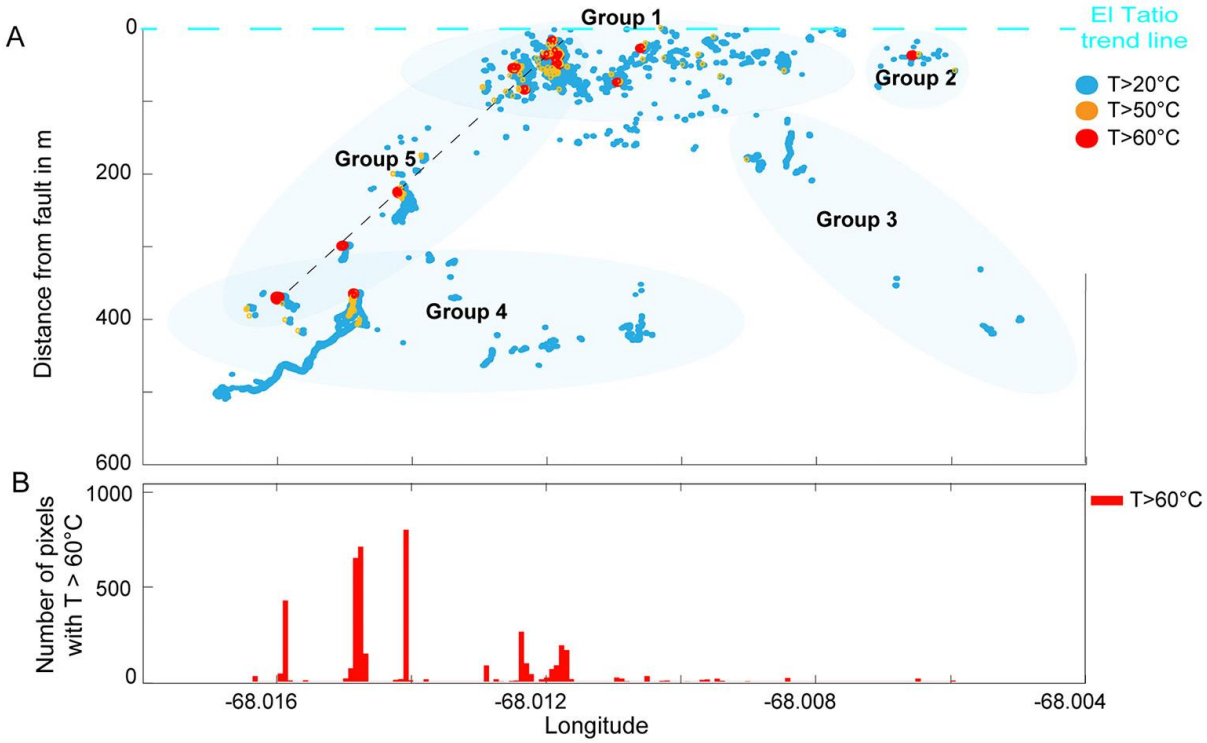

Fig. 2.10 A) Thermal anomalies cluster in distinct groups. The spatial distribution of pixels with temperatures >20, >50, and >60 °C is plotted with respect to the Tatio fault (light blue dashed line). High temperatures of over 60 °C were observed mainly in groups 1 and 5. They appear in the vicinity of the Tatio fault or along a pronounced linear trend highlighted by the black dashed line in group 5. Groups 3 and 4 are characterized by intermediate temperatures. B) The barplot at the bottom of the Figure shows the frequency of pixels >60 °C, with respect to their position along the Tatio fault. The western part of El Tatio has an apparently higher thermal activity, with the majority of high-temperature pixels associated with large hot springs in group 5.

With increasing distance to the trend line, the maximum temperatures appear lower, especially in the southern and southeastern sections so that temperatures of >50 °C are not observed in group 3 and the eastern part of group 4. In the western section, however, we observe high-temperature pixels also at a greater distance to the trend line along the central axis of group 5 and the intersection of groups 4 and 5. This is coincident with a sudden change of the

orientation of vent arrangements, now following an oblique pattern towards an almost N-S direction (Group 5 in Fig. 2.10), oblique to the average trend in the upper basin by − 40°.

Next to the varying orientation and maximum temperature distribution, we also observe a change in the quantity of high-temperature pixels. Although the vast majority of objects were mapped within group 1, the majority of high-temperature pixels (T > 60 °C) occur coincident with group 5 and are associated with few large hot springs, as demonstrated by the barplot in Fig. 2.10. This suggests a transition from episodic to permanent or artesian discharge. As the directions of discharging systems are commonly both, topographically and structurally controlled, below we will further discuss the geologic implications of the observed trends.

2.4.6 Energy budget

The thermal infrared maps were already used to generate the geothermal object inventory and geospatial analysis described above. In this section, we consider the energy release as determined by our data. The current eruptive activity was inferred from the thermal data based on the extent and amplitude of thermal anomalies, and the cumulative energy released by single objects or regions (Table 2.2 and Figs. 2.10 and 2.11). To separate single objects or eruptive units spatially, we used the 0 °C isotherms, which are also used as a lower threshold for the radiance calculation. Values will be given in the following for the total radiation and the background corrected radiation (in brackets in Table 2.2 and in the following chapters) from which the background of average − 12 °C is subtracted. We calculated a range of radiant power from the surface of selected geothermal objects and regions ranging from 312 to 430 W/m^2 (61–179 W/m^2).

The area with the highest cumulative energy release is area A1, coincident with the largest plateau detected. A1 is composed of two spatially separate clusters A1.1 and A1.2 (Fig. 2.9), each characterized by a high vent density, and covers an area of 6091 m^2 (based on 0 °C outline). The cumulative energy release (Radcum in Table 2.2) is 1.39 MW and 0.76 MW (418 KW and 202 KW) for areas A1.1 and A1.2, which translates to 359 W/m^2 (108 W/m^2) in the east and 342 W/m^2 (90 W/m^2) in the western cluster respectively. The energy release of region A2 (Fig. 2.9), the second largest cluster of the main plateau with a high object density, is with 329 W/m^2 (78 W/m^2) distributed on 35 eruptive units comparably low.

Table 2.2: Overview of the energy release for active regions and single objects, showing the cumulative radiation (Radcum in KW), the area covered in m^2, average radiative power (Radpow in W/m^2) for total and background corrected radiation (in brackets), as well as maximum (Tmax in °C) and mean temperatures (Tmean in °C) observed for the respective eruptive units. Total radiation values for Radcum and Radpow are the upper values, background corrected radiation values are the values in brackets. The average total radiant flux ranges from 312 to 430 W/m^2 or 61 to 179 W/m^2 when subtracting the background radiation. Parts of the active region A range from 329 to 359 W/m^2 (78–108 W/m^2). Large single hot springs show an energy release similar to the energy release of complete regions built up by hundreds of vents. Large hot springs in the southwestern part are characterized by higher radiant fluxes of >369 W/m^2 (118 W/m^2). Consider also the average temperatures for the eruptive units, which are highest for large hot springs (X1, X2, X5, and X8).

Energy release	**A1.1**	**A1.2**	**A2**	**X1**	**X2**	**X3**	**X4**	**X5**	**X6**	**X7**	**X8**
Radcum In KW	1389 (418)	761 (202)	338 (87)	712 (296)	469 (155)	1139 (222)	290 (74)	228 (72)	359 (91)	329 (83)	50 (17)
Area in m²	3866	2225	998	1654	1248	3647	857	619	1064	979	130
Radpow In W/m²	359 (108)	342 (90)	329 (78)	430 (179)	376 (125)	312 (61)	338 (86)	369 (118)	337 (86)	336 (84)	388 (137)
Tmax in °C	66	65	34	60	63	28	33	68	29	18	44
Tmean in °C	12	8	7	25	15	2	8	13	8	7	17

The highest energy release per vent and m^2 occurs in the southwestern and southern parts of El Tatio, which is dominated by a few but large hot springs, coincident with Group 5. The area is located in a topographic depression, with an altitude that is up to 12 m lower than the geyser belt. The discharge of hot fluids in this area is apparently higher, which is also indicated by the bright orange colorization of the hot springs in our optical dataset (Fig. 2.5M-O). The largest of the hot springs (X1 in Fig. 2.9) is located in a topographic low of the basin and its cumulative energy release is similar to the cumulative energy release of the whole area A2. X1 is discharging directly into Rio Salado and heating the river's waters to over 60 °C. The water temperatures remain high and drop slowly to 30 °C over a distance of 300 m downstream,

highlighting the vast supply of hot water. An exact hot water flux cannot be determined, but we estimate the area covered by the heated waters of X1 with 1654 m^2 (165.4 m^3 with 0.1 m water level). The total radiant energy emitted by X1 is 712 KW (296 KW) with the highest average radiant power of 430 W/m^2 (179 W/m^2). X1 has by far the largest single vent discharge, followed by X2 to X8. X3 (Fig. 2.9) located further east has low radiation values of 312 W/m^2 (61 W/m^2) only. In contrast to the large hot springs in the southwest, runoff temperatures in the region further east (X3, X6, X7 in Fig. 2.9) are low with water temperatures of <30 °C only. Further, we can distinguish the geothermal objects from Group 5 (> 118 W/m^2) and Group 4 (<86 W/m^2) by their radiant power values. A generally increasing water flux and energy release with decreasing altitude can be constrained from the east towards the southwest (Fig. 2.11) where the majority of large eruptive units, often represented by a single hot spring or vent cluster, is located.

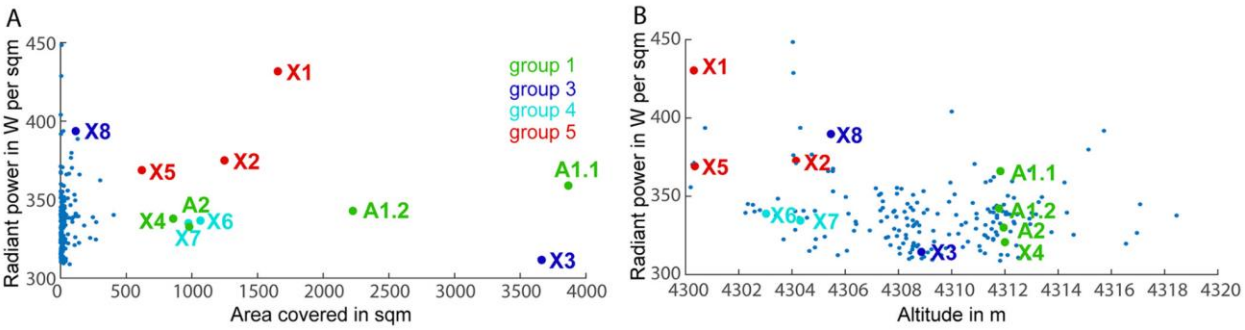

Fig. 2.11 Total thermal energy release is shown as radiant power (in W/m^2) compared to the area covered (A) and altitude of the vent (B). (A) Thermal energy release compared to the area covered by the discharge. Especially in the southwestern part of El Tatio, single large hot springs with a high radiant flux per vent are observed. X1, X2, and X5 show a high energy release with radiant power values >369 W/m^2 while covering broad areas. Objects of group 1 show a lower thermal energy release of 329 to 359 W/m^2. Note that only the largest features, also shown in Fig. 2.9 are labeled here. (B) Thermal energy release compared to the altitude of the vent. Vents in topographic lows show high radiant power values, especially X1, X2, X5, and X8. Objects of group 4 show in general lower values (<350 W/m^2) although located at a similar altitude, but further east. Note that only prominent objects are labeled here. Single small-scaled objects reach high radiant power values but are due to the small size not considered here.

2.5 Discussion

2.5.1 Benefits and limitations of methods and data presented

Developments in UAS and sensor technology combined with modern photogrammetric processing routines (SfM) allow for the acquisition and generation of high-resolution data sets

and provide a good database for detailed structural studies. Especially the combination of optical and thermal infrared data was found to be beneficial for the investigation of hydrothermal systems at the surface. However, there are limitations that will be discussed in the following.

The quality of the presented data sets is varying. Pixel resolutions of the processed images, depending on the flight altitude chosen, and the image quality, depending on the quality of the camera system and light conditions during the acquisition, have a direct impact on the point cloud density in the SfM processing and, therewith, on the quality and resolution of the resulting orthomosaic and DEM. For repeated studies of an area or time series, the flight parameters, weather and illumination conditions (when possible), and the quality of the camera systems used should be chosen similarly to obtain the best and comparable data products. However, at times of the data acquisition for this study, copters, and camera systems were still in development, which is why our database is rather heterogeneous. The point cloud density of the 2014 data is, with 423 points per sqm, about 35 times higher than the 2016 and 7 times higher than the 2020 data. This leads to differences in the resolution, which range from 1.5 cm per pixel for the Ricoh dataset (2014) to 14.5 cm per pixel for the 2016 data set, and therewith also in the feature detection thresholds within the data sets. The Ricoh data set contains more detail, which potentially results in a higher density of mapped objects. All data sets cover the geyser belt (group 1), which was the main focus, but the broader El Tatio geothermal region is much larger and our regions 3 and 4 are only covered by the 2016 and 2020 data. Therefore, object numbers and distribution densities of vents might be underestimated in these regions with respect to mapping results of the 2014 data, mainly covering group 1.

The spatial accuracy of 3D models processed in the SfM workflow is dependent on data quality and correct acquisition geometries. The within-model error is typically in the range of ~0.2 m (Kalacska et al., 2020). The absolute spatial positioning accuracy of data sets derived by modern UAS is typically in the order of ~5 m horizontally, while the vertical positioning can have offsets of easily tens of meters. Additional ground control points measured by DGPS are desirable and can reduce the horizontal and vertical offsets to a few cm.

The infrared data was acquired at ~100 m flight altitude and therefore has a resolution of 0.15 m. The temperatures presented are “apparent temperatures” which are temperatures perceived by the sensor. These apparent temperatures are affected by the vent size to pixel ratio, the emissivity factor of the recorded object, atmospheric effects, or water vapor or steam plumes of the erupting vents themselves. Especially the latter can have a strong influence on the

amplitude of recorded infrared data (Müller et al., 2021). Therefore, apparent temperatures appear lower than the real in situ object temperatures. Although the boiling temperature at the altitude of El Tatio is commonly at ~86 °C, the maximum apparent temperature observed in our data is 68.8 °C. All constitutive calculations like radiant power and energy release would be biased accordingly. The infrared data has a gap in the central part, which can be explained by the fact that at the time the IR data was acquired no live view on the screen was available, and the operator was basically flying blind. After comparison with our optical data, we concluded that no major vents are located in this gap and that the influence on the results and general interpretation of this study is low.

The area covered by our data is showing only the upper basin and neighboring groups. Southwest, the middle basin, similar in size but with an NW-SE trend almost perpendicular to the upper basin, would follow. This area is characterized by large hot springs and might be associated with the second dominant fault system in El Tatio (Lucchi et al., 2009). A detailed analysis of vent sizes, eruptive characteristics, but especially dominant trends in this area would be desirable to draw the complete picture. Unfortunately, we cannot give more detailed information about this region, as in recent years it is difficult to achieve a working permit from the local authorities as a direct restricting consequence of a borehole blowout in 2012.

2.5.2 Spatial organization of the El Tatio geothermal field

Based on high-resolution optical and thermal infrared data, we performed a hydrothermal object mapping. The high resolution of the acquired data allows for the detection of a large number of objects related to hydrothermal activity at the surface, ranging from small holes in the ground to large geyser cones and sinter mounds up to sinter plateaus. A detailed spatial analysis of the mapped objects, their topological relationships, and the dominance of certain object types in certain regions indicates a high degree of organization over scales. On a larger scale, objects can be grouped into 5 pronounced regions, similar to previous studies (Glennon and Pfaff, 2003), holding specific characteristics and vent compositions. These regions cover thousands of m^2 each and are characterized by a high vent or object density. The regions are elongated and show orientations that are in accord with the local dominating N*E*-SW trend (groups 1 and 4), but also oblique (groups 3 and 5).

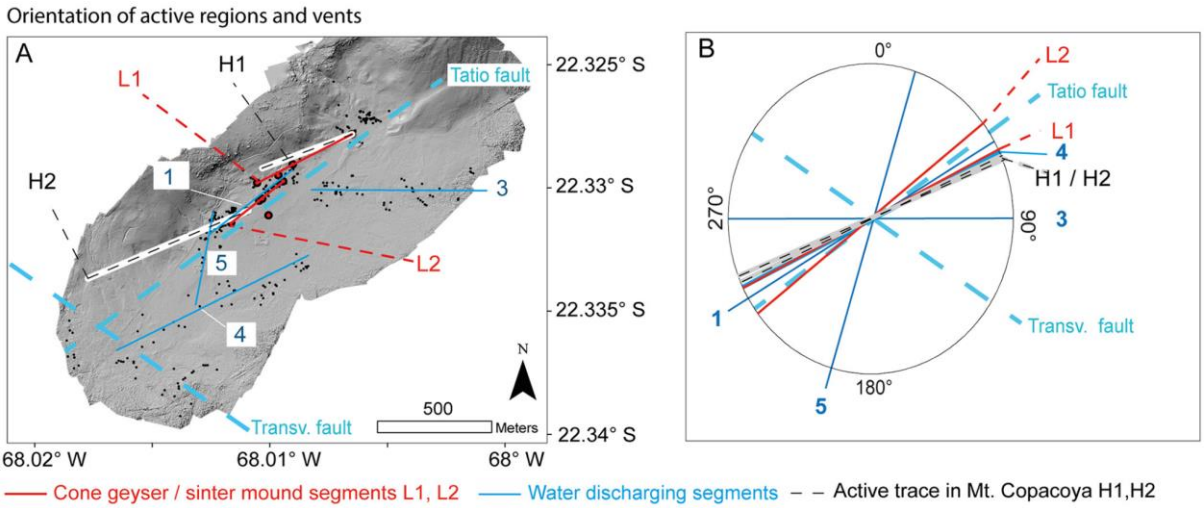

Fig. 2.12 Location and orientation of active segments with respect to the Tatio fault. The general trend of groups 1 and 4 and the cone geyser and sinter mound segments L1 and L2 are in accord with the orientation of the Tatio fault. Groups 3 and 5 are oblique.

The location and general orientation are thought to be controlled by a local fault, described earlier (Lahsen, 1976; Montecinos-Cuadros et al., 2021). This fault apparently acts as a boundary for the lateral migration of hydrothermal waters, which are thought to enter the Tatio basin from the southeast (Lahsen, 1976). This association can account for the general location and orientation of the active regions, also considering the abundance of the majority of hydrothermal surface manifestations in the close vicinity to the fault. This is highlighted by group 1, the area with the highest mapped object density, the biggest number of active geysers, cone geysers, and sinter mounds, and pronounced thermal activity, located coincidentally and in azimuth. The same is true for the two detected cone geyser and sinter mound lineaments L1 and L2 (Fig. 2.12), or two apparent segments of hydrothermal influence that can be traced into the flanks of Mount Copacoya (H1, H2 in Fig. 2.12 and Appendix A2.1).

However, it cannot account for the main orientations or locations of other active regions in the Tatio basin, groups 3 and 5 for instance, or observations made on a smaller scale. Group 4 is located in azimuth but with a lateral offset of some hundred meters further south. The intersecting groups 3 and 5 are oblique by +37° and − 40°. Specific object compositions of these groups or discharge particularities follow rather the NE-SW trend or are apparently influenced by the vent altitude. On a smaller scale, eruptive units or vent clusters often follow a geometric order with elongated vents aligned along lineaments or intersecting lineaments. Observed mainly in region 1, they indicate a vent formation along shallow fractures or joints

with two dominant azimuth orientations, an E-W trend, and in azimuth with the local NE-SW trend.

2.5.3 Processes controlling the location of the studied objects

The observed alignments of geothermal objects along trends or lineaments almost parallel to the prominent Tatio fault may suggest a structural control (Fig. 2.12). The processes causing such alignments may be more complex, however, as the spacing and appearance may vary along these trends. Locations of geothermal objects are generally controlled by the permeability structure in the underground. Different lithology or rock types develop different permeability and favor or prevent fluid flow. In addition, existing faults and fracture trends may provide a higher or anisotropic permeability, affecting fluid pathways and consequently the development of surface features. This may explain the observed organization of geothermal objects at El Tatio. However, the details of the origin of these alignments and lineaments are likely more complex and remain challenging to elucidate.

We may speculate that the generally observed high density and orientation of group 1 and respective object alignments are controlled by the Tatio fault as they follow similar trends. This, however, does not necessarily mean that a causal relationship between the fault and fluid paths really exists. The Tatio fault is an old structure, and is responsible for the formation of the Tatio basin, which was infilled by pyroclastic and redeposited (sedimentary) materials so that lithological controls cannot be ruled out.

Therefore, alternative processes controlling the location of the studied object may be found in secondary post-depositional processes. Clastic materials are compacting and gradually losing porosity. Those clastic materials emplaced in a morphological depression are constrained, so that post-depositional compaction may be governed by the pre-existing morphology. A morphological valley controlled by the Tatio fault consequently will affect post-depositional compression and, therefore, indirectly lead to structural arrangement apparently co-aligned with the Tatio fault, thus in association with the morphologic expression of Mt. Copacoya. In this view, the structures controlling the geothermal objects are to be considered secondary structures and not primary or regionally expressed structures.

We note that the aligned vents are identified manually. Thus also other trends may exist and be identified by researchers, possibly providing a more complex structural framework depicted by geothermal objects.

Vent arrangements along intersecting lineaments could indicate polygonal fracture systems. However, we observed a clear dominance of two azimuthal directions, *E*-W and NE-SW. Although speculative, the same two azimuthal directions are displayed by a rock formation located right north above group 1 (Appendix A2.2), possibly indicative of a structural arrangement even at depth (beneath the younger deposits) that may have affected fluid pathways. However, the shape and orientation of these joints or fractures suggest the importance of a pre-existing pattern, controlling the evolution of vents in this central part of the Tatio geothermal field by anisotropic permeability facilitating the ascent of hydrothermal fluids.

Therefore, we can conclude that the organization of the geothermal objects is in agreement with tectonic features, however, the processes controlling these arrangements in detail are still unclear. The reason for this complexity is that local structures, including the Tatio fault and other fracture systems, act as passive elements reopened by non-tectonics processes. The direction of groundwater circulation, thermal contraction, and re-dissolution of a saline endurance crust underlying the geothermal field can be responsible for this control. Locations of degassing and fumaroles at Ebeko (Kuriles) were found to follow similar trends to locations of explosive craters (Walter et al., 2020). Therefore, the different fluids, magmatic or hydrothermal, are following similar pathways, and thus studying one system may help better understand the location of the other system. Similarly, locations of hydrothermal fluid flow at the Yellowstone caldera were found to be related to fracture permeability in the underlying Lava Creek Tuff, forming NE and NW-trending zones of geothermal objects visible in thermal infrared maps (Jaworowski et al., 2006). Also, other independent techniques and surveys confirmed that geysers may be related to shallow fracture sets (Jaworowski et al., 2020). At these sites, the origin of the fracture is not primary tectonic, but considered secondary, which is explaining the high degree of the spatial organization of geothermal activity but also underlining the challenge of interpreting the alignments with a regional tectonic process.

For the Hot Spring Basin and Norris Geyser Basin (both USA) a fracture-related change in temperature and fluid flow was documented (Neale et al., 2016). The finding of a fracture control is relevant for El Tatio and beyond, as it may allow the assessment and monitoring of gradual changes along pre-defined pathways.

2.5.4 Hydrological influence on eruptive activity

The observed differences in object compositions of group 1 to 5 and associated eruptive characteristics or thermal energy release for single objects suggest an additional hydrological influence.

We observe an apparent transition from steam-dominated low-volume discharge of boiling mud ponds in the east (group 2), over episodic steam-dominated eruptions of geysers (group 1) in the central part, to high-volumetric or possibly even artesian discharge of natural-, medium temperature-, or hot springs in the southern and especially southwestern section of El Tatio. This transition in eruptive characteristics occurs from northeast to southwest and is also coincident with elevation changes from a higher to a lower altitude. We discuss this based on a simplified hypothetic hydrological setup in Fig. 2.13. If we assume an equally pressurized hydrothermal groundwater body, a certain depth to water table throughout the Tatio basin, the lowest point of our DEM as a reference point (0 hPa), and consider elevation differences between vents in terms of pressure levels of standing water columns, the higher elevated vents would need the higher pressure in order to erupt from a vent.

The change in topographic altitude between the low-lying large hot springs of group 5 and objects of group 1 are in the order of 12 m. Using the equation for hydrostatic pressure

$$p(h) = pg(h(DEM) - h(min)) \tag{3}$$

with p = density of water (1000 kg/m^3), g = gravity (9.81 m/s^2) and h (height of water column), 12 m elevation difference would equal 1177 hPa, roughly twice the amount of the air pressure at this altitude. This is a rather large potential difference. Reports of changes in eruptive characteristics of geysers following monthly or annual patterns (Hurwitz et al., 2008; Hurwitz et al., 2012), or debate about eruption interval changes (Hurwitz and Manga, 2017) due to atmospheric effects like strong wind gusts on pool geysers or changing pressure conditions indicate a high sensitivity and complexity of such systems.

We may therefore see evidence that even the slight variability of conditions within a geothermal field has essential control on the evolution of either hot spring, geyser, or cone geyser, due to specific requirements that need to be met for these objects in order to develop. A higher-frequent and higher-volume discharge would inevitably lead to dispersion and sedimentation of hydrothermal minerals over a broader area and possibly more flat shapes.

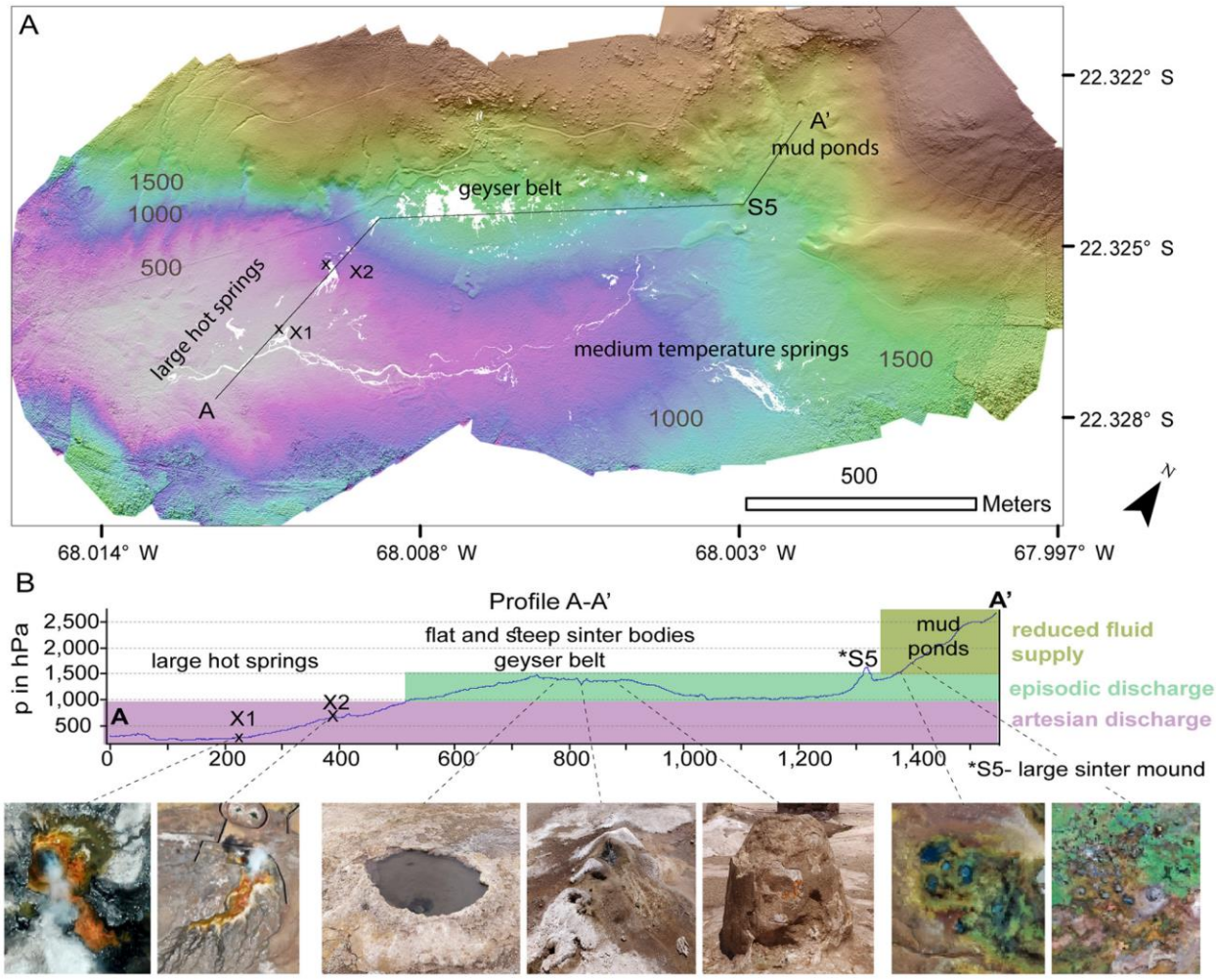

Fig. 2.13 Pressure levels with reference to the lowest point of the DEM illustrating the transition between episodic eruptions and apparently artesian discharge in the topographic lows. (A) Thermal anomalies above T > 0 °C are highlighted for localization purposes in white only. The gray lines illustrate lines of equal hydrostatic pressures with reference to the lowest point of the DEM. Artesian discharge and large hot springs are observed below the 1000 hPa isobar, the geyser belt is located above 1000 hPa, and the mud pond area is located above 1500 hPa, also shown along Profile A-A' in Fig. B.

Whereas, the water content of small volume and less frequent discharging vents would vaporize locally, leading to more local silicate precipitation and, with time, steeper shapes. Although speculative, the object compositions and specific characteristics observed in El Tatio, however, would match such a systematic.

The large hot springs of the southwestern section (especially group 5), which show the highest discharge, high thermal energy release of 369–430 W/m^2 (118–179 W/m^2), and the larger flow channels in our data, occur exclusively below the 1000 hPa isobar, associated with a topographic low. Geysers and objects of group 1 occur above the 1000 hPa isobar. Although

we observe a high cumulative energy release in this area, the energy release per vent is small. It is distributed over an area of 4092 m^2 (A1 + A2 in Fig. 2.9) and on hundreds of vents. The radiant power observed is slightly lower with <359 W/m^2 (<108 W/m^2) than observed for the large hot springs of group 5. Evidence for rather episodic eruptive behavior is given by splash areas surrounding the main vent systems, rather than flow channels or developed runoff systems. Else than in group 5, we here observe the formation of objects like geyser cones or sinter mounds and even an apparent shift within this group from west to east. The western section has a higher energy release, a higher number of vents, and hot springs that accomplish the conditions for high-temperature microbes (Dunckel et al., 2009) to exist. The eastern part, in contrast, hosts a larger number of objects with strong topographies, like cone geysers or sinter mounds. Discharge, cumulative energy release, and radiant power are apparently lower although both sections are separated by a lateral short distance of a few tens of meters. This may indicate a reduced availability of hydrothermal fluids from west to east.

Following the same approach, group 2 located further east and higher would support this. It is the highest elevated group, located above the 1500 hPa isobar, and composed mainly of mud ponds. Mud ponds form under similar conditions to geysers, but with reduced fluid supply so that dissolved soil particles remain in the conduit system. The widespread vegetation, which is unusual for this environment and completely absent in other parts of the upper basin, emphasizes less harsh conditions than in the central parts. Whereas, the largest sinter mound and its active neighboring vent, although spatially associated with the Vega Rinconada region (group 2), fall inside the 1000–1500 hPa zone, the same as the geyser belt (group 1).

Further evidence for an effect of increased vent altitude may be given by the discrepancy between discharging vents and topographic objects (e.g. cone geysers) during the data acquisition, that we observe in the spatially strong confined group 1. Cone geysers and vents along fractures or flat sinter slabs are located directly neighboring. However, we found that the majority of currently active discharging vents are not associated with evolved larger sinter mounds or geyser cones. Cone geysers in general tend to erupt episodic and quiescent periods of minutes to days were reported by Glennon and Pfaff (2003), while many geysers erupting from flat sinter slabs show higher eruption intervals or even appear as perpetual spouters. Vents that were actively discharging during our data acquisitions are consequently the ones with higher eruption frequency but typically show no or minor topography. Vent clusters that have produced discharge during the acquisition are located rather along the southern parts of the active regions A1 and A2, in contrast to topographic objects that are distributed equally or

dominantly in the northern sections of the mentioned parts, especially in area A2. This effect is indicated in Appendix A2.3.

Considerations here are hypothetical but supported by the very specific setup and vent compositions showing clear dominance of certain objects in certain spatially confined areas. A dominant control of hydrological conditions on the appearance and object composition in El Tatio, next to primary or secondary structures, seems evident. Regarding vents of group 3 and the eastern section of group 4 which are largely located below the 1000 hPa isobar as well, we observe a discrepancy that can not be explained by this simplified approach. Here we observe an apparently different thermal regime with high discharge volumes, evidenced by extensive flow channels, but only moderate water temperatures and low energy release of <337 W/m^2 (<86 W/m^2), up to ~100 W/m^2 less than for the large hot springs of group 5. As illustrated by Munoz-Saez et al. (2018) for an N-S profile through the Tatio basin, we suppose the different thermal regimes to be caused by a similar effect of a probably topography-driven mixing with shallow meteoric waters but additionally in an *E*-W direction.

2.6 Conclusion

Based on high-resolution optical and infrared mapping, we identified over 1800 objects related to hydrothermal activity. This provides a unique data inventory allowing the analysis of the density distribution and activity of hydrothermal vents in the Tatio basin. We find a high degree of organization, where geothermal vents cluster and align along preferred pathways that have an azimuthal consistency with both the basin valley and regional faults. Specifically, our results highlight the dominance of two trends of which one, the NE-SW trend, is in accordance with the orientation of the previously identified Tatio fault. The second dominant observed trend is oriented E-W. These trends were observed especially in vent arrangements along lineaments or intersecting lineaments.

Similar trends can be observed in an exposed rock formation north of our study area, with two main orientations resembling the azimuths of vent orientations within the Tatio basin. In this respect, the study implies that alignments of hydrothermal vents provide an indirect view of the subterranean and commonly hidden structural architecture, predefining the vent generation along preexisting fractures or joints.

Next to structural controls, we suggest a hydrological control on the type and magnitude of fluid eruption by topographic particularities, especially the absolute elevation of vents. Size

and energy release of single vents are distinctly increasing from the Vega Rinconada, an area dominated by mud ponds, over the geyser belt, dominated by rather episodic, low-volume eruptions of a rather steam-driven regime to the low-lying hot springs in the west and southwest.

With this study, we showed the high potential of high-resolution close-range remote sensing and associated structural studies for the identification and understanding of local processes and structures on the generation of hydrothermal systems in their different characteristics at the surface.

2.7 Author contributions

D.M. performed all data analysis and led the manuscript writing. T.R.W. provided all funding, acquired the data, and supervised and supported the writing of the manuscript. M.Z. and G.G. supported this project due to their long-term engagement in Chile and supported the writing of the manuscript.

2.8 Acknowledgments

Field support and accompaniment by students and colleagues is greatly appreciated, especially by Christian Kujawa, Jackie Salzer, Masoud Allahbakshi, Stefan Mikulla, Mehdi Nikkhoo, Rene Mania, as well as logistic support by Ayleen Gaete Rojas and Klaus Bataille. This is a contribution to TecVolSA (Tectonics and Volcanoes in South America), which is a Helmholtz project dedicated to the development of Earth Observation (EO) data exploitation systems for monitoring various geophysical activities in South America. Travel support is provided by GFZ through IPOC (Integrated Plate Boundary Observatory Chile), which is a European-South American network of institutions and scientists organizing and operating a distributed system of instruments and projects dedicated to the study of earthquakes and deformation at the continental margin of Chile.

Chapter 3

Surveying fumarole sites and hydrothermal alteration by unoccupied aircraft systems (UAS) at the La Fossa cone, Vulcano Island (Italy)

Daniel Müller (1), Stefan Bredemeyer (1), Edgar Zorn (1), Erica De Paolo (2), Thomas R. Walter (1)

1: GFZ German Research Centre for Geosciences, Telegrafenberg, 14473 Potsdam, Germany
2: INGV Istituto Nazionale di Geofisica e Vulcanologia, Rome

This article was published in:
Journal of Volcanology and Geothermal Research, Vol. 413, Müller, D., Bredemeyer, S., Zorn, E., De Paolo, E. & Walter, T.R., Surveying fumarole sites and hydrothermal alteration by unoccupied aircraft systems (UAS) at the La Fossa cone, Vulcano Island (Italy), 107208,

Abstract

Degassing volcanic systems, expressed by fumaroles, thermal anomalies, and hydrothermal alteration and deposition at the surface provide insights into the underlying structural architecture and the magmatic system. While the fumarole sites are easily identified and investigated, areas of diffuse degassing and associated hydrothermal alteration are barely explored. Here we investigate high-resolution optical and thermal infrared (TIR) data, acquired by unoccupied aircraft systems (UAS) at the La Fossa cone (Vulcano Island) in November 2018. The data provide insights into the structural complexity of degassing sites and associated processes at the surface. Applying the Structure from Motion (SfM) approach, we generate a photomosaic database with a 0.05 m and 0.7 m pixel resolution for the optical and infrared datasets, respectively. A Principal Component Analysis (PCA) was applied to the optical data to detect, define and extract areas of hydrothermal alteration and sulfuric deposition on a pixel base, with a feature detection threshold of up to 25 cm². By comparing optical data, PCA results, and the IR data, we found a broad alteration zone dominated by diffuse degassing

surrounding the main fumaroles, which with ~ 60,000 m² is ten times larger than the area covered by fumaroles and yellowish sulfuric deposits. Spectral and thermal characteristics of this alteration zone suggest a segmentation into at least 13 distinct subregions. Hydrothermal alteration and deposition were analyzed considering their pixel density and spectral signature (RGB) and show the highest pixel density in the center of the fumarole field, accompanied by a systematic color shift. The same region is characterized by a systematic change in azimuths of thermal lineaments and sulfuric clusters from the dominating trend NW-SE by ~90 degrees to NE-SW. We conjecture this to be controlled by a permeability contrast due to a subsurface structure or crater intersection, facilitating a more direct gas ascent in the center of the fumarole field. We provide a precise and complete database for the state and extent of the La Fossa fumarole field, which can be used for comparative monitoring of spatiotemporal changes within the hydrothermal system at the surface.

3.1 Introduction

Fumaroles are the surface expression of hydrothermal systems, often associated with emerging or cooling volcanism, releasing large amounts of magmatic and/or hydrothermal gases (Fischer and Chiodini, 2015). Fumaroles have been intensely investigated at volcanoes worldwide, as their appearance, temperature, and chemistry can be used for monitoring purposes (Chiodini et al., 1993) and signal volcanic unrest and coupling of the hydrothermal system to the environment (Zimmer et al., 2017). Hydrothermal systems develop important sulfur and ore deposits, resources that are often exploited for industrial use (Arnórsson et al., 2015). The appearance of fumaroles is related to narrow permeable conduits or cracks that channel fluids from depth toward the surface, affected by topography, structure, and aquifers. They are visible at the surface by extensive mineral precipitation (Gresse et al., 2018) and elevated temperatures but are also associated with broad zones of diffuse degassing (Chiodini et al., 1996). Nevertheless, the distribution and characteristics of the surface expression of fumaroles may be much more complex and the exact extent of fumarole fields has remained difficult to analyze and monitor, due to the often high number and clustering of fumarole vents, their high temperature, and aggressive acidic gas chemistry. Determining the extent of fumaroles can thus be challenging, as the surface expression involves the actual degassing site, various degrees of mineral coatings, such as native sulfur covering surrounding rock surfaces, and also areas subject to deep-reaching extensive mineral alteration associated with gas-rock, gas-water, gas-

gas and gas-atmosphere interactions, condensation, and sublimation of the gaseous phase (Aguilera et al., 2016). Hydrothermal alteration is associated with dissolution and remineralization of the original rock material and is typically accompanied by leaching of rocks (Azzarini et al., 2001; Fulignati et al., 2002) reflected by a color shift towards light gray tints. Hydrothermal deposition indicates locations of fumarole vents by yellowish sulfuric deposits, precipitating from the fumarole plume. As both processes, alteration, and deposition, are visually expressed in the field, optical remote sensing may contribute to differentiate between them.

As we will show in this work for the degassing sites at Vulcano Island, Italy, a detailed analysis of the fumarole-related surface expression may provide important clues to the degassing sites and underground permeability structure. Fumaroles often display a geometric organization controlled by the underlying structure, being clustered or aligned along preferred pathways (Schopa et al., 2011; Hutchison et al., 2015; Walter et al., 2020). Previous studies on the distribution and appearance of fumaroles showed that they follow the structural architecture of a volcano on a large scale (Hutchison et al., 2015), possibly being aligned along prominent faults, fracture zones, and lithology layers (Schopa et al., 2011) and changing with time (Neale et al., 2016). As fumaroles are associated with the rise of a fluid/gas mixture along a permeable structure, their detailed mapping may be used for inferring hidden structural arrangements at depth. The structural control is dominant on different scales and may be well distinguished on a large edifice scale but obscured on smaller scales by other processes and effects (Hutchison et al., 2015). Moreover, fumarole locations may be affected by the stress field in a volcano, with gas flow following the principle of least effort at macro fractures or zones of higher permeability, but also being attracted to topographic highs (Schopa et al., 2011). The degree of hydrothermal alteration and high-sulfidation ore mineralization typically decreases with increasing distance to the fumarolic conduits (Mayer et al., 2016). Around the conduit usually an inner leaching and amorphous silica zone are developed, surrounded by less acidic alteration zones in which the formation of Alunite and Kaolinite is promoted (see also Robb, 2005). Details of this alteration aureoles and zonation at distinct volcanic fumaroles are commonly not accessible and often remain difficult to determine. An aureole may obscure the location of the fumarole and be governed by structural and permeability anisotropies. Therefore, investigating the arrangement of fumarole degassing sites in detail requires the consideration of alteration aureoles and sulfuric deposits.

Remote sensing is particularly useful for observing, mapping, and monitoring fumaroles (Harris and Stevenson, 1997). Earlier studies relied on satellite and airborne imagery using Landsat, JERS-1, SPOT, AVHRR digital imagery, and space-borne photographs (Oppenheimer et al., 1993; Aguilera et al., 2016). Thermal infrared remote sensing is a successful tool for the identification and precise location of fumarole sites (Oppenheimer et al., 1993; Harris and Stevenson, 1997; Tratt et al., 2011). The use of lightweight thermal infrared cameras mounted on unoccupied aircraft systems (UAS) has greatly advanced these fields in recent years (James et al., 2019; Jordan, 2019). UAS equipped with optical cameras are providing high-resolution data. Due to the low flight altitudes, the spatial resolution of the UAS images is much higher than the best available satellite data. This is associated with more distinct spectral pixel information, resolving even localized color variations. Therefore we can image fumarole fields in great detail and potentially resolve novel structures and processes. However, the information extraction and interpretation of such high-resolution data are still challenging tasks.

The analysis of image band combinations, Principal Component Analysis (PCA), and image classification are common tools in geoinformatics, potentially useful for image analysis (Lillesand et al., 2015). PCA is a statistical instrument that helps to identify variables accountable for variations within a data set. Applied to image data, it allows to reveal hidden information and therefore is widely used in remote sensing. PCA was found highly successful, for instance, in identifying biological and geological units (Loughlin, 1991), structures and water bodies on the ground (Rathinamet al., 2007), patterns in agriculture and forestry (Adao et al., 2017), and hydrothermal alteration from satellite imagery (Xu et al., 2019). Applications at volcanoes include geologic mapping of hydrothermal mineralizations (Rejas et al., 2012), and gas and ash cloud detection from balloons (Vernier et al., 2020) or satellite data (Li et al., 2014).

Applied to UAS-derived data on volcanoes, PCA is particularly beneficial for the detection and characterization of processes and deposits associated with eruptions and hydrothermal activity. Rearranging the data points according to the maximum variances, PCA provides a decorrelated variance or covariance (depending on the algorithm) representation of the original image data (Loughlin, 1991), and therewith can be understood as a detector for optical anomalies, which would barely be seen by the naked eye in the raw optical data. The use of UAS data and PCA in volcanology and especially fumarole research is particularly promising, as our study reveals.

3.2 Study area

Fumarole and geothermal activity at Vulcano Island are closely related to the tectonic, geologic, and volcanic history (De Astis et al., 1997). Vulcano is the southernmost island of the Aeolian Arc, located within the Aeolian Tindary Letojanni Fault system (ATLF), a dextral NNW-SSE trending strike-slip system (Cultrera et al., 2017). The ATLF is tectonically active, as evidenced by frequent earthquakes and dextral oblique-slip motion (Mazzuoli et al., 1995; Ventura et al., 1999). Vulcano Island (Fig. 3.1A) hosts a composite volcanic system that is made up of the edifice dissected 100 ka ago by arcuate faults from the Piano Caldera followed by the cyclic subsidence of the La Fossa Caldera 80 ka to 15 ka ago (De Astis et al., 2013). Since that time, activity has mainly concentrated in the northern part of the island, which is punctuated by vents that are aligned in the N–S direction (Gioncada et al., 2003). Details of the stratigraphy and geochronology of the La Fossa cone are summarized in Di Traglia et al. (2013). La Fossa has been active since 5.5 ka (Frazzetta et al., 1983) with an estimated 15 effusive and explosive eruptions in historical times (Arrighi et al., 2006). The most recent eruption terminated in 1890 and consigned the La Fossa cone as present today (Arrighi et al., 2006). La Fossa continued outgassing ever since, with multiple hazards that originate from the crater region (Selva et al., 2020).

The La Fossa cone is made up of at least four overlapping eruption centers (De Astis et al., 2013) identified in stratigraphy and morphology (Fig. 3.1A). The geomorphology of the La Fossa cone shows a high height/base area ratio (H/Wb = 0.55) and a summit area/base area ratio (Ws/Wb = 0.57) that reveals a cone volume of 0.53 km³ that has a highly regular conical shape (Grosse et al., 2014). The edifice base is elliptical, and the summit area is characterized by ESE–WNW trending major axes (Di Traglia et al., 2013). Pronounced historic crater structures are truncating the morphometry of the regularly shaped La Fossa cone, such as the CE 1988 landslide scar (Tinti et al., 1999; Bonaccorso et al., 2010; Romagnoli et al., 2012), and several nested crater rims identified at the summit area (Frazzetta et al., 1983; Di Traglia et al., 2013). The more recent craters at La Fossa are located in the western sector of the summit area, while the older ones are located in the northeastern part, thus their assembly is forming a relatively flat-topped cone shape (Di Traglia et al., 2013).

Sustained activity is expressed by degassing throughout the entire central and northern part of Vulcano Island, where especially diffuse CO_2 degassing from soils is present over broad areas (Baubron et al., 1990; Capasso et al., 2000; Carapezza et al., 2011; Inguaggiato et al., 2012; Di Martino et al., 2016). In the summit region of the La Fossa cone, extensive degassing from

low- and high-temperature fumaroles occurs in several separate regions. Active degassing sites are present on the outer and inner crater rims referred to as Cr2, Cr3, and Cr4 (Fig. 3.1) in the south, east, and north, respectively. They are associated with the units of Pietre Cotte and Caruggi formation (De Astis et al., 2013) and expressions of larger hydrothermal complexes (Revil et al., 2008). The hydrothermal activity of the most recent 1888 - 1890 eruption crater Cr4 especially occurs on its northern rim, expressed by multiple high-temperature fumaroles and diffuse degassing sites, referred to as main fumarole field MF (Fig. 3.1A-C). The MF consists of an upper and a lower segment that intersect in the center of the fumarole field. Dominant fumaroles have been mapped and described in previous works (Bukumirovic et al., 1997; Madonia et al., 2011; Madonia et al., 2016), of which the most prominent are shown in Fig. 3.1C. The spatial segmentation of the fumaroles is associated with variabilities in the gas composition, with a generally higher magmatic composition at the inner fumaroles (Tedesco et al., 1991; Chiodini et al., 1996; Aiuppa et al., 2005; Paonita et al., 2013). Selected high-temperature fumaroles are permanently monitored and thus provide a time series of over 25 years (Diliberto, 2017).

Vulcano Island has undergone several periods of unrest during its documented history (Capasso et al., 1999; Vita et al., 2012; Capasso et al., 2014; Diliberto, 2013; Diliberto, 2017), which were identified by changes in the gas composition (Aiuppa et al., 2005; Paonita et al., 2013), increased groundwater and soil temperatures (Aubert et al., 2008), increased fumarole temperatures (Sicardi, 1955; Martini, 1983; Madonia et al., 2013; Diliberto, 2011; Diliberto, 2017), but also by an increase in the size of the fumarole field. During the period 1983 to 1995, a growth of the fumarole field from 50 m² to 2400 m² was observed (Bukumirovic et al., 1997). Fumarole activity at the La Fossa cone has led to the buildup of deposits mantling surrounding rocks (Cheynet et al., 2000) and widespread hydrothermal alteration around the sites of volcanic degassing (Azzarini et al., 2001; Fulignati et al., 2002). As the fumarole expression is thus an important indicator of Vulcano's state of activity, detailed mapping and cataloging are particularly relevant. The wide distribution of the fumaroles, however, makes pointwise measurements challenging and time-consuming, which is why remote sensing imaging techniques are found to be beneficial. The herein-presented study aims to detect, analyze and quantify hydrothermal alteration and sulfuric deposition within the La Fossa cone, based on a Principal Component Analysis of high-resolution UAS-derived image data. By this, we are testing a simple but highly accurate methodology for the monitoring of fumarole fields and

associated phenomena of the diffuse degassing regime, which might rapidly change during periods of volcanic unrest.

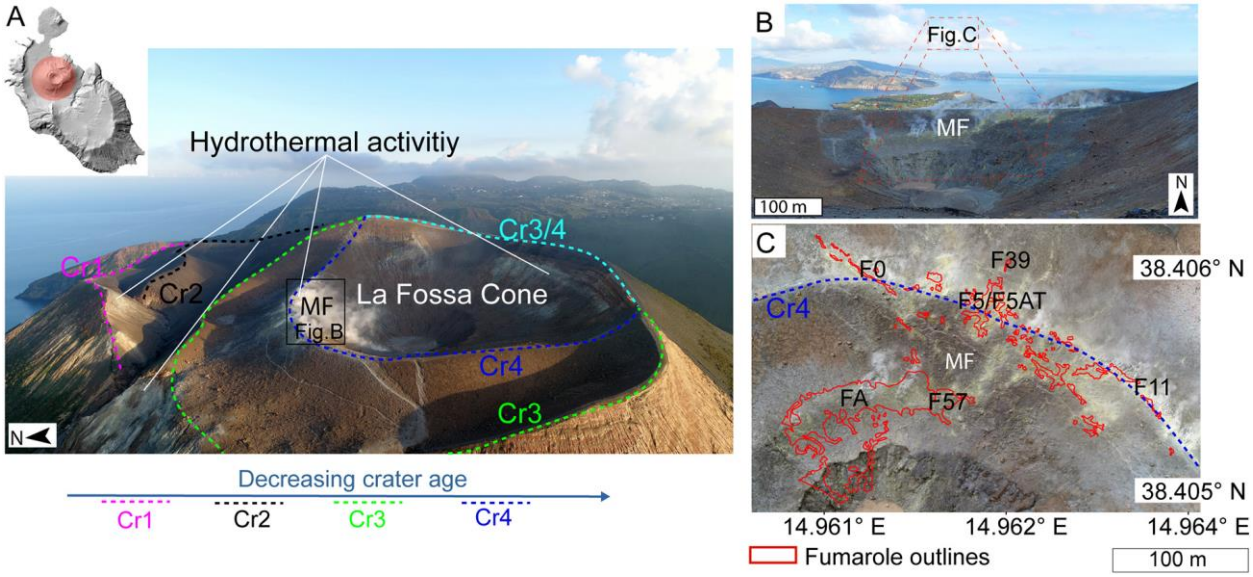

Fig. 3.1 (A) Oblique aerial view from the UAS over the La Fossa cone, viewing towards the east, depicting the temporal evolution of crater formation by colored dashed lines after Di Traglia et al. (2013). The La Fossa cone is characterized by extensive degassing from numerous distinct locations, especially on the northern rim of crater Cr4 where the main fumarole field (MF) is located. The insert shows a shaded relief map of Vulcano Island and the location of the La Fossa cone highlighted in red. (B) Panoramic view from the southern crater rim towards the north onto the main fumarole field (MF), highlighting the degassing activity. The dashed outline represents the outline of (C). (C) Close UAS nadir view of the main fumarole field with outlines of high-temperature fumaroles in red (Bukumirovic et al., 1997; Madonia et al., 2016).

3.3 Data and methods

3.3.1 UAS field campaign

The La Fossa cone on Vulcano Island is well suited for unoccupied aircraft system (UAS) campaigns, as it is low in morphology, easy to access, and has a small area that can be covered even by small consumer drones. In November 2018 (13-15th) we repeatedly overflew the La Fossa cone with a DJI Phantom 4 Pro, a small quadcopter-UAS equipped with both optical and thermal infrared camera sensors. As the launching point of most UAS flights, we used a concrete platform (referred to as above ground level or agl in the following) located on the northern rim of the La Fossa crater.

The optical images were acquired during noontime when shadowing within the crater is low. The data was acquired with a gimbal-stabilized camera, which has a 1″ CMOS sensor providing

20-megapixel images (5472×3648 pixels in 4:3 mode). The UAS flight velocity and acquisition rate of images (0.5 Hz) were set in a way to ensure a minimum overlap of 70% between images. Flight paths were pre-planned but followed manually to quickly react to changing wind conditions. To obtain a general overview at a reasonable resolution, we performed overflights at a height of 250 m above ground level (agl). Most of the analysis presented in this work is based on this 250 m (agl) optical data set. Selected regions of interest were additionally overflown at a lower altitude at 100 m (agl) to acquire a higher spatial resolution of the image data.

Infrared surveys were performed in the early morning before sunset when the air and ground temperatures are still low. This scheduled data acquisition allowed for gathering the highest possible temperature contrast in the data and avoiding irregular surface heating due to solar radiation exposure (Stevenson and Varley, 2008). This way, we achieve the sensor's best sensitivity and ensure to image the thermal radiation caused by the hydrothermal system exclusively. For the acquisition, we used the same DJI Phantom 4 Pro Quadcopter but additionally equipped with a 95 g Flir Tau 2 640 infrared camera attached to a Teax Thermal Capture 2 data logger and an external GPS receiver for geotagging. The system measures in a spectral range of 7.5–13 μm and stores radiometric thermal images with temperatures for 640 × 512 pixels at an interval of 8 Hz and was successfully used already in other studies on volcanoes (Zorn et al., 2020; Walter et al., 2020). Logged images are provided with GPS coordinates and time stamps, easing later photogrammetric and radiometric processing.

Thermal data acquired by remote sensing platforms represents apparent temperatures, as it depends on the object and environmental properties, such as the distance and viewing angle to the object, its emissivity, solar reflection, atmospheric attenuation, or the presence of particles/gases in the electromagnetic radiation path (Spampinato et al., 2011). These parameters need to be considered to improve the results (Ball and Pinkerton, 2006). To avoid resolution-related effects, only images of a constant flight altitude were selected for further processing. Environmental effects, that may influence the derived temperature, were considered using the radiometric correction theme in the ThermoViewer Software. We defined an emissivity of 0.95 (emissivity for gravel). An environmental and path temperature of 17 °C and a humidity of 50% were measured by a portable hygrometer in the field. Especially the effect of emissivity on pixel temperatures can not be neglected, as it influences the calculated pixel temperature (Appendix 3.1). Temporal fluctuations of these parameters during the measurement campaign were not further considered. The calibrated temperature range of the

IR sensor is −40 °C to +180 °C at a thermal resolution of 0.04 K, thus apparent temperatures greater than 180 °C would appear saturated. In all data sets, a saturation of the apparent temperatures was not reached, so that the considered temperature range was found adequate (see also the description of limitations in the discussion section). For the low altitude (90 m agl) overflight data, focused on the acquisition of the fumarole field only, the temperature peaks at 179.5 °C. In total, we acquired ~ 6500 optical images and ~60,000 IR images, which after a preselection were then further processed using the Structure from Motion (SfM) approach and analyzed as detailed below.

3.3.2 UAS data processing

The UAS image data was processed in Agisoft Metashape (Version 1.5.2.7838), a widely used commercial Structure from Motion (SfM) software package. SfM allows for generating two main data products relevant to this study: i) a reconstruction of 3D point clouds from 2D photographs providing Digital Elevation Models (DEM), and ii) high-resolution orthomosaic data (Smith and Vericat, 2015; James et al., 2019; Jiang et al., 2020), merging the high resolution of hundreds of photographs to cover larger areas. We generated the DEM and orthomosaic from the optical data sets and a thermal mosaic from infrared images.

After preselection and quality control, 610 optical images were processed in the high-resolution mode in Agisoft Metashape, eventually resulting in a point cloud containing 265 million points. Drone internal sensors provide positioning and other flight parameters, stored in flight logs, and the metadata of each photo during the acquisition. An algorithm uses the metadata to preselect pairs of overlapping images to accelerate the processing and reduce computing time. The used onboard GNSS geotagging of the Phantom 4 Pro drone is used for SfM processing, typically ensuring a within-model horizontal distance measurement error of 2–3 decimeters ($0.21<\mu<0.26$ m), whereas the absolute horizontal positional error may approach 3 m or more (Kalacska et al., 2020).

The infrared (IR) image data was examined and pre-processed in ThermoViewer 3.0, allowing the definition of a constant emissivity, transmissivity, and mean path temperature. Colored infrared images provide a contrast-optimized visualization and are especially beneficial for generating overview maps. However, In order to analyze the infrared data quantitatively, a linear color scheme (grayscale) is required as colored infrared palettes influence the data values and produce artificial patterns (Appendix 3.1). The data was exported as 16-bit grayscale TIFF

images, and two infrared data sets were generated. From a high-altitude overflight (230 m agl) 1027 infrared images were selected and processed in Agisoft Metashape, similar to the optical data, eventually resulting in an infrared mosaic covering the whole La Fossa cone with 5.7 km² at a resolution of 0.78 m. A second data set from a lower flight altitude (90 m agl), processed from 544 images covers the main fumarole field only (0.16 km²), but at a high resolution of 0.16 m per pixel. Only images of a stable flight altitude were selected for the processing, no ascending or descending images, as the changing spatial resolution would locally affect the measured thermal radiation at the sensor. An overview of the processed data sets is provided in Table 3.1. The resulting DEM, orthomosaics, and infrared mosaics were then exported to a GeoTiff format and further processed in the ArcGIS Geo-Information System (GIS) in the WGS84 coordinate system. The DEM was used to generate a shaded relief background map. The ortho- and infrared mosaic was used for investigative analysis, feature detection, and associated structural analysis.

Table 3.1: Overview of the processed datasets for high and low overflights and coverage for optical and thermal infrared overflights respectively.

Dataset	Number of images	Flight altitude in m	Ground resolution in m	Coverage in km²	Point cloud Nr. of points
Optical overview	610	250	0.05	2.11	264.986.723
Optical MF	125	100	0.02	0.116	64.649.828
IR overview	1027	230	0.78	5.77	8.615.770
IR MF	544	90	0.16	0.164	6.311.603

3.3.3 Data analysis

3.3.3.1 Image analysis, PCA, and classification

Optical images are graphically represented by a proportion of the red, green, and blue pixel values (RGB). The detection and extraction of features from photographs of volcanoes are challenging, as image data of volcanoes is poorly colorized and dominated by greyish colors. Visualizing the RGB information of volcanoes in a 3-dimensional RGB space, they tend to form elongated narrow clusters along the RGB main axis from black (RGB 0,0,0) to white

(RGB 255,255,255), comprising mainly gray tints. This is shown in Fig. 3.2, which is a subset of the colors encountered at the La Fossa crater, measured at 50,000 random points within the crater Cr3.

The elongated and narrow data cluster visually demonstrates the low data variance and the limited interpretability. Further, it indicates that the information of the single RGB bands is correlated, which necessitates a 3-dimensional approach. Principal Component Analysis (PCA) is often used in remote sensing for dimensionality reduction (Kwarteng and Chavez, 1989) and may be particularly useful for this attempt. By reorganizing the data points along the perpendicular axes of highest variance/covariance, PCA allows a decorrelation of the data and eventually provides a variance representation of the original data set. The PCA method is known to be highly efficient for alteration mapping (Loughlin, 1991). Therefore, we applied a PCA (implemented in the classification toolbox in ArcGIS) to the RGB values of the orthomosaic maps that were produced by the SfM processing of the UAS data collected on Vulcano Island.

The single Principle Components (PC) are stored in separate single-channel images, where PC1 contains the highest variance (93.9%), with the variance decreasing with increasing PC number (5.3% for PC2 and 0.8% for PC3). A table of Eigenvectors, Eigenvalues, and variance of the single PC is provided in Appendix A3.2. After the PCA, pixel values span a wider range in the PC space, and variability in the data is represented more distinctly. PCA, therefore, helps, based on variance or covariance representations, to detect patterns in image data that could be termed “optical anomalies” and eventually, due to the decorrelation of the RGB channels, PCs provide a far better separability of data portions of interest.

We used this effect to define the extent and boundaries of optically anomalous areas that are representing hydrothermal alteration and deposition and to extract these respective areas from the original orthomosaic. This has two advantages, a reduced amount of data pixels and a decreased spectral range, which allows a more sensitive analysis. This was realized by extracting the single Principle Components in the respective value range and then clipping the extracted single Principal Components from PC1 to PC3 with each other. This way we achieved a PC raster, combining the relevant information of all 3 PCs, which further was used as a clipping mask to extract the respective areas from the original true color (RGB) orthomosaic. We obtained two sub-datasets of which one is representing the variously colorized alteration zone. The second sub-data set is representing areas densely covered by hydrothermal deposits like sulfur and associated materials (referred to as sulfuric deposits or sulfur pixels in the

following). The high resolution of 5 cm allows a feature detection threshold of 25 cm². For further analysis of their spectral characteristics and geospatial patterns, an image classification was applied to the extracted RGB alteration zone data. Due to the high resolution, the data is heterogeneous which makes the application of a supervised classification not feasible. Therefore the approach of an unsupervised classification with a high number of classes (50) was chosen, further combining classes in a way that they eventually resemble optical units in the original data best. This way we defined 5 main classes resembling different intensities and brightness of grey colors. Based on patterns observed that are similar in the RGB data, PCs, classification results, and also IR data, we distinguished 13 subregions and analyzed their spectral characteristics based on the relative class compositions. A second PCA was applied to the extracted hydrothermal deposit data (RGB). Due to the reduced spectral range of this extracted data set, the second PCA provides an even more sensitive approach and far more detailed results.

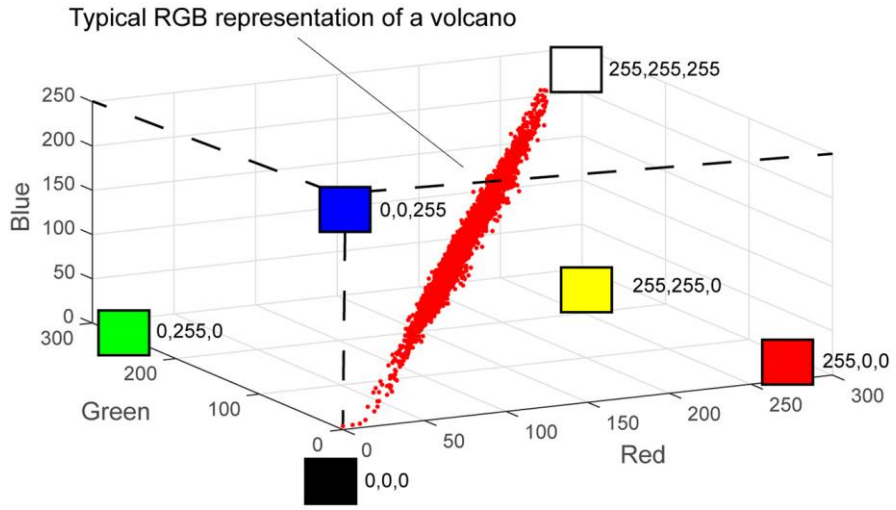

Fig. 3.2 Representation of the La Fossa volcano crater in the RGB space, measured exemplary at 50,000 points within the crater Cr3, appearing as a narrow elongated cluster along the main RGB axis from black RGB(0,0,0) to white RGB(255,255,255). Colors along this main axis comprise all shades of grey. This figure demonstrates that RGB is, due to the low data variance, not a distinct data representation to resolve color differences of volcanic deposits.

3.3.3.2 IR and structural analysis

The study of lineaments allows for the structural analysis of hydrothermal systems as they often resemble faults or fractures at different scales (Offield, 1975; Jaworowski et al., 2020). Therefore they might indicate locations and orientations of a facilitated gas ascend, that might

be controlled by permeability- or lithological contrasts, structures at depth, but also related to topographic effects or the present stress regime. Lineaments were investigated based on linear features observed in the thermal infrared data and the extracted sulfuric deposits. From the thermal infrared mosaic, an apparent temperature map was calculated.

Thereof, pixels with a temperature above certain thresholds (>25 °C, >30 °C, >60 °C) were extracted and converted to vector point data, providing coordinates and a temperature for each point. Based on these coordinates, a cluster analysis was performed, using a density-based cluster algorithm DBSCAN in the statistical software R (Hahsler et al., 2019), with a minimum object number of 4 to form a cluster and search distances of 0.5 to 5 m. It turned out that 1 m (width of two pixels) is an appropriate measure for the clustering, resulting in up to 382 clusters. The identified clusters were then analyzed by calculating a Standard Deviational Ellipse (Yuill, 1971), providing the orientation and the standard deviations for the two main axes (short and long axis of the ellipse) of every cluster. The ratio of the long to the short axis of the standard deviational ellipse was used as a form factor, giving information about the shape and linearity of the respective cluster. The thermal clusters were visualized in the respective thermal range in rose diagrams weighted by the form factor. The combination of PCA, DBSCAN, and SDE provides a toolset to systematically analyze large amounts of data points as received from UAS campaigns and has the potential to be applied as a standard method. Due to the locally high density of degassing spots, not all structural features could be clustered correctly. Therefore an additional comparative manual lineament mapping was performed on the extracted vectorized temperature data starting from 80 °C in 10 °C steps towards lower temperatures (20 °C).

3.4 Results

3.4.1 Data overview and geomorphology

The UAS data allows us to generate high-resolution optical and infrared three-dimensional point clouds of the La Fossa cone that eventually provides us with data sets to precisely map the expression, morphology, and apparent temperature field of the fumarole fields. The orthomosaic, DEM, and thermal infrared map of the 250 m / 230 m altitude overflight data are provided in Fig. 3.3.

The orthomosaic map (Fig. 3.3A) was generated at a ground resolution of up to 0.05 m and covers an area of 2.1 km², the entire cratered region of La Fossa. Especially the central parts of the La Fossa cone, the flat crater floor, the nested crater rims, the main fumaroles (MF in Fig.

3.3A-C) located on the northern crater rim, and the more deeply eroded parts of the outer crater walls in the north, are represented in great detail. The locations of hydrothermal activity are depicted by the yellowish to white colorization of hydrothermal deposits like sulfur and associated hydrothermal minerals, but also greyish colorization of hydrothermally altered ground. Several distinct hydrothermally active regions can be identified throughout the La Fossa cone (highlighted in grey in Fig. 3.3B), especially on the deeply eroded upper parts of the southern, eastern, and northern crater rims Cr1 and Cr3, related to the Caruggi formation (De Astis et al., 2013).

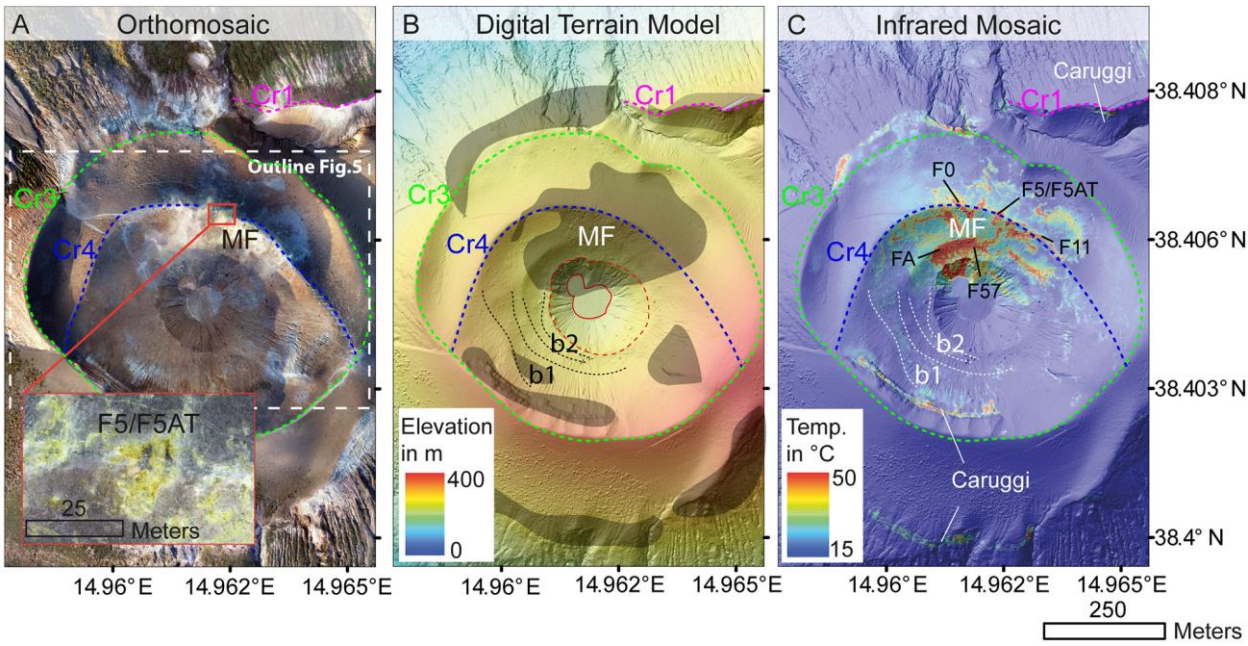

Fig. 3.3 Overview of the SFM processing results. (A) Orthomosaic of the La Fossa cone with a resolution of 5 cm/pixel. Indicated in colored dashed lines are crater rims of different eruptive periods, with Cr4 (dark blue stippled line) being the most recent. The Inset outlined in red shows a close-up of the high-temperature fumaroles F5/F5AT in the main fumarole field (MF). The white dashed line is indicating the outline of Fig. 3.5. (B) Shaded relief map of the La Fossa cone with altitudes depicted by color-coding. Areas of hydrothermal activity or alteration are schematically highlighted in grey. The continuous and stippled red lines are indicating the nested craters. (C) Infrared representation of the La Fossa cone highlighting the dominant main fumarole field (MF) in the northern part of crater Cr4, as well as some smaller thermal anomalies distributed within and outside the crater. Two belts of localized small anomalies (b1/b2) are outlined by white dotted lines.

The most recent activity is related to the northern segment of crater Cr4, hosting the main fumarole field MF, but also at several sites of variable sizes within the crater Cr4. Closeup views show that individual fumaroles can be distinguished, like the high-temperature fumaroles

F5 and F5AT, characterized by a dark center of blank bedrock free from sulfuric deposits, surrounded by whitish, yellowish, and pale brownish aureoles (inset in Fig. 3.3A). As the optical camera flights were realized during daytime in the afternoon, the effect of condensing steam and associated blurring of the ground is found to be minor only.

The DEM was constructed from the 3D optical point cloud at a pixel resolution of 0.1 m (Fig. 3.3B). It shows the relatively smooth terrain of the more or less concentrically nested crater walls, formed during the last eruptions. A series of at least 4 distinct craters can be identified (Cr1-Cr4) of which Cr4 is the most recent one (for location see Fig. 3.3). The unit of the Cr4 eruption appears as a nested crater, with a smaller northwestern crater (~1000 m² at the crater floor) and a bigger southeastern crater (~4500 m² at the crater floor), surrounded by a rim exposing radial erosion gullies. The intersection of both is pointing toward NNE and W, whereby in the NNE direction a bend is visible in azimuth in the crater rims Cr3 and Cr1, but not in the most recent Cr4. Further, the inner Cr4 crater consists of 3 terrace-like steps, most prominent in the northern part and vanishing slowly towards the southwest, while the southern and eastern part of the inner Cr4 appears as a single cliff, exposing lithology layers on the inner southern crater rim. The DEMs hardly allow recognition of fumarole active sites, but in combination with the IR data emphasize the preferred location of fumarole sites at topographic highs and permeable upper parts of the steep crater slopes (Fig. 3.3B).

The thermal infrared mosaic (Fig. 3.3C) covers an area of 5.7 km² at a mean pixel resolution of 0.78 m and a radiometric resolution of 0.04 K, illustrating the apparent temperature field of the complete La Fossa cone, delimited by the Levante Bay in the North and Monte Saraceno in the South. A second data set with a higher pixel resolution of 0.16 m per pixel provides a more accurate apparent temperature representation of the fumarole field (MF). As the infrared data was acquired during nighttime, we can identify even the smallest thermal anomalies above the background soil temperature (17 °C). The thermal infrared mosaic is highlighting the above-mentioned multiple broader degassing sites but is also revealing small localized spots at a detection threshold of 0.6 m² for the area of the La Fossa cone and 0.03 m² for the MF. The most dominant thermal anomaly is the main fumarole field MF, located in the northern part of crater Cr4 (Fig. 3.3C). A broad region of increased apparent soil temperatures covering an area of ~70,000 m² (bounded by the 20 °C isotherm) surrounds the MF, pierced by stronger anomalies. Localized fumarole vents accumulate and cluster to sub-areas of increased hydrothermal activity and increased soil temperatures, that in some cases, form pronounced alignments. But also smaller point-like thermal anomalies occur, e.g. several small, square

meter scaled low-temperature anomalies located in two circumferential belts in the central southern crater, each associated with the inner crater wall (b1/2 in Fig. 3.3C). In total, 441 isolated thermal anomalies with a temperature above 20 °C and a size > 1.2 m² (2 pixels) were identified within the crater Cr3. The highest apparent temperatures of over 170 °C were observed at 7 isolated hot spots related to fumaroles F0 and F1, followed by temperatures above 150 °C observed in F5, GBC, F11, F14, and F17 (Fig. 3.4A). The highest temperatures observed are closely related to the upper crater rim Cr4 and are distributed within a belt of 15 m on both sides of Cr4 (Fig. 3.4B). A further overview of the frequency distributions of the values of all datasets is shown in histograms in Appendix A3.3.

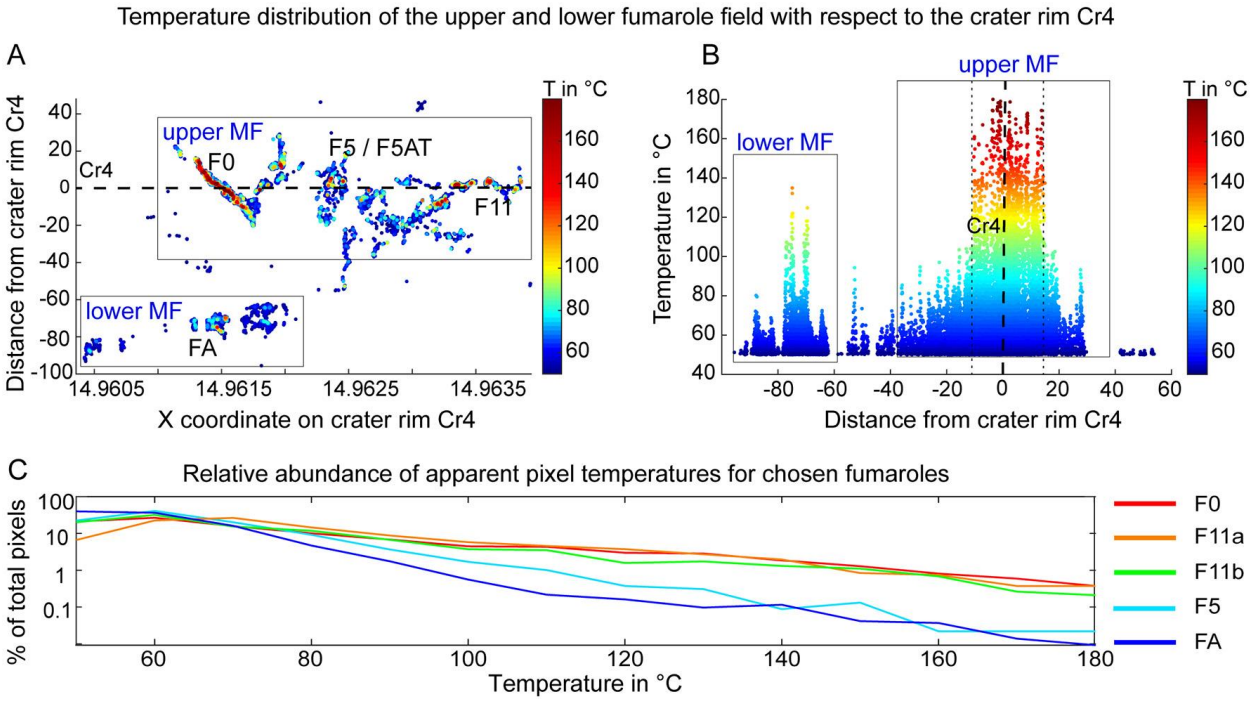

Fig. 3.4 (A) Spatial temperature distribution of fumaroles in the MF with distance to the upper crater rim Cr4. The locations are calculated based on infrared pixels with a distance perpendicular to the crater rim Cr4, represented by the dashed line. The topology is geometrically detrended according to the crater rim curvature. Visible are the different orientations for different fumarole clusters along Cr4. F0 is intersecting the rim at an azimuth of ~ 45° degrees, while F5 is oriented almost perpendicular and F11 is running crater parallel. (B) The highest temperatures occur within a 30 m narrow band along Cr4. (C) Relative temperature pixel abundances for selected fumaroles F0, F5, F11, and FA. Fumarole F11 further is subdivided into an eastern (F11a) and a western (F11b) vent site.

3.4.2 Alteration Detection with Principal Component Analysis

The results of the Principal Component Analysis are provided in Figs. 3.5 and 3.6. Fig. 3.5 is showing the same image section of the La Fossa cone in a direct comparison as the RGB image (Fig. 3.5A), all Principal Components in a multi-band raster image (Fig. 3.5B), and thermal Infrared image (Fig. 3.5C). The multi-band PCA map highlights zones in reddish-purple color tints, where the specific spectral characteristics in the RGB are different from the overall reddish-brown deposits characterizing the inner La Fossa crater. Those zones, a broad region surrounding the fumaroles, and also erosion gullies and hiking trails appear as grayish areas (reddish-purple in PCA map), or as whitish-yellowish fumarole areas (light-blue in the PCA map) in the RGB data. Therefore, they can be barely distinguished by eye, but are clearly expressed as anomalies in the PCA map. These grayish zones surrounding the MF and found elsewhere are denoted as alteration zones or aureoles in the following.

The alteration zone that surrounds the main fumarole field (MF in Fig. 3.5B) extends to a distance of 35 to 100 m away from the main fumarole vents and covers an area of ~60,000 m², with a well-defined almost sharp delimiting boundary in its periphery. Many smaller optical anomalies seen in the PCA map are identified on the inner western crater rim (C1, C2 in Fig. 3.5B). Two larger zones are located on the inner southwestern and southeastern crater rim (C3 and C4 in Fig. 3.5B), whereby C4 has a slightly different signal. The hiking trails identified in the PCA map (p in Fig. 3.5B) appear to have a similar signature in the PCA and the same grayish colorization in the RGB. Therefore, all of the optical anomalies are also characterized in the PCA map, while the PCA map allows identifying and discriminating additional zones that are difficult to discern in the optical map only. Similar patterns as those observed in RGB and PCA (Fig. 3.5A,B) are also visible in the thermal infrared data. Fig. 3.5C is showing an area of increased soil temperatures, bounded by the 20 °C isotherm (3 °C above background temperature), coincident with the aureole surrounding the MF in the optical data and PCA.

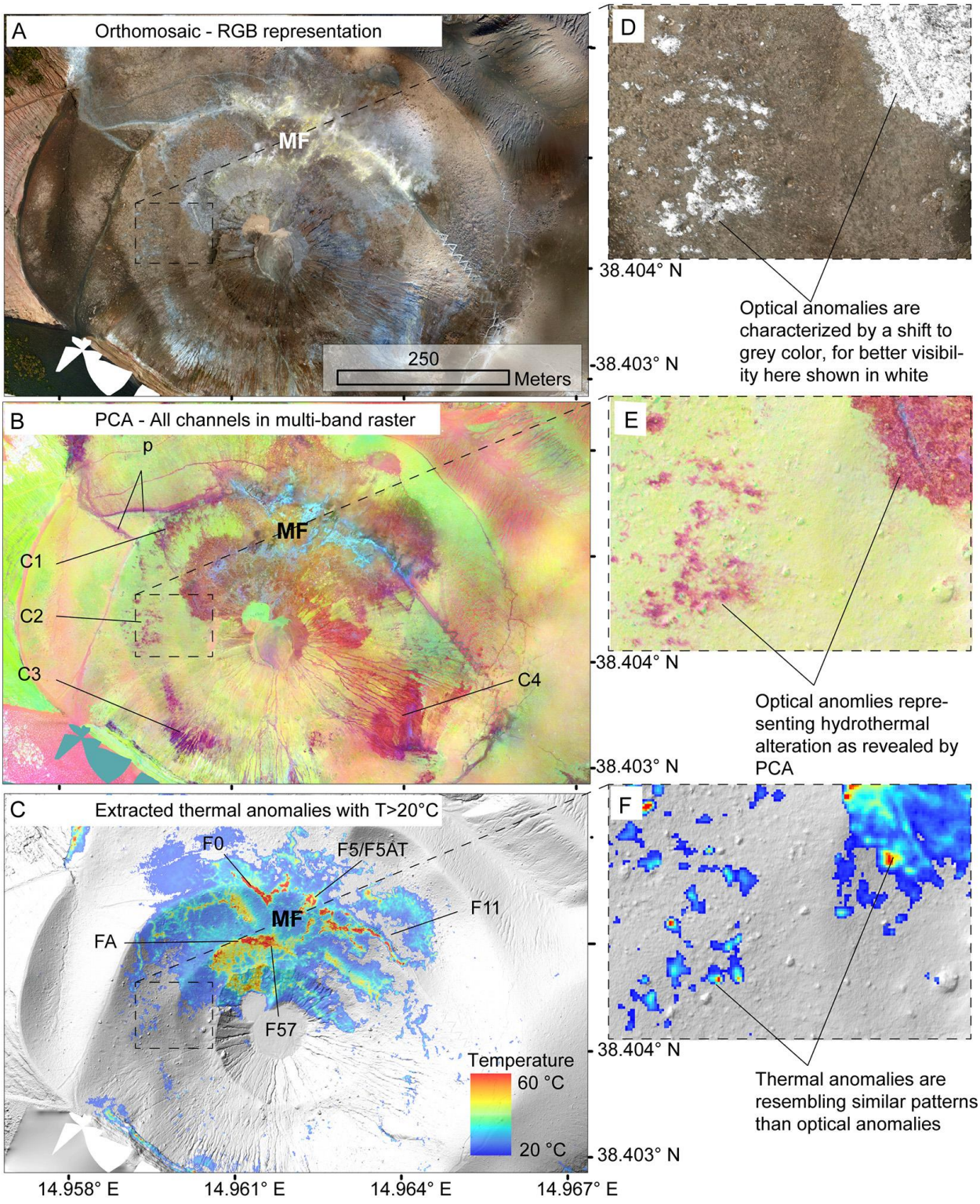

Fig. 3.5 Comparison of RGB, PCA, and TIR data. (A)The central La Fossa cone as it is represented in the RGB image. Hydrothermally active sites could be inferred from grayish to yellow colorization, but not very distinct. (B) The same area is represented by all PCs in a multiband raster, highlighting hydrothermally altered areas in reddish tints, revealing a clear outline and sharp boundary, as well as some smaller spots that could not easily be recognized in the RGB data. (C) Apparent temperature above 20 °C (3 °C above background) measured from 230 m flight altitude. The patterns observed in all 3 data representations are almost

identical and imply a strong correlation between temperature and rock color at the surface. This is true for even the smallest anomalies in the order of 1 m², as is shown by Figs. 3.5*D-F.*

The small insets D-F in Fig. 3.5 are highlighting the effect that optical anomalies in RGB and PCA are similar in size and location to thermal anomalies, even at the scale of 1 m²-sized localized spots.

The individual Principal Components (PCs) 1–3 are illustrated as grayscale raster data in Fig. 3.6A-C. The orientation (Eigenvector) and extent (Eigenvalue) of the single PC are represented by the colorization and extent of the point clusters in the 3-dimensional scatter plot, representing the RGB space (Fig. 3.6E). PC1, the component with the highest variance, is oriented along the long axis of the RGB cluster (RGB (0,0,0) – RGB (255,255,255)), basically representing brightness effects. Although representing the highest variance, PC1 is not a distinct representation of hydrothermal alteration and deposition, and therefore not further considered for the following analysis. PC2 (Fig. 3.6B) is oriented perpendicular to PC1, pointing from the central main axis (PC1 respective gray shades) towards the color end members (red or green) and therefore effectively affects the color depth towards more distinct color representations. PC2 provides a very distinct representation of the hydrothermal alteration zone, with a sharp boundary towards the surrounding volcanic material. PC 3 (Fig. 3.6C), in turn, provides a good representation of the fumarole sites and hydrothermal deposits and compares to the high-temperature thermal infrared anomalies (Fig. 3.3) originating at punctuated and aligned vents.

Due to the data transformation into a new data coordinate system, with the main axes representing the perpendicular vectors of the highest variance, PCA decorrelates the data and facilitates a more clear data separability. Fig. 3.6F illustrates the separability of hydrothermally altered areas in PC2 along Profile A-D, with gray values > 120 representing the signature of the alteration zone. This is similarly true for areas covered by hydrothermal deposits in PC3. This separability was used to extract the alteration area and sulfur deposits from the PC rasters (Fig. 3.6D), which in turn were used as a mask for the extraction of the respective areas from the original RGB data set.

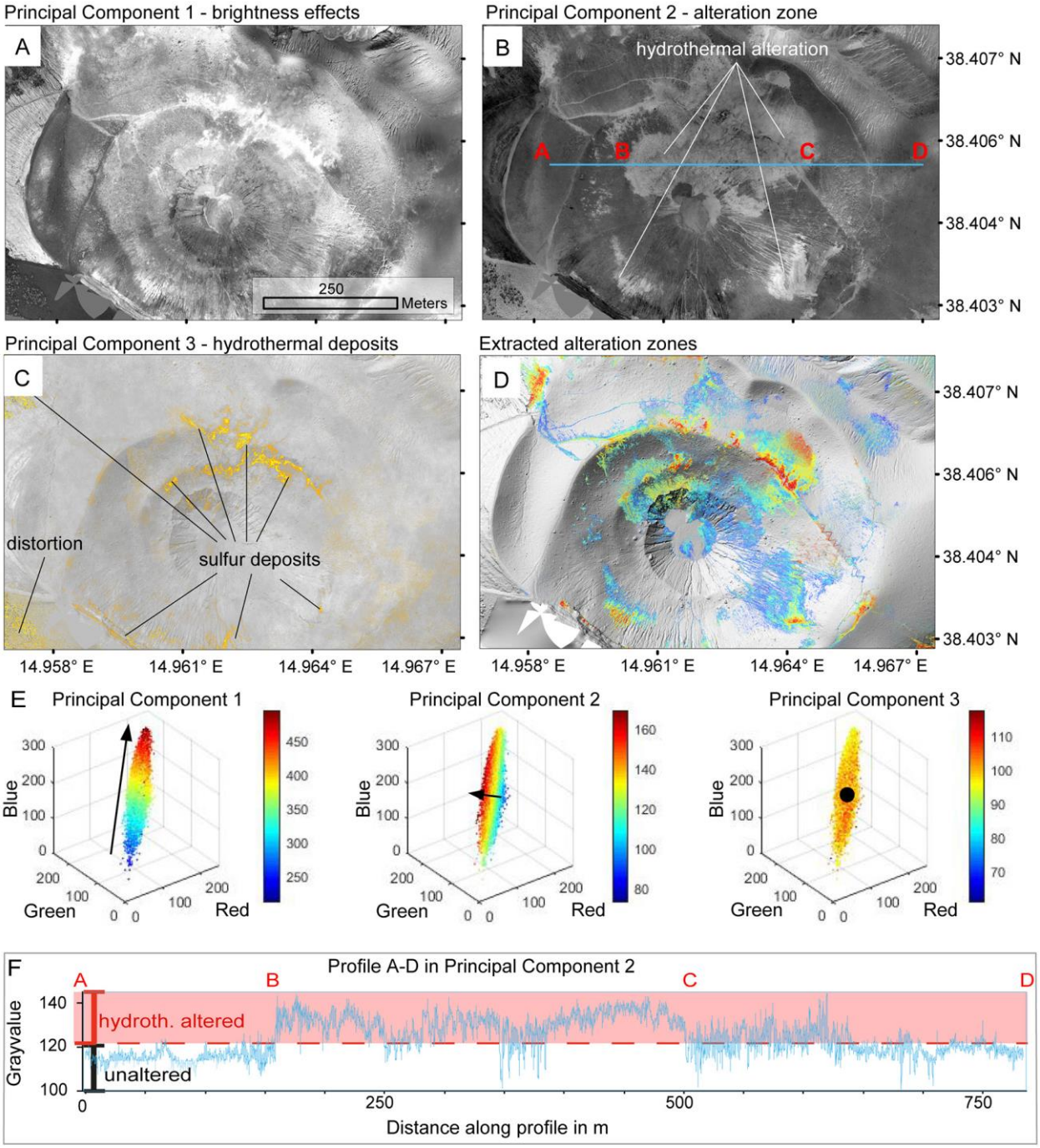

Fig. 3.6 Single Principle Components displayed as grayscale raster images. (A) PC1, the component with the highest variance is mainly showing brightness differences. (B) PC2 is revealing a clear and sharply bounded outline of the alteration zone and allows a clear distinction of hydrothermally altered to non-altered material at the surface (Profile A-D in Fig. 3.6*B/F). (C) Inferred hydrothermal sulfuric deposits, here color-coded in yellow for better visualization, as observed from PC3. (D) Extracted alteration area. The image is color-coded according to the multiband PCs and implies heterogeneities within the alteration zone. (E) Orientation of PCs 1–3 in the RGB space, exemplary measured for 50,000 points within the crater Cr3. (F) The profile A-D demonstrates the good separability of hydrothermally altered surfaces in PC2.*

Therewith we achieve a precise and clean representation of the recent appearance and extent of the alteration zone and sulfur deposits, based on the analysis of millions of pixels, preserving heterogeneities within the alteration zone, as demonstrated by the colorization in Fig. 3.6D. However, the central part of the fumarole field (Fig. 3.6D) is not reproduced in the extracted data set. This central part was affected by the condensed gas plume but has also a different spectral appearance compared to the grayish material characterizing hydrothermal alteration, and the average reddish-brown volcanic products dominating the La Fossa cone. Therefore, it may be considered another distinct unit, also with respect to the rather cold surface temperatures of this area located in the center of the fumarole field.

3.4.3 Zonation of the hydrothermal alteration zone

The color coding of the extracted PC raster (Fig. 3.6D) already indicates a particular zonation within the fumarole field. A close view of the main fumarole field provided in Fig. 3.7A highlights the yellowish colorized inner part associated with the fumarole vents, surrounded by pale and greyish outer parts, clearly different from the dominant average reddish brownish surface.

To investigate the spectral and spatial heterogeneities within the fumarole field more closely, we applied an image classification to the extracted alteration RGB data and eventually defined five classes (labeled A-E in Fig. 3.7B). The significance of each of the classes is demonstrated in the boxplots (Fig. 3.7C), representing the distribution of values in the single RGB bands for the respective classes A–E. The color values of the defined classes are overlapping in the single RGB channels, but in combination are distinguishable. The defined classes in some cases also differ concerning their apparent temperatures. A prominent example of such a zone is the inner core of the lower fumarole field (region 0 and 13 in Fig. 3.7A/B), characterized by a brighter light gray colorization and higher temperature of average 30 °C compared to the 22 °C of the zone adjoining west. The optical data, infrared data, PCA, and classification results allow us to define 13 subregions (Fig. 3.7B). Each of these subregions may represent a characteristic alteration and deposition zone. We evaluated the spectral characteristics of each subregion based on the analysis of the respective occurrences of classes A - E (density plots of the defined classes are Appendix A3.4).

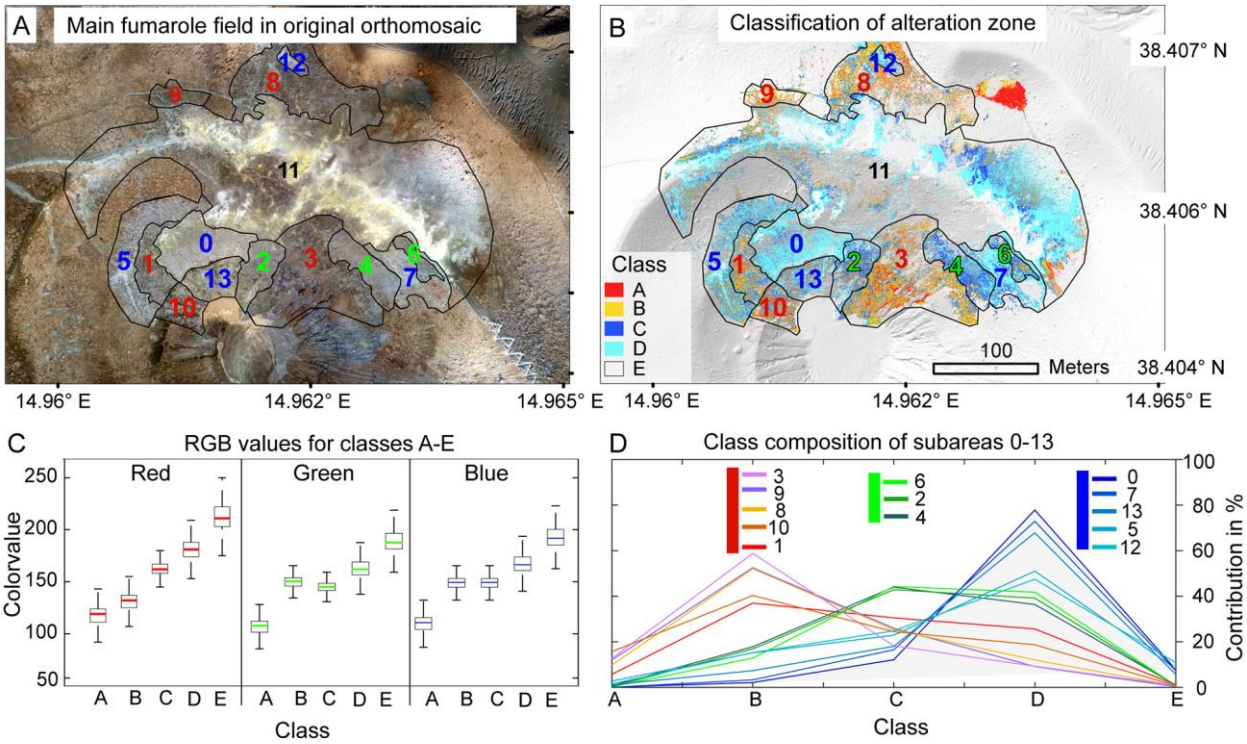

Fig. 3.7 (A) Classification of hydrothermally altered areas as revealed by heterogeneities in colorization. The black outlines depict the boundaries of defined subareas in the alteration zone numbered 0 to 13. ID numbers of the respective subregions are color-coded with red, blue, and green for spectrally similar regions. (B) Thirteen subareas superimposed on our classification of alteration zones (color classes A-E). Visible is the dominance of single classes and therewith the segmented pattern of alteration. (C) Test of distinctiveness for the defined classes A-E, clearly showing the spectral significant differences between the defined classes. (D) Composition (in % of total area extent on Y-axis) of classes A-E (X-axis) found within every defined subregion 0–13 (graphs). The thirteen subregions cluster in three groups of areas with similar class compositions (indicated by red, green, and blue bars) and therewith similar spectral characteristics. Region 11 is not considered due to the strong influence of bright steam plumes.

We observed that the subregions (Fig. 3.7D, one graph for each subregion) tend to form 3 groups of regions with a similar composition of classes. Spatially detached subregions show similar class compositions while neighboring subregions often are significantly different. This is evidencing that the alteration zone surrounding the fumaroles can not be considered a homogeneous unit, but is rather divided into zones with certain spectral characteristics, that may represent the surface expression of different degrees of hydrothermal activity, mineralization, and alteration. The central part (area 11 in Fig. 3.7A/B) of the fumarole field is not considered in this study. For this central part, we found a strong influence of the dispersing gas plume interfering with the spectral background signals of the underlying surface.

3.4.4 Distribution of sulfuric deposits

Sulfuric deposits at the surface are one of the most common and prominent features of extensive degassing and their occurrence is a good indicator for the presence of ongoing or extinct hydrothermal degassing activity, involving sulfurous gas species (SO_2 and/or H_2S). Native sulfur precipitates rapidly from the cooling fumarole gases, as soon as certain pressure and temperature conditions are met (Mayer et al., 2016 and references therein). From our UAS bird's-eye view, these yellowish-colored deposits are surrounding vent locations and allow us to indirectly infer locations and scales of such sulfuric deposition areas based on their appearance in the PCA. We extracted pixels representing sulfuric deposits, from the original RGB data, utilizing PC3 (Fig. 3.6C), and analyzed them considering their orientation and density distribution (Fig. 3.8A). We applied a second PCA iteration to the extracted sulfur pixel data (RGB) and evaluated their spectral characteristics (note that the Eigenvectors are rotated in the second PCA with respect to the first iteration).

In total, the area of extracted pixels, representing sulfuric deposits, covers 5775 m^2. The deposits appear to be clustered, often resembling directed and elongated shapes. The most dominant regions are three linear NW-SE trending segments on the upper crater rim (a,b, and d in Fig. 3.8A), whereby the western segment (a) is obliquely traversing the crater rim, while the eastern segments (b,d) are oriented following along the crater rim. Two clusters (c,h respectively FA and F57) on the lower crater rim are forming a bent segment of 150 m length resembling the lower crater rim (c and h in Fig. 3.8A). A sudden change in azimuths by 90° of sulfur-pixel clusters for both the lower and upper fumarole field (e, f, and g in Fig. 3.8A respectively F1, GBC, F5, F14) is observed in the center of the fumarole field, where the lower and upper fumaroles merge. While the upper fumaroles are rather oriented in an NW-SE direction (120° for a and 124° for b), the central part is oriented almost perpendicular, striking NE-SW (42° for g and 52° and 55° for e and f). This azimuthal change in the center of the fumarole field is accompanied by the highest sulfur-pixel density (f and d in Fig. 3.8A) and a systematic shift in the sulfur-pixel colors, demonstrated by the variation of PC2 (second iteration applied to extracted sulfur data) in Fig. 3.8B. While the sulfuric deposits generally appear in relatively bright colors (whitish to bright yellow), which is true for the majority of the deposits of the eastern lower and upper crater rim as well as for the western rim (a,b,c,h in Fig. 3.8), in the center of the fumarole field PC2 values are showing rather low values. Low PC2 values of this second PCA iteration are pointing away from the RGB main axis (decreasing blue values, increasing red and green values) towards less bright and more distinct colors, and

also with a shift towards a higher red component, especially in the locations of cluster f and d (Fig. 3.8A).

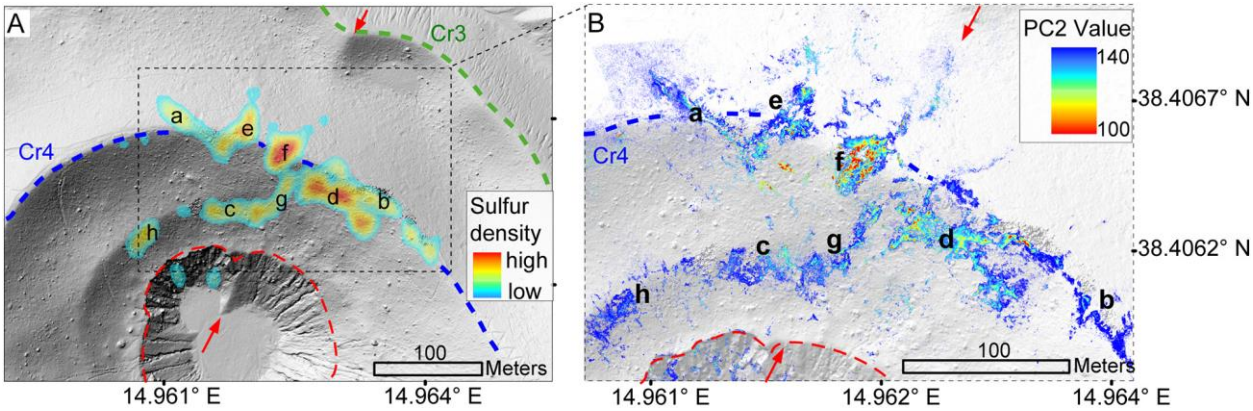

Fig. 3.8 Overview of sulfur deposit data extracted from PC3. (A) Pixel density of sulfur-pixels, extracted from PC3. Multiple elongated directed clusters can be observed with the main trend (a,b,d) NW-SE. In the center of the fumarole field, the highest density is observed, and an azimuthal change by 90 degrees towards a NE-SW direction (e,f,g), on the lower and upper fumarole field. (B) Variations in spectral characteristics of sulfur deposits in PC2 with especially low PC2 values in the center of the fumarole field associated with fumarole F5/F5AT. The red arrows mark a topographic particularity that is a possible cause for the observed variabilities in sulfur density and sulfur color, an intersection of two craters visible by the morphological kink in the inner crater, as well as visible by kinks in the outer craters Cr3 and Cr1.

3.4.5 Structural analysis based on IR data

Location, distribution, intensity, and geometric shape of thermal anomalies can imply details about permeability, and dimensions of permeable materials, but also indicate structural components. Previous studies suggest that fumarole sites arrange along inferred faults (Harris et al., 2012), topographic highs, and lithological contrasts (Schopa et al., 2011), and their pathways are diverged in the presence of impermeable sediments of the crater floor (Pantaleo and Walter, 2014). From our UAS dataset (230 m agl overflight with an apparent temperature range of 17–120 °C) we can infer at least 3 types of thermal anomalies, similar to Harris et al. (2012): low-, medium-, and high-temperature sites.

Low-temperature sites were defined as sites that have an elevated temperature compared to the background soil surface temperature of 17 °C, but where temperatures are only slightly increased (2–7 °C above the background). A broad low-temperature area is surrounding the main fumarole field (Fig. 3.9). Already the 19 °C isotherm encloses the main fumarole field at a broader distance. It includes diffuse degassing clusters (C1/2) and indicates a thermal

connection, linking the main fumarole field with the fumaroles on the northern outer crater slope. This implies that these spatially distinct degassing regions might be considered as a unit. Within this area, only minor degassing can be observed at the surface and hydrothermal deposits are only sparsely visible.

With 116,740 m^2, this area of slightly increased soil temperatures is covering almost one-third of the central La Fossa cone and indicates a large complex influenced by ascending hot gases, next to the obvious fumarole activity. Higher isotherms are enclosing the main fumarole field more closely. The 21 °C isotherms resemble the outline of the mentioned alteration zone. Therewith they mark a boundary where we can observe color changes in the RGB from reddish-brown towards a gray colorization.

Moderate temperature sites were defined based on the 25 °C isotherms. The 25 °C isotherms are outlining all actively degassing sites and vent accumulations, and are a good representation of the shape and extent of the degassing structures at the surface. The 25 °C isotherms were chosen as they resemble the high activity zone on the lower crater rim, which in the optical data is characterized by a significantly brighter colorization. A shift towards higher isotherms (30 °C or more) reveals polygon-shaped degassing patterns, especially in the high-activity zone of the lower fumarole field, and eventually allows the identification of single hot spots or clusters of vents. In the center of the fumarole field, we observed two subregions with relatively low temperatures (a1, a2 in Fig. 3.9), but showing clear signs of hydrothermal alteration and deposition of a former degassing activity. We interpret those as a sealed surface as supported by sulfur deposition along polygon-shaped cracks (Fig. 3.9B).

High-temperature thermal anomalies indicate locations of fumarole vents and are associated with sulfuric deposits, often resembling lineament shapes or in places polygonal-shaped arrangements. A cluster analysis provides information about their distribution and orientation. The rose plots in Fig. 3.9C show the orientation of observed thermal anomalies, clustered in steps from >25 °C, >30 °C, and >60 °C, weighted by the form factor of the Standard Deviational Ellipse. While for low temperatures we observe a random distribution, pixel clusters representing higher temperatures show a domination of preferred orientations. Towards higher temperatures (>60 °C), the 130° trend is dominating, supplemented by an almost perpendicular trend (20–30°), mainly corresponding to thermal lineaments in the center of the MF, and a roughly east-west oriented trend. Two elongated thermal anomalies resembling the 130° trend are showing no signs of precipitated sulfur (Fig. 3.9A) and therewith venting activity. Cluster algorithms allow us to get a first overview of the distribution and

orientation of clusters. An additional structural mapping based on a combination of thermal lineaments and sulfur deposits revealed similar but even more detailed results. We observed the following dominant orientations: i) lineaments oriented in a crater rim parallel manner, ii) lineaments oriented in a radial pattern, iii) lineaments oriented in an NW-SE orientation (dominating trend due to the size of lineaments), similar to the local tectonic trend (Mazzuoli et al., 1995; Ventura et al., 1999), and iv) lineaments oriented NE-SW. The NE-SW orientation is observed especially in the center of the fumarole field, where we also observe the highest density and more distinct colorization of sulfur pixels, coincident with the axis linking the border of the inner nested crater (crater floor) with an embayment in the outer crater rim.

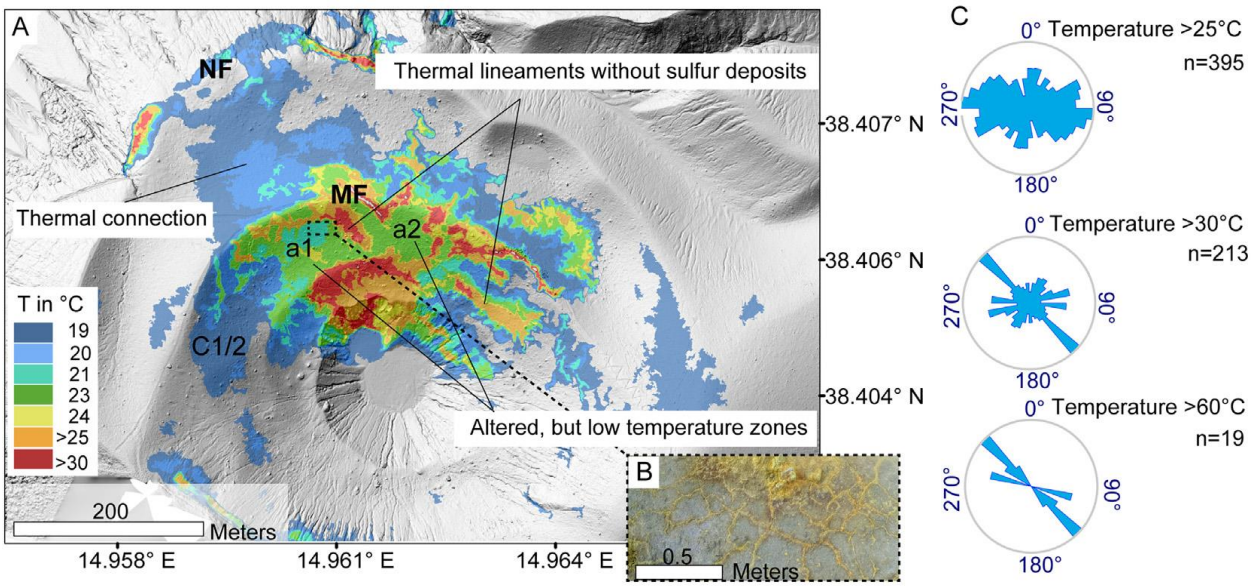

Fig. 3.9 (A) Apparent temperature field derived from low-temperature isotherms, indicating a continuous influence of diffuse degassing over broad regions and associated heating of soil, and the existence of a thermal connection between the main fumarole field (MF) and fumaroles on the northern outer flank (NF). Regions of higher thermal activity are depicted by orange-reddish colors. On the inner crater slope, within the center of the fumarole field, areas of low temperatures can be observed (a1, a2). These are likely due to the sealing of the surface by mineral precipitation (B). (C) Rose plots depict the spatial orientation of elongated temperature clusters. For higher temperatures, a clear dominance of an NW-SE trend can be observed. Comparing this figure with Fig. 3.8 moreover reveals two thermal lineaments at the inner crater wall that lack deposition of native sulfur.

3.5 Discussion

Volcanic fumaroles are dynamic sites expelling hazardous gases. However, their exact location and extent are often difficult to identify due to coating, alteration, and sealing processes, as

well as vent migration (Madonia et al., 2016). Details on the dimensions and locations of the fumaroles consequently often remain limited. By using UAS we were able to record a high-resolution optical and thermal infrared dataset. We applied the Structure from Motion workflow to identify the general appearance and distribution of fumarole sites. Then we perform a Principal Component Analysis to identify and separate surface expressions of hydrothermal activity, such as the small-scaled exhalation sites and widespread aureoles. Comparing the fumarole hot spots as well as the aureoles further allows an interpretation in a structural sense as discussed further below.

3.5.1 Limitations and potential of the methods

New small UAS and lightweight sensor systems together with SfM processing routines provide the possibility to acquire high-resolution data at a low cost and, therefore, allow us to approach the fumarole sites at unprecedented resolution and detail. However, some limitations are coming with the UAS technique, the application, and the handling of large datasets.

The used UAS are off-the-shelf products. Their advantage is that they are small and lightweight, but strong enough to carry additional weight. The average flight time of ~30 min per battery lowers to 20 min if the infrared camera was carried, and thus limits the operative range and mapping campaigns. Depending on the desired resolution, the flight altitude needs to be adapted. We realized the complete coverage of the La Fossa cone with 5 batteries. The chosen drone and camera combination performs excellent for the mapping of small craters like the 1–2 km^2 of La Fossa on Vulcano Island.

The accuracy of the absolute positioning of the drone's internal GPS is in the typical range for single-frequency GPS, with an absolute positioning error that can be easily on the order of 5 m or more (Kalacska et al., 2020), while the vertical offset can easily be on the order of tens of meters. The processed models will have a spatial offset which should be corrected by ground control points or geocoded reference data. The relative accuracy within the processed models is strongly dependent on the type of UAV used and the onboard camera system, but also correct acquisition geometries and general quality of the acquired data. The used Phantom 4 Pro copter performs well and results have an average within-model error of ~0.2 m (Kalacska et al., 2020), which is above average for this mid-price segment. To achieve geodetic precision, an RTK system could reduce the within-model error to a few centimeters only (Kalacska et al., 2020).

The SfM processing of hundreds of our aerial images leads to large datasets (over 250 million

data points for the optical dataset and 6 million points for the infrared dataset) so that the analysis became a task requiring sufficiently large computation power. From the combination of optical and thermal infrared data, we could identify and distinguish fumaroles and alteration zones from original deposits within the La Fossa cone. However, in the optical data in some cases, it was not possible to separate pixels showing whitish gas plumes from pixels showing very bright-to-yellowish sulfur deposits. This needs to be taken into account and handled with care especially considering quantitative, or temporal change detection analysis. Similarly, the infrared signal was highly affected by steam and water vapor from fumarole plumes, attenuating the signal transmission and lowering the measured apparent temperatures on the ground. We further examined this by comparing in situ measurements to UAS measurements. At the fumarole F5 / F5AT we measured 309 °C on a local spot at the ground, which then appears with only 65 °C in the 230 m (agl) UAS overflight data, which means a loss of 80% in amplitude. Therefore the apparent temperature measured by infrared must not be confused with the real temperature. The apparent temperature strongly depends on environmental parameters but also resolution (Spampinato et al., 2011), which must be considered when observing small and steam-exhaling fumaroles. Considering steam as the main limitation, we can provide an optical and thermal infrared data set preserving the state and extent of the fumarole fields and altered areas in the La Fossa cone from November 2018, which can be used as a reference for short and long term monitoring of the evolution of the fumarole fields and related activity. Although some fumaroles may be on a scale well below the resolution of our cameras, results are providing a level of detail that could not be achieved by satellite data. While high-resolution optical satellites barely exceed 1 m resolution (Spot, Ikonos, Pleiades) and may allow depicting and monitoring the general appearance of the fumarole fields and their aureoles, the resolution of thermal infrared satellites is 1–2 orders lower and allow only general heat fluctuations to be observed (Mannini et al., 2019).

The RGB information of the ground as seen from a bird's-eye view is dependent on hydro-meteorological conditions. Therefore also the interpretation and image analysis is likely dependent on cloud cover, sun position, humidity, reflections, and other optical effects. A time-dependent analysis would need to take these optical changes into account. We applied PCA to different data sets, acquired in different UAS surveys. In a qualitative comparison, we found that the observed patterns are similar in all data sets (Appendix A3.5). This makes us confident that also repeated surveys, in similar data acquisition conditions and under consideration of the Eigenvectors and Eigenvalues of the PC, might allow probing changes in the fumaroles and

their aureoles.

The centimeter-scale combination of our UAS-based optical data, PCA, and IR data is of high value, as it eases the recognition and quantification of characteristic patterns, like aureole formation around high-temperature fumaroles. Hereby, the application of a PCA is beneficial, which due to the Variance / Covariance representation, provides a far more distinct data representation, valuable for the detection of optical anomalies in volcanic regions.

Associated is a better separability (Fig. 3.10) that can be used to extract the data of interest from the original raster data, which has two advantages. First, it reduces the spectral variance in the data allowing us to perform even more sensitive analysis. Second, it enables us to reduce the number of data points, which considering the size of such high-resolution datasets, can be essential for the analysis of computing capacities.

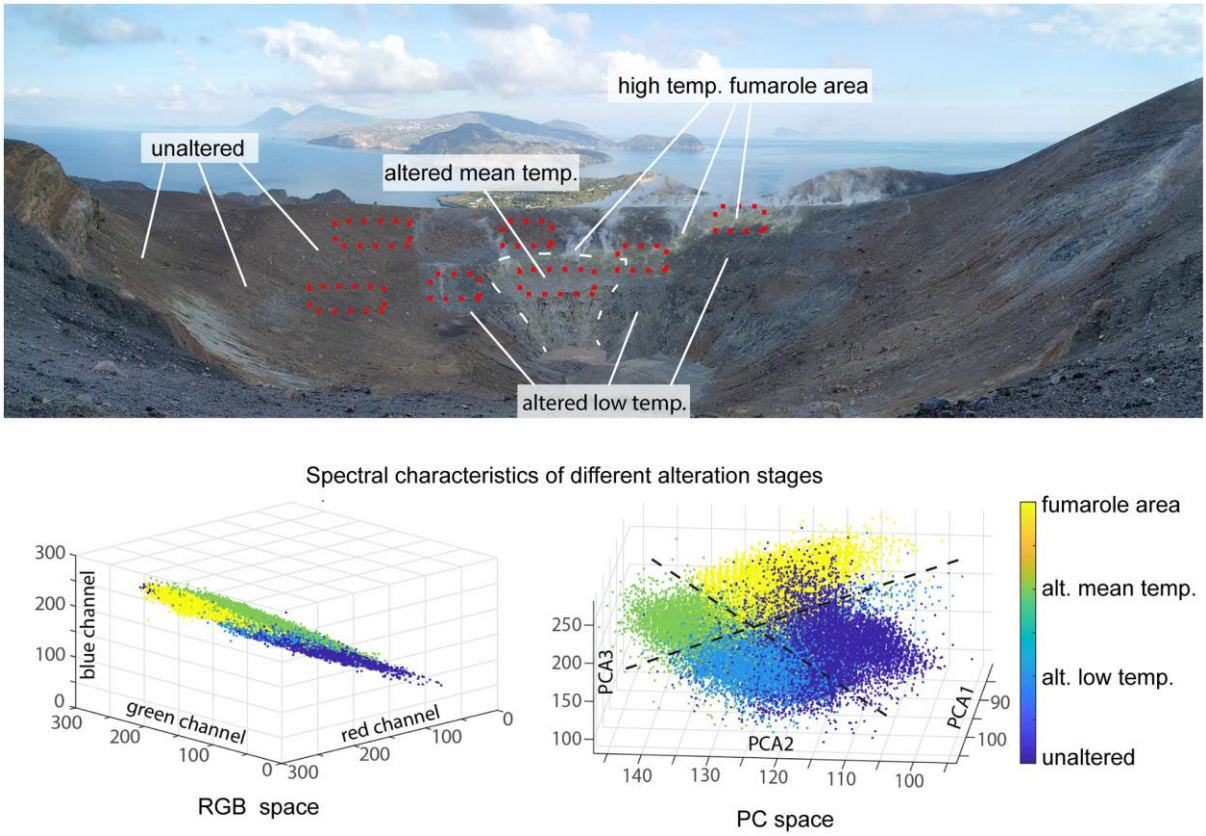

Fig. 3.10 (A) Panoramic view of the northern crater rim showing color differences of areas affected by hydrothermal activity. (B) RGB and PCA space representations of spectral contents of different alteration surfaces that were identified in the RGB Orthomosaic. Note the stretching of spectral information obtained through Principal Component Analysis, causing the color values of respective alteration classes to span a much wider range in the PCA space and thus to be more distinct than in RGB space.

The extracted data volume is still in the order of millions of data points. Here especially, the combination of cluster algorithms (Hahsler et al., 2019) and standard deviational ellipse (Yuill, 1971) provides an efficient toolset for the structural analysis of UAS-derived data. Applied systematically, the here presented tools eventually have the potential to contribute to the monitoring of the spatiotemporal evolution of hydrothermal systems on volcanoes. At La Fossa, earlier works detecting temporal and spatial changes relied on in situ fumarole field observations. Bukumirovic et al. (1997) for example showed extensive growth of the fumarole field during 12 years. Especially on similar occasions, a raster-based approach like the presented work could provide very detailed and especially complete insights into such spatiotemporal events. Applied as the first step in pre-site investigations, this methodology has a high potential to improve the planning and operation of geochemical investigations on volcanoes or could be especially beneficial for the design of measurement networks.

3.5.2 Sub-area segmentation and structural controls

Fumaroles at La Fossa appear to be located at several distinct sites, showing characteristic temperatures, gas compositions, and also gas flux. Time series analysis published earlier suggests a strong temporal variability of selected fumarole vents (Diliberto, 2017), but also spatial changes such as fumarole field growth or lateral fumarole migration (Bukumirovic et al., 1997). Earlier studies concentrated on the sites of high-temperature fumaroles, associated temperatures, and gas compositions as well as temporal changes (Tedesco et al., 1991; Bolognesi, 1999; Capasso et al., 1999; Aiuppa et al., 2005; Harris et al., 2009; Harris et al., 2012; Diliberto, 2013; Madonia et al., 2013; Diliberto, 2017). However, processes altering the surrounding areas of fumaroles are barely investigated. Rock coatings might form due to the interaction of the ground with the acid plume, thought to be mainly dependent on source distance and wind drift. The alteration may be driven from depths, by the ascent of acid fluids along permeable paths, or by surface effects like the combination of acid gases with meteoric waters, or combinations thereof. While rock coatings are found throughout the La Fossa cone, hydrothermal alteration and sulfuric deposition on La Fossa have been coarsely mapped and appear to be limited to isolated regions. Especially 3 types of alteration, silicic, advanced argillic, and intermediate argillic alteration were identified (Azzarini et al., 2001; Fulignati et al., 2002). The revealed optical anomalies in this study resemble the outlines of the silicic alteration facies within the La Fossa cone (Azzarini et al., 2001; Fulignati et al., 2002), but

indicate a possibly much higher level of complexity. Within the alteration zone, we observe a heterogeneity, expressed by distinct spectral characteristics and associated soil temperature regimes, which allowed us to distinguish at least 13 subregions. Some of these subregions are similar to each other in their appearance but spatially divided, while neighboring subregions have different characteristics. The observed segmentation (indicated in Fig. 3.7) in the alteration zone can have different reasons, such as a variability in the underground material and permeability, variability of gas flux and composition in the diffuse degassing regime itself, or structural controls.

Spatial variability of gas compositions (H_2O, CO_2, SO_2, H_2S, HCl, HF, HBr) within the fumarole field is proposed earlier (Aiuppa et al., 2005) with higher contents of magmatic gases in the lower fumaroles towards higher contents of hydrothermal components on the upper rim and outer fumaroles. Spatially dense investigations of soil degassing parameters in accordance with the identified segmentation will contribute to a better understanding of links between alteration processes and gas geochemistry in the future. A structural effect on the location of fumaroles was proposed earlier (Barde-Cabusson et al., 2009; Harris et al., 2009). According to these studies, major fumarole vents are aligned along the main tectonic trend striking approximately NW-SE and also curving along the crater walls. The NW-SE alignment could not be confirmed by other studies exploiting thermal data (Schopa et al., 2011). Nevertheless, the most dominant fumarole sites are known to align along open cracks and fractures (Barde-Cabusson et al., 2009; Harris et al., 2009; Schopa et al., 2011). The structural analysis of lineaments of our UAS data and the PCA analysis of hydrothermal deposits revealed systematic changes. In general, we identified 4 dominant azimuths of lineaments throughout the whole study area, which are: radial to the crater, crater rim parallel, a NW-SE component that is by far dominating, and a NE SW component.

Especially in the center of the fumarole field, we observe a systematic change in azimuths of thermal lineaments and sulfur clusters of ~90° clockwise from the dominating NW-SE to NE-SW (Fig. 3.11). This is accompanied by the largest extent of the alteration zone with respect to the crater rims, a higher density of sulfur deposits (pixel density), and a more distinct colorization of hydrothermal deposits. The last two appear systematically with decreasing sulfur (pixel) density (Fig. 3.11C) and lower PC2 values respectively less distinct colors (Fig. 3.11B) with distance from the center (red dashed line/arrows in Fig. 3.11).

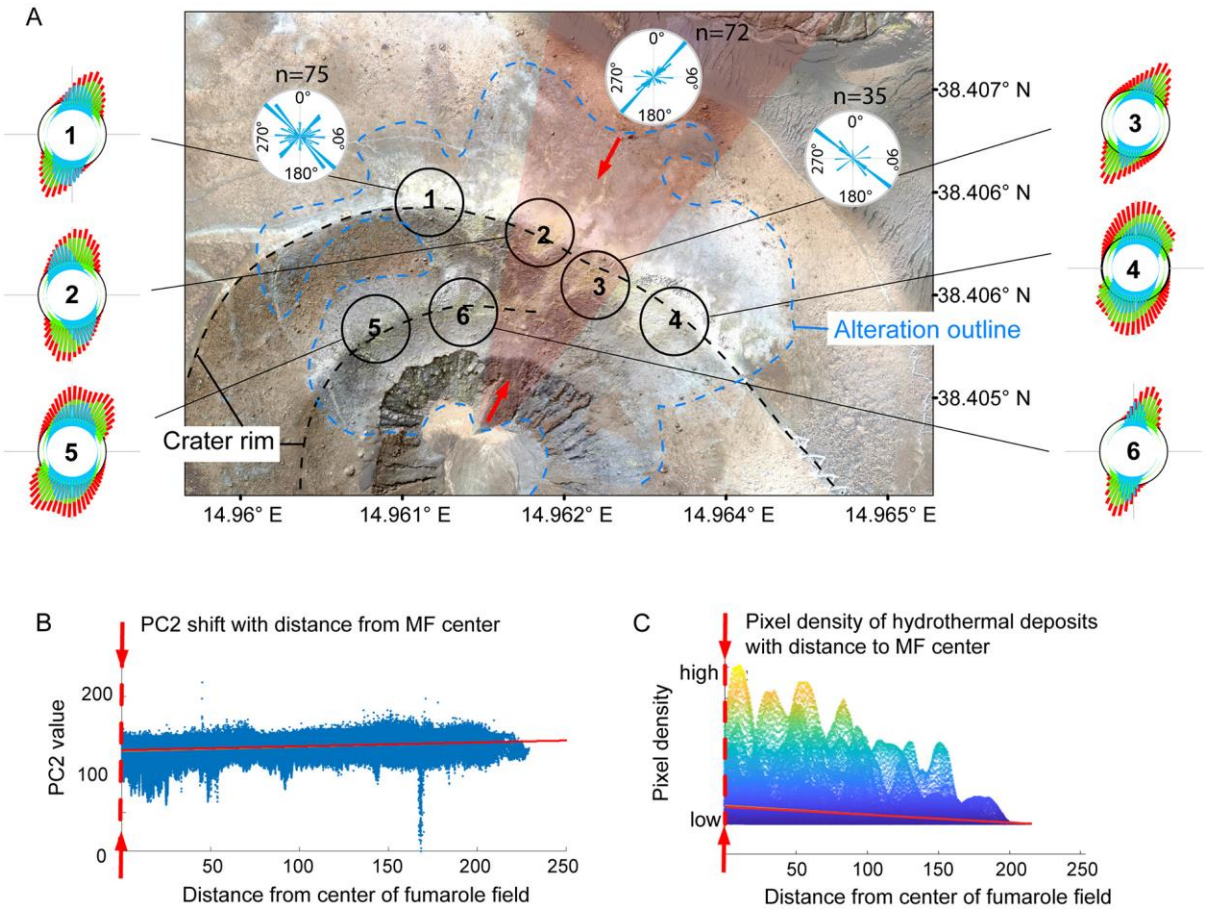

Fig. 3.11 Color variations of hydrothermal deposits and pixel density variations with distance from the center of the fumarole field (N35° alignment indicated by red arrows). (A) Image of the central crater, with the red arrows depicting the intersection of the northern and southern craters. The zone of intense hydrothermal alteration is outlined in light blue. Numbered circles are representing different positions in the fumarole field for which color values of sulfur deposits have been investigated. The color distribution of these single regions in the single RGB channels is depicted in the circular plots, showing the distribution of pixel values for red, green, and blue projected on a circular histogram. Especially for areas 2 and 3, we observe a higher deviation in the blue channel towards lower values, representing the shift towards darker, more distinct colors. The rose plots depict the azimuthal change of thermal lineaments from a dominating NW-SE direction for the western and eastern areas of the fumarole field and a by ~90° rotated NE-SW azimuth for the central part of the fumarole field, shaded in red. (B) The general increase of the PC2 with distance from the crater intersection (red dashed line), which is equivalent to more bright less distinct colorization. (C) The density of pixels representing deposited sulfur is decreasing with distance from the center of the fumarole field.

The color change is especially visible in the PC2, with a relatively high deviation of the blue channel compared to red and green (circular plots 2 and 3 in Fig. 3.11A). According to the distribution of colors in the RGB space, a lower blue value equals a shift away from the central RGB axis (gray) towards stronger, more distinct colors. These systematic changes are coincident with the particularities of the crater topography.

The crater floor of the Cr4 crater appears as a nested crater with a smaller northwestern and a bigger southeastern crater. In azimuth of the intersection of both, a bend in the crater rims Cr1 and Cr3 can be observed (red dashed line Fig. 3.11). In this view, the finding of the separation and abrupt ending of the distinguished subregions can be interpreted as boundaries between different historically grown fluid paths, that preferentially formed along the borders of (now hidden) geologic units. The different units linked to different nested crater structures may create permeability affecting the ascent of gases. This would be supported by the fact that the fumaroles with the highest temperatures (F5/ F5AT) are located in azimuth, similar to the only fumaroles that sit in between and thus connect lower and upper fumarole fields.

Degassing of the lower fumarole field occurs exclusively west of the crater intersection (Fig. 3.12) and is characterized by a relatively higher magmatic composition of emitted gases compared to the upper fumarole field (Aiuppa et al., 2005; Tamburello et al., 2011). The central part of the lower fumarole field is enclosing an area of 5600 m^2, having an average soil temperature of 30.2 °C (white dashed line in Fig. 3.12). These temperature measures are elevated if compared to the 22.3 °C of the surrounding. Associated is a brighter light-grey colorization of this region. Towards the east, it is sharply confined by the crater intersection.

This indicates an ascent of gases west of this structural boundary, feeding the lower fumarole field. All vents of the lower fumarole field are located on the inner side of the inner crater rim (black dashed line in Fig. 3.12), which therefore appears to act as a structural boundary as well, obstructing vents to form above the inner rim.

The few fumaroles located between upper and lower fumarole fields are located on, or nearby this inner crater rim, demonstrating a strong control of both of the mentioned structures. The crater at La Fossa is assumed to be made up of inward-dipping inner deposits (often reworked material) and outward-dipping outer deposits, which are possibly delimited by a crater wall unconformity (Wohletz and Heiken, 1992). This may explain this specific expression of degassing activity at La Fossa (Fig. 3.12). While vents of the lower fumarole field are located on the inner steep side of the inner crater rim only, fumarole vents of the upper fumarole field are located almost equally distributed in and outside the crater rim. A generally strong spatial bond of fumarole vent locations to the crater rims and intersections is observed, with the majority of vents being located within a 50 m distance to the crater rim and the largest extent away from the crater at the mentioned controlling structure in the center of the fumarole field.

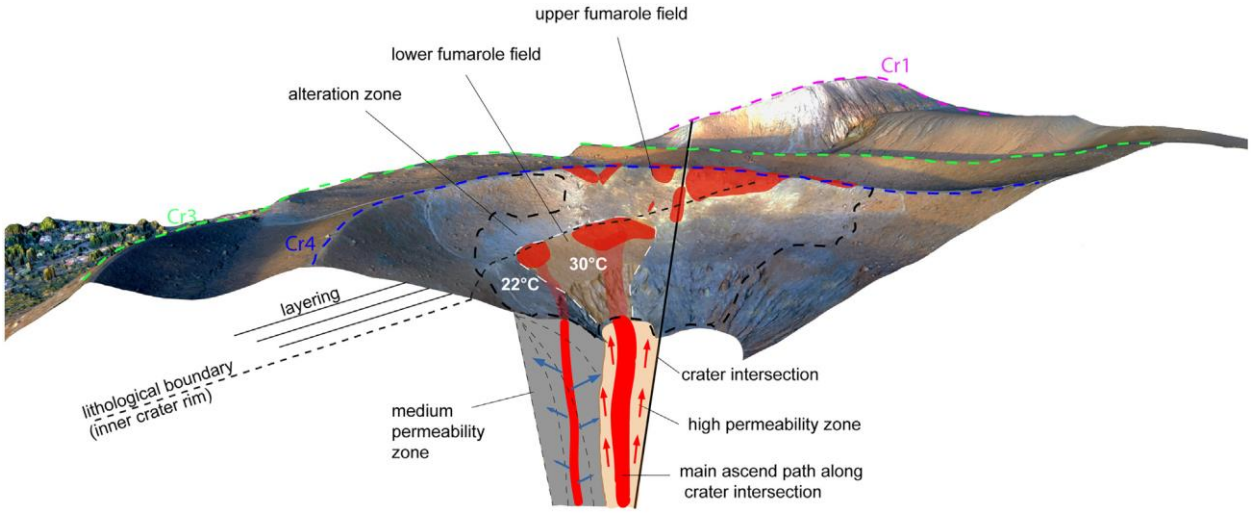

Fig. 3.12 Schematic sketch of the feeding of the La Fossa fumarole field. We suggest a preferred gas ascend along the western side of the crater intersection, appearing as a structural boundary, as all hydrothermal activity on the lower fumarole field occurs west. The broader area of increased soil temperature (orange indication within white dashed line on surface) might be caused by a higher permeability (orange indication at depth) and/or the more direct ascent of gases. It is bound to the west by a grayish hydrothermally altered zone (gray indication). The extent of this alteration zone at depth can not be estimated. This can be a deep-rooted or a surface effect, therewith possible boundaries are indicated by the stippled lines. The red and blue arrows indicate the diffuse gas flux away from the main ascent paths. The inner crater rim is interpreted to be a lithological boundary, as all of the fumaroles of the lower fumarole field are occurring on the inner steep portion of this crater rim, clogged by an impermeable zone on top. Additionally, fumaroles located in between upper and lower fumarole fields are located on this structure. For the lower fumaroles except for the very western ones, a higher magmatic composition is described (Aiuppa et al., 2005), while the upper fumaroles are characterized by a higher hydrothermal admixture. In general, the distribution of fumaroles seems to be highly controlled by the combination of these structural and lithological controls.

3.6 Conclusions

This study aims at the exploration of the hydrothermal surface manifestations of the actively degassing fumarole field at the La Fossa cone, Vulcano Island. We used unmanned aircraft systems (UAS) equipped with optical and infrared cameras to generate high-resolution optical and infrared mosaic data sets. By application of a principal component analysis (PCA), we generate a variance representation of the original RGB data, highlighting a systematically changing ground colorization associated with fumarole activities. The PCA turned out to be especially beneficial for the identification of areas subject to hydrothermal alteration and (sulfuric) mineral deposition. In the present dataset, PC2 was mainly beneficial for mapping

hydrothermal alteration zones, whilst PC3 was found efficient for identifying yellowish-colored hydrothermal deposits. By combining optical and thermal infrared data, we could further verify that optical anomalies identified in PCA correlate with thermal anomalies. We identified a large zone of increased temperature and different colorization. Covering an area of 60,000 m^2, it is ten times larger than the active fumarole region. Spectral and/or thermal heterogeneities within this zone indicate a segmentation of the alteration into at least 13 segments. This segmentation is interpreted to be related to permeability-driven heterogeneities of diffuse degassing surrounding the main fumarole vents. An analysis of the orientation of thermal anomalies and sulfur deposits revealed the following systematic changes in the center of the fumarole field: (1) We find a sudden shift in azimuths of thermal lineaments and sulfur deposits by 90° towards a NE direction, and (2) a systematic color shift and the highest sulfur-pixel density, coinciding with the highest fumarole temperatures. We interpret this as an effect of a structural or lithological boundary governing the fluid pathways, possibly associated with a crater intersection. This study shows that UAS-derived optical data can have a great benefit for the structural investigation of volcanic hydrothermal systems at the surface. Based on the analysis of millions of pixels and a feature detection threshold of 25 cm^2, this study provides an accurate and complete image of the recent state and extent of the La Fossa fumarole field. The presented method has the potential to be implemented in the monitoring of fumarole fields elsewhere, especially considering spatiotemporal processes like activity migration, surface sealing, or fumarole field growth during unrest periods. The high complexity and presented details address a number of new aspects that should be considered and open new scientific questions regarding the relation between observed alteration heterogeneities and spatial variations of gas flux and gas composition in the diffuse degassing system.

3.7 Author contribution

D.M. acquired, processed, and analyzed the data and led the manuscript writing. S. B. acquired data in the field, supported the writing, and reviewed the manuscript. E. Z. acquired overflight data in the field and reviewed the manuscript. E. D. P. acquired data in the field and reviewed the manuscript. T. R.W. supervised the project and the writing of the manuscript. All authors have read and agreed to the published version of the manuscript.

3.8 Acknowledgments

Financial support by the GFZ Potsdam through Expedition Grant is greatly appreciated. We thank Stefan Mikulla and Sylvio Mielitz for assisting with the UAS and thermal camera mounting and preparation. This is a contribution to VOLCAPSE, a research project funded by the European Research Council under the European Union's H2020 Programme/ ERC consolidator grant n. [ERC-CoG 646858]. All data presented is available on request from the corresponding author of this study.

Chapter 4

Anatomy of a fumarole field; drone remote sensing and petrological approaches reveal the degassing and alteration structure at La Fossa cone, Vulcano Island, Italy

Daniel Müller (1), Thomas R. Walter (1), Valentin R. Troll (2,3), Jessica Stammeier (1), Andreas Karlsson (4), Erica de Paolo (5), Antonino Fabio Pisciotta (6), Martin Zimmer (1), Benjamin De Jarnatt (1)

1: GFZ German Research Centre for Geosciences, Telegrafenberg, 14473 Potsdam, Germany
2: Dept. of Earth Sciences, Natural Resources and Sustainable Development, Uppsala University, Sweden
3 Istituto Nazionale di Geofisica e Vulcanologia (INGV), Rome, Italy
4: Department of Geosciences, Swedish Museum of Natural History, Box 50007, SE-104 05 Stockholm, Sweden
5: University of Milano-Bicocca, Department of Earth and Environmental Sciences, Piazza della Sciencza 4 – 20126 Milano, Italy
6: Istituto Nazionale di Geofisica e Vulcanologia (INGV), Palermo, Italy

This article was published in:

Müller, D., Walter, T. R., Troll, V. R., Stammeier, J., Karlsson, A., De Paolo, E., ... & De Jarnatt, B. (2023). Anatomy of a fumarole field; drone remote sensing and petrological approaches reveal the degassing and alteration structure at La Fossa cone, Vulcano Island, Italy. *EGUsphere*, *2023*, 1-45.

Abstract

Hydrothermal alteration processes can affect the physical and chemical properties of volcanic rocks and develop via complex degassing and fluid flow systems and regimes. Although alteration can have far-reaching consequences for rock stability and permeability, little is known about the detailed structures, extent, and dynamic changes that take place in hydrothermal venting systems. By combining drone-based remote sensing with mineralogical and chemical analyses of rock and gas samples, we analyzed the structure and internal anatomy of a dynamic evolving volcanic degassing and alteration system at the La Fossa cone, Vulcano Island (Italy). From drone image analysis, we revealed a ~70,000 m² sized area subject to

hydrothermal activity, for which we could determine distinct alteration gradients. By mineralogical and geochemical sampling of the zones of those alteration gradients, we study the relation between surface coloration and mineralogical and chemical composition. With increasing pixel brightness towards higher alteration gradients, we find a loss of initial mineral fraction and bulk chemical composition and a simultaneous gain in sulfur content. Using this approach, we defined and spatially constrained alteration units and compared them to the present-day thermally active surface and degassing pattern. The combined results permit us to present a detailed anatomy of the La Fossa fumarole field, highlighting 7 major units of alteration and present-day diffuse activity that, next to the high-temperature fumaroles, significantly contribute to the total activity.

4.1 Introduction

4.1.1 Volcanic degassing and hydrothermal alteration

Volcanic degassing at the Earth's surface is typically expressed in the form of localized fumarole fields and diffuse gas escape, yet the association of localized and diffuse degassing is not well constrained. A fumarole is a vent or opening in the Earth's surface that releases steam and gas, including sulfur dioxide, carbon dioxide, and hydrogen sulfide, into the atmosphere (e.g. Giggenbach, 1996; Giammanco et al., 1998; Halldorsson et al., 2013). Fumaroles are typically found near volcanic areas or geothermal regions where there is intense heat beneath the surface. Fumaroles are of interest to scientists studying volcanoes and geothermal systems, as they provide information on the composition of underlying magmatic systems, the degassing processes of such magmatic systems, and the dynamic changes in the degassing passways exploited by such systems (e.g. Chiodini et al., 1993; Aiuppa et al., 2005; Paonita et al., 2013). The gas emissions by fumaroles, moreover, provide information on the possible interaction between underground water and hot rocks or magma and thus the state of a hydrothermal system through time (e.g. Chiodini et al., 1993; Capasso et al., 2000; Nuccio et al., 2001; Troll et al., 2012; Paonita et al., 2013).

The degassing of hot and acid volcanic gases leads to versatile fluid-rock interactions at the surrounding volcanic rock, summarized as hydrothermal alteration (Pirajno, 2009; Chiodini et al., 2013; Fulignati, 2020). Alteration can affect the mineral assemblage by dissolution and remineralization up to complete destruction of the original mineral matrix and eventually influence essential rock parameters with potentially far-reaching consequences for the shallow

hydrothermal system and the stability of a volcanic building (Reid & Brien, 2001; Heap & Violay, 2021). Mechanical strength tests of hydrothermally altered rocks showed considerable mechanical weakening (e.g. Julia et al., 2014; Heap et al., 2019; Darmawan et al., 2022), which is usually accomplished by mineral dissolution and mineral re-precipitation that affect rock strength and permeability and can in cases even seal gas pathways. Hydrothermal alteration can thus lead to sealed rock masses and hence to pressure build-up in a shallow volcanic system and consequently influence volcanic activity (e.g. Heap et al., 2019). It is therefore important to better understand the degassing and alteration structures in active hydrothermal crater regions of hazardous volcanic systems.

In this study of the fumaroles of La Fossa Vulcano Island - Italy, we aim to detect and quantify alteration-related spatial and compositional parameters in order to provide improved insight into the dynamic changes of hydrothermal venting systems to help identify temporal and potentially critical developments and to better understand the associated features of diffuse and localized degassing.

4.1.2 Structure and extent of degassing sites

Recent advances in volcanic geothermal areas suggest that fumaroles are often only localized expressions of a much larger area of degassing (e.g Toutain et al., 2009; Liuzzo et al., 2015). Indeed, fumaroles and hydrothermal degassing zones are often accompanied by broader fields of activity, characterized by diffuse degassing processes, associated mineral changes, and intense surface recoloration (e.g. Donoghue et al., 2008; Berg et al., 2018; Darmawan et al., 2022) and fumaroles activity can vary in time (Troll et al., 2012; Fischer et al., 2015) and in size (Lynch et al., 2013; Gertisser et al., 2023). Previous works at Vulcano, for instance, have shown that fumaroles are surrounded by extensive areas of diffuse degassing (Carapezza et al., 2011; Chiodini et al., 2005; Manini et al., 2019). Our previous work showed that diffuse degassing leads to distinct zones classified by temperatures and visual expression (Müller et al., 2021). Those diffuse zones are also constrained based on CO_2 measurements but are also subject to the diffuse flow of acid gas driving díffuse alteration processes. However, these diffuse degassing and alteration processes are often difficult to recognize without specialized sampling strategies (Toutain et al., 2009), leading to a limited understanding of the anatomy and extent of degassing and alteration systems. Understanding the dynamic changes and

internal architecture of hydrothermal activity of fumarole fields and the true dimensions of their field of activity is of relevance for the study of volcanic hazards and resources.

4.1.3 Surface effects and remote sensing of alteration

Hydrothermal alteration can cause significant changes in the physical and chemical properties of volcanic rock, such as density, compressive strength, and permeability (e.g. Donoghue et al., 2008, 2010; Berg et al., 2018; Heap et al., 2019; Darmawan et al., 2022). The replacement of primary minerals by secondary minerals, element mobility of fluid-mobile components, enrichment of refractory elements, and physical and textural changes of rock properties are often accompanied by changes in the color or spectral reflectance characteristics and can be traced employing remote sensing techniques.

Several studies have investigated the relationship between coloration and hydrothermal alteration. The use of rock color or spectral reflectance particularities as an indicator of alteration has been explored since the 1970s and led to the development of a variety of remote sensing techniques using satellite imagery from ETRS multispectral imagery (Rowan et. al., 1976), Landsat Thematic mapper mission (Carranza et al., 2002), ETM+ (Mia et al., 2012) or ASTER data (Di Tommaso et al., 2007) or hyperspectral analysis (e.g. Van De Meer et al., 2012; Tayebi et al., 2015). These techniques can detect subtle changes in color that may not be visible to the naked eye, allowing for the identification of mineral deposits (Mielke et al., 2016), hydrothermal alteration, or volcano stability (Kereszturi et al., 2020).

However, for analyzing details of localized degassing and alteration systems, the resolution of satellite data often is a limiting factor. Some of the best available optical satellite data have a resolution of 0.5 m in the nadir acquisition position. The resolution of thermal satellite data is on the order of tens to hundreds of meters per pixel. That allows the general detection of degassing and alteration systems, but the imaging of details of such systems requires the use of very high-resolution data. Modern UAS (unmanned aerial systems) equipped with high-resolution sensors allow imaging of volcanic surfaces at cm scales and, therefore, permit the analysis of degassing and alteration systems in great detail. In combination with Structure from Motion (SfM) processing, they are efficient for first-site investigations and allow the creation of high-resolution structural maps to identify structures of degassing systems to assist first-order hazard analysis or guide further in-depth studies.

4.1.4 Aim of the study

The aim of this work is to image and analyze the degassing and alteration structure of the La Fossa fumarole field and better understand the association of diffuse and localized degassing at a fumarole field. We advance previous results (Müller et al., 2021) by considering new data, and by integrating them with the mineralogical and chemical analysis of alteration distribution in collected rock samples. We show systematic changes in the effects of alteration on the surface coloration and how drone-derived RGB data (Red, Green, Blue, standard color coding of images) can be used for the efficient detection and classification of degassing and alteration features. Combining UAS-based optical and infrared remote sensing with mineralogical- and geochemical analysis, and diffuse surface degassing measurements, we can infer the detailed anatomy of degassing and alteration systems at the surface, highlight active degassing domains versus areas of surface sealing, and determine their importance for the system based on their contribution to the total thermal energy release.

4.2 Study area

Vulcano is the southernmost of a group of 7 small volcanic islands forming the Aeolian Archipelago north of Sicily. They are located within the Aeolian Tindary Letojanni Fault System (ATLFS), an NNW-SSE striking local deformation belt connecting the central Aeolian Islands with the eastern section of Sicily (Barreca et al., 2014; Cultrera et al., 2017). The ATLFS is the interface between two larger tectonically active compartments, an extensive one in the northeast and a contractional one in the west (Cultrera et al., 2017). Frequent seismic activity and right lateral extensional displacements indicate ongoing tectonic activity (Billi et al., 2006) and the active shaping of the islands.

Vulcano is made up of volcanic edifices of which the northern section of the islands is the most recently active. The oldest volcanic activity at Vulcano is reported for 130 ka (De Astis et al., 2013). Six main stages of volcanic activity have been identified (De Astis et al.1997), of which the geologically younger active parts, the La Fossa Cone and Vulcanello, have been active during historical times <8 ka, showing mainly vulcanian and strombolian activity (De Astis et al., 2013). The last eruptive period of the La Fossa Cone from 1888-1890 was characterized by strong phreatic eruptions and witnessed and documented by Guiseppe Mercalli who later coined the term Vulcanian eruptions (Clarke et al., 2015).

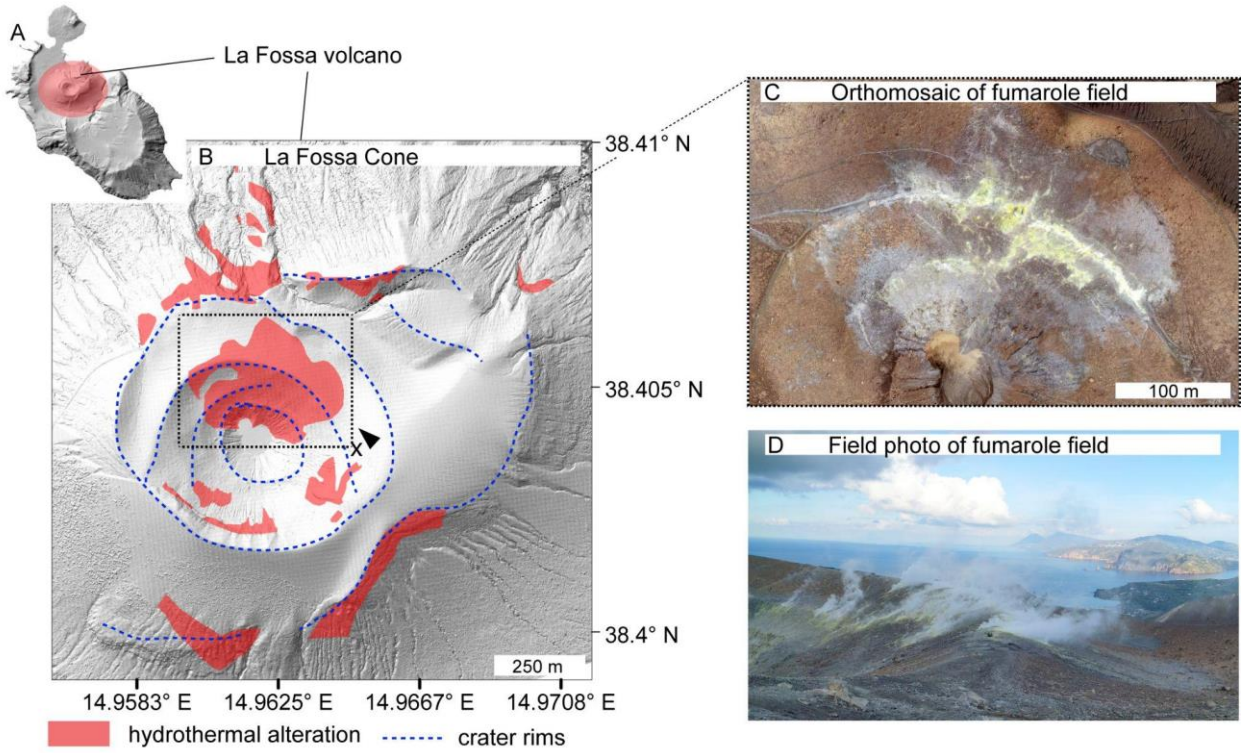

Figure 4.1 Overview of the degassing sites at La Fossa cone, Vulcano Island (Italy). A) Vulcano Island as shaded relief map. The red circle indicates the location of the La Fossa cone. B) Central summit region of the La Fossa Cone. Blue dashed lines depict crater rimes of different eruptive episodes. Areas of degassing and hydrothermal alteration are highlighted by red patches after Müller et al. (2021). The dashed box outlines the most prominent center of degassing and alteration, the high-temperature fumarole field. C) The high-temperature fumarole field from a birds-eye view. D) Field photograph over the fumarole field. Location and viewing direction are indicated by an x and arrow (B).

Vulcano since then is in a quiescent period and volcanic activity mainly expresses in degassing. gases are provided from a magmatic-hydrothermal system fed by a shallow magmatic reservoir beneath La Fossa volcano. The hydrothermal system is likely to have been partitioned into a hypersaline brine and a vapor phase (Henley and McNabb, 1978). The denser brine phase is confined at depth and contributes to the formation of metasomatic facies observed in deep-seated xenoliths (Adrian et al., 2007). The vapor phase, enriched with SO_2, H_2S, HCl, and HF, ascends to the surface and partly emerges directly from the high-temperature fumarolic field (Bolognesi and D'Amore, 1993; Capasso et al., 1997; Chiodini et al., 2000).

Volcanic degassing is present throughout the entire central and northern part of the island concentrating in degassing clusters at Baja Di Levante, within Vulcano Porto, and in clusters along the base and summit of La Fossa Cone (Chiodini et al., 1996; Carapezza et al., 2011; Diliberto et al., 2021; Inguaggiato et al., 2022 and many others) where frequently higher fluxes

of CO_2 are observed. The most prominent degassing sites are the high-temperature fumaroles at the summit of Vulcano that occur in several clusters on the outer rims of La Fossa cone and are most prominent in the high-temperature fumarole field (Figure 4.1). Degassing at the summit of La Fossa is persistent but subject to fluctuations. Gases of the high-temperature fumaroles (HTF) emerge with temperatures >300 °C, but temperatures have been exceeded in the past. Temperatures of >500 °C were reported (Harris et al., 2012; Diliberto, 2017) during previous volcanic crises.

Several periods of unrest have been reported and were accompanied by increasing fumarole temperatures (Harris et al., 2012; Diliberto, 2013; Madonia et al., 2013; Diliberto, 2017), increasing soil and groundwater temperatures (Capasso et al., 2014), changing gas compositions (Paonita et al., 2013), changes in gas flux (Inguaggiato et al., 2022), or a spatial growth of the fumarole field (Bukomirovic et al., 1997). The most recent crisis occurred in 2021 and led to increased thermal radiation (Coppola et al., 2022), deformation (INGV Bulletin reports), and localized structural changes like the formation of new major fumarole complexes. The rapid dynamics during volcanic crises and potentially negative effects of alteration on permeabilities, and therewith the potential to drain gases from the surface, highlight the importance of a better understanding of the structure and state of degassing systems.

Early studies about the structural setup of the Gran Cratere fumarole field of the La Fossa Cone were provided by Bukumirovic et al. (1997) and later modified (Harris et al., 2009; Madonia et al., 2016). Fulignati et al. (1999) analyzed alteration facies at Vulcano and constrained the central crater region to be a large silicic alteration complex characterized by the presence of chalcedony and amorphous silica. Outwardly to the central silicic alteration zone, advanced argillic (alunite ± gypsum) alteration develops, probably originating from the progressive neutralization of the acid fluids by weathering and dilution by meteoric waters (Fulignati et al., 1998). Müller et al. (2021) previously showed that degassing and alteration can be traced from remote sensing data far beyond the extent of the high-temperature fumarole locations. Based on surface color variability due to degassing and alteration processes they showed evidence for a more complex setup with alteration gradients within the silicic alteration complex and important structural units that will be complemented here. Examples of degassing and alteration-related surface color variability are shown in Figure 4.2.

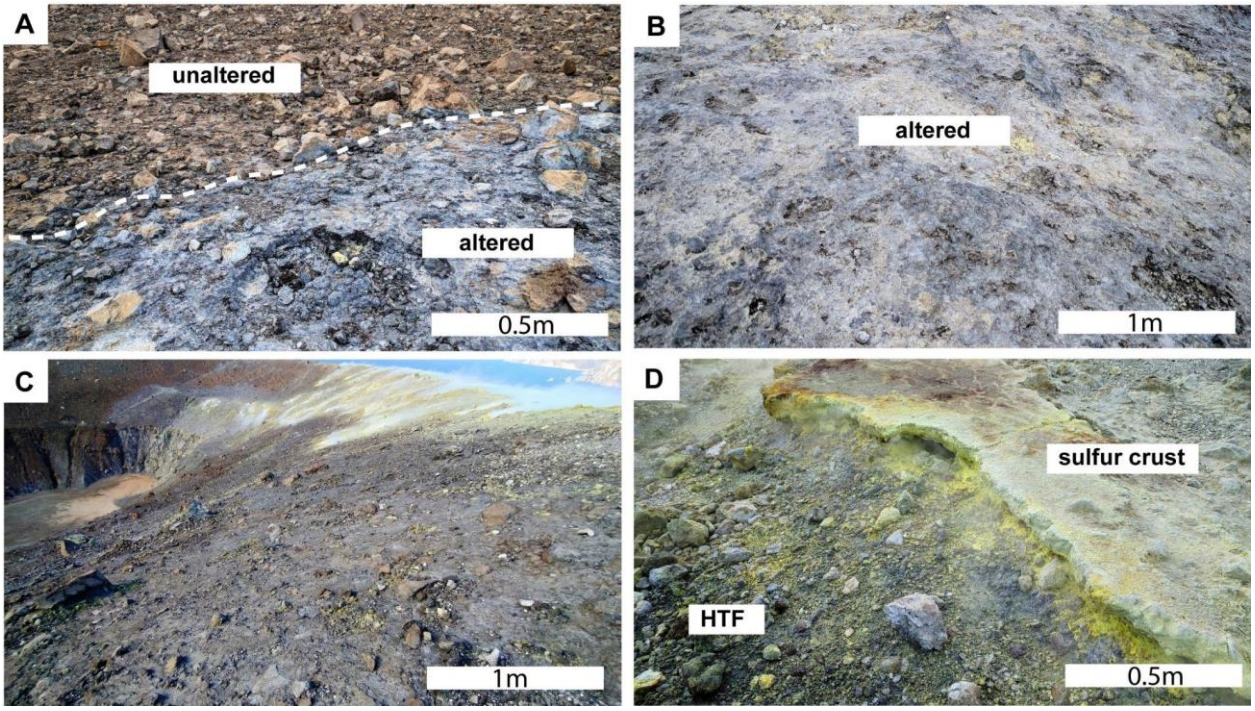

Figure 4.2 Different surface types and colorations in the La Fossa cone. A) Transition from unaltered to altered bleached surface. B) Intensely altered and bleached surface. C) View from the east onto sealed surfaces D) High-temperature fumarole and deposited sulfur crust.

4.3 Data and methods

To analyze the degassing and alteration structure at Vulcano, we used a combination of UAS-derived remote sensing data (optical and thermal infrared imagery), image analysis, and field-based ground-truthing by mineralogical and geochemical analysis of rock samples and surface degassing measurements. A simplified sketch of the workflow is shown in Figure 4.3.

1) An anomaly detection (chapter 4.3.2) based on UAS-derived data, employing image analysis techniques like Principal Component Analysis (PCA), and spectral and thermal classification (similar to Müller et al., 2021) provides the detailed optical and thermal anomaly pattern. Anomalies can be revealed based on slight color changes in the volcanic surface that occur due to degassing and hydrothermal alteration processes, or increased surface temperatures.

2) To verify observed anomalies, we carried out ground-truthing by mineralogical (XRD X-Ray Diffraction) and geochemical (XRF X-Ray Fluorescence) lab analyses of representative rock samples. Further, we performed surface degassing measurements to image the present-day degassing pattern and compared it to the observed anomaly pattern. Combining this information we can infer a detailed anatomy of the degassing and alteration structure at the surface and define and parameterize major structural units.

3) A temporal Infrared-monitoring carried out from 2018 to 2022, covering the volcanic crisis 2021 at Vulcano allows us to monitor the thermal evolution and response of the identified units to an event of increased gas flow with further implications of critical processes like localized surface sealing. Details on the single analysis steps are provided below.

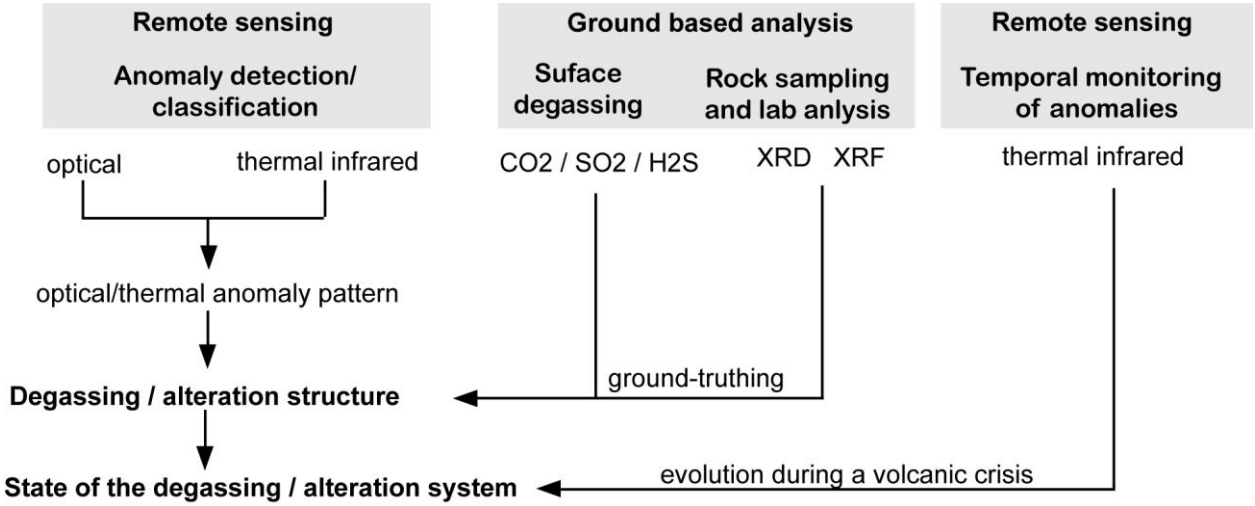

Figure 4.3 General workflow from anomaly detection from remote sensing data to ground truthing by mineralogical and geochemical investigation.

4.3.1 Acquisition and processing of UAS-based optical and thermal infrared data

The data acquisition was performed using a DJI Phantom 4 Pro quadcopter, equipped with a gimbal-stabilized 20 MP camera with a real shutter system, recording up to 0.5 HZ. Optical overflights were performed in the daytime at an altitude of 150 m above the fumarole field, ensuring a minimum overlap of 90 % for later photogrammetric processing. Thermal infrared image data was acquired by a Flir Tau 2 radiometric thermal infrared camera system attached to the DJI Phantom 4 Pro. The FLIR Tau 2 measures in the spectral range of thermal infrared between 7.5 and 13 µm, has a resolution of 640 x 512 pixels and is a fully radiometric sensor system. The infrared image data is recorded at 8 Hz by a Teax Thermal Capture 2 data logger. The camera was attached to the copter with a standard camera bracket on a self-made carrier frame and is powered by an external 11.1 V lithium-polymer battery, supplying voltage to the camera system (transformed down to 5.2 V in) and to an external GPS antenna (>8V required) which provides coordinates for each infrared image. Infrared overflights were performed in the early morning hours, before the sun illuminates the crater area, to avoid disturbances of

irregular surface heating due to solar radiation exposure (Stevenson and Varley, 2008). In this way, we ensure to map the thermal signal from the hydrothermal system exclusively.

All image data were processed using the Structure from Motion (SfM) approach in Agisoft Photoscan (Version 1.5.2.7838). The image data were inspected and images were preselected ensuring an overlap of 90%. Images of poor quality or out of focus were excluded and only images of a constant flight altitude were used for the processing. This is particularly important for the processing of infrared data, as varying altitudes might alter the radiation information due to changing pixel size to vent ratios. The infrared data was pre-inspected in Thermoviewer 3.0 and exported in a 16-bit tiff format in grayscale. We followed the typical workflow of sparse point cloud-, dense point cloud- and mesh generation, aiming to obtain a 3-dimensional model and eventually orthomosaic, digital elevation model (DEM), and infrared mosaic. The original images and processing results are roughly georeferenced, but their geolocation was optimized by manual co-registration using the ArcGIS georeferencing toolbox. An overview of the acquired and processed data sets can be found in Table 4.1.

Table 4.1: Overview of the processed data sets that were used for the following analyses. From The optical data, an orthomosaic and DEM were generated covering 3.74 km² with pixel resolutions of 8.6 x8.6 to 17.3 x 17.3 cm. From the high altitude infrared overflight, an infrared mosaic was acquired covering 3.23 km² with 41.2 x 41.2 cm resolution. All data sets cover the complete central section of the La Fossa cone.

Data set	Acquisition date	Pixel resolution in cm	Coverage in km²	Point density in p/m²
2019 orthomosaic	14.11..2019	8.6 x 8.6	3.74	135.20
2019 DEM	14.11.2019	17.3 x 17.3	3.74	33.41
2018 IR mosaic	15.11.2018	41.2x 41.2	3.23	5.64

4.3.2 Anomaly detection - Principal Component Analysis (PCA) and spectral classification for alteration mapping

The alteration mapping was performed on an orthomosaic data set acquired in 2019 that, due a poor fumarole activity, provides an almost distortion-free image of the central crater region. Using an approach similar to Müller et al. (2021), the alteration structure was revealed by applying a Principal Component Analysis allowing further constraints on the zonation of the fumarole area and expanding the interpretation by geochemical and mineralogical ground

truthing. PCA is a statistical tool that can detect and highlight optical anomalies within an RGB data set by transforming the data values of the initial RGB channels onto their perpendicular axes of the highest data variance. The resulting Principal Components are variance representations and can be used to detect and highlight optical anomalies like color changes due to alteration processes. PCA further promotes a decorrelation of the initial RGB bands, a dimensionality reduction, and associated better data separability so that color variations, before expressed by changes in the three RGB bands (3-dimensional problem), can now be accessed in single bands, the single Principal Components (PC). While Principal Component 1 (PC) resembles ~91.3 % (95) of the initial data variance, it mainly shows brightness changes within the image. PC 2 and 3 contain 7.4 (4.5) and 2.3 (0.5) % of the data variance, resemble color changes, and are suitable to resolve optical anomalies related to hydrothermal alteration.

Hydrothermally altered areas were defined based on the PC3, with pixel values > 85 representing hydrothermal alteration. We used this as a mask to crop the respective pixel locations in the original orthomosaic, resulting in a 16 Mio pixel alteration raster subset. This raster subset allows for a more sensitive image analysis due to the reduced spectral range with respect to the original orthomosaic. An unsupervised classification (implemented in ArcGIS) with 32 classes was applied to the PCA of the hydrothermal alteration raster subset and used to classify optical units. By combining classes in a way that they resemble optical spatial units best, we defined 4 Types of surface (Types 1-4) and analyzed their spectral characteristics and spatial distribution. Boxplots of the distribution of RGB values in the 32 classes and the spectral range of Type 1-4 surfaces are shown in Appendix A4.1. The optical structure of the fumarole field and alteration zone is similar to the thermal structure and will be discussed in Chapter 4.4.3.

4.3.3 Infrared analysis - thermal structure and time series analysis

The SfM-derived infrared mosaic represents the thermal radiation in a 16-bit tiff format, resembling values between 0 and 65536. To obtain a temperature map from the IR mosaic we calculated the apparent pixel temperatures Tp by

$$Tp\ (in\ K) = grayvalue\ *\ 0.04 \qquad (1)$$

where Tp is the apparent pixel Temperature in K, gray value is the radiation value of the original infrared mosaic and 0.04 is the scaling factor (radiometric resolution). The thermal structure was analyzed by defining temperature thresholds above background temperature, that highlight thermal spatial units best. A temperature threshold of T>40 °C was used to highlight high-temperature fumarole (HTF in the following) locations and a threshold of >22 °C to 40 °C (min. 5 °C above background) highlights areas of a rather diffuse thermal surface heating (Figure 4.4 B/D). To compare the thermal emissions of detected structural units, we calculate radiant flux and radiant exitance values by applying the modified Boltzmann law.

$$Q = e * b * A * (Tp^4 - To^4) \qquad (2)$$

The emissivity (e) was assumed to be 0.95 (often used as an assumption for volcanic surfaces), the Boltzmann constant (b) is 5.670737×10^{-8} $Wm^{-2}K^4$, the area of a pixel (A) is 0.024 m². *Tp* is the pixel temperature and *To* is the average background mean temperature, calculated based on 9 reference areas that are anomaly free. The flight altitude of 150 m (above the fumarole field) in combination with the low resolution of infrared sensors results in a pixel resolution of 0.41x0.41 m.

Note that remotely sensed Infrared data always represents apparent temperatures that might differ from the real object temperature due to the radiation properties of the measured object itself (emissivity), the distance of the sensor to the measured object, the pixel-to-object size ratio, but also due to atmospheric or hydro-meteorological effects (Ball and Pinkerton, 2006) influencing the detected radiation values. Therefore apparent temperatures typically are lower than in situ vent temperatures. Real fumarole vent temperatures can reach more than 300 °C (Diliberto, 2013) while temperatures in our infrared mosaic range to max. 163 °C only. With this data set, we do not aim to provide precise fumarole temperatures but to analyze the thermal structure of the fumarole field and the broader field of activity.

4.3.4 Ground-truthing by mineralogical and geochemical analysis

4.3.4.1 Rock sampling

Rock samples were collected at predefined representative locations aiming to include all alteration end members, during field campaigns in 2019 and 2022. We sampled along 3 transects following the postulated hydrothermal alteration gradients and crosscutting major alteration units, of which transect A is located on the lower fumarole field, transect b along the

upper crater rim, and transect c is located in the eastern crater crosscutting several alteration units (locations for samples in chapter 4.4.2.2). Samples were in the size of ~2000cm³ (hand-sized) retaining the undisturbed surface crust, but also subsurface material to a depth of ~ 10 cm. The samples were mechanically crushed, ground to 63 µm, and split for XRD and XRF analysis, respectively. In total 21 samples were collected of which 9 were prepared for the XRD and XRF analysis and 12 for XRF analysis exclusively.

4.3.4.2 X-ray diffraction (XRD)

Between 1 and 3 mg of whole rock powder was used to determine the mineral composition of each sample through powder X-ray diffraction (pXRD). The analysis was conducted using a PANalytical X'pert diffractometer equipped with an X'Celerator silicon-strip detector at the Department of Geoscience, Swedish Museum of Natural History, Stockholm. The instrument was operated at 45 kV and 40 mA using Cu-Kα radiation ($\lambda = 1.5406$ Å). Samples were analyzed between 5° and 70° (2θ) for 20 min in step sizes of 0.017° in continuous scanning mode while rotating the sample. Data were collected with "divergent slit mode" and converted to "fixed slit mode" for Rietveld refinement. The collected data show several peaks of X-ray diffraction intensity which represent the characteristic of crystalline minerals, the proportions of mineral phases were then refined using the Rietveld refinement method in the High Score Plus 4.6e software. The XRD analytical procedure was performed twice for each sample to ensure optimal quality control. Some samples contained contents of amorphous material of more than 50%. Those will be marked with a * in the following but we will consider the mineral composition normalized to 100 % non-amorphous material.

4.3.4.3 X-ray fluorescence (XRF)

Bulk chemical composition was determined by X-ray fluorescence analysis (XRF) at the ElMiE Lab at the German Center for Geosciences (GFZ). Main and trace elements were measured on fused beads with an AXIOS spectrometer (Malvern Panalytical, UK). Loss of ignition (LOI) was determined by analysis of H_2O/CO_2 using an Eltra element analyzer. Reproducibility was determined on three certified reference materials (CRM) and is within the analytical precision, which is better than 2% for main elements and better than 10% for trace elements.

4.3.4.4 Surface degassing measurements (CO_2, SO_2, H_2S)

The surface degassing was measured at ~ 200 points within the northern part of the La Fossa cone (Figure 4.6) in September 2021 and November 2022 using a simplified multi-gas accumulation chamber approach (Appendix A4.2). The measurement unit, a Dräger XAM 8000 handheld Multigas device, was equipped with 6 sensors measuring CO_2, CH4, SO_2, H_2S, H_2, and O2 simultaneously of which CO_2, SO_2, and H_2S are considered here. The simplified accumulation chamber approach was an adaption as a consequence of uncertainties encountered in previous multi-gas measurement campaigns. Due to different sensor reaction times for ascending and especially descending gas concentrations, the comparison of direct sensor readings might lead to odd gas ratios with an artificial shift towards magmatic components. For that reason, we use the slope of the ascending gas concentration within a defined volume as quantification for a relative surface flow. More detailed information about the gas measurement approach is provided in the supplementary materials. Note that the aim of the gas measurements was not to provide accurate flux estimates but to highlight the spatial variability of the gas flow of certain gas species from the surface.

4.4 Results

4.4.1 Thermal- and optical anomaly pattern

Degassing and hydrothermal alteration at La Fossa as seen in drone imagery can be traced by mainly two effects.

1) The transition from unaltered to hydrothermally altered surface can be traced by a general color shift in the drone images from reddish to grayish (Figure 4.2A and 4.4A). This allowed us to constrain a distinct ~70,000 m² sized area surrounding the fumarole field in a circumferential manner. This area is hereafter referred to as the Alteration Zone (ALTZ in Figure 4.4A/B), and represents the maximum extent of at surface observable alteration effects that can be associated with the fumarole field. It includes effects ranging from weak surface alteration to strong alteration with intense surface bleaching and remineralization, to complete destruction of the host material. The extent of the ALTZ exceeds the area covered by the high-temperature fumarole (HTF) site by ~50 times (Figure 4A/B), indicating the widespread influence of diffuse degassing and alteration processes.

2) Within the ALTZ we observe a segmentation characterized by brightness and color variability expressed in different shades of gray (Figure 4.4A), the second optical effect, indicating local alteration gradients. Analyzing the ALTZ for this spectral variability by PCA

and image classification we can constrain pixels of low-, increased-, or intense surface bleaching and alteration (light blue, dark blue, and red pixels in Figure 4.4B) and define an alteration index represented by 4 surface Types (1-4), of which Type 1 is the most altered and Type 4 the least altered surface.

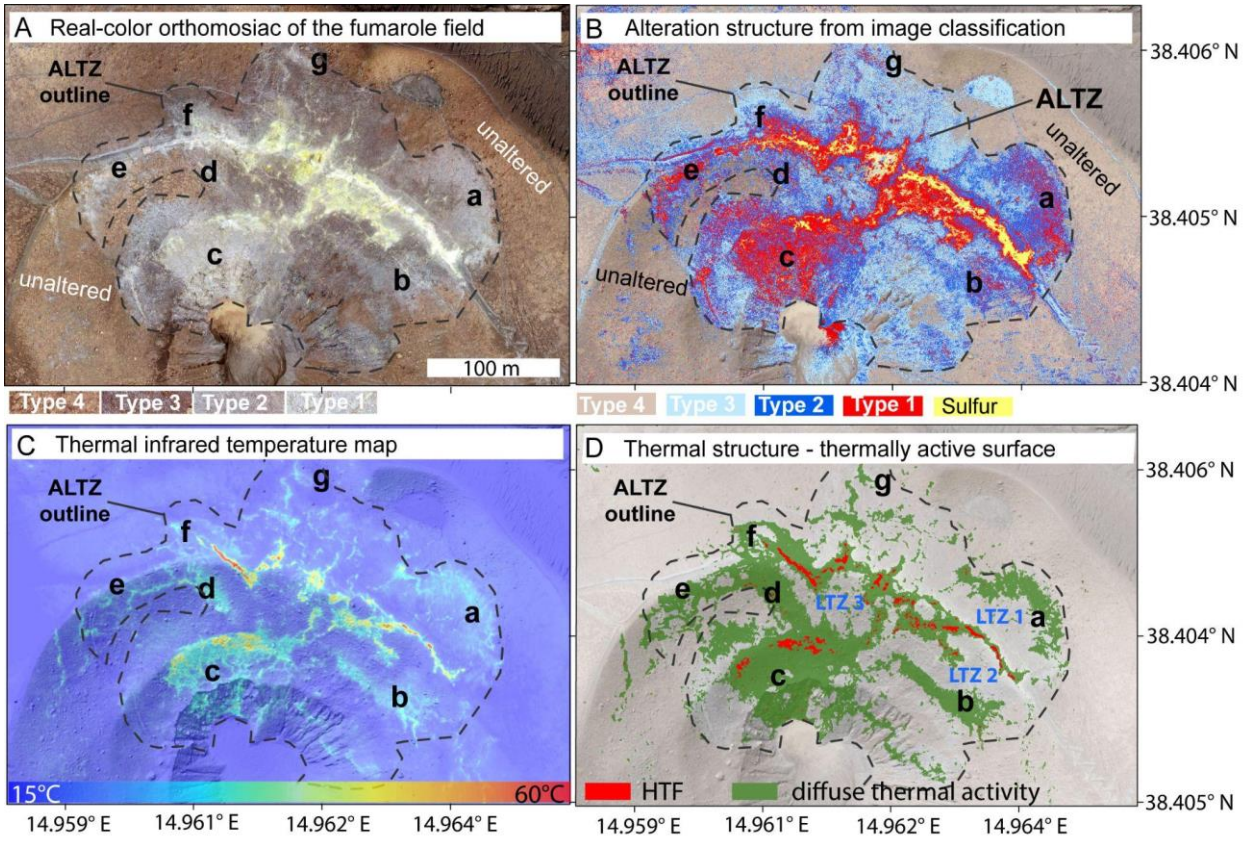

Figure 4.4 Alteration structure of the La Fossa fumarole field. A) True color image of the high-temperature fumarole field. B) Alteration structure of the fumarole field revealed by PCA and image classification, represented by surface Types 1-4. C) Thermal infrared image of the fumarole field. D) Simplified thermal structure of the fumarole field highlighting high-temperature fumarole location in red and diffuse thermal activity in green. Labels a-g represent notable large-scale anomaly units that can be observed in both, the alteration data and the thermal data. Note that the contrast of the background image has been reduced for highlighting in sub-figures B and D.

Type 1 surfaces are bright grayish intensely bleached surfaces or sulfuric deposits and represent the strongest alteration end members that we can detect optically from our data. Type 1 mainly resembles the fumarole sites and surrounding areas (Figure 4.4A/B) but also larger isolated regions that can not be associated with major vent systems. With increasing distance to the degassing centers, we observe a shift towards darker grey (Type 2) and brownish (Type 3) surface colors. Type 2 is characterized by a gray but comparatively less bright coloring. It

typically occurs at the boundaries between Type 1 and Type 3 regions and largely surrounds Type 1 areas, but it also forms several isolated clusters typically embedded in Type 3 areas (units b,d,g in Figure 4.4). Type 3 is generally darker and more reddish in color, similar to the unaltered parts of the crater surface, but can be well distinguished from the unaltered surfaces by PCA. It makes up ~50% of the ALTZ and dominates in the central northern and southeastern parts. Type 4 is a reddish, apparently oxidized surface that dominates the La Fossa cone surrounding the ALTZ.

The surfaces within the ALTZ are generally mixed and composed of more than one type. The ALTZ is characterized by a generally high density of Type 3 pixels, with locally high densities of Type 1 and Type 2 pixels, which then become the dominant surface type and form larger spatial units, indicating locally higher alteration gradients or larger structural units (units a-g in Figure 4.4 and details in Appendix A4.3). The largest of these units covers several thousand square meters.

The thermally active surface (Figure 4.4C) can be divided into high-temperature fumaroles (HTF in Figure 4.4D) and diffuse thermally active surface (green pixels in Figure 4.4D). HTFs are the visible part of the activity that can be constrained by the naked eye in the field, while the diffuse thermally active surface is largely imperceptible. The thermally active surface largely mirrors the alteration pattern observed in the optical data. An analysis of the temperatures obtained at all pixels of Type 1 to 4 surface show a general increase of mean pixel temperatures from Type 4 to Type 1 surface by an average of 2 degrees (Figure 4.5). In particular, areas dominated by Type 1 and 2 surfaces reflect the thermal structure well while areas of Type 3 dominance largely coincide with low-temperature surfaces (Figure 4.4B/D). An additional Spearman correlation test, applied to the classified surface (32 classes unsupervised, for comparison see Appendix A4.1) and the thermal data (in °C) shows a moderate positive correlation between optical and thermal anomalies (Appendix A4.4). This shows that the detected optical anomalies are meaningful and that degassing and alteration variability occurs even at local scales and can be traced in our close-range drone remote sensing data.

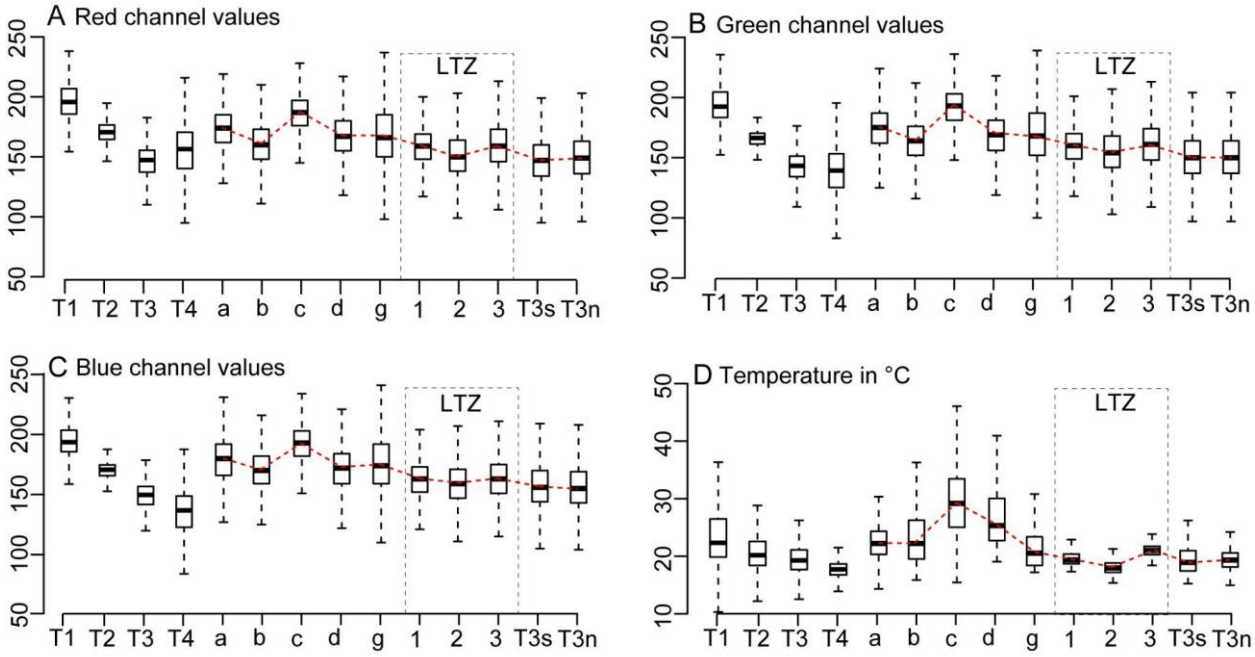

Figure 4.5 Color value- and temperature distributions for surface Types 1-4 (T1-T4), selected areas a-g, and associated low-temperature zones LTZ1-3 (location see Figure 4.4B/D). A) Red color value distribution. B) Green color value distribution. C) Blue color value distribution. D) Temperature value distribution. Values are based on analysis of 6.8 million pixels within the ALTZ.

The spatial coincidence of both optical and thermal anomalies highlights the relationship between variations in the surface coloration, caused by alteration processes, and the ongoing influence of diffuse gas flow. A general coincidence of increasing brightness (simultaneously increasing the RGB values) with increasing surface temperature of an area can be constrained (Figure 4.5).

4.4.2 Structural units revealed from optical and thermal data

The optical and thermal anomalies form distinct spatial units of alteration and elevated surface temperature (units a-g in Figure 4.4D), which now allow us to infer the following surface structure of the fumarole field and its wider field of activity.

The centers of degassing activity are high-temperature fumaroles (HTF). These are the "visible" part of the activity that can be perceived in the field (red pixels in Figure 4.4D). We spatially constrain the HTFs based on apparent temperature values with T>40 °C in our 150 m overflight data. Using this as a threshold we find that the HTFs cover an area of 1223 m², and

occur exclusively in the Type 1 surface. However, HTFs represent only a fraction of the active surface.

The total extent of the surface that has to be considered active is much larger. The surface with elevated temperature covers ~30000 m² (green pixels in Figure 4.4D, T>22 °C or 5 °C above the background), exceeding the area covered by HTF by a factor of 25. The surface that is considered hydrothermally altered (ALTZ ~70,000 m²) exceeds the area covered by HTF by a factor of ~60, highlighting the widespread influence of diffuse degassing and alteration processes. Besides the HTF we have constrained larger units of elevated surface bleaching and surface temperatures that can be considered structurally important and centers of diffuse degassing activity.

Units a and b are diffuse features of increased surface bleaching (Type 1 and 2) and surface temperature, embedded in the Type 3 surface and surrounding the eastern fumarole field in the form of an aureole shape. Neither can be associated with major vents. The observed maximum surface temperature for unit a is 43.7 °C (0.43 m resolution) and the average temperature is 25 °C, ~8 °C above the background. It is located at a distance of 25 to 50 m downslope from the eastern rim fumarole complexes, separated by a low-temperature zone (LTZ). Unit b, the southern part of the aureole is a 120 m long and 20 - 35 m wide anomaly located subparallel on the inner side of the crater. It extends over ~2100 m² and has a maximum surface temperature of 46 °C and an average temperature of 26 °C (9 °C above the background). The temperature range and spatial extent of units a and b are comparable. In the field, both are difficult to identify as there is little or no evidence of degassing (Appendix A4.5). Like unit a, unit b is also separated from the main fumarole vents by the LTZ. Its northern boundary corresponds exactly to the positions and curvature of the fumarole alignments at a relatively constant distance of 30 meters. In unit b, we observe a temperature gradient with higher temperatures at greater distances from the fumarole vents and an apparently more active center in the southeastern corner. Another thermal anomaly with a similar shape and orientation is located further south inside the crater.

Units d and f are similar aureole-like features in the western fumarole field, associated with fumarole complex F0. They circumferentially surround fumarole complex F0 at a distance of 5 to 15 m, also separated from the HTF by a Low-Temperature Zone (LTZ), but to a lesser extent than that observed for units a and b of the eastern fumarole field. The southwestern section of this aureole, unit d, appears as a larger heated complex with stronger surface bleaching (Type 1) and higher temperature (mean T=27 °C), and a temperature gradient with

higher temperatures further away from the major fumarole complex. The boundary to the low-temperature zone is sharp with a sudden drop in temperature of 10 to 20 °C and strong associated color shift (Appendix A4.3). The aureoles of F0 and F11 have in common that they are encircled by a network of polygonal net-shaped thermal anomalies in the far field.

Low-temperature zones (LTZs) dominate the central parts of the fumarole field. The LTZ have only slightly elevated temperatures relative to the background (18-21 °C or 1-4 °C above background) and can be optically constrained by a darker Type 3 surface coloration. From field observations, we have constrained that these LTZ form a strong, apparently sealed surface complex. Therefore LTZ might indicate largely sealed sections of the fumarole field which inhibit gas flow at the surface. The 3 central LTZ1-3 (Figure 4.4D) cover an area of ~12,000 m².

Unit c is a broad complex of highly altered material (Type 1) and significantly high surface temperatures. It is potentially the most altered member in the central crater region. It covers an area of ~8000 m² and the maximum and average apparent temperatures observed are 87 °C and 29 °C. It is associated with the HTF FA and F58. Considering the thermal structure of unit e, it is a heterogeneous unit formed by a network of higher temperature anomalies embedded in lower but, with respect to the background, significantly increased tempered surface. This area is associated with the northwestern crater unit, which is the most recent explosion crater.

Unit e is a large branching thermal and optical anomaly of the upper fumarole field. It can be constrained by its gray coloration embedded in the reddish unaltered surface and also by its increased surface temperature. It is a 120 to 150-m-long branch-shaped network of anomalies on the inner crater wall. The central feature is oriented E-W and located ~ 20 m south and below the helicopter platform and the crater rim. We constrained its size to ~2500 m² (only the western branch, without intersection to h) and the recorded maximum and average apparent temperatures are 45.0 °C and 25.9 °C respectively. Some smaller clusters of localized degassing, alteration, and increased surface temperature are observed in the northern section of the fumarole field (unit g) towards La Forgia.

4.4.3 Ground truthing - verification of observed anomalies

We have carried out mineralogical (X-ray diffraction) and geochemical (X-ray fluorescence) analyses of bulk rock samples collected at representative locations and surface degassing measurements. The aim is to verify the observed anomaly pattern of alteration gradients and

distinct active units and to investigate the relationship between the optical and thermal anomaly pattern and modern degassing and hydrothermal alteration processes. In this way, we provide ground truthing and demonstrate that the anomalies observed are significant.

4.4.3.1 Present-day surface degassing pattern

The measurements of diffuse degassing from the surface allow us to compare the present-day surface degassing pattern to the observed optical and thermal anomalies (Figure 4.6A/B). We performed surface degassing measurements of CO_2, H_2S, and SO_2 simultaneously in the diffuse degassing regime at 200 measurement points (~100 points within and outside the ALTZ) throughout the whole northern crater section (details of gas measurements in Appendix A4.2). The observed relative flux values for CO_2 range from 0 to ~9000 ppmv/s with an average of ~900 ppmv/s. They are considerably higher ($x*10^3$) than the SO_2 and H_2S flux at the respective locations. For both, SO_2 and H_2S a maximum gas flux of <10 ppmv/s was measured and the average is below 0.5 ppmv/s.

Looking at the spatial distribution of the measured gas we observed generally higher gas levels within the alteration zone ALTZ and at the ALTZ boundary, for each of the measured gas (Figure 4.6C/D). The average CO_2 flux is 660 ppmv/s outside the ALTZ and 923 ppmv/s within the ALTZ. Thus, the averaged CO_2 flux inside the ALTZ is about 1.4 times higher than outside, but is particularly high in some of the constrained units a-g. However, the CO_2 flux has a wide spatial distribution and high flux values of above 2000 ppmv/s can also be observed outside the ALTZ and at a distance to the ALTZ boundary (Figure 4.6A/C).

SO_2 and H_2S in contrast appear spatially stronger confined, and significant flux values can be exclusively observed within the ALTZ (Figure 4.6B/D). Values for SO_2 and H_2S inside the ALTZ exceed the outside-ALTZ values by 13 and 15 times. This higher diffuse flux, although at average low concentrations, might promote a surficial process of chemical weathering and surface bleaching, potentially causing the observed color shift from a reddish-oxidized surface toward gray and will be discussed further based on analyses of the geochemical composition of rock samples in Chapter 4.5.2.

Comparing the surface degassing to the observed optical and thermal anomaly pattern (Figure 4.6E-G), we see that high values were observed especially in units a or b on the eastern side of the fumarole field, coincident with increased alteration (Type 1 and 2) and thermally active surface, followed by other constrained units c-g. However, the strongly bleached and

apparently highly altered unit c shows, other than expected, rather small values, although its surface temperature is significantly increased with respect to other identified units. This might indicate reduced surface permeability and surface sealing processes and will be discussed in Chapter 4.5.3.

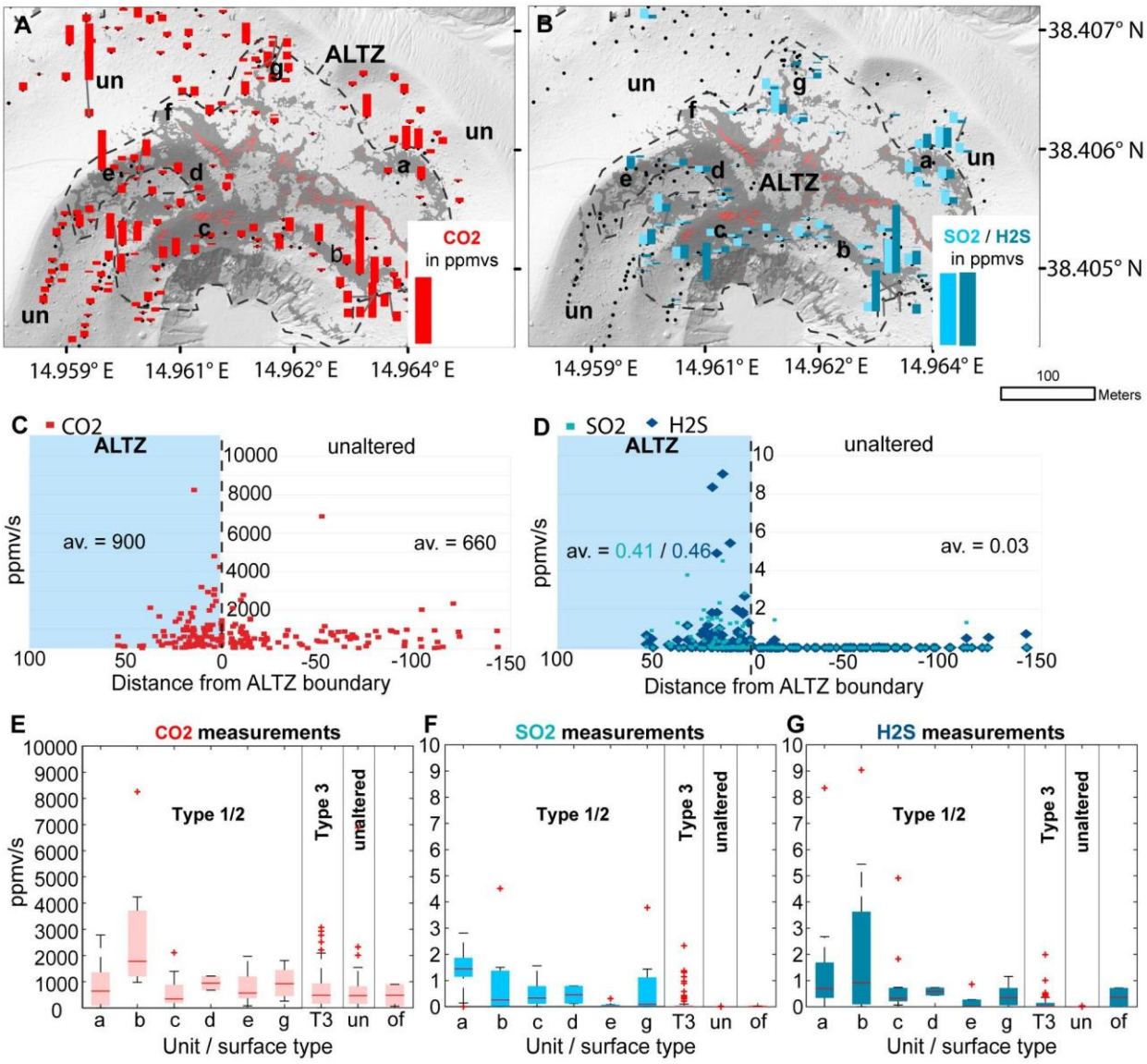

Figure 4.6 A/B) Spatial distribution and flux values for CO_2 *(red bars in A),* SO_2 *and* H_2S *(B) in a map view. The dashed line highlights the ALTZ boundary. Dark grey features in the background highlight the thermally active surface (compare Figure 4.4D). C/D) Flux values within or outside the ALTZ plotted by distance to the ALTZ boundary. A generally higher flux is observed within the ALTZ, but while* CO_2 *(C) is also abundant outside the ALTZ, significant* SO_2 *and* H_2S *fluxes were observed exclusively within the ALTZ, especially on the outer edges. E-G) Flux values for identified units a-g, Type 3 surface and the unaltered surface (un) highlight the lower flux of sulfuric gas species in the unaltered regime.*

While SO_2 or H_2S flux values for Type 1 and 2 surfaces are increased, only low fluxes were constrained for the Type 3 surface and no flux for the unaltered surface (un in Figure 4.6E-G). Note that the central sections of the fumarole field were not sampled due to the close vicinity to HTF and expected high flux values. The data shown here is only representative for the diffuse degassing domain.

4.4.3.2 Mineralogical composition of the alteration gradients

XRD Analysis was performed along two transects A and B, and XRF analysis was performed on samples taken along three transects A-C (Figure 4.7), crossing postulated alteration gradients.

Transect A crosses from the unaltered surface over Type 3 into the Type 1 surface of the highly altered unit c. Transect B is oriented along the HTF on the crater rim in an east-west orientation from Type 1 surface into the LTZ (Type 3). Transect C crosses the eastern fumarole field from the unaltered surface, through the Type 1 and 2 surfaces in unit b, the LTZ (Type 3) on both sides of the HTF, to Type 1 and 2 surfaces of unit a, and eventually the unaltered material outside the ALTZ.

Results of all samples support local alteration gradients within the ALTZ and show significant changes in the mineralogical and geochemical compositions (Table of XRD results in Appendix A4.6). The dominant mineral phases observed in samples of transects A and B are sanidine, cristobalite, and elemental sulfur (Figure 4.7). Additionally, most samples contain amorphous material, representing glassy phases typical for volcanic sequences. For comparability, mineralogical concentrations refer to the crystalline phase, while amorphous contents are stated with respect to the total. Note, however, that bulk rock geochemistry refers to both phases and cannot analytically distinguish between amorphous and crystalline.

Considering compositional changes along transect A we observe a high proportion of sanidine feldspar and lesser cristobalite in the relatively unaltered samples (Type 4). With an increasing degree of alteration, we observe a general loss of cristobalite and sanidine while sulfur contents increase (Figure 4.7). Samples from the unaltered reddish Type 4 surface (A1) outside the ALTZ and Type 3 surface (A2/3) inside the ALTZ are similar in composition and show high sanidine and cristobalite contents of 86-87 % and 13-14% in the crystalline part, respectively, yet low to no sulfur contents. These samples were taken in areas of no or only slightly increased surface temperatures of <22 °C (i.e. <5 °C above the background). Samples A4-6 are taken in

unit c, a complex of high alteration and increased mean surface temperatures of 28 °C (~10 °C above background).

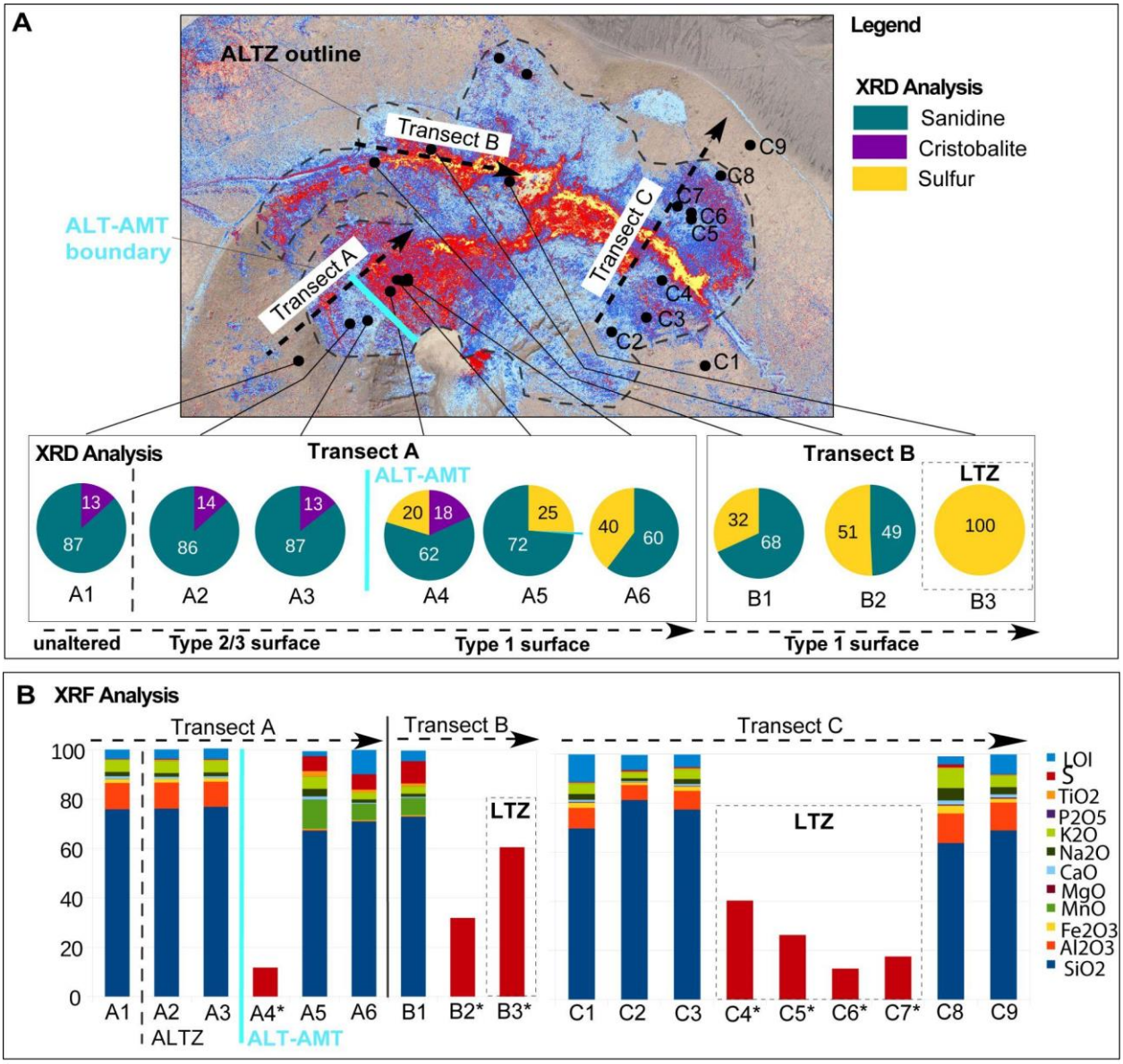

Figure 4.7 Mineral and chemical composition of samples along 3 transects A-C crosscutting alteration gradients and structural units. Transect A/B) With increasing alteration intensity we observe a relative decrease of the initial mineral phases sanidine and cristobalite whereas the sulfur content increases. Note that the mineral composition in this figure is normalized to 100 % non-amorphous minerals. In the chemical composition, we observe a significant decrease of Al_2O_3 and Fe_2O_3 but an increase of MnO, TiO_2, and S with increasing alteration, especially at the ALT-AMT boundary. At transect C we observe a dominant increase of S 17-40% for samples taken within the LTZ. Else than observed for the other transects, changes in Al_2O_3, Fe_2O_3, TiO_2, and MnO are less significant, even in the active units a and b. For samples marked with an asterisk (*) XRF results are not available.

In this strongly altered unit, cristobalite is absent, along with a decrease in sanidine to 60-70 % relative to the least altered samples and an increase in sulfur contents of up to 20-40 % in the crystalline portion of the rock sample. However, the amorphous components constitute a high proportion of these sample(s), showing ca. 50% in samples A6 and B1.

Samples taken on the upper rim along transect B in the high-temperature fumarole regime (V-AHT) contain total sulfur contents of 50 to 100%, while cristobalite is absent in these samples. Sample B3, a piece of grayish crust is taken from LTZ3 (~21 °C, 4 °C above background) in between the high-temperature fumaroles F0 and F5 and contains 100% sulfur, highlighting the precipitation and sealing potential of degassing activity at the surface.

Comparing the changes of surface coloration with changes in the mineralogical composition we can constrain no significant effect at the ALTZ boundary, i.e., the transition from unaltered to altered surface (A1-A2/3), although the optical effect is major. However, significant compositional changes, e.g. the complete loss of cristobalite and increasing sulfur content are observed at the ALT - AMT boundary (blue mark in Fig. 4.6), coincident with the shift from Type 3 to Type 1 surface into unit c.

4.4.3.3 Bulk geochemical composition of the alteration gradients

For samples without amorphous fraction, bulk geochemical composition correlates reasonably well with mineralogy determined by XRD, assuming ideal stoichiometry. The difference between theoretical bulk composition and true composition is within 10% of the respective element, which we consider a good estimate given sample heterogeneity. Only for sample A5, the high Mn content remains unmatched by XRD analysis. Subtracting the theoretical bulk composition of the crystalline fraction from the true bulk composition, we can thus estimate the chemical composition of the amorphous fraction. The amorphous fraction is similar to the crystalline counterpart mainly composed of SiO_2 and some minor (<5 wt%) phases, as well as elevated Mn contents. The high Mn contents were only observed in samples with medium alteration and elevated temperatures, both in samples with and without a significant contribution portion of amorphous material. It is thus likely that Mn is contained in the crystalline phase, yet could not be detected due to the high SiO_2 signals derived from sanidine and amorphous material.

The bulk geochemical composition (Figure 4.7 and data table in Appendix A4.7) agrees with the mineralogical composition. All samples are high in SiO_2 content and, therefore, can be considered to belong to the large silic-alteration complex earlier described by Fulignati et al. (1999). The samples show a slight variability of SiO_2 between 67-82 wt. % and plot on the rhyolite field within the TAS diagram (Middlemost, 1994; not shown here). The amorphous component, typical for rhyolite, consists of mainly SiO_2, with minor amounts of Fe and Al, based on the difference between the theoretical and actual geochemical composition calculated from stoichiometric mineralogy. Three samples also have significant MnO, possibly caused by hydrothermal leaching and precipitation as amorphous crusts. However, the variability of MnO will not be detailed further in this study.

Dominant in transect A is the loss of Al_2O_3 from the unaltered Type 4 surface (>10 wt.%) outside ALTZ to the Type 1 surface of the highly altered unit c (<0.4 wt.%). Similarly, Fe_2O_3 is decreasing from an average of 1.6 to 0.3 wt.%. The loss of Al_2O_3, and Fe_2O_3 is likely related to the alteration of sanidine and the elution of iron- and aluminum-sulfates formed due to the contact with sulfuric gas. The most significant changes occur, similar as observed in the mineralogy, not at the transition from unaltered to altered (ALTZ-boundary) but at the ALT-AMT boundary (blue line in Figure 4.7) at the transition from Type 3 to Type 1 surface.

Transect C crosses from the unaltered surface through unit a, the northern LTZ, the southern LTZ, unit b, Type 3 surface, and eventually the unaltered surface. Compositional changes from unaltered (Type 4) to altered (Type 1 and 2) surface of units a and b, here, are minor with relatively stable values for Al_2O_3 (6-12%), Fe_2O_3 (1-3%), TiO_2 (<0.5) and Mn (~0). At the transition from active units a and b (Type 1 and 2 surface) to the LTZ (Type 3), we observe a significant increase of sulfur content from <2% to 12-40%. However, this increasing sulfur content here is not coincident with the systematically brighter surface color observed for other altered units. LTZ show the same rather dark surface observed for Type 3 surface elsewhere, which is a discrepancy to the effects observed in the western fumarole field and indicates that LTZ have to be considered subject to different surficial processes. This will be discussed in Chapter 4.5.3.

4.5 Discussion

In this study, combining close-range remote sensing, image analysis, mineralogical and geochemical analyses of rock samples, and the investigation of the present-day surface

degassing, we investigate the degassing and alteration structures of the fumarole field and the broader field of activity at La Fossa cone on Vulcano. Based on image analysis (similar to Müller et al., 2021) of new better quality drone-derived high-resolution image data, we resolve the general pattern of degassing and alteration effects at the surface, spatially constrain them and complement our previous work with more detail and extensive ground truthing. In our previous work parts of the central fumarole field could not be analyzed in detail due to stronger gas plume distortion in our image data. Also, some parts of the results presented here are results of additional and intense fieldwork and lead to an adapted interpretation of observed effects especially considering the diffuse activity pattern in the eastern fumarole field.

From UAS-derived RGB imagery, we identified a ~70,000 m² sized zone that is outlining the maximum extent of observable alteration effects. We showed variability within the ALTZ that represents local alteration gradients or structural units. We show that effects of diffuse degassing and alteration can be traced far beyond the activity of high-temperature fumaroles. Alteration effects can be observed in an area (ALTZ) that is actually ~50 times larger, and a thermally active surface that is ~25 times larger than the area covered by high-temperature fumarole complexes.

Analyses of mineralogical and bulk-geochemical compositions of representative rock samples support our observations of local strong alteration gradients and allow to constrain relations between remotely sensed surface coloration and degassing and alteration processes. A general shift from reddish to gray surface coloration allows us to infer areas of increased diffuse gas flow. Variability in surface brightness and gray hues allows for the detection of alteration gradients and major active units. A largely coincident optical and thermal anomaly pattern highlights the relation between surface temperature and surface color and allows to constrain major structural units. Some of these units represent large complexes of diffuse activity and are apparently important structural features for the degassing system as will be discussed in chapter 5.3.

The presented combination of methods provides an efficient tool for first-site investigation of volcanic degassing and alteration systems and can be applied to volcanoes elsewhere. Structural findings and implications for the degassing and alteration system provide information for further and more detailed alteration research.

4.5.1 ALTZ controlled by sulfuric gases and elution processes

The ALTZ, characterized by a surface color shift from reddish to gray, is coincident with the area of higher SO_2/H_2S flux and apparently represents the zone of diffuse acid gas flow (Figure 4.4). All measurements with a significant flow of sulfuric gas species were measured inside the ALTZ, while the flux of CO_2 was also high outside the ALTZ.

We therefore suggest the general color shift from reddish to gray to be related to this higher flux of sulfuric gases, promoting a process of surficial chemical leaching of iron oxides, via the reduction of the initially contained iron oxides to iron sulfates, which are easily soluble in rain or condensing water vapor and prone to rapid elution. Iron oxide content in our analyzed samples ranges from 1.5% (A1) in the unaltered regime, to 1.1-1.4% for A2/3 samples to 0.3 for samples of the highly altered unit c (A4-6). There is a gradual reduction following the postulated alteration gradient, with the strongest changes occurring on the ALT-AMT boundary (blue line in Figure 4.7). The 1.5% Fe_2O_3 for our rock sample of the unaltered regime is a rather low value and might be related to the fact that the sample was taken very close to the ALTZ boundary and consists of >50% amorphous material. Fulignati et al. (1999), who provide a broader sampling database estimated Fe_2O_3 contents of unaltered 1988-1990-eruptive products with 2.46-6.65%, which reduces to an average value below 1% in the silic-alteration regime (Fulignati et al., 1998; Fulignati et al., 1999; Boyce et al., 2007).

Evidence for chemical leaching can also be found on the crater floor, where deposits form a colored layer resembling the color spectra widely observed on La Fossa, with bright reddish deposits close to the fumarole field resembling classic fluvial patterns. We believe that the optically anomalous gray surface at Vulcano can generally be used to infer areas of present higher gas flux or former discharge of acid gases at even low flux rates. Analyzing the broader area of the central crater region we can infer multiple other areas where we observe similar (Müller et al., 2021).

4.5.2 Alteration gradients on local scales

With average high SiO_2 contents of >70%, the sampled areas correspond to the large silicic alteration complex suggested by Fulignati et al. (1999), Azzarini et al. (2001), Boyce et al. (2007), and others. In our study, we show evidence for strong local alteration gradients and structurally important units, spatially constrain them, and complement detail to earlier studies.

Color shifts observed within the ALTZ (brightness effects, hues of gray) are likely controlled by the degree of hydrothermal alteration, secondary mineral formation, and especially sulfur content in the respective surface samples. Coincident with characteristic changes in the surface coloration from Type 4 towards stronger bleached surfaces of Type 1, we observe a relative decrease of the initial mineral and element composition by simultaneously increasing sulfur content (Figure 4.7) for most of the obtained samples. While sulfur content in Type 1 surface ranges from 6 to 31 %, for Type 2 it is already below 2%, and for the unaltered fraction below 0.2%. We can, therefore, confirm a general link between alteration gradients/sulfur contents and surface brightness or surface Types in our remote sensing data (Figure 4.8).

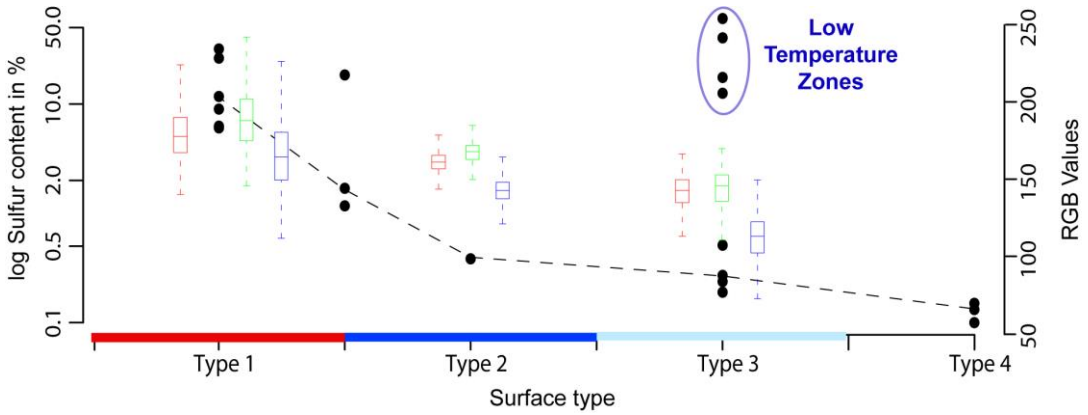

Figure 4.8 Overview of the relation of sulfur content of rock samples and brightness or inferred surface Type. Black dots mark the sulfur contents of rock samples, and the color-coded box plots the respective value range in the RGB values. With decreasing surface Type from highest altered (Type 1) to unaltered (Type 4), the measured sulfur contents decrease. An exemption is Type 3 surfaces where we observe two distinct clusters, one with low S-values and one with extraordinarily high S-values.

An exception from this systematic are sulfur contents of the Type 3 surface. Here we observe two distinct clusters, one with values below 0.5% and one with extraordinarily high sulfur contents of 12 to >60%, both showing a similar surface coloration. All Type 3 samples with high sulfur contents are exclusively taken from LTZ. This strong discrepancy of sulfur content and surface coloration within the low-temperature zones suggests next to alteration gradients also surficial or shallow processes of mineral deposition and formation of sulfur-rich encrustations that form sealed surfaces, especially in the near field of fumaroles. The low temperatures observed within LTZ and the limited surface degassing highlight the efficiency of such sealing processes. So far we can not distinguish LTZ from Type 3 surfaces in our

optical data (Figure 4.8). A distinction, however, would be beneficial as it would provide a method allowing for the precise spatial constraint of sealed surfaces from simple UAS-derived RGB imagery.

The intensity of optical and thermal effects and associated changes in mineralogical or chemical composition or degassing are not always equally significant. Although the general shift from unaltered surface to altered surface (ALTZ-boundary, shift reddish to gray) is a major criterion for the identification of degassing and alteration extent in our data, the associated changes in compositions are minor (Figure 4.9).

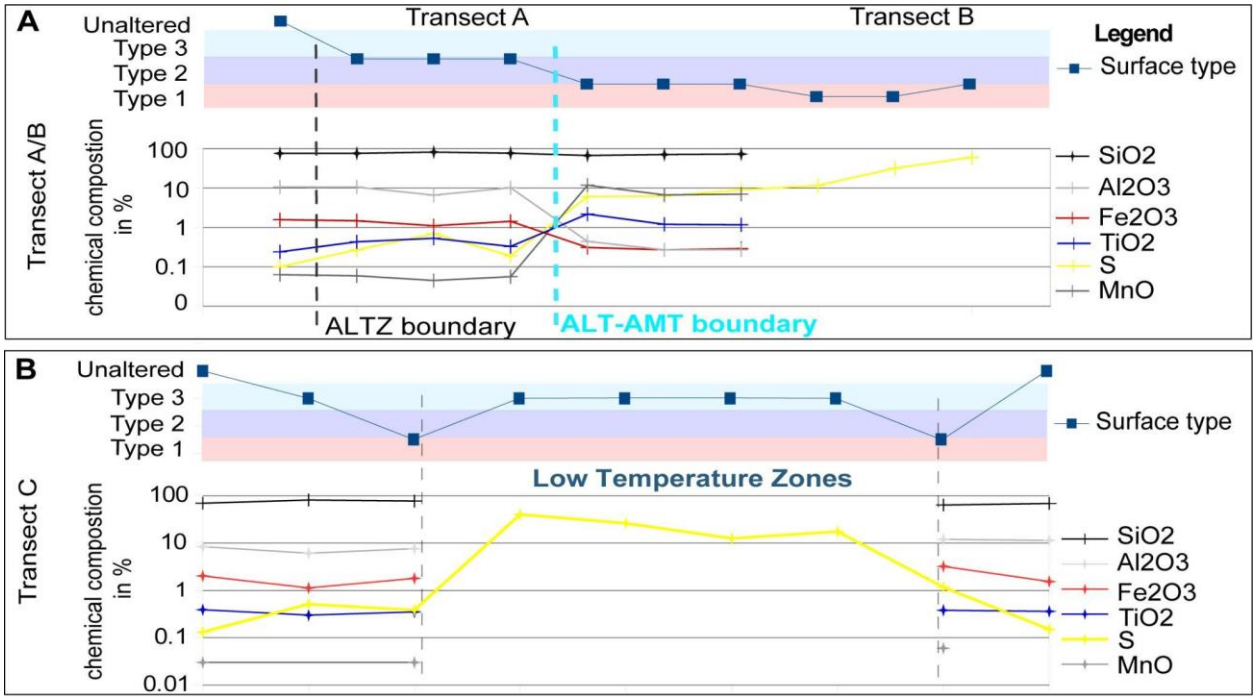

Figure 4.9 Geochemical changes observed along transect A-C. A) With increasing alteration from Type 4 to Type 1 surface we observe a reduction of Fe_2O_3 and Al_2O_3 and an increase in S. Strongest changes are observed at the ALT-AMT boundary. B) Changes observed in the eastern fumarole field are less significant, with the exception of extraordinarily high sulfur content for Type 3 samples, which represent the LTZ.

The larger changes are observed within the ALTZ at the ALT-AMT boundary. Here we observe a sudden decrease in the initial mineral and bulk geochemical composition and equally increasing sulfur content. We interpret the rather low changes at the transition from unaltered to altered at the ALTZ boundary to be related to rather weak or surficial alteration effects. The size of obtained samples was on the order of ~2000 cm² including the surficial part but also material up to 10 cm depth. This way it was not possible to trace mineralogical or geochemical

changes at the surface only. The samples obtained at the ALT-AMT boundary, on the other hand, show strong changes and reveal the general systematics of alteration effects, especially those samples taken in unit c, which might be considered one of the strongest alteration end members of the central crater region.

4.5.3 Heat budget - evidence for diffuse activity and surface sealing

Based on the gained information we outlined the surface structure of the degassing and alteration system of Vulcano (simplified in Figure 4.10 and detailed views of the different alteration and thermal units in Appendix A4.3) and constrained major diffuse active units besides the HTF. To quantify their importance for the degassing and alteration system, we weigh them based on a comparison of their thermal energy release (Figure 4.10) for both, the contribution of anomalies with T>22 °C, and identified units based on a spatial constraint, also including values >22 °C.

High-temperature fumaroles of the upper fumarole field have high average radiant exitance values of 82 W/m² but can only account for 28 % of the total emitted thermal energy (calculations based on pixels with T > 22 °C and a corrected background of T = 16.71 °C). The rest of the thermal energy is released by the diffuse features described above. Next to the HTF, multiple larger anomaly units have apparent structural importance for the degassing system. This becomes evident when analyzing the different units for their thermal energy release (Figure 4.10).

The second important unit is unit c. It has the second-highest average radiant exitance of 76 W/m² but exceeds the cumulative radiant flux of HTF with a contribution to the total thermal radiation of 29 %. Although it is a highly altered complex with a strongly bleached surface and increased surface temperatures there is a discrepancy to the current degassing activity. Relative gas flux values measured within unit c are lower than observed for units a and b, for instance. This might be a consequence of the dynamics of hydrothermal alteration and indicate permeability reduction or sealing processes due to the advanced state of alteration like proposed by Heap et al., 2019. This would be supported by a strong variability in mineralogical and bulk geochemical composition and associated remineralization or mineral precipitation observed in unit c.

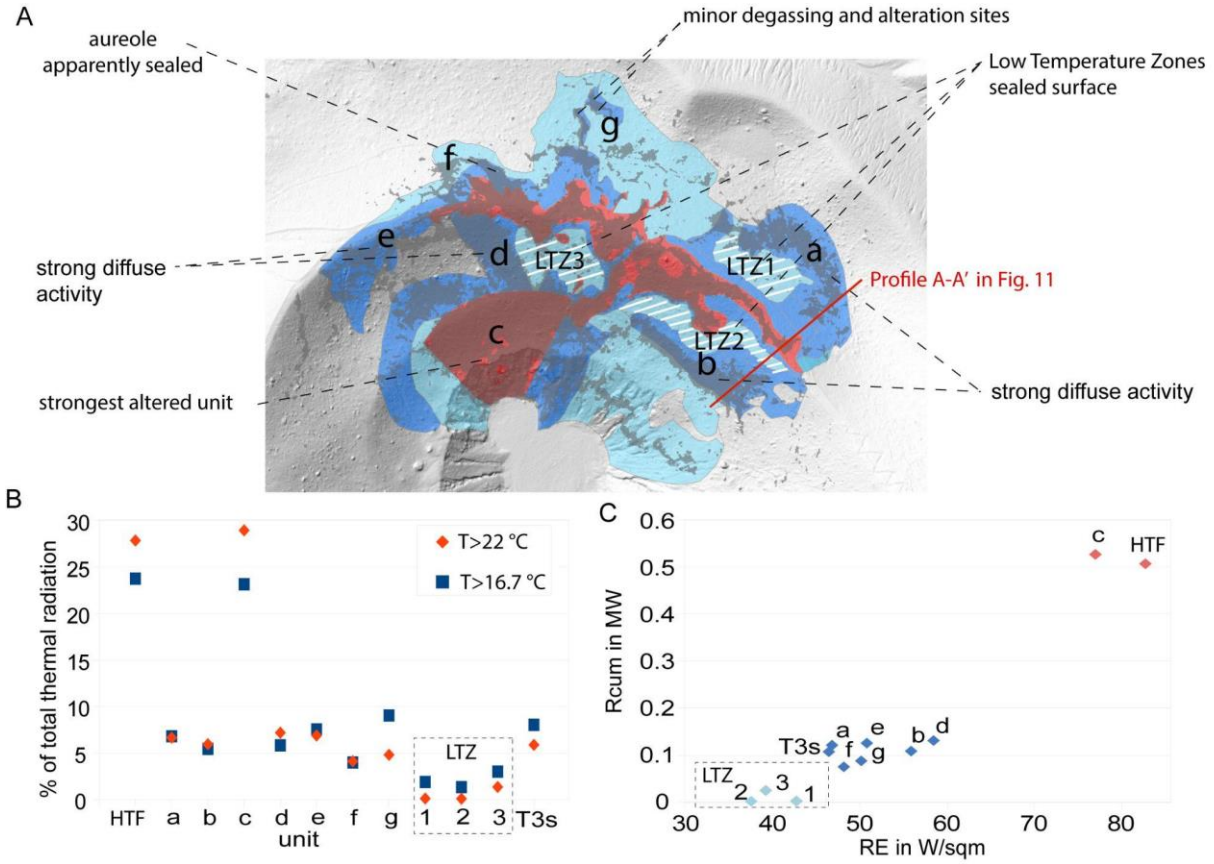

Figure 4.10 Anatomy of the fumarole field. A) Simplified structure of the fumarole field highlighting surface types and structural units of increased diffuse activity or apparent surface sealing (LTZ marked by white lines). B) Contribution in % to the total radiation for anomalies with T>22 °C and for identified units based on a spatial constraint, also including temperatures <22 °C. C) Radiant exitance (RE) in W/m² and cumulative radiation (Rcum) in MW. Note that for Rcum and contribution to the total thermal radiation only anomalies with T>22 °C were used.

Diffuse aureoles (unit a/b) on the eastern side of the fumarole cover several thousand m² each, more than the area covered by HTF, and contribute with 6 to 7 %, or about 25 % of the energy emitted by the HTF each, to the total thermal energy release. Additionally, the bleached surface, increased surface temperatures (Figure 4.4), and higher gas flow values (Figure 4.6E-G) highlight their importance for the surficial gas-drainage capability.

Unit d and e are large diffuse features of the western fumarole field of which d is a part of the thermal aureole surrounding F0 and e a ~200m long branched anomaly, located rim parallel west of F0. Both have a similar contribution to the total thermal energy release than a and b. Unit d is separated from F0 by a low-temperature zone (LTZ3). The transition from LTZ 3 to unit d is sudden and accompanied by a temperature jump of ~20 °C. The difference in the average temperature between unit d and LTZ3 is on the order of 5 °C. Also here we observe

apparent surface sealing for the whole central fumarole field. Unit f, the northern section of the F0 aureole, and anomalies in the area north of the fumarole field (g) have a minor contribution. LTZ1-3 separating diffuse aureoles from the HTF have a Type 3 surface coloration, significantly lower temperatures, and radiant flux and exitance values than the neighboring aureole regions, which indicates processes of surface sealing. Indeed, no gas flux could not be constrained for the LTZ of the eastern fumarole field. From field observations and lab analyses (Figure 4.7), we constrained the LTZ as strong, sulfur-rich surface complexes which are apparently effectively sealing the surface and inhibiting gas flow. The depth of these sealed complexes can not be constrained by our data, but we can roughly constrain the spatial extent. Considering only the 3 LTZ of the central and eastern fumarole field they together cover at least an area of ~12000 m², which is a significant fraction of the ALTZ. In other words, ~ 20 % of the surface of the ALTZ is apparently sealed and forces lateral gas flow to the aureole regions. This was proven by observations during the 2021 volcanic crisis at La Fossa. While at fumarole sites and diffuse active units like units a and b showed increasing mean temperatures and thermal energy release, the radiation within LTZ remained stable and low highlighting the efficiency of sealing processes. This was observed for all central LTZ and is exemplarily demonstrated by a cross-section through the eastern fumarole field section (Figure 4.11D).

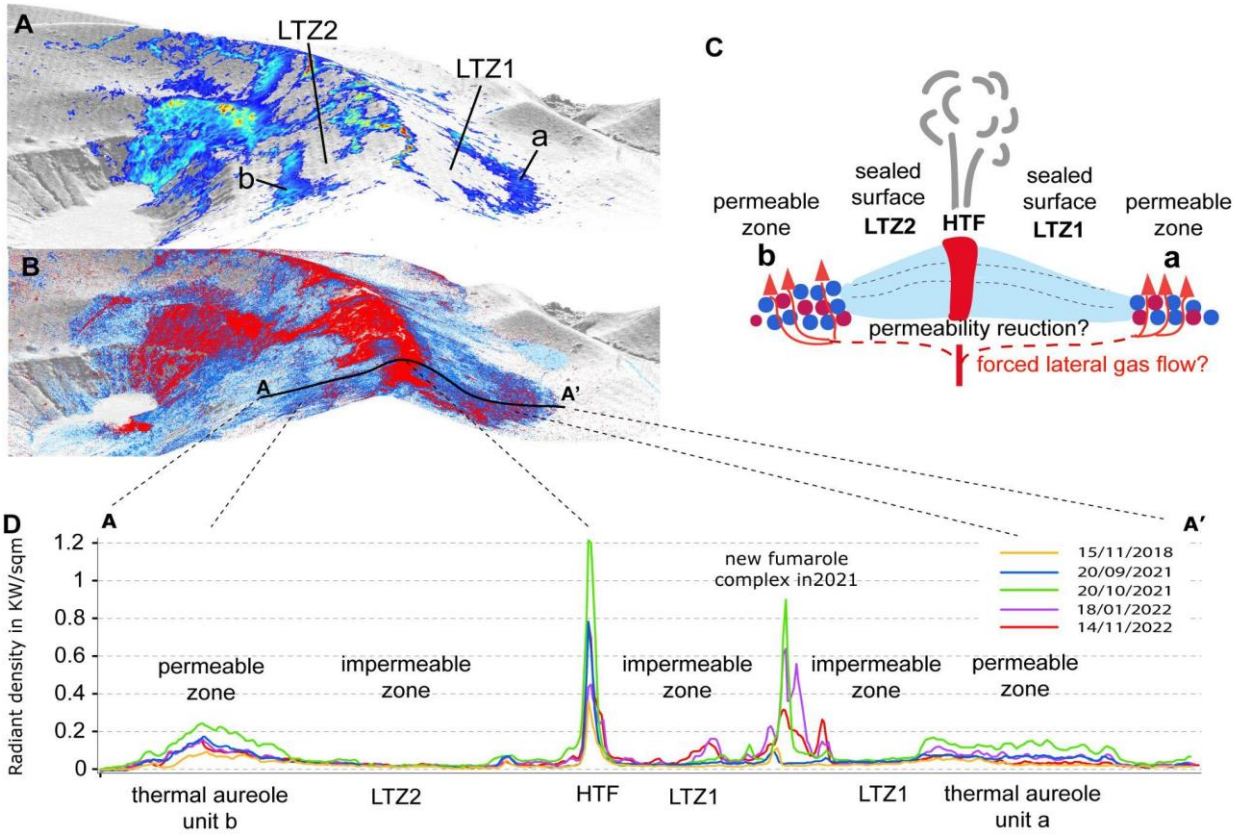

Figure 4.11 Cross Section of the eastern fumarole field along Profile A-A' (Fig. 4.10) highlighting the structural setup from high-temperature fumaroles in the center to LTZ and diffuse aureoles at a distance. A) Thermal structure along the cross-section. B) Alteration structure along the cross-section. C) Schematic sketch along cross-section A-A', highlighting the central LTZ that might be controlled by surface sealing processes or deeper effects of permeability reduction in the vicinity to the high-temperature fumaroles due to long-term gas-rock interaction and alteration processes. D) Evolution of thermal radiation values during a volcanic crisis. While thermal radiation at fumaroles and aureoles increased, radiation values of LTZ remain unchanged, therefore highlighting the efficiency of surface sealing.

4.6 Conclusion

Our investigation of the fumarole field of La Fossa cone allowed us to constrain the degassing and alteration structure, define major units of activity and quantify their importance for the degassing system, highlighting in particular large diffuse degassing areas and localized surface sealing. Our experience from the study of the degassing and alteration system at Vulcano demonstrates that close-range remote sensing studies can greatly contribute to the understanding of structural architecture or intrinsic complexities of fumarole fields. Such studies will prove beneficial for pre-site reconnaissance surveys, the detection of sampling locations for alteration-related studies and sampling grid design, and, importantly, for regular routine monitoring of hazardous volcanic crater areas and associated risk assessment.

4.7 Author contributions

D.M conceptualized the study, collected data, performed the remote sensing and gas analysis, and led the manuscript writing. T.R.W. provided funding, supported the conceptualization, and supervised the writing. V.T. supported the conceptualization, initiated and interpreted the XRD analysis, and supervised the writing. J.S. performed XRF analysis and supported the writing. A.K. performed XRD analysis and supported the writing. E.D.P. collected data and samples, supported all field works and the writing of this manuscript. A.F.P. supported fieldwork and on the ground logistics, acquired data, and supported the writing. M.Z. supported the gas measurement campaign and supported the writing. B.D.J. supported the fieldwork and writing of this manuscript.

4.8 Acknowledgments

We are grateful for the financial and material support provided to realize this study. This work is contributing to the focus cite Etna and was financially supported by GFZ Potsdam. Financial support to realize this study was also provided by DAAD research grant Nr. 57556282. We thank INGV Palermo for collaboration and their support especially during the 2021 crisis, without parts of this study could not have been realized. Further, we want to acknowledge the Swedish Research Council.

Chapter 5

Summary and discussion of the works

5.1 Thesis summary

In this thesis, I have outlined and applied appropriate UAS-based photogrammetric methods, image, and spatial analysis techniques, and in situ measurements to analyze surficial volcanic hydrothermal systems. The goals of this work were to better understand structures, processes, and process dynamics associated with volcanic hydrothermal systems, to evaluate how much such studies can contribute to a gain of knowledge and a better understanding of these systems, and to develop new conceptual models of structures, processes, and dynamics associated with such hydrothermal systems. With a resolution an order of magnitude higher than the best optical satellite data, one can achieve an unprecedented level of detail, opening a window to structures and processes that were previously invisible.

Photogrammetric datasets have been obtained for a fluid-dominated system, the El Tatio geyser field in Chile, and for the active degassing system of the La Fossa cone on the island of Vulcano (Italy). Both provide a high-resolution database that allows the analysis of structures, topologies, or spatial and temporal dynamics of processes associated with degassing or discharging activity of volcanic hydrothermal systems in unprecedented detail. As this is a relatively new field of remote sensing, established analytical approaches for accessing and extraction of information largely have to be developed. I have used a combination of image analysis and statistical and spatial analysis approaches to identify structures associated with hydrothermal activity, to analyze topologies, clustering, and orientations of objects and object clusters, to identify potential controls, but also to identify processes that indicate the temporal evolution of such systems, some of which highlighting potentially critical developments. The strength of this work is the deep exploration of secondary information hidden in the data. Although the two systems studied are among the most studied of their kind, we have been able to contribute new insights that lead to a better understanding of these particular systems, which have implications for similar systems elsewhere. We were able to answer some of the research questions posed, but we also point out new aspects that should be studied in more detail. Studies like the one presented here have implications for many scientific fields, but especially for alteration research and thermal monitoring, or monitoring of volcanic degassing.

5.2 Outcomes in the context of the posed research questions

This dissertation demonstrates different approaches to make the most out of UAS-based imagery and provides several geoscientific advances related to the study of structures and dynamics of hydrothermal volcanic systems. These advances are summarized below, addressing the research questions posed and highlighting potential applications of the presented methods and results for a future perspective.

5.2.1 What can we learn from high-resolution studies about specific structural arrangements, controls, and process dynamics of volcanic hydrothermal systems and how much do these insights contribute to the existing state of knowledge for the respective system?

Volcanic hydrothermal systems are expressions of volcanic activity and their existence is generally dependent on heat, fluid supply, and a fracture or pore system that provides pathways for circulating and ascending fluids. They are thought to develop under specific conditions and are usually structurally controlled. However, when looking at different scales other controls may become more relevant for the particular system.

We have analyzed high-resolution data with feature detection thresholds of centimeters. Using image analysis techniques, as well as secondary information derived from statistical-, spatial-, distribution-, and orientation analyses of objects associated with hydrothermal activity, we show that a variety of factors contribute to specific structural setups in addition to the primary structural control. The identified controls range from secondary geologic processes, hydrologic influence, and local variability of fluid supply, to secondary processes associated with the discharge and degassing activity itself, such as hydrothermal alteration, mineral precipitation, and formation of silica- or sulfur crusts, but also permeability reduction or local surface sealing. We will discuss these based on the results of our studies and place them in the context of current knowledge of the respective system.

Previous studies at El Tatio have shown that the thermal waters are likely to be heated in the laguna colorada complex and then propagate over tens of kilometers along deeper aquifers into the Tatio basin, ascending along fracture and fault systems (Healy and Hochstein, 1973; Lahsen, 1976; Giggenbach, 1978; Lucchi et al., 2009; Montecinos-Quadros et al., 2021). El Tatio, therefore, is thought to be structurally controlled and associated with two major fault

systems that provide pathways for thermal water to rise but also act as a boundary for further lateral migration. Statistical analysis of our hydrothermal object mapping database (Chapter 2) showed that the majority of objects are densely clustered along an elongated NE-SW striking belt at the northern boundary of El Tatio, consistent with the hypothesized location of a local fault that constrains the Tatio basin to the north (Lahsen, 1976; Lucchi et al., 2009; Montecinos-Quadros et al., 2021). However, the high degree of organization of vent arrangements at local scales implies a more complex control than a single fault. Vent arrangements along lineaments or intersecting lineaments of two preferred orientations indicate the influence of a pre-existing fracture pattern. Indeed, a sheared bedrock formation on the northern margin of El Tatio that resembles similar main azimuths suggests a pre-existing pattern that influences the local vent arrangements. Evidence for additional hydrological controls is provided by the organization of vent types, such as hot springs, geysers, moderately temperate springs, and mud ponds, which occur clustered in spatially distinct areas, following an apparent transition of activity within the basin from east to west and also with elevation. Different regimes of thermal waters from high-chloride to more moderate waters due to mixing with shallow meteoric or colder groundwater bodies have been stated earlier by Giggenbach (1978) or Cortecci et al (2005). In our data, we can trace them thermally, but also by colors of stream flows caused by local abundances of thermophilic microbial mats similar to Dunckel et al. (2009) and by the abundance of vegetation, which is absent in high chloride water areas but can be found associated with moderate temperate waters. Such systematics have not yet been resolved for El Tatio. While such insights into fluid-dominated systems are primarily of interest for prospecting and exploitation purposes or for chemical monitoring of fluids, details of degassing systems have a different relevance.

Similar to geyser fields, fumaroles often appear clustered or oriented, apparently controlled by the structural architecture of a volcano (Hutchison et al., 2015) at a larger scale, or by prominent faults, fracture zones, or lithologies (Schöpa et al., 2011; Walter et al., 2020) at the smaller scale.

We have analyzed the locations and orientations of high-temperature pixels and sulfur deposits (representative of fumarole vents) and show several preferred orientations that are aligned in the dominant NW-SE orientations, similar to the local tectonic trend, but also a perpendicular NE-SW trend, a rim-parallel trend, and a radial trend from the central craters. However, such structural trends cannot account for all the observations made. Large areas show a significant influence of diffuse degassing, exceeding the areas covered by high-temperature fumaroles

multiple times. We could constrain this to be related to an increased diffuse flux of acidic gas species such as H_2S and SO_2, that are apparently spatially stronger confined than the CO_2 flux. Further, we could constrain multiple centers of diffuse activity clustering to spatially confined units. Large areas of diffuse activity, separated from the major vent systems by low-temperature zones for instance, indicate the influence of secondary processes associated with degassing and alteration, and may indicate changes in permeability, surface sealing and forced lateral gas migration. Such observations are particularly valuable and one of the most important results of our studies, as they allow us to indicate processes of a spatiotemporal evolution from a remote sensing perspective. Such processes could otherwise only be constrained by extensive laboratory analysis. Approaches for the monitoring of alteration and spatially constraining sealing processes on a pixel base would be extremely valuable, as those are important aspects for risk assessment in volcanic degassing systems.

.

5.2.2 How can we detect and track degassing and hydrothermal alteration effects of volcanic degassing systems?

A common approach in remote sensing when tackling a new problem, for which there are no established analysis workflows available yet, is to perform anomaly detection, analysis, and validation of observed anomalies by ground-truthing. Anomalies in optical data primarily mean that we observe contrasts, in temperature, brightness, or coloration/spectral reflectance. In natural systems, such contrasts are often synonymous with material contrasts, different chemical or mineralogical contents, but potentially also different key physical parameters. Therefore the detection, analysis, and validation of anomalies have potentially broad implications for structural studies, the identification of surface processes, or also potentially hazardous developments in natural systems.

For example, volcanic degassing often leads to changes in the optical and spectral reflectance properties of the volcanic material, due to multiple fluid-rock interactions in the affected volcanic rock (Pirajno, 2009; Chiodini et al., 2013; Fulignati, 2020) that can cause mineral dissolution, leaching or remineralization. The importance of a better understanding of the extent and strength of alteration effects, or monitoring of degassing and alteration systems, is fundamentally explained by the effects of alteration on the chemical and physical parameters of the affected rock, such as mechanical weakening, reduced compressive rock strength or reduced permeabilities and sealing of gas pathways (Heap et al., 2019; Julia et al., 2014;

Darmawan et al., 2022) that have potentially far-reaching consequences for the stability of the volcanic building (Reid & Brien, 2001; Heap et al., 2019; Heap & Violay, 2021).

Research on hydrothermal alteration is typically conducted using satellite remote sensing or in situ, based on mineralogical, geochemical, isotope, or rock mechanical analyses (Donoghue et al., 2008; Berg et al., 2018; Heap et al., 2019; Daramawan et al., 2022). However, all methods have their limitations. Satellite-based analysis is useful for detecting larger alteration provinces, but often cannot resolve local hydrothermal systems at the scales typically observed at volcanoes. In turn, in situ measurements of physical or chemical parameters can only be obtained at discrete points. But working on the ground on volcanoes and facing degassing or alteration complexes covering several tens of thousands of square meters can obscure our view of the systematics and characteristics of such systems. Furthermore, it is difficult to infer the broader context of a volcanic building from a point measurement.

Here UAS-based remote sensing studies such as presented by Müller et al. (2021, 2023) unfold their potential for studying volcanic degassing and alteration systems. The problem of a poorly colored volcanic surface is overcome by approaching the data with iterative Principal Component Analysis (PCA) and variance-based data fractionation. By applying PCA on the original orthomosaic data, we create variance representations that can be used to distinguish data fractions of interest, and to extract them based on a single band raster mask (single principal component) from the original data. This dimensionality reduction is one of the benefits of PCA, providing good data separability. By performing iterative PCA on the extracted raster, PCA adapts to the new, reduced spectral range and allows a more sensitive image analysis.

This allowed us to resolve the general pattern of hydrothermal alteration, outline a zone of hydrothermal alteration influence, termed the diffuse flux zone by Manini et al. (2019), and to define alteration gradients within this zone but also larger structural units, such as areas of diffuse degassing or sealed surfaces. The remote sensing approach presented here is particularly valuable as it allows for the detection, analysis, and spatial constraint of any anomalous feature in a raster dataset. The combination of optical and thermal data, and measurements of the diffuse degassing surface is particularly beneficial as it resolves both, the alteration structure and the structure of present-day thermal anomalies. These results therefore allow us to distinguish the present-day activity from the long-term evolution of alteration effects. Discrepancies observed between the thermal, degassing, and alteration patterns may be

particularly interesting as they potentially indicate secondary effects of the spatiotemporal evolution, such as permeability changes or surface sealing.

The results of such studies are accurate and complete because the detection of anomalies is pixel-based, from analysis of rasters with tens or hundreds of millions of pixels. This allows us to approach alteration processes even in heterogeneous surfaces, where we observe mixing of unaltered and altered surfaces, and quantify them based on pixel density, for example. A ground-truthing that follows the anomaly detection, which may include bulk chemical or mineralogical compositions, mechanical tests of rock physical parameters such as strength or porosity, or isotope analyses, for instance, verifies that observed anomalies are meaningful, but in turn, can also be used to start parameterizing observed units to infer properties of sample point locations to the broader context.

The presented combination of methods and analyses provides a comprehensive approach to resolving detailed structures of degassing and alteration systems. The presented studies contribute to the advances in the analysis of UAS-derived image data and show efficient approaches for the detection and analysis of hydrothermal alteration structures and dynamics. The work further reveals new insights into the degassing and alteration structure of the La Fossa degassing system and provide the to date most detailed and complete anatomy of the surficial degassing system with implications for alteration research and monitoring of volcanic degassing. The methods presented can be applied for any anomaly detection or on volcanic hydrothermal systems elsewhere.

5.2.3 How can UAS-based studies contribute to the monitoring of degassing and alteration on volcanoes?

Studies such as those presented in this thesis are in first order good first-site investigations. They come with the advantages of centimeter-scale resolution while allowing for complete coverage of a surficial hydrothermal system and provide great advancements for resolving structures and dynamics observable at the surface. Although both case studies analyzed by us belong to the most studied systems of their kind, we were able to resolve and add various new insights into often intriguing systematics and contribute to a better understanding of the structures and dynamics of these systems.

One of the most important applications of such studies will therefore be to support and guide related research on hydrothermal systems. The range of applications is broad, from resolving

structural complexities to recommendations on where to place permanent monitoring equipment, assisting in the identification of sample locations, or even improving the design of sampling grids, and perhaps most importantly, identifying potentially hazardous developments by indicating hidden processes that could otherwise only be revealed by extensive lab analysis. Some of these applications are discussed in more detail below.

5.2.3.1 Relevance for alteration studies

The identification and classification of hydrothermal alteration gradients at local degassing sites from a remote sensing perspective is a valuable step towards a better understanding of a degassing and alteration system. Providing a database with a detailed surface structure of such a system, including its various components, alteration gradients, and their spatial extent allows for a focused probing, lab analysis, and parameterization of such units, but also to extrapolate results of such analyses to their real spatial extent. The high resolution of the data hereby is a boost for the degree of detail and complexity that can be accessed and studied.

In our study, the parameterization has been done by analysis of the mineralogical and bulk chemical composition, also used for ground truthing. A logical next step would be the parameterization by physical properties such as compressive rock strength or permeability measurements, as these are parameters that become relevant in terms of the hazard potential of degassing and alteration systems (Donoghue et al., 2008, 2010; Berg et al., 2018; Heap et al., 2019; Darmawan et al., 2022). The relevance of such observations may vary from case to case. For example, while changes of compressive strength in a center crater fumarole system may not be of primary importance, the detection of degassing and alteration-related anomalies outlining blocks on steep parts of a volcanic building for instance (observed by us at other study locations, but not shown here) is indeed of great importance, as they indicate potential material contrasts that could favor the generation of slip planes by alteration-related weakening effects (Heap et al., 2019). Having a toolset that allows us to identify potential zones of alteration-related rock weakening and potential slip planes from a remote sensing perspective, and being able to distinguish them from other fracturing or faulting mechanisms, would be of great benefit and greatly contribute to future risk assessment.

Another important aspect resulting from the combined analysis of optical and thermal anomaly patterns is the indication of potential sealing processes (Heap et al., 2019; Gertisser et al., 2023). Such sealing effects may be of particular importance to small island volcanoes, with a

complex composite crater structure and major fault systems, prone to phreatic or phreatomagmatic activity. Vulcano could be such a case, hosting a major degassing fumarole field in the vicinity of a very steep altered flank, embedded in older crater structures acting as lithological boundaries, spatially predetermining and limiting possibilities for lateral gas flow in case of significant surface sealing. We observed a generally good correspondence between optical and thermal anomalies in our data but there are also discrepancies that may be interesting to focus on. The optical (RGB) anomaly pattern in first order represents the alteration surface, created by processes during a long-term evolution, and therefore resembles the historical activity pattern to some extent. The thermal anomaly pattern, in turn, shows the actual state of degassing activity, so the present-day activity pattern. In the presented studies, it is shown that some of the thermal features are apparently shifted with respect to optical anomalies. This could indicate an ongoing spatiotemporal evolution of the system and, in this particular case, potentially a reduction of permeability, or sealing processes that force the gases to lateral migration. And indeed we show that significant parts of the central fumarole field are sealed. Although to a degree speculative at this point, this can now be further evaluated in an upcoming study. However, being able to indicate and spatially constrain such processes from a remote sensing perspective is one of the greatest strengths of the used approaches, because the only other way to constrain them would be through extensive lab analysis.

5.2.3.2 Relevance for thermal monitoring

Satellite-based thermal monitoring of volcanoes can signal volcanic unrest (e.g. Coppola et al., 2020; Massimetti et al., 2020; Girona et al., 2021), but has limitations. Due to sensor- and obtained ground resolutions, or temporal resolutions of acquisitions “there is currently no operative satellite hot spot detection system capable of automatic daily monitoring of a fumarole field”, as stated by Coppola et al. (2022). Furthermore, the common infrared bands of satellites can also be limiting factors. VRP (volcanic radiant power) for instance, often used for temporal monitoring (Coppola et al., 2022) measures the radiant power using the mid-infrared spectral radiance, a spectral range suitable for high-temperature thermal anomalies. However, it may underestimate the "total radiant power” of fumarole fields, mainly because it fails to measure the radiation emitted by a large part of the crater at temperatures slightly higher than the background (Coppola et al., 2022), emitted by diffuse degassing for instance. Indeed the VRP measured by VIIRS (Visible Infrared Imaging Radiometer Suite) at Vulcano (Coppola

et al., 2022) correlates well with the vent flux zone constrained by Manini et al. (2019), which coincides with the central high-temperature fumarole field.

In situ temperature monitoring, on the other site, provides long-term time series with precise temperature estimates but only at a few selected discrete point locations. In this way, absolute changes in the gas temperature can be tracked (Diliberto 2011, 2013, 2017), but changes in the spatial domain can not be assessed.

UAS-based studies with thermal infrared sensors can fill this gap and contribute in two ways. On one side we can detect changes at a high resolution in the thermal and the spatial domain. On the other hand, using the thermal infrared band 8-13 µm allows us to also consider low temperatures, and, in combination with the high resolution, to detect and precisely constrain also diffuse degassing effects. In our works, we analyzed thermal data, defined distinct active units based on spatial or thermal thresholds, and evaluated their contributions to the total thermal energy release, showing that diffuse activity indeed can significantly contribute to the total thermal energy release. Further, data acquired during a volcanic crisis showed that next to increasing fumarole radiations also thermal radiations in the diffuse regime respond to increased gas flux (publication on the volcanic crisis 2021 in preparation but not part of this dissertation). This opens up new possibilities for in situ monitoring approaches, moving away from the precise but also expensive and fragile high-temperature fumarole monitoring, but also towards a more comprehensive monitoring network including the diffuse activity, which is an important but underestimated part of the degassing system.

Chapter 6

Conclusion and future perspective

The work summarized in this thesis has demonstrated the great potential of UAS-based high-resolution imaging and photogrammetric processing for the analysis of volcanic hydrothermal systems at the surface. The high resolution of such data opens up a new perspective on the structures, processes, and dynamics that can be observed at the surface, in many cases revealing what was previously invisible. It allows the identification and monitoring of processes from a remote sensing perspective at a detail that could otherwise only be realized on the ground. It is now possible to detect and analyze features at centimeter scales and reveal secondary information from object topologies, density distributions, and orientations but also vent type or discharge peculiarities. Such information is valuable and allows one to analyze structures and processes from a much denser database but also a different scale. It provides a unique link between the completeness of observations from satellites and the detail of observations from the ground.

Results of this work provide detailed structural makeups of both studied systems and reveal information that goes far beyond the actual state of knowledge, allowing the inference of interesting aspects about their structural controls over scales. The revealed controls range from local tectonic controls, to the dominance of secondary fault or fracture patterns, spatiotemporal dynamics, such as sealing due to permeability changes or surficial mineral precipitation, to hydrogeological controls due to a potentially varying fluid supply or mixing with meteoric groundwater.

This broad range of observations over scales shows the real potential of such studies and also possible fields for contributions from structural geology over analyses of local stress fields or subsurface structures, monitoring of spatiotemporal evolution of hydrothermal systems, up to hydrogeological studies, and prospection or volcano activity monitoring. In the first order, studies as performed in this thesis are the best site investigation tools and will be applied more widely in the future.

A particular focus of such future studies may be the study of hydrothermal alteration and the monitoring of degassing activity at volcanoes. The possibility to detect, spatially constrain, and monitor areas affected by localized stronger acid gas flow from anomalies in optical data is valuable because it can help to identify and assess hazard potentials, for instance by indicating possible slip planes, in case of anomalies outlining blocks at steep flanks. In any case, such

studies can guide us to conduct sampling campaigns and risk assessment in the right spots, by providing a complete picture of the extent of alteration units but also highlighting different alteration gradients or alteration end members. The studies in this thesis provide a starting point and more similar studies will likely be carried out. This will hopefully lead to a broader database of optical effects of alteration at different volcanic systems, but also to linking of relevant rock-physical parameters to observed anomalies, so that an operative stage can be reached where relevant stability parameters can be assessed from UAS surveys. Monitoring would further be aided by incorporating UAS-based infrared approaches into volcano activity monitoring. These can greatly contribute to resolving changes in both the thermal and spatial domains, including effects of the diffuse degassing regime that can contribute to 50% or more to the total degassing activity as shown by our works. Further, repeated UAs-based infrared surveys have the potential to resolve dynamics in the evolution of degassing systems during volcanic crises at high resolution and therefore indicate secondary processes like, for instance, reduced surface gas flow due to sealing processes.

7 References

Agisoft, L. L. C. (2016). Agisoft PhotoScan user manual: professional edition, Version 1.2. User Manuals, 97(346), 347.

Ai, L., Walter, T. R., Aguilera, F., Layana, S., Mania, R., Kujawa, C., ... & Inostroza, M. (2023). Crater morphology, nested ring structures, and temperature anomalies studied by unoccupied aircraft system data at Lascar volcano, northern Chile. Journal of Volcanology and Geothermal Research, 107840. https://doi.org/10.1016/j.jvolgeores.2023.107840

Aiuppa, A., Federico, C., Giudice, G., & Gurrieri, S. (2005). Chemical mapping of a fumarolic field: La Fossa crater, Vulcano Island (Aeolian Islands, Italy). Geophysical Research Letters, 32(13). https://doi.org/10.1029/2005GL023207

Armbrust, G. A., Arias, J., Lahsen, A., & Trujillo, P. (1974). Geochemistry of the hydrothermal alteration at El Tatio geothermal field, Chile. In Proc. IAVCEI Symp. Int. Volcanologia, Santiago, Chile.

Arnórsson, S., Thórhallsson, S., Stefánsson, A., 2015. Utilization of geothermal resources. The Encyclopedia of Volcanoes. Elsevier, pp. 1235–1252.

Arrighi, S., Tanguy, J.-C., Rosi, M., 2006a. Eruptions of the last 2200 years at Vulcano and Vulcanello (Aeolian Islands, Italy) dated by high-accuracy archeomagnetism. Phys. Earth Planet. Inter. 159 (3-4), 225–233. https://doi.org/10.1016/j.pepi.2006.07.010

Aubert, M., Diliberto, S., Finizola, A., Chebli, Y., 2008. Double origin of hydrothermal convective flux variations in the Fossa of Vulcano (Italy). B Volcanol 70 (6), 743–751. https://doi.org/10.1007/s00445-007-0165-y

Azzarini, F., Pareschi, M., Sbrana, A., Favalli, M., Fulignati, P., 2001. Surface hydrothermal alteration mapping at Vulcano Island using MIVIS data. Int. J. Remote Sens. 22 (11), 2045–2070. https://doi.org/10.1080/01431160118291

Ball, M., Pinkerton, H., 2006. Factors affecting the accuracy of thermal imaging cameras in volcanology. J. Geophys. Res. Solid Earth 111 (B11). https://doi.org/10.1029/2005JB003829

Barde-Cabusson, S., Finizola, A., Revil, A., Ricci, T., Piscitelli, S., Rizzo, E., Angeletti, B., Balaco, M., Bennati, L., Byrdina, S., Carzaniga, N., Crespy, A., Di Gangi, F., Morin, J., Perrone, A., Rossi, M., Roulleau, E., Suski, B., Villeneuve, N., 2009. New geological insights and structural control on fluid circulation in La Fossa cone (Vulcano, Aeolian Islands, Italy). J. Volcanol. Geotherm. Res. 185 (3), 231–245. https://doi.org/10.1016/j.jvolgeores.2009.06.002

Barreca, G., Bruno, V., Cultrera, F., Mattia, M., Monaco, C., & Scarfì, L. (2014). New insights in the geodynamics of the Lipari–Vulcano area (Aeolian Archipelago, southern Italy) from geological, geodetic and seismological data. Journal of Geodynamics, 82, 150-167. https://doi.org/10.1016/j.jog.2014.07.003

Baubron, J.C., Allard, P., Toutain, J.P., 1990. Diffuse volcanic emissions of carbon-dioxide

from Vulcano-Island, Italy. Nature 344 (6261), 51–53. https://doi.org/10.1038/344051a0

Beckhoff, B., Kanngießer, B., Langhoff, N., Wedell, R., & Wolff, H. (Eds.). (2007). Handbook of practical X-ray fluorescence analysis. Springer Science & Business Media. https://doi.org/10.1007/978-3-540-36722-2

Berg, S. E., Troll, V. R., Harris, C., Deegan, F. M., Riishuus, M. S., Burchardt, S., & Krumbholz, M. (2018). Exceptionally high whole-rock δ18O values in intra-caldera rhyolites from Northeast Iceland. Mineralogical Magazine, 82(5), 1147-1168. https://doi.org/10.1180/mgm.2018.114

Billi, Andrea, et al. Tectonics and seismicity of the Tindari Fault System, southern Italy: Crustal deformations at the transition between ongoing contractional and extensional domains located above the edge of a subducting slab. Tectonics, 2006, 25. Jg., Nr. 2. https://doi.org/10.1029/2004TC001763

Bitelli, G., Girelli, V. A., & Sammarini, G. (2018). 4-dimensional recording and visualization of urban archeological excavations. Applied Geomatics, 10(4), 415-426. https://doi.org/10.1007/s12518-018-0239-x

Bolognesi, L., & D'Amore, F. (1993). Isotopic variation of the hydrothermal system on Vulcano Island, Italy. Geochimica et Cosmochimica Acta, 57(9), 2069-2082. https://doi.org/10.1016/0016-7037(93)90094-D

Bolognesi, L., 1999. Comment on "Chemical features and isotopic composition of gaseous manifestations on Vulcano Island, Aeolian Islands, Italy: an interpretative model of fluid circulation". Geochim. Cosmochim. Acta 63 (16), 2467–2469. https://doi.org/10.1016/S0016-7037(97)00163-4

Bonaccorso, A., Bonforte, A., Gambino, S., 2010. Thermal expansion-contraction and slope instability of a fumarole field inferred from geodetic measurements at Vulcano. B Volcanol 72 (7), 791–801. https://doi.org/10.1007/s00445-010-0366-7

Boyce, A. J., Fulignati, P., Sbrana, A., & Fallick, A. E. (2007). Fluids in early stage hydrothermal alteration of high-sulfidation epithermal systems: A view from the Vulcano active hydrothermal system (Aeolian Island, Italy). Journal of Volcanology and Geothermal Research, 166(2), 76-90. https://doi.org/10.1016/j.jvolgeores.2007.07.005

Branca, S., De Beni, E., Chester, D., Duncan, A., & Lotteri, A. (2017). The 1928 eruption of Mount Etna (Italy): Reconstructing lava flow evolution and the destruction and recovery of the town of Mascali. Journal of Volcanology and Geothermal Research, 335, 54-70. https://doi.org/10.1016/j.jvolgeores.2017.02.002

Bukumirovic, T., Italiano, F., Nuccio, P.M., 1997. The evolution of a dynamic geological system: the support of a GIS for geochemical measurements at the fumarole field of Vulcano, Italy. J. Volcanol. Geotherm. Res. 79 (3–4), 253–263. https://doi.org/10.1016/S0377-0273(97)00032-2

Burrato, P., Mattia, M., Musumeci, C., Scarfi, L., 2017. Structural architecture and active deformation pattern in the northern sector of the Aeolian-Tindari-Letojanni fault system (SE Tyrrhenian Sea-NE Sicily) from integrated analysis of field, marine geophysical, seismological and geodetic data. Ital. J. Geosci. 136 (3), 399–417. https://doi.org/10.3301/IJG.2016.17

Capasso, G., Favara, R., Inguaggiato, S., 1997. Chemical features and isotopic composition of gaseous manifestations on Vulcano Island, Aeolian Islands, Italy: an interpretative model of fluid circulation. Geochim. Cosmochim. Acta 61, 3425–3440 https://doi.org/10.1016/S0016-7037(97)00163-4

Capasso, G., Favara, R., Francofonte, S., Inguaggiato, S., 1999. Chemical and isotopic variations in fumarolic discharge and thermal waters at Vulcano Island (Aeolian Islands, Italy) during 1996: evidence of resumed volcanic activity. J. Volcanol. Geotherm. Res. 88 (3), 167–175.
https://doi.org/10.1016/S0377-0273(98)00111-5

Capasso, G., Favara, R., Inguaggiato, S., 2000. Interaction between fumarolic gases and thermal groundwaters at Vulcano Island (Italy): evidences from chemical composition of dissolved gases in waters. J. Volcanol. Geotherm. Res. 102 (3–4), 309–318. https://doi.org/10.1016/S0377-0273(00)00193-1

Capasso, G., Federico, C., Madonia, P., Paonita, A., 2014. Response of the shallow aquifer of the volcano-hydrothermal system during the recent crises at Vulcano Island (Aeolian Archipelago, Italy). J. Volcanol. Geotherm. Res. 273, 70–80. https://doi.org/10.1016/j.Jvolgeores.2014.01.005

Carapezza, M. L., & Granieri, D. (2004). CO2 soil flux at Vulcano (Italy): comparison between active and passive methods. Applied Geochemistry, 19(1), 73-88.
https://doi.org/10.1016/S0883-2927(03)00111-2

Carapezza, M.L., Barberi, F., Ranaldi, M., Ricci, T., Tarchini, L., Barrancos, J., Fischer, C., Perez, N., Weber, K., Di Piazza, A., Gattuso, A., 2011. Diffuse CO2 soil degassing and CO2 and H2S concentrations in air and related hazards at Vulcano Island (Aeolian arc, Italy). J. Volcanol. Geotherm. Res. 207 (3–4), 130–144. https://doi.org/10.1016/j.Jvolgeores.2011.06.010

Carranza, E. J. M., & Hale, M. (2002). Mineral imaging with Landsat Thematic Mapper data for hydrothermal alteration mapping in heavily vegetated terrane. International journal of remote sensing, 23(22), 4827-4852. https://doi.org/10.1080/01431160110115014

Carrivick, J. L., & Tweed, F. S. (2019). A review of glacier outburst floods in Iceland and Greenland with a megafloods perspective. Earth-Science Reviews, 196, 102876. https://doi.org/10.1016/j.earscirev.2019.102876

Chang, W. L., Smith, R. B., Wicks, C., Farrell, J. M., & Puskas, C. M. (2007). Accelerated uplift and magmatic intrusion of the Yellowstone caldera, 2004 to 2006. Science, 318(5852), 952-956. https://doi.org/10.1126/science.1146842

Clarke, A. B., Ongaro, T. E., & Belousov, A. (2015). Vulcanian eruptions. In The encyclopedia of volcanoes (pp. 505-518). Academic Press. https://doi.org/10.1016/B978-0-12-385938-9.00028-6

Cheynet, B., Dall'Aglio, M., Garavelli, A., Grasso, M., Vurro, F., 2000. Trace elements from fumaroles at Vulcano Island (Italy): rates of transport and a thermochemical model. J. Volcanol. Geotherm. Res. 95 (1–4), 273–283. https://doi.org/10.1016/S0377-0273(99)00122-5

Chiodini, G., Cioni, R., Marini, L., 1993. Reactions governing the chemistry of crater fuma roles from Vulcano-Island, Italy, and implications for volcanic surveillance. Appl. Geochem. 8 (4), 357–371. https://doi.org/10.1016/0883-2927(93)90004-Z

Chiodini, G., Cioni, R., Marini, L., & Panichi, C. (1995). Origin of the fumarolic fluids of Vulcano Island, Italy and implications for volcanic surveillance. Bulletin of Volcanology, 57, 99-110. https://doi.org/10.1007/BF00301400

Chiodini, G., Frondini, F., & Raco, B. (1996). Diffuse emission of CO 2 from the Fossa crater, Vulcano Island (Italy). Bulletin of Volcanology, 58, 41-50. https://doi.org/10.1007/s004450050124

Chiodini, G., Cioni, R., Guidi, M., Raco, B., & Marini, L. (1998). Soil CO2 flux measurements in volcanic and geothermal areas. Applied geochemistry, 13(5), 543-552. https://doi.org/10.1016/S0883-2927(97)00076-0

Chiodini, G., Allard, P., Caliro, S., Parello, F., 2000. 18O exchange between steam and carbon dioxide in volcanic and hydrothermal gases: Implications for the source of water. Geochim. Cosmochim. Acta 64, 2479–2488 https://doi.org/10.1016/S0016-7037(99)00445-7

Chiodini, G., Granieri, D., Avino, R., Caliro, S., Costa, A., & Werner, C. (2005). Carbon dioxide diffuse degassing and estimation of heat release from volcanic and hydrothermal systems. Journal of Geophysical Research: Solid Earth, 110(B8). https://doi.org/10.1029/2004JB003542

Coppola, D., Laiolo, M., Cigolini, C., Donne, D. D., & Ripepe, M. (2016). Enhanced volcanic hot-spot detection using MODIS IR data: results from the MIROVA system. Geological Society, London, Special Publications, 426(1), 181-205. https://doi.org/10.1144/SP426.5

Coppola, D., Laiolo, M., Cigolini, C., Massimetti, F., Delle Donne, D., Ripepe, M., ... & William, R. (2020). Thermal remote sensing for global volcano monitoring: experiences from the MIROVA system. Frontiers in Earth Science, 7, 362. https://doi.org/10.3389/feart.2019.00362

Coppola, D., Laiolo, M., Campus, A., & Massimetti, F. (2022). Thermal unrest of a fumarolic field tracked using VIIRS imaging bands: The case of La fossa crater (Vulcano Island, Italy). Frontiers in Earth Science, 10, 964372. https://doi.org/10.3389/feart.2022.964372

Cortecci, G., Boschetti, T., Mussi, M., Lameli, C. H., Mucchino, C., & Barbieri, M. (2005). New chemical and original isotopic data on waters from El Tatio geothermal field, northern Chile. Geochemical Journal, 39(6), 547-571. https://doi.org/10.2343/geochemj.39.547

Cultrera, F., Barreca, G., Ferranti, L., Monaco, C., Pepe, F., Passaro, S., Barberi, G., Bruno, V.,
Cucchiaro, S., Fallu, D. J., Zhao, P., Waddington, C., Cockcroft, D., Tarolli, P., & Brown, A. G. (2020). SfM photogrammetry for GeoArchaeology. In developments in earth surface processes (Vol. 23, pp. 183-205). Elsevier. https://doi.org/10.1016/B978-0-444-64177-9.00006-0

Cusicanqui, H. (1975). The geochemistry of the El Tatio geothermal field, Northern Chile. In Second United Nations Symposium on the Development and Utilization of Geothermal Resources, San Francisco, 1975 (p. 703).

Darmawan, H., Walter, T. R., Brotopuspito, K. S., & Nandaka, I. G. M. A. (2018). Morphological and structural changes at the Merapi lava dome monitored in 2012–15 using unmanned aerial vehicles (UAVs). Journal of Volcanology and Geothermal Research, 349, 256-267. https://doi.org/10.1016/j.jvolgeores.2017.11.006

Darmawan, H., Walter, T. R., Troll, V. R., & Budi-Santoso, A. (2018). Structural weakening of the Merapi dome identified by drone photogrammetry after the 2010 eruption. Natural hazards and earth system sciences, 18(12), 3267-3281. https://doi.org/10.5194/nhess-18-3267-2018

Darmawan, H., Troll, V. R., Walter, T. R., Deegan, F. M., Geiger, H., Heap, M. J., ... & Müller, D. (2022). Hidden mechanical weaknesses within lava domes provided by buried high-porosity hydrothermal alteration zones. Scientific Reports, 12(1), 3202. https://doi.org/10.1038/s41598-022-06765-9

De Astis, G., La Volpe, L., Peccerillo, A., Civetta, L., 1997. Volcanological and petrological evolution of Vulcano island (Aeolian Arc, southern Tyrrhenian Sea). J. Geophys. Res. Solid Earth 102 (B4), 8021–8050. https://doi.org/10.1029/96JB03735

De Astis, G., Lucchi, F., Dellino, P., La Volpe, L., Tranne, C., Frezzotti, M., Peccerillo, A., 2013. Geology, volcanic history and petrology of Vulcano (central Aeolian archipelago). Geol. Soc. Lond. Mem. 37 (1), 281–349. https://doi.org/10.1144/M37.11

De Silva, S. L. (1989). Altiplano-Puna volcanic complex of the central Andes. Geology, 17(12), 1102-1106. https://doi.org/10.1130/0091-7613(1989)017%3C1102:APVCOT%3E2.3.CO;2

Di Martino, R.M.R., Capasso, G., Camarda, M., 2016. Spatial domain analysis of carbon dioxide from soils on Vulcano Island: implications for CO2 output evaluation. Chem. Geol. 444, 59–70. https://doi.org/10.1016/j.chemgeo.2016.09.037

Di Tommaso, I., & Rubinstein, N. (2007). Hydrothermal alteration mapping using ASTER data in the Infiernillo porphyry deposit, Argentina. Ore Geology Reviews, 32(1-2), 275-290. https://doi.org/10.1016/j.oregeorev.2006.05.004

Di Traglia, F., Pistolesi, M., Rosi, M., Bonadonna, C., Fusillo, R., Roverato, M., 2013. Growth and erosion: the volcanic geology and morphological evolution of La Fossa (Island of Vulcano, Southern Italy) in the last 1000 years. Geomorphology 194, 94–107. https://doi.org/10.1016/j.geomorph.2013.04.018

Diliberto, I.S., 2011. Long-term variations of fumarole temperatures on Vulcano Island (Italy). Ann. Geophys. 54 (2), 175–185. https://doi.org/10.4401/ag-5183

Diliberto, I.S., 2013. Time series analysis of high temperature fumaroles monitored on the island of Vulcano (Aeolian Archipelago, Italy). J. Volcanol. Geotherm. Res. 264, 150–163. https://doi.org/10.1016/j.jvolgeores.2013.08.003

Diliberto, I.S., 2017. Long-term monitoring on a closed-conduit volcano: a 25 year long time-series of temperatures recorded at La Fossa cone (Vulcano Island, Italy), ranging from 250 degrees C to 520 degrees C. J. Volcanol. Geotherm. Res. 346, 151–160. https://doi.org/10.1016/j.jvolgeores.2017.03.005

Diliberto, I., Pedone, M., Jácome Paz, M., Inguaggiato, S., Mazot, A., Cangemi, M. and Pisciotta, A.F., 2021. Volcanic Gas Hazard Assessment in the Baia di Levante Area (Vulcano Island, Italy) Inferred by Geochemical Investigation of Passive Fluid Degassing. Environmental Geosciences, 11. https://doi.org/10.3390/geosciences11110478

Dulong, F. T., & Jackson, J. C. (1997). X-ray powder diffraction. US Geological Survey. https://doi.org/10.3133/70220360

Dunckel, A. E., Cardenas, M. B., Sawyer, A. H., & Bennett, P. C. (2009). High-resolution in-situ thermal imaging of microbial mats at El Tatio Geyser, Chile shows coupling between community color and temperature. Geophysical Research Letters, 36(23). https://doi.org/10.1029/2009GL041366

Donoghue, E., Troll, V. R., Harris, C., O'Halloran, A., Walter, T. R., & Torrado, F. J. P. (2008). Low-temperature hydrothermal alteration of intra-caldera tuffs, Miocene Tejeda caldera, Gran Canaria, Canary Islands. Journal of Volcanology and Geothermal Research, 176(4), 551-564. https://doi.org/10.1016/j.jvolgeores.2008.05.002

Donoghue, E., Troll, V. R., & Harris, C. (2010). Fluid–rock interaction in the Miocene, Post-Caldera, Tejeda intrusive complex, Gran Canaria (Canary Islands): insights from mineralogy, and O-and H-isotope geochemistry. Journal of Petrology, 51(10), 2149-2176. https://doi.org/10.1093/petrology/egq052

Doronzo, D. M., Di Vito, M. A., Arienzo, I., Bini, M., Calusi, B., Cerminara, M., ... & Zanchetta, G. (2022). The 79 CE eruption of Vesuvius: A lesson from the past and the need of a multidisciplinary approach for developments in volcanology. Earth-Science Reviews, 231, 104072. https://doi.org/10.1016/j.earscirev.2022.104072

Dzurisin, D., Wicks, C. W., & Poland, M. P. (1788). History of surface displacements at the Yellowstone Caldera, Wyoming, from leveling surveys and InSAR observations, 1923–2008. US geological survey professional paper, 1, 68.

Eibl, E. P., Müller, D., Walter, T. R., Allahbakhshi, M., Jousset, P., Hersir, G. P., & Dahm, T. (2021). Eruptive cycle and bubble trap of Strokkur geyser, Iceland. Journal of Geophysical Research: Solid Earth, 126(4), e2020JB020769. https://doi.org/10.1029/2020JB020769

Epp, J. (2016). X-ray diffraction (XRD) techniques for materials characterization. In Materials characterization using nondestructive evaluation (NDE) methods (pp. 81-124). Woodhead Publishing.
https://doi.org/10.1016/B978-0-08-100040-3.00004-3

Ester, M., Kriegel, H. P., Sander, J., & Xu, X. (1996, August). A density-based algorithm for discovering clusters in large spatial databases with noise. In kdd (Vol. 96, No. 34, pp. 226-231).

Fernandez-Turiel, J. L., Garcia-Valles, M., Gimeno-Torrente, D., Saavedra-Alonso, J., & Martinez-Manent, S. (2005). The hot spring and geyser sinters of El Tatio, Northern Chile. Sedimentary Geology, 180(3-4), 125-147. https://doi.org/10.1016/j.sedgeo.2005.07.005

Fischer, T. P., & Chiodini, G. (2015). Volcanic, magmatic and hydrothermal gases. In The encyclopedia of volcanoes (pp. 779-797). Academic Press.
https://doi.org/10.1016/B978-0-12-385938-9.00045-6

Fischer, T. P., Ramírez, C., Mora-Amador, R. A., Hilton, D. R., Barnes, J. D., Sharp, Z. D., ... & Shaw, A. M. (2015). Temporal variations in fumarole gas chemistry at Poás volcano, Costa Rica. Journal of Volcanology and Geothermal Research, 294, 56-70. https://doi.org/10.1016/j.jvolgeores.2015.02.002

Frazzetta, G., La Volpe, L., Sheridan, M.F., 1983. Evolution of the Fossa cone, Vulcano. J. Volcanol. Geotherm. Res. 17 (1–4), 329–360. https://doi.org/10.1016/0377-0273(83)90075-6

Friedman, G. M. (2007). Structurally controlled hydrothermal dolomite reservoir facies: An overview: Discussion. AAPG bulletin, 91(9), 1339-1341. https://doi.org/10.1306/04300706142

Fulignati, P., Gioncada, A., & Sbrana, A. (1998). Geologic model of the magmatic-hydrothermal system of vulcano (Aeolian Islands, Italy). Mineralogy and Petrology, 62(3-4), 195.

Fulignati, P., Gioncada, A., & Sbrana, A. (1999). Rare-earth element (REE) behaviour in the alteration facies of the active magmatic–hydrothermal system of Vulcano (Aeolian Islands, Italy). Journal of Volcanology and geothermal research, 88(4), 325-342.
https://doi.org/10.1016/S0377-0273(98)00117-6

Fulignati, P., Sbrana, A., Luperini, W., Greco, V., 2002. Formation of rock coatings induced by the acid fumarole plume of the passively degassing volcano of La Fossa (Vulcano Island, Italy). J. Volcanol. Geotherm. Res. 115 (3–4), 397–410. https://doi.org/10.1016/S0377-0273(02)00209-3

Fulignati, P. (2020). Clay minerals in hydrothermal systems. Minerals, 10(10), 919. https://doi.org/10.3390/min10100919

Gertisser, R., Troll, V. R., Walter, T. R., Nandaka, I. G. M. A., & Ratdomopurbo, A. (Eds.). (2023). Merapi Volcano: Geology, Eruptive Activity, and Monitoring of a High-Risk Volcano. Springer Nature. https://doi.org/10.1007/978-3-031-15040-1

Giggenbach, W. F. (1978). The isotopic composition of waters from the El Tatio geothermal field, Northern Chile. Geochimica et Cosmochimica Acta, 42(7), 979-988. https://doi.org/10.1016/0016-7037(78)90287-9

Giggenbach, W.F. (1996). Chemical Composition of Volcanic Gases. In: Monitoring and Mitigation of Volcano Hazards. Springer, Berlin, Heidelberg. https://doi.org/10.1007/978-3-642-80087-0_7

Gioncada, A., Mazzuoli, R., Bisson, M., Pareschi, M.T., 2003. Petrology of volcanic products younger than 42 ka on the Lipari-Vulcano complex (Aeolian Islands, Italy): an example of volcanism controlled by tectonics. J. Volcanol. Geotherm. Res. 122 (3–4), 191–220. https://doi.org/10.1016/S0377-0273(02)00502-4

Girona, T., Realmuto, V., & Lundgren, P. (2021). Large-scale thermal unrest of volcanoes for years prior to eruption. Nature Geoscience, 14(4), 238-241. https://doi.org/10.1038/s41561-021-00705-4

Glennon, J. A., & Pfaff, R. M. (2003). The extraordinary thermal activity of El Tatio geyser field, Antofagasta Region, Chile. GOSA Trans, 8, 31-78.

Gracchi, T., Tacconi Stefanelli, C., Rossi, G., Di Traglia, F., Nolesini, T., Tanteri, L., & Casagli, N. (2022). UAV-based multitemporal remote sensing surveys of volcano unstable flanks: a case study from stromboli. Remote Sensing, 14(10), 2489. https://doi.org/10.3390/rs14102489

Gresse, M., Vandemeulebrouck, J., Byrdina, S., Chiodini, G., Roux, P., Rinaldi, A.P., Wathelet, M., Ricci, T., Letort, J., Petrillo, Z., Tuccimei, P., Lucchetti, C., Sciarra, A., 2018. Anatomy of a fumarolic system inferred from a multiphysics approach. Sci. Rep., 8 https://doi.org/10.1038/s41598-018-25448-y

Grosse, P., Euillades, P.A., Euillades, L.D., de Vries, B.V.W., 2014. A global database of composite volcano morphometry. B Volcanol 76 (1), 784. https://doi.org/10.1007/s00445-013-0784-4

Hahsler, M., Piekenbrock, M., Doran, D., 2019. dbscan: fast density-based clustering with r. J. Stat. Softw. 91 (1), 1–30. https://doi.org/10.18637/jss.v091.i01

Halldórsson, S. A., Hilton, D. R., Troll, V. R., & Fischer, T. P. (2013). Resolving volatile sources along the western Sunda arc, Indonesia. Chemical Geology, 339, 263-282. https://doi.org/10.1016/j.chemgeo.2012.09.042

Harris, A.J.L., Stevenson, D.S., 1997. Thermal observations of degassing open conduits and

fumaroles at Stromboli and Vulcano using remotely sensed data. J. Volcanol. Geotherm. Res. 76 (3–4), 175–198. https://doi.org/10.1016/S0377-0273(96)00097-2

Harris, A. J. L., & Maciejewski, A. J. H. (2000). Thermal surveys of the Vulcano Fossa fumarole field 1994–1999: evidence for fumarole migration and sealing. Journal of Volcanology and Geothermal Research, 102(1-2), 119-147. https://doi.org/10.1016/S0377-0273(00)00184-0

Harris, A.J.L., Lodato, L., Dehn, J., Spampinato, L., 2009. Thermal characterization of the Vulcano fumarole field. B Volcanol 71 (4), 441–458. https://doi.org/10.1007/s00445-008-0236-8

Harris, A., Alparone, S., Bonforte, A., Dehn, J., Gambino, S., Lodato, L., Spampinato, L., 2012. Vent temperature trends at the Vulcano Fossa fumarole field: the role of permeability. B Volcanol 74 (6), 1293–1311. https://doi.org/10.1007/s00445-012-0593-1

Hahsler, M., Piekenbrock, M., & Doran, D. (2019). dbscan: Fast density-based clustering with R. Journal of Statistical Software, 91, 1-30. https://doi.org/10.18637/jss.v091.i01

Healy, J., Hochstein, M.P., 1973. Horizontal flow in hydrothermal systems. J. Hydrol. N. Z. 71–82.

Heap, M.J., Troll, V.R., Kushnir, A.R.L., Gilg, H.A., Collinson, A.S.D., Deegan, F.M., Darmawan, H., Seraphine, N., Neuberg, J. and Walter, T.R., 2019. Hydrothermal alteration of andesitic lava domes can lead to explosive volcanic behaviour. Nature Communications, 10(1): 5063. https://doi.org/10.1038/s41467-019-13102-8

Heap, M. J., & Violay, M. E. (2021). The mechanical behaviour and failure modes of volcanic rocks: a review. Bulletin of Volcanology, 83(5), 33. https://doi.org/10.1007/s00445-021-01447-2

Heinicke, J., Fischer, T., Gaupp, R., Götze, J., Koch, U., Konietzky, H., & Stanek, K. P. (2009). Hydrothermal alteration as a trigger mechanism for earthquake swarms: the Vogtland/NW Bohemia region as a case study. Geophysical Journal International, 178(1), 1-13. https://doi.org/10.1111/j.1365-246X.2009.04138.x

Henley, R. W., & McNabb, A. (1978). Magmatic vapor plumes and ground-water interaction in porphyry copper emplacement. Economic Geology, 73(1), 1-20. https://doi.org/10.2113/gsecongeo.73.1.1

Hurwitz, S., & Manga, M. (2017). The fascinating and complex dynamics of geyser eruptions. Annual Review of Earth and Planetary Sciences, 45, 31-59.

Hurwitz, S., Kumar, A., Taylor, R., & Heasler, H. (2008). Climate-induced variations of geyser periodicity in Yellowstone National Park, USA. Geology, 36(6), 451-454. https://doi.org/10.1130/G24723A.1

Hurwitz, S., Hunt, A. G., & Evans, W. C. (2012). Temporal variations of geyser water chemistry in the Upper Geyser Basin, Yellowstone National Park, USA. Geochemistry, Geophysics, Geosystems, 13(12). https://doi.org/10.1029/2012GC004388

Hutchison, W., Mather, T.A., Pyle, D.M., Biggs, J., Yirgu, G., 2015. Structural controls on fluid pathways in an active rift system: a case study of the Aluto volcanic complex. Geosphere 11 (3), 542–562. https://doi.org/10.1130/GES01119.1

Inguaggiato, S., Mazot, A., Diliberto, I.S., Inguaggiato, C., Madonia, P., Rouwet, D., Vita, F., 2012. Total CO2 output from Vulcano island (Aeolian Islands, Italy). Geochem. Geophys. Geosyst. 13 (2). https://doi.org/10.1029/2011GC003920

Inguaggiato, S., Vita, F., Diliberto, I. S., Inguaggiato, C., Mazot, A., Cangemi, M., & Corrao, M. (2022). The volcanic activity changes occurred in the 2021–2022 at Vulcano island (Italy), inferred by the abrupt variations of soil CO2 output. Scientific Reports, 12(1), 21166. https://doi.org/10.3390/rs14051283

James, M.R., Chandler, J.H., Eltner, A., Fraser, C., Miller, P.E., Mills, J.P., Noble, T., Robson, S., Lane, S.N., 2019. Guidelines on the use of structure-from-motion photogrammetry in geomorphic research. Earth Surf. Process. Landf. 44 (10), 2081–2084. https://doi.org/10.1002/esp.4637

James, M. R., Antoniazza, G., Robson, S., & Lane, S. N. (2020). Mitigating systematic error in topographic models for geomorphic change detection: accuracy, precision and considerations beyond off-nadir imagery. Earth Surface Processes and Landforms, 45(10), 2251-2271. https://doi.org/10.1002/esp.4878

James, M. R., Carr, B., D'Arcy, F., Diefenbach, A., Dietterich, H., Fornaciai, A., ... & Zorn, E. (2020). Volcanological applications of unoccupied aircraft systems (UAS): Developments, strategies, and future challenges. Volcanica, 3(1), 67-114. https://doi.org/10.30909/vol.03.01.67114

Jaworowski, C., Heasler, H. P., Hardy, C. C., & Queen, L. P. (2006). Control of hydrothermal fluids by natural fractures at Norris Geyser Basin. Yellowstone Sci, 14(1), 13-23.

Jaworowski, C., Lynne, B.Y., Heasler, H., Foley, D., Smith, I.J., Smith, G.J., 2020. Detecting natural fractures with ground penetrating radar and airborne night-thermal infrared imagery around Old Faithful Geyser, Yellowstone National Park, USA. Geothermics 85, 101775. https://doi.org/10.1016/j.geothermics.2019.101775

Jenness, J. (2014). Polar plots for ArcGIS. Jenness Enterprises.

Jiang, S., Jiang, C., Jiang, W., 2020. Efficient structure from motion for large-scale UAV images: a review and a comparison of SfM tools. Isprs J. Photogramm. 167, 230–251. https://doi.org/10.1016/j.isprsjprs.2020.04.016

Jordan, B.R., 2019. Collecting field data in volcanic landscapes using small UAS (sUAS)/ drones. J. Volcanol. Geotherm. Res. 385, 231–241.

https://doi.org/10.1016/j.jvolgeores.2019.07.006

Julia, F., Vladimir, L., Sergey, R., & David, Z. (2014). Effects of hydrothermal alterations on physical and mechanical properties of rocks in the Kuril–Kamchatka island arc. Engineering Geology, 183, 80-95. https://doi.org/10.1016/j.enggeo.2014.10.011

Kalacska, M., Lucanus, O., Arroyo-Mora, J.P., Laliberté, É., Elmer, K., Leblanc, G., Groves, A., 2020. Accuracy of 3D landscape reconstruction without ground control points using different UAS platforms. Drones 4 (2), 13. https://doi.org/10.3390/drones4020013

Kereszturi, G., Schaefer, L. N., Miller, C., & Mead, S. (2020). Hydrothermal alteration on composite volcanoes: mineralogy, hyperspectral imaging, and aeromagnetic study of Mt Ruapehu, New Zealand. Geochemistry, Geophysics, Geosystems, 21(9), e2020GC009270. https://doi.org/10.1029/2020GC009270

Kern, C., Aiuppa, A., & de Moor, J. M. (2022). A golden era for volcanic gas geochemistry?. Bulletin of Volcanology, 84(5), 43. https://doi.org/10.1007/s00445-022-01556-6

Kwarteng, P., & Chavez, A. (1989). Extracting spectral contrast in Landsat Thematic Mapper image data using selective principal component analysis. Photogramm. Eng. Remote Sens, 55(1), 339-348.

Lahsen, A. (1976). Geothermal Exploration in Northern Chile--Summary: Geothermal Energy.

Li, C.F., Dai, Y.Y., Zhao, J.J., Yin, J.Y., Dong, J.S., 2014. Volcanic ash cloud detection from re mote sensing images using principal component analysis. Comput. Electr. Eng. 40 (8), 204–214. https://doi.org/10.1016/j.compeleceng.2014.08.014

Lillesand, T., Kiefer, R.W., Chipman, J., 2015. Remote Sensing and Image Interpretation. John Wiley & Sons.

Liuzzo, M., Di Muro, A., Giudice, G., Michon, L., Ferrazzini, V., & Gurrieri, S. (2015). New evidence of CO2 soil degassing anomalies on P iton de la F ournaise volcano and the link with volcano tectonic structures. Geochemistry, Geophysics, Geosystems, 16(12), 4388-4404. https://doi.org/10.1002/2015GC006032

Loughlin, W.P., 1991. Principal component analysis for alteration mapping. Photogramm. Eng. Remote Sens. 57 (9), 1163–1169.

Lucchi, F., Tranne, C. A., Rossi, P. L., Gallardo, C., De Astis, G., & Pini, G. A. (2009). Volcanic and tectonic history of the El Tatio area (central Andes, northern Chile): explanatory notes to the 1: 50,000 scale geological map. GeoActa, 2, 1-29.

Luhmann, T. (2004). A historical review on panorama photogrammetry. International Archives of the Photogrammetry, Remote Sensing and Spatial Information Sciences, 34(5/W16), 8.

Lynch, D.K., Hudnut, K.W. and Adams, P.M., 2013. Development and growth of recently-exposed fumarole fields near Mullet Island, Imperial County, California. Geomorphology, 195: 27-44. https://doi.org/10.1016/j.geomorph.2013.04.022

Madonia, P., Pecoraino, G., Sammarco, C., 2011. Georeferenced cartography dataset of the La Fossa crater fumarolic field at Vulcano Island (Aeolian Archipelago, Italy): conver sion and comparison of data from local to global positioning methods. Ann. Geophys. 54 (3), 297–303.

Madonia, P., Cusano, P., Diliberto, I.S., Cangemi, M., 2013. Thermal anomalies in fumaroles at Vulcano island (Italy) and their relationship with seismic activity. Phys. Chem. Earth 63, 160–169. https://doi.org/10.1016/j.pce.2013.06.001

Madonia, P., Cangemi, M., Costa, M., Madonia, I., 2016. Mapping fumarolic fields in volca nic areas: a methodological approach based on the case study of La Fossa cone, Vulcano island (Italy). J. Volcanol. Geotherm. Res. 324, 1–7. https://doi.org/10.1016/j.jvolgeores.2016.05.014

Manga, M., & Brodsky, E. (2006). Seismic triggering of eruptions in the far field: Volcanoes and geysers. Annu. Rev. Earth Planet. Sci, 34, 263-291.

Mannini, S., Harris, A.J., Jessop, D.E., Chevrel, M.O., Ramsey, M.S., 2019. Combining ground- and ASTER-based thermal measurements to constrain fumarole field heat budgets: the case of Vulcano Fossa 2000–2019. Geophys. Res. Lett. 46 (21), 11868–11877. https://doi.org/10.1029/2019GL084013

Martini, M., 1983. Variations in surface manifestations at Vulcano (Aeolian Islands, Italy) as a possible evidence of deep processes. Bull. Volcanol. 46 (1), 83–86. https://doi.org/10.1007/BF02598247

Massimetti, F., Coppola, D., Laiolo, M., Valade, S., Cigolini, C., & Ripepe, M. (2020). Volcanic hot-spot detection using SENTINEL-2: a comparison with MODIS–MIROVA thermal data series. Remote Sensing, 12(5), 820. https://doi.org/10.3390/rs12050820

Mayer, K., Scheu, B., Montanaro, C., Yilmaz, T.I., Isaia, R., Aßbichler, D., Dingwell, D.B., 2016. Hydrothermal alteration of surficial rocks at Solfatara (Campi Flegrei): petrophysical properties and implications for phreatic eruption processes. J. Volcanol. Geotherm. Res. 320, 128–143. https://doi.org/10.1016/j.jvolgeores.2016.04.020

Mazzuoli, R., Tortorici, L., Ventura, G., 1995. Oblique rifting in Salina, Lipari and Vulcano Islands (Aeolian Islands, Southern Italy). Terra Nova 7 (4), 444–452. https://doi.org/10.1111/j.1365-3121.1995.tb00540.x

Mia, B., & Fujimitsu, Y. (2012). Mapping hydrothermal altered mineral deposits using Landsat 7 ETM+ image in and around Kuju volcano, Kyushu, Japan. Journal of Earth System Science, 121, 1049-1057. https://doi.org/10.1007/s12040-012-0211-9

Middlemost, E. A. (1994). Naming materials in the magma/igneous rock system. Earth-science reviews, 37(3-4), 215-224. https://doi.org/10.1016/0012-8252(94)90029-9

Mikhail, E. M., Bethel, J. S., & McGlone, J. C. (2001). Introduction to modern photogrammetry. John Wiley & Sons.

Minissale, A., Donato, A., Procesi, M., Pizzino, L. and Giammanco, S., 2019. Systematic review of geochemical data from thermal springs, gas vents and fumaroles of Southern Italy for geothermal favourability mapping. Earth-Sci Rev, 188: 514-535. https://doi.org/10.1016/j.earscirev.2018.09.008

Montecinos-Cuadros, D., Díaz, D., Yogeshwar, P., & Munoz-Saez, C. (2021). Characterization of the shallow structure of El Tatio geothermal field in the Central Andes, Chile using transient electromagnetics. Journal of Volcanology and Geothermal Research, 412, 107198. https://doi.org/10.1016/j.jvolgeores.2021.107198

Müller, D., Bredemeyer, S., Zorn, E., De Paolo, E., & Walter, T. R. (2021). Surveying fumarole sites and hydrothermal alteration by unoccupied aircraft systems (UAS) at the La Fossa cone, Vulcano Island (Italy). Journal of Volcanology and Geothermal Research, 413, 107208. https://doi.org/10.1016/j.jvolgeores.2021.107208

Müller, D., Walter, T. R., Zimmer, M., & Gonzalez, G. (2022). Distribution, structural and hydrological control of the hot springs and geysers of El Tatio, Chile, revealed by optical and thermal infrared drone surveying. Journal of Volcanology and Geothermal Research, 432, 107696. https://doi.org/10.1016/j.jvolgeores.2022.107696

Müller, D., Walter, T. R., Troll, V. R., Stammeier, J., Karlsson, A., De Paolo, E., Pisciotta, A. F., Zimmer, M., and De Jarnatt, B.: Anatomy of a fumarole field; drone remote sensing and petrological approaches reveal the degassing and alteration structure at La Fossa cone, Vulcano Island, Italy, EGUsphere [preprint], https://doi.org/10.5194/egusphere-2023-1692, 2023. https://doi.org/10.5194/egusphere-2023-1692

Munoz-Saez, C., Namiki, A., & Manga, M. (2015). Geyser eruption intervals and interactions: examples from El Tatio, Atacama, Chile. Journal of Geophysical Research: Solid Earth, 120(11), 7490-7507. https://doi.org/10.1002/2015JB012364

Munoz-Saez, C., Manga, M., & Hurwitz, S. (2018). Hydrothermal discharge from the El Tatio basin, Atacama, Chile. Journal of Volcanology and Geothermal Research, 361, 25-35. https://doi.org/10.1016/j.jvolgeores.2018.07.007

Munoz-Saez, C., Manga, M., Hurwitz, S., Slagter, S., Churchill, D. M., Reich, M., ... & Morata, D. (2020). Radiocarbon dating of silica sinter and postglacial hydrothermal activity in the El Tatio geyser field. Geophysical Research Letters, 47(11), e2020GL087908. https://doi.org/10.1029/2020GL087908

Neale, C. M., Sivarajan, S., Akasheh, O. Z., Jaworowski, C., & Heasler, H. (2009, September). Monitoring geothermal activity in Yellowstone National Park using airborne thermal infrared remote sensing. In Remote Sensing for Agriculture, Ecosystems, and Hydrology XI (Vol. 7472, pp. 243-249). SPIE. https://doi.org/10.1117/12.834225

Neale, C., Jaworowski, C., Heasler, H., Sivarajan, S., Masih, A., 2016. Hydrothermal monitor ing in Yellowstone National Park using airborne thermal infrared remote sensing. Remote Sens. Environ. 184, 628–644. https://doi.org/10.1016/j.rse.2016.04.016

Neall, V. E. (2009). Volcanic soils. Land use, land cover and soil sciences, 7, 23-45.

Nuccio, P. M., Paonita, A., & Sortino, F. (1999). Geochemical modeling of mixing between magmatic and hydrothermal gases: the case of Vulcano Island, Italy. Earth and planetary Science letters, 167(3-4), 321-333. https://doi.org/10.1016/S0012-821X(99)00037-0

Nuccio, P. M., & Paonita, A. (2001). Magmatic degassing of multicomponent vapors and assessment of magma depth: application to Vulcano Island (Italy). Earth and Planetary Science Letters, 193(3-4), 467-481. https://doi.org/10.1016/S0012-821X(01)00512-X

Offield, T.W., 1975. Thermal-infrared images as a basis for structure mapping, Front Range and adjacent plains in Colorado. Geol. Soc. Am. Bull. 86 (4), 495–502.

Oppenheimer, C., Rothery, D.A., Francis, P.W., 1993. Thermal distributions at fumarole fields - implications for infrared remote-sensing of active volcanos. J. Volcanol. Geotherm. Res. 55 (1–2), 97–115. https://doi.org/10.1016/0377-0273(93)90092-6

Oyedotun, T. D. T. (2018). X-ray fluorescence (XRF) in the investigation of the composition of earth materials: a review and an overview. Geology, Ecology, and Landscapes, 2(2), 148-154. https://doi.org/10.1080/24749508.2018.1452459

Pantaleo, M., Walter, T., 2014. The ring-shaped thermal field of Stefanos crater, Nisyros Is land: a conceptual model. Solid Earth 5 (1), 183–198. https://doi.org/10.5194/se-5-183-2014

Paonita, A., Federico, C., Bonfanti, P., Capasso, G., Inguaggiato, S., Italiano, F., Madonia, P., Pecoraino, G., Sortino, F., 2013. The episodic and abrupt geochemical changes at La Fossa fumaroles (Vulcano Island, Italy) and related constraints on the dynamics, structure, and compositions of the magmatic system. Geochim. Cosmochim. Acta 120, 158–178. https://doi.org/10.1016/j.gca.2013.06.015

Pirajno, F. (2009). Hydrothermal Processes and Wall Rock Alteration. In: Hydrothermal Processes and Mineral Systems. Springer, Dordrecht. https://doi.org/10.1007/978-1-4020-8613-7_2

Procesi, M. (2014). Geothermal potential evaluation for Northern Chile and suggestions for new energy plans. Energies, 7(8), 5444-5459. https://doi.org/10.3390/en7085444

Rathinam, S., Almeida, P., Kim, Z.W., Jackson, S., Tinka, A., Grossman, W., Sengupta, R., 2007. Autonomous searching and tracking of a river using an UAV. 2007 American Control Conference. vol. 1–13, pp. 2035–2040.

Reed, M. H., Munoz-Saez, C., Hajimirza, S., Wu, S. M., Barth, A., Girona, T., ... & Manga, M. (2021). The 2018 reawakening and eruption dynamics of Steamboat Geyser, the world's tallest active geyser. Proceedings of the National Academy of Sciences, 118(2), e2020943118. https://doi.org/10.1073/pnas.2020943118

Reid, M. E., Sisson, T. W., & Brien, D. L. (2001). Volcano collapse promoted by hydrothermal alteration and edifice shape, Mount Rainier, Washington. Geology, 29(9), 779-782. https://doi.org/10.1130/0091-7613(2001)029%3C0779:VCPBHA%3E2.0.CO;2

Rejas, J.G., Martinez-Frias, J., Bonatti, J., Martinez, R., Marchamalo, M., 2012. Anomaly de tection and comparative analysis of hydrothermal alteration materials trough hyperspectral multisensor data in the Turrialba Volcano. Xxii Isprs Congress, Techni cal Commission Vii. 39(B7), pp. 151–155.

Revil, A., Finizola, A., Piscitelli, S., Rizzo, E., Ricci, T., Crespy, A., Angeletti, B., Balasco, M., Cabusson, S.B., Bennati, L., Boleve, A., Byrdina, S., Carzaniga, N., Di Gangi, F., Morin, J., Perrone, A., Rossi, M., Roulleau, E., Suski, B., 2008. Inner structure of La Fossa di Vulcano (Vulcano Island, southern Tyrrhenian Sea, Italy) revealed by high resolution electric resistivity tomography coupled with self-potential, temperature, and CO2 diffuse degassing measurements. J. Geophys. Res. 113 (B7). https://doi.org/10.1029/2007JB005394

Rinehart, J. S. (1980). Geysers and geothermal energy (Vol. 223). New York: Springer-Verlag.

Robb, R., 2005. Introduction to Ore-forming Processes, Book. Blackwell Science Ltd a Blackwell Publishing Company.

Romagnoli, C., Casalbore, D., Chiocci, F.L., 2012. La Fossa Caldera breaching and submarine erosion (Vulcano island, Italy). Mar. Geol. 303, 87–98. https://doi.org/10.1016/j.margeo.2012.02.004

Rosas-Carbajal, M., Komorowski, J. C., Nicollin, F., & Gibert, D. (2016). Volcano electrical tomography unveils edifice collapse hazard linked to hydrothermal system structure and dynamics. Scientific reports, 6(1), 29899. https://doi.org/10.1038/srep29899

Rosi, M., Vezzoli, L. U. I. G. I. N. A., Castelmenzano, A., & Grieco, G. (1999). Plinian pumice fall deposit of the Campanian Ignimbrite eruption (Phlegraean Fields, Italy). Journal of volcanology and geothermal research, 91(2-4), 179-198. https://doi.org/10.1016/S0377-0273(99)00035-9

Rowan, L. C., Wetlaufer, P. H., & Stewart, J. H. (1976). Discrimination of rock Types and detection of hydrothermally altered areas in south-central Nevada by the use of computer-enhanced ERTS images.

Rowan, L. C., Hook, S. J., Abrams, M. J., & Mars, J. C. (2003). Mapping hydrothermally altered rocks at Cuprite, Nevada, using the Advanced Spaceborne Thermal Emission and Reflection Radiometer (ASTER), a new satellite-imaging system. Economic Geology, 98(5), 1019-1027. https://doi.org/10.2113/gsecongeo.98.5.1019

Ruff, S. W., & Farmer, J. D. (2016). Silica deposits on Mars with features resembling hot spring biosignatures at El Tatio in Chile. Nature communications, 7(1), 13554. https://doi.org/10.1038/ncomms13554

Schopa, A., Pantaleo, M., Walter, T.R., 2011. Scale-dependent location of hydrothermal vents: stress field models and infrared field observations on the Fossa Cone, Vulcano Island, Italy. J. Volcanol. Geotherm. Res. 203 (3–4), 133–145. https://doi.org/10.1016/j.jvolgeores.2011.03.008

Selva, J., Bonadonna, C., Branca, S., De Astis, G., Gambino, S., Paonita, A., Pistolesi, M., Ricci, T., Sulpizio, R., Tibaldi, A., 2020. Multiple hazards and paths to eruptions: a review of the volcanic system of Volcano (Aeolian Islands, Italy). Earth Sci. Rev. 207, 103186. https://doi.org/10.1016/j.earscirev.2020.103186

Sicardi, L., 1955. Captazione ed analisi chimica dei gas della esalazione solfidrico-solforosa dei vulcani in fase solfatarica. Bull. Volcanol. 17 (1), 107–112.

Siebert, L., Cottrell, E., Venzke, E., & Andrews, B. (2015). Earth's volcanoes and their eruptions: An overview. The encyclopedia of volcanoes, 239-255. https://doi.org/10.1016/B978-0-12-385938-9.00012-2

Sigmundsson, F., Hooper, A., Hreinsdóttir, S., Vogfjörd, K. S., Ófeigsson, B. G., Heimisson, E. R., ... & Eibl, E. P. (2015). Segmented lateral dyke growth in a rifting event at Bárðarbunga volcanic system, Iceland. Nature, 517(7533), 191-195. https://doi.org/10.1038/nature14111

Smith, M.W., Vericat, D., 2015. From experimental plots to experimental landscapes: to pography, erosion and deposition in sub-humid badlands from Structure-from Motion photogrammetry. Earth Surf. Process. Landf. 40 (12), 1656–1671. https://doi.org/10.1002/esp.3747

Spampinato, L., Calvari, S., Oppenheimer, C., Boschi, E., 2011. Volcano surveillance using infrared cameras. Earth Sci. Rev. 106 (1–2), 63–91. https://doi.org/10.1016/j.Earscirev.2011.01.003

Spetsakis, M., & Aloimonos, J. Y. (1991). A multi-frame approach to visual motion perception. International Journal of Computer Vision, 6(3), 245-255. https://doi.org/10.1007/BF00115698

Stevenson, J.A., Varley, N., 2008. Fumarole monitoring with a handheld infrared camera: Volcán de Colima, Mexico, 2006–2007. J. Volcanol. Geotherm. Res. 177 (4), 911–924. https://doi.org/10.1016/j.jvolgeores.2008.07.003

Szeliski, R., & Kang, S. B. (1994). Recovering 3D shape and motion from image streams using nonlinear least squares. Journal of Visual Communication and Image Representation, 5(1), 10-28. https://doi.org/10.1006/jvci.1994.1002

Tamburello, G., Kantzas, E.P., McGonigle, A.J.S., Aiuppa, A., Giudice, G., 2011. UV camera measurements of fumarole field degassing (La Fossa crater, Vulcano Island). J. Volcanol. Geotherm. Res. 199 (1–2), 47–52. https://doi.org/10.1016/j.Jvolgeores.2010.10.004

Tayebi, M.H., Tangestani, M.H. & Vincent, R.K. Sub-pixel mapping of iron-bearing minerals using ALI data and MTMF algorithm, Masahim volcano, SE Iran. Arab J Geosci 8, 3799–3810 (2015). https://doi.org/10.1007/s12517-014-1400-4

Tedesco, D., Toutain, J.P., Allard, P., Losno, R., 1991. Chemical variations in fumarolic gases at Vulcano Island (Southern Italy) - seasonal and volcanic effects. J. Volcanol. Geotherm. Res. 45 (3–4), 325–334. https://doi.org/10.1016/0377-0273(91)90066-9.

Thomaidis, K., Troll, V. R., Deegan, F. M., Freda, C., Corsaro, R. A., Behncke, B., & Rafailidis, S. (2021). A message from the 'underground forge of the gods': History and current eruptions at Mt Etna. Geology Today, 37(4), 141-149. https://doi.org/10.1111/gto.12362

Thordarson, T., & Self, S. (2003). Atmospheric and environmental effects of the 1783–1784 Laki eruption: A review and reassessment. Journal of Geophysical Research: Atmospheres, 108(D1), AAC-7. https://doi.org/10.1029/2001JD002042

Tinti, S., Bortolucci, E., Armigliato, A., 1999. Numerical simulation of the landslide-induced tsunami of 1988 on Vulcano Island, Italy. B Volcanol 61 (1–2), 121–137. https://doi.org/10.1007/s004450050267

Troll, V. R., Hilton, D. R., Jolis, E. M., Chadwick, J. P., Blythe, L. S., Deegan, F. M., ... & Zimmer, M. (2012). Crustal CO2 liberation during the 2006 eruption and earthquake events at Merapi volcano, Indonesia. Geophysical Research Letters, 39(11). https://doi.org/10.1029/2012GL051307

Tocchi, E. (1923). Studio geologico e geotermico del Tatio cileno. Reserved report to Larderello SA: Italy.

Toutain, J.-P., Sortino, F., Baubron, J.-C., Richon, P., Surono, Sumarti, S. and Nonell, A., 2009. Structure and CO2 budget of Merapi volcano during inter-eruptive periods. B Volcanol, 71(7): 815-826. https://doi.org/10.1007/s00445-009-0266-x

Tratt, D.M., Young, S.J., Lynch, D.K., Buckland, K.N., Johnson, P.D., Hall, J.L., Westberg, K.R., Polak, M.L., Kasper, B.P., Qian, J., 2011. Remotely sensed ammonia emission from fumarolic vents associated with a hydrothermally active fault in the Salton Sea Geothermal Field, California. J. Geophys. Res. 116 (D21). https://doi.org/10.1029/2011JD016282

Van der Meer, F. D., Van der Werff, H. M., Van Ruitenbeek, F. J., Hecker, C. A., Bakker, W. H., Noomen, M. F., ... & Woldai, T. (2012). Multi-and hyperspectral geologic remote sensing: A review. International Journal of Applied Earth Observation and Geoinformation, 14(1), 112-128. https://doi.org/10.1016/j.jag.2011.08.002

Ventura, G., Vilardo, G., Milano, G., Pino, N.A., 1999. Relationships among crustal structure, volcanism and strike-slip tectonics in the Lipari-Vulcano Volcanic Complex (Aeolian Islands, Southern Tyrrhenian Sea, Italy). Phys. Earth Planet. Inter. 116 (1–4), 31–52. https://doi.org/10.1016/S0031-9201(99)00117-X

Vernier, J.-P., Kalnajs, L., Diaz, J., Reese, T., Corrales, E., Alan, A., Vernier, H., Holland, L., Patel, A., Rastogi, N., 2020. VolKilau: Volcano rapid response balloon campaign during the 2018 Kilauea eruption. Bull. Am. Meteorol. Soc. 101 (10), E1602–E1618.

https://doi.org/10.1175/BAMS-D-19-0011.1

Vita, F., Inguaggiato, S., Bobrowski, N., Calderone, L., Galle, B., Parello, F., 2012. Continuous SO2 flux measurements for Vulcano Island, Italy. Ann. Geophys. 55 (2), 301–308. https://doi.org/10.4401/ag-5759

Walter, T. R., Haghshenas Haghighi, M., Schneider, F. M., Coppola, D., Motagh, M., Saul, J., ... & Gaebler, P. (2019). Complex hazard cascade culminating in the Anak Krakatau sector collapse. Nature communications, 10(1), 4339. https://doi.org/10.1038/s41467-019-12284-5

Walter, T.R., Belousov, A., Belousova, M., Kotenko, T., Auer, A., 2020. The 2019 eruption dynamics and morphology at Ebeko Volcano monitored by unoccupied aircraft systems (UAS) and field stations. Remote Sens. Basel 12 (12), 1961. https://doi.org/10.3390/rs12121961

Westphal, T., Füllmann, T., & Pöllmann, H. (2009). Rietveld quantification of amorphous portions with an internal standard—Mathematical consequences of the experimental approach. Powder Diffraction, 24(3), 239-243. https://doi.org/10.1154/1.3187828

Westoby, M. J., Brasington, J., Glasser, N. F., Hambrey, M. J., & Reynolds, J. M. (2012). 'Structure-from-Motion'photogrammetry: A low-cost, effective tool for geoscience applications. Geomorphology, 179, 300-314. https://doi.org/10.1016/j.geomorph.2012.08.021

Willis, M. D., Koenig, C. W., Black, S. L., & Castañeda, A. M. (2016). Archeological 3d mapping: the structure from motion revolution. Journal of Texas Archeology and History, 3, 1-36. https://doi.org/10.21112/ita.2016.1.110

Wilmeth, D. T., Nabhan, S., Myers, K. D., Slagter, S., Lalonde, S. V., Sansjofre, P., ... & Van Zuilen, M. A. (2020). Depositional evolution of an extinct sinter mound from source to outflow, El Tatio, Chile. Sedimentary Geology, 406, 105726. https://doi.org/10.1016/j.sedgeo.2020.105726

Wohletz, K., Heiken, G., 1992. Volcanology and Geothermal Energy. 432. University of California Press, Berkeley.

Xu, K., Wang, X., Kong, C., Feng, R., Liu, G., Wu, C., 2019. Identification of hydrothermal al teration minerals for exploring gold DEPOSITS Based on SVM and PCA using ASTER data: a case study of Gulong. Remote Sens. Basel 11 (24), 3003. https://doi.org/10.3390/rs11243003

Yuill, R. S. (1971). The standard deviational ellipse; an updated tool for spatial description. Geografiska Annaler: Series B, Human Geography, 53(1), 28-39. https://doi.org/10.1080/04353684.1971.11879353

Zandt, G., Leidig, M., Chmielowski, J., Baumont, D., & Yuan, X. (2003). Seismic detection and characterization of the Altiplano-Puna magma body, central Andes. Pure and Applied Geophysics, 160, 789-807. https://doi.org/10.1007/PL00012557

Zorn, E. U., Walter, T. R., Johnson, J. B., & Mania, R. (2020). UAS-based tracking of the Santiaguito Lava Dome, Guatemala. Scientific Reports, 10(1), 8644. https://doi.org/10.1038/s41598-020-65386-2

8 Appendices

Appendix Chapter 2

Appendix A2.1 Evidence for hydrothermal activity beyond the Tatio-basin

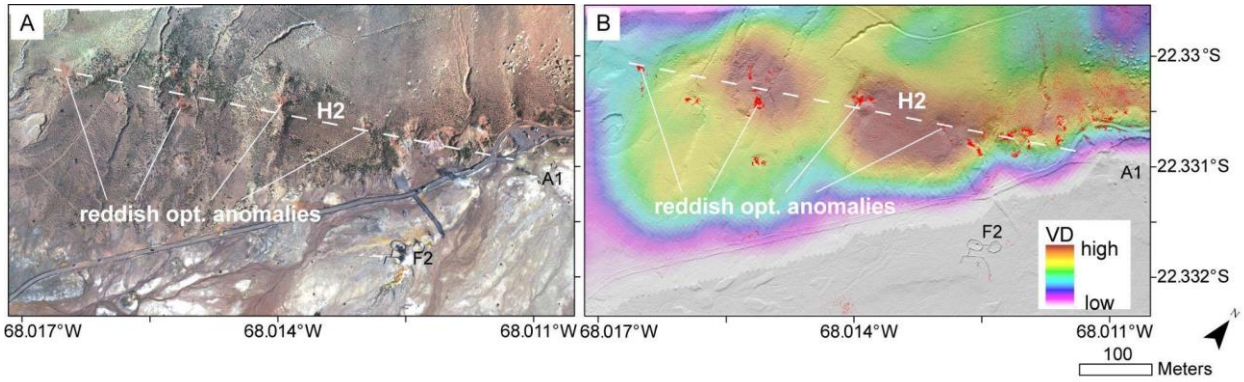

A2.1 Hydrothermal activity can be traced beyond the Tatio basin and shows pronounced indications for hydrothermal alteration in two segments, H1 and H2 into the flank of Mt Copacoya. Ground colorization anomalies, topographic effects, but also plant growth considering size and vegetation density (VD) indicate an ongoing hydrothermal influence. Orientation and extent of these segments are inferred based on soil color shifts towards reddish tints (A and B) indicating hydrothermal alteration.

Appendix A2.2 Azimuths of a fractured bedrock formation

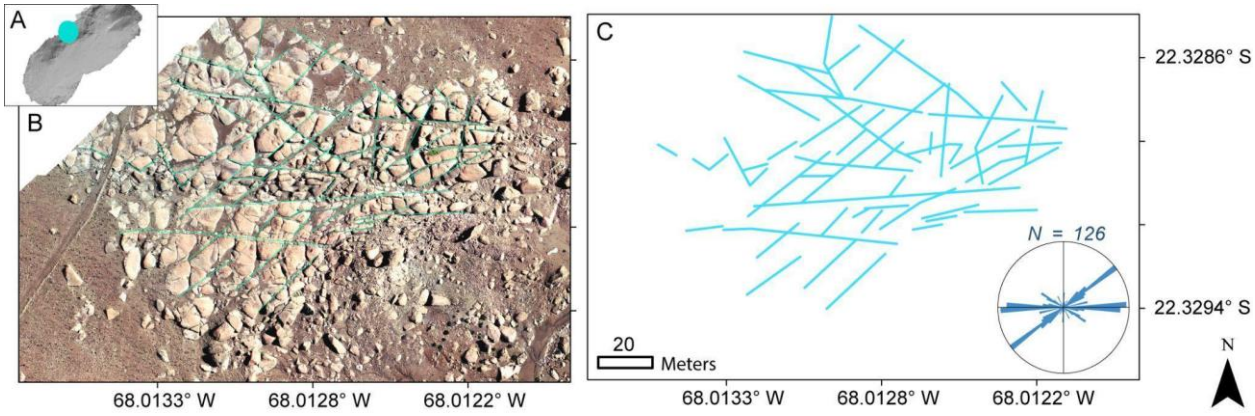

A2.2 Fractured rock formation north of the geyser belt. The location of the rock formation is indicated by a blue dot in Fig. A. (B, C) Rock fracture axes were mapped manually, based on our orthomosaic, and are indicated in light blue. Azimuths resemble azimuths for intersecting lineaments and vent arrangements described earlier. This indicates that vent arrangements are controlled by preexisting joint- or fracture networks that form predefined axes of higher porosity.

Appendix A2.3 Discrepancy of current high discharge and vents of large/high sinter bodies

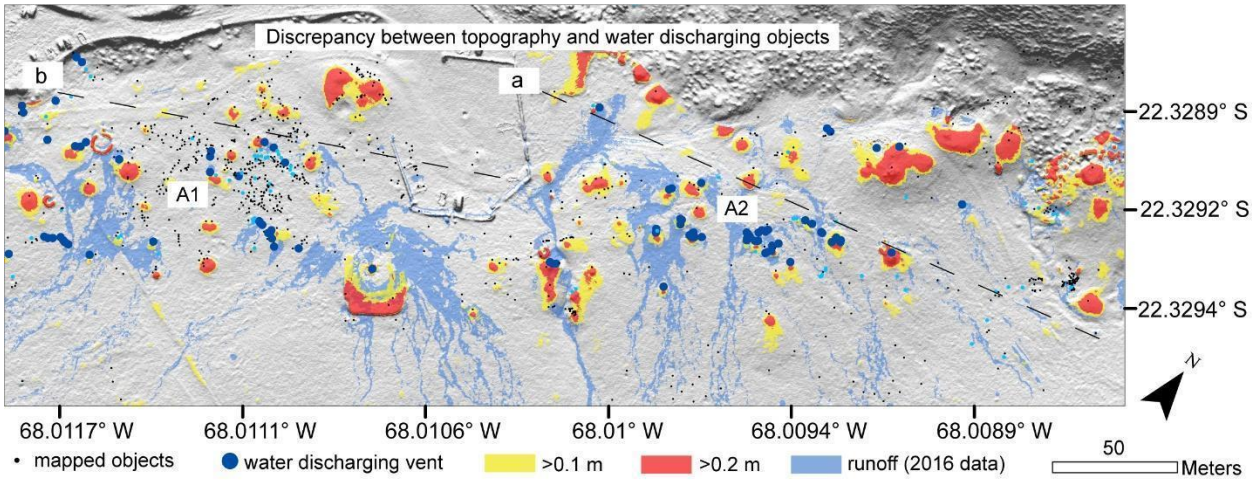

A2.3 Comparison of topography and water discharging objects. Yellow and red patches denote objects with a clear topographic expression elevating higher than 0.1 m or 0.2 m respectively above the surrounding, calculated by subtracting a mean DEM from the drone DEM. Blue areas denote surface water discharge. Note that the source regions of major discharge are not coincident with topographic objects. Currently discharging vents dominate in the central southern sections, while evolved sinter bodies dominate in the northern margins of parts A1 and A2. Dashed black lines a and b were drawn to illustrate the boundary between both.

Appendix Chapter 3

Appendix A3.1 Influence of emissivity and color palette on calculated pixel-temperatures

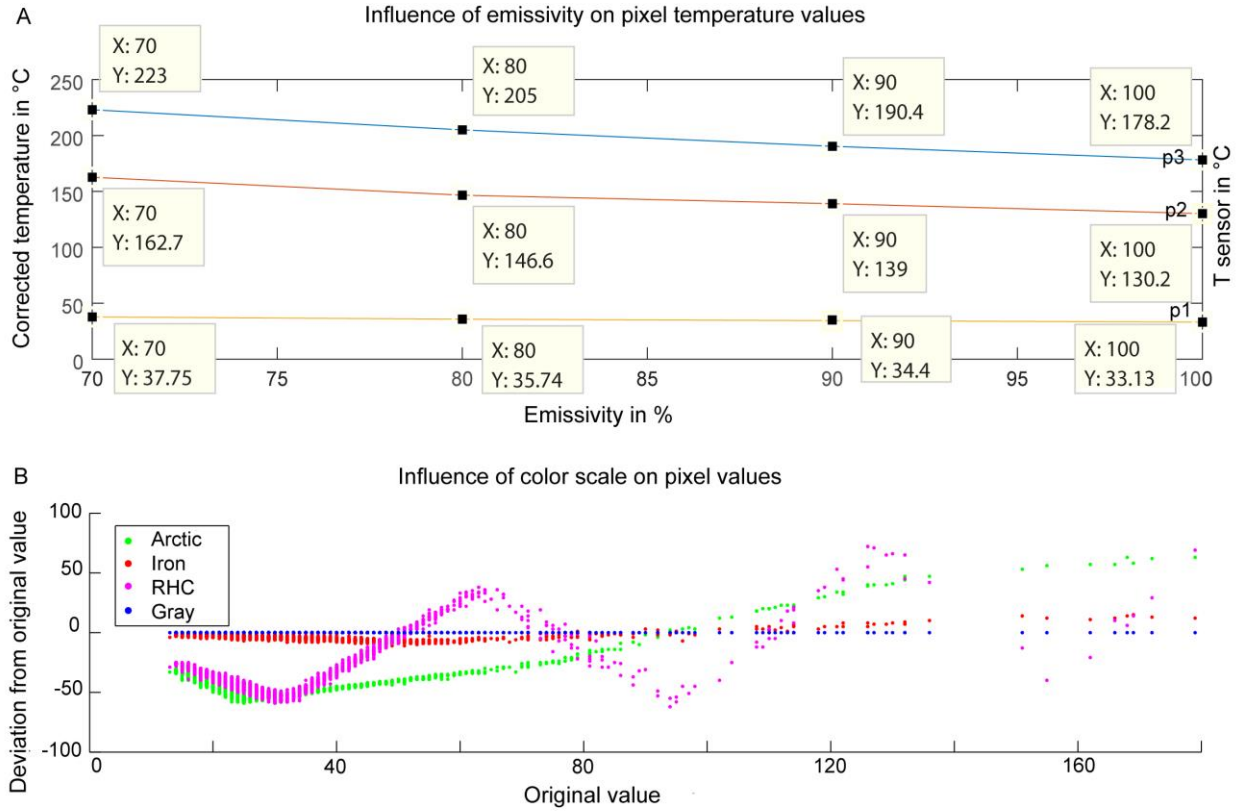

A3.1 (A) Influence of the emissivity on calculated pixel temperatures shown for 3 pixels p1-p3. Assuming a 10% lower emissivity value for a pixel results in a pixel temperature increase of 3-7%. The original pixel value measured at the sensor is given on the right y-axis, the respective values for a decreased emissivity are marked by black dots in the plot. (B). Deviation of temperatures compared to the original value, depending on the color palette applied to the infrared data. To use the infrared data quantitatively, a linear color scheme such as greyscale is recommended, as colored representations would introduce artificial patterns and lead to over- or underestimated temperatures.

Appendix A3.2 Eigenvector and Eigenvalues of PCA analysis

```
# Data file produced by Principal Components
#         Input raster(s):
#                 D:\Vulcano2018\work_in_progress\20181115_ortho.tif
#         The number of components = 4
#         Output raster(s):
#                 D:\Vulcano2018\arcGis_shp\1115pca


#             COVARIANCE MATRIX

#  Layer          1          2          3          4
# ---------------------------------------------------------------------------
     1      4935.82565   4512.35716   4316.07863  -7874.12690
     2      4512.35716   4306.86545   4186.15229  -7419.98889
     3      4316.07863   4186.15229   4190.53811  -7266.99265
     4     -7874.12690  -7419.98889  -7266.99265  16237.43535
# ===========================================================================


#             CORRELATION MATRIX

#  Layer          1          2          3          4
# ---------------------------------------------------------------------------
     1        1.00000    0.97868    0.94902   -0.87956
     2        0.97868    1.00000    0.98537   -0.88729
     3        0.94902    0.98537    1.00000   -0.88097
     4       -0.87956   -0.88729   -0.88097    1.00000
# ===========================================================================


#           EIGENVALUES AND EIGENVECTORS

# Number of Input Layers    Number of Principal Component Layers
        4                   3
# PC Layer          1          2          3
# ---------------------------------------------------------------------------
# Eigenvalues
          27826.86667   1580.51056    234.91125
# Eigenvectors
# Input Layer
     1        0.40148    0.45239   -0.72646
     2        0.37865    0.43231    0.11463
     3        0.37013    0.40857    0.67757
# ===========================================================================

#           PERCENT AND ACCUMULATIVE EIGENVALUES

# PC Layer   EigenValue   Percent of EigenValues   Accumulative of EigenValues
     1  27826.86667        93.8756            93.8756
     2   1580.51056         5.3319            99.2075
     3    234.91125         0.7925           100.0000
# ===========================================================================
```

A3.2 Details of the applied principal components analysis, representing covariance and correlation matrix, as well as Eigenvector and Eigenvalues and variance / cumulative variance for every single component.

Appendix A3.3 Histograms of RGB value and temperature distribution

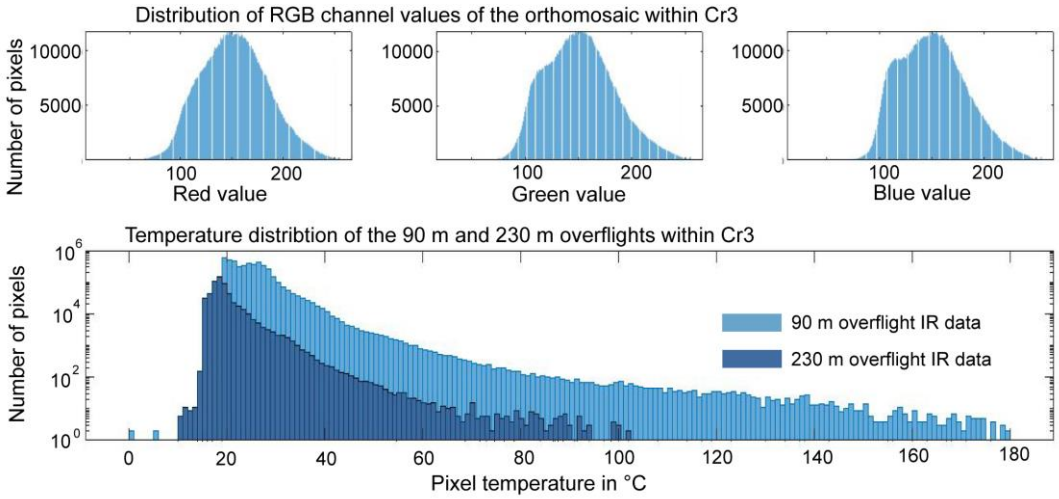

A3.3 Histograms showing the frequency distribution of RGB values of the orthomosaic and the temperature distribution of the 90m / 230m agl infrared overflights within the crater Cr3.

Appendix A3.4 Density distribution of image classification

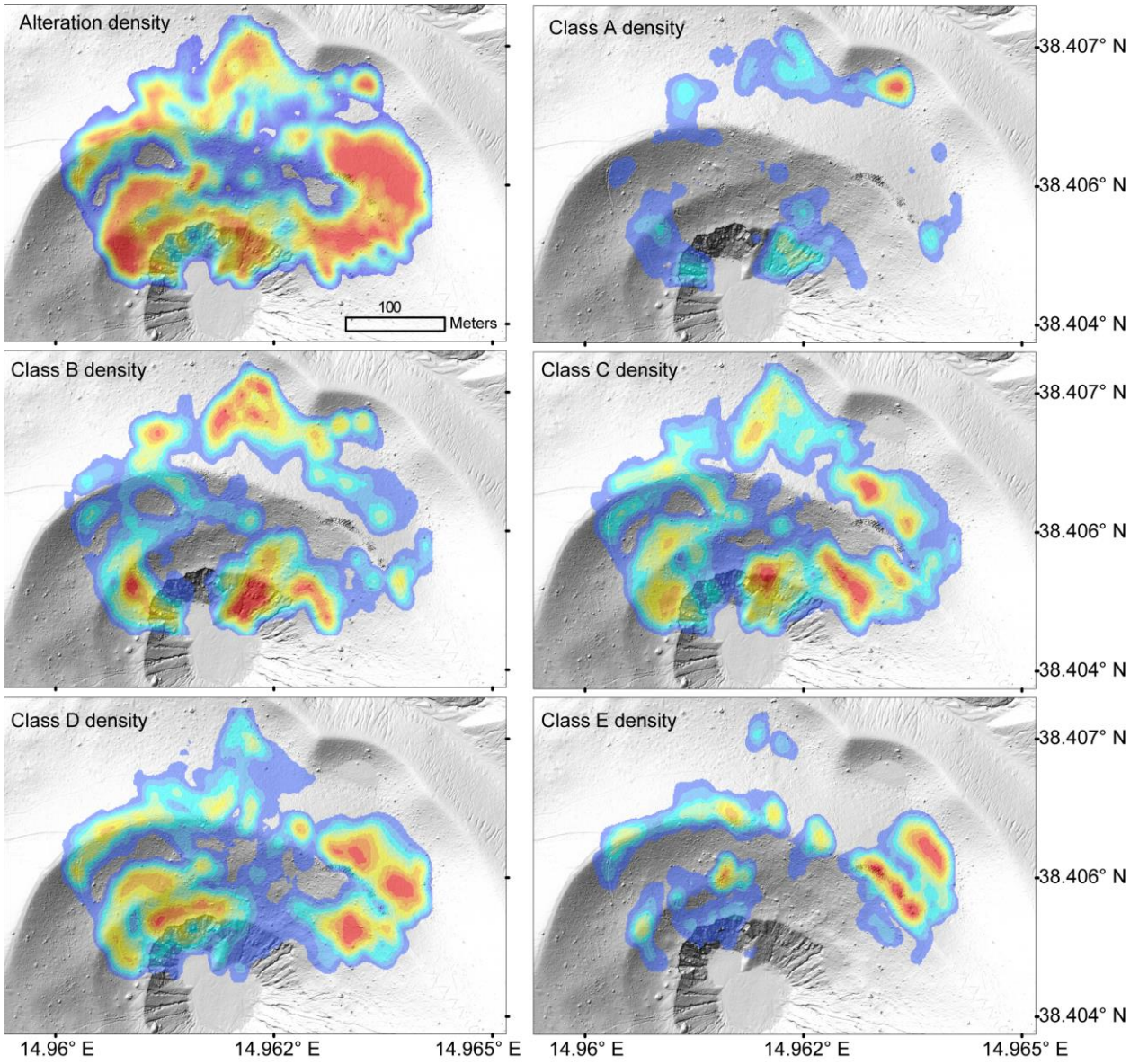

A3.4 The spatial pattern of the density distribution of classified pixels of classes A-E is demonstrating a clear segmentation.

Appendix A3.5 Qualitative comparison of PCA analyses of two different data sets

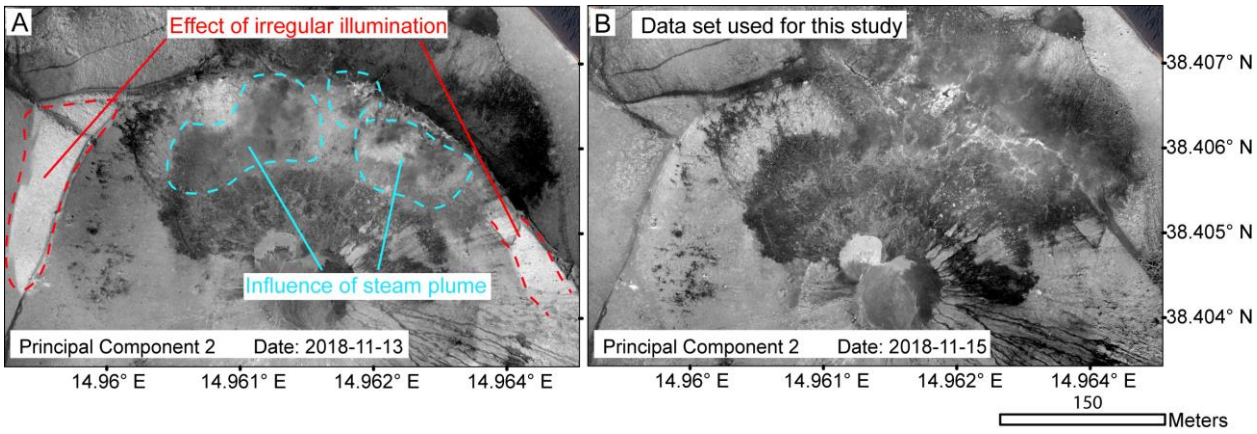

A3.5 Qualitative comparison of the results of the PCA, applied on two different datasets. The general patterns observed are equal, but illumination differences or a variable steam plume lead to differences in the Principal Components. For time series analysis, such effects as well as Eigenvectors and Eigenvalues of the single PCs need to be considered.

Appendix Chapter 4

Appendix A4.1 Boxplot of RGB value and temperature distribution

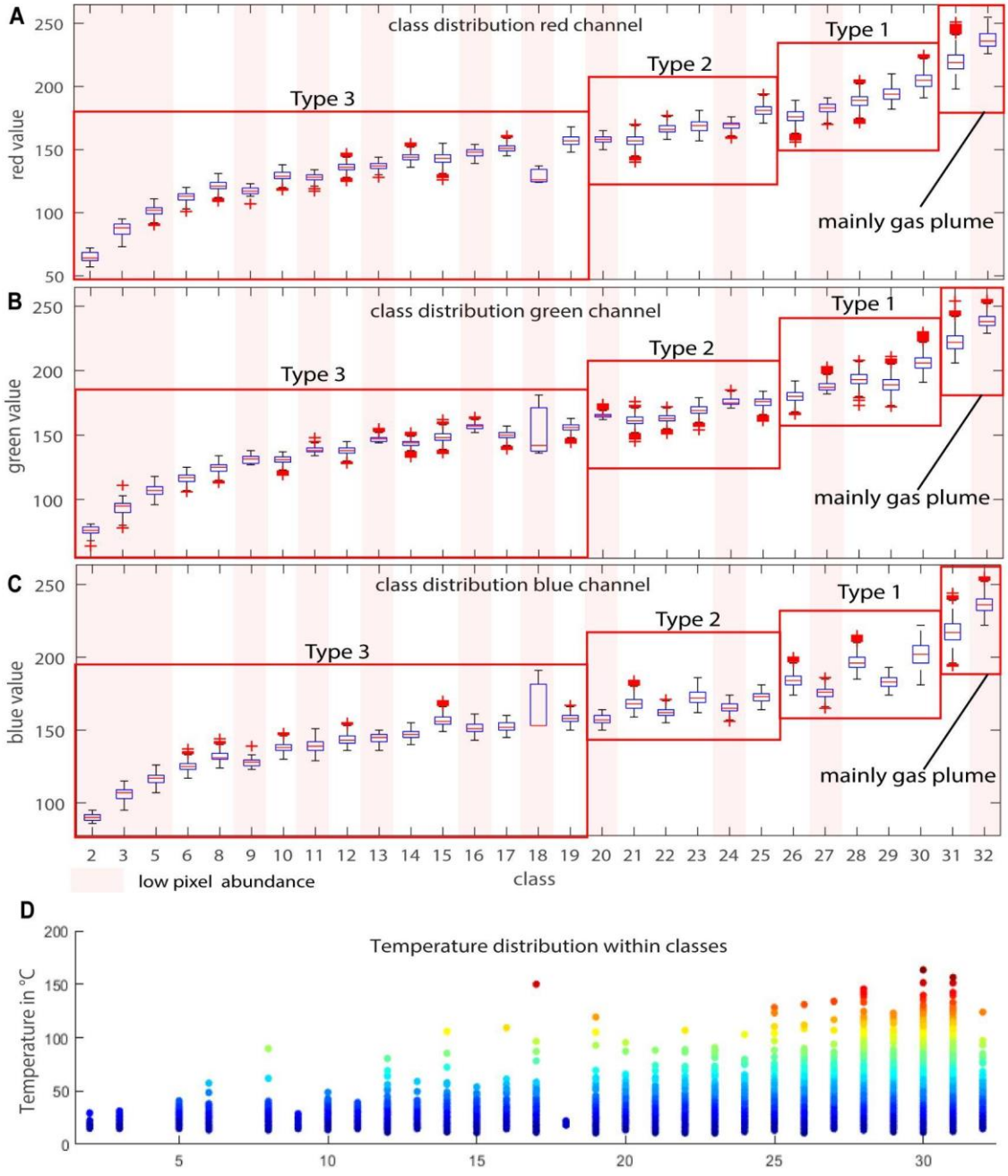

A4.1 Boxplots of RGB value distribution for the defined surface Types 1-3. Classes (unsupervised classification 32 classes) marked with the transparent red bar only have minor pixel abundances. Red boxes depict the spectral range of Type 1-3 surfaces. Class 31 and 32 are mainly associated with the fumarole steam plume.

Appendix A4.2 Gas measurement procedure - simplified accumulation chamber approach

To compare the observations from remote sensing to present-day surface degassing, measurement campaigns were performed in September 2021 and November 2022. The surface degassing was measured at 200 points within the northern part of the la fossa cone (Figure 6 in the main manuscript), in a simplified multi-gas accumulation chamber approach.

The simplified accumulation chamber consists of the measurement unit, a Dräger Xam 8000, coupled to a 10.3 cm diameter and 16.5 cm long plastic chamber by a 116 cm long tube with an inner diameter of 0.5 cm, resembling a simplified accumulation chamber. The plastic chamber has a volume of 1374.8 cm^3, the tube has a volume of 91.1 cm^3 so that the total system volume is 1465.934 cm^3. The pumping rate is 0.35 liter per minute. The plastic chamber was equipped with an open valve which was a necessity as the Dräger is an actively pumping system. Therefore, concentration increases in the chamber can be considered as surface flow and as independent from pumping effects. The Measurement unit is protected by a 2 µm filter, preventing dust and vapor to enter the unit. Note that we use Flux values in this study only for relative comparison and detection of the spatial variability of certain gas species and flows. A precise flux estimate is beyond the scope of this publication and can not be constrained as we did not measure gas temperatures and humidity at sampling locations.

The measurement unit, a Dräger XAM 8000 handheld Multigas device was equipped with 6 sensors, measuring CO_2, CH4, SO_2, H_2S, H_2, and O_2 simultaneously. The relevant species for this work are CO_2, SO_2, and H_2S, therefore only these will be considered in detail. The CO_2 sensor is a Non-Dispersive Infrared (NDIR) sensor. NDIR sensors use the absorption characteristics of CO_2 at ~ 4 µm, which leads to a concentration-dependent amplitude loss of the internally emitted IR light. The sensor has a detection threshold of 0.01 vol% CO_2 and is calibrated for measuring CO_2 in a range of 0-5 vol % at a resolution of 50 ppm under normal (-20-50 °C, 10-95 % RH, and 700-1300 hPa) atmospheric conditions. The response rate is < 10 sec for reaching T50- and < 15 sec for reaching T90 concentrations. The H_2S sensor is an electrochemical sensor with a detection limit of 0.4 ppm and a resolution of 0.1 ppm, measuring in a range of 0-100 ppm H_2S under normal atmospheric conditions. The response time for T90 values is >15 seconds and the accuracy of the measurement is +-5% of the measured value. The SO_2 sensor is an electrochemical sensor with a detection limit of 0.1 ppm and a resolution of 0.1 ppm, measuring as well in a range of 0-100 ppm under atmospheric conditions. The response time for T90 values is <15 seconds and the accuracy of the measurement is 2% of the

measured value. The NDIR CO_2 sensor is robust against cross-sensitivities. However, electrochemical sensors can be vulnerable to cross sensitivities (SO_2, H_2S, Cl_2), resulting in uncertainties of the measurement of a few percent of the measurement value.

The approach of combining the Dräger multigas with an accumulation chamber was developed and adapted as a consequence of uncertainties encountered in previous campaigns. The different sensors have slightly different reaction times for ascending gas concentrations and significantly different reaction times for descending gas concentrations. Comparing sensor readings directly therefore might lead to odd gas ratios. For that reason instead of the direct gas readings, we use the slope of the ascending gas concentration within the accumulation chamber to produce more reliable estimates of the surface flow (Figure A4.2).

For a relative comparison of degassing rates of the single measurement points, the gas data was plotted and the representative part of the graph, resembling a constantly ascending slope, was used to calculate the concentration increase by linear regression. Data points of the "Dead Bands" at the beginning and end of each graph were removed. In this way, we achieve a relative gas flux from soil that allows us to analyze spatial variations of gas flux throughout the study area. An overview of all gas measurement points is given in Figure 4.6. The aim of the gas measurements was not to provide accurate flux estimates but to highlight and quantify the spatial variability of the surface flux of certain gas species.

Each measurement was performed under similar conditions. Locations were selected in a way that they represent similar surface conditions, such as a spatial distance to fumarolic vents and an unsealed surface, for instance. Measurement locations typically were small areas with a naturally "open surface", often embedded in broader areas of the sealed surface. Such spots typically can be identified by loose gravel on the surface and in case slightly different coloration. For the measurement, the surface was cleaned and gravel was removed to provide a flat contact surface. Then the measurement was started, and the plastic chamber was placed on the ground and sealed on the bottom with fine-grained material. The average measurement duration was 2 min. In case of very rapidly ascending SO_2 or H_2S gas concentrations, the chamber was removed from the ground before and the system was flooded with fresh air, to protect the sensors from critically high acid concentrations. This procedure was chosen to ensure a fresh air flooded chamber at the beginning of each measurement and to record the initial atmospheric gas concentration. Further, it allows better identification of the measurement start- and end-points within the respective data sets, as each data series has two dead bands, one at the beginning and one at the end. Figure A 4.2 shows a typical graph of a

CO_2 measurement, with the Dead-Band at the beginning and end of each measurement and the constant ascending graph, representing the gas concentration increase within the chamber. The "Dead Bands" represent parts of the measurement where the accumulation chamber was placed on the ground but not sealed yet, or removed from the soil at the end of the measurements. Dead Bands at the beginning of the measurement were typically on the order of 20- 30 s.

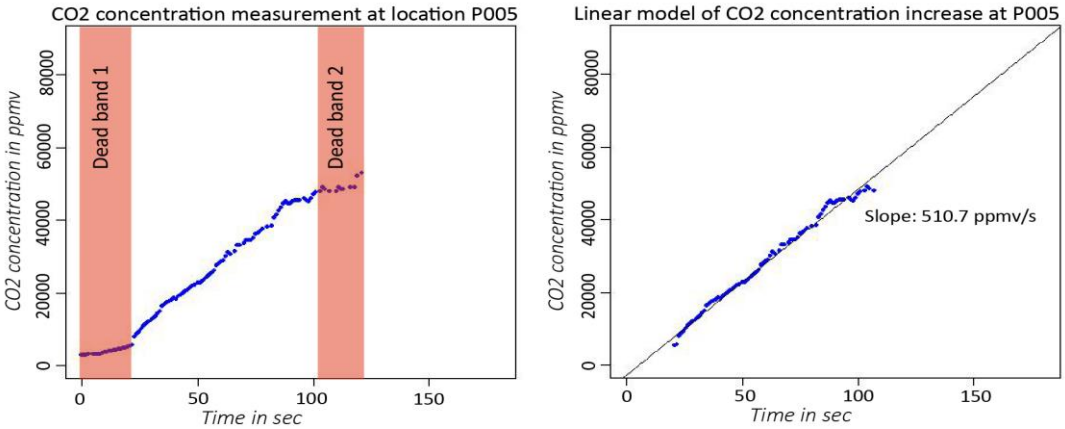

A4.2 CO_2 measurement at location P005, here shown representative for all measurement points. Dead bands at the beginning and end of the measurement were removed and the intensity of gas flux was obtained by linear regression through the constantly ascending part of the graph. The slopes of the linear model allow a relative comparison of single measurement points.

Appendix A4.3 Detail views of distinct active units

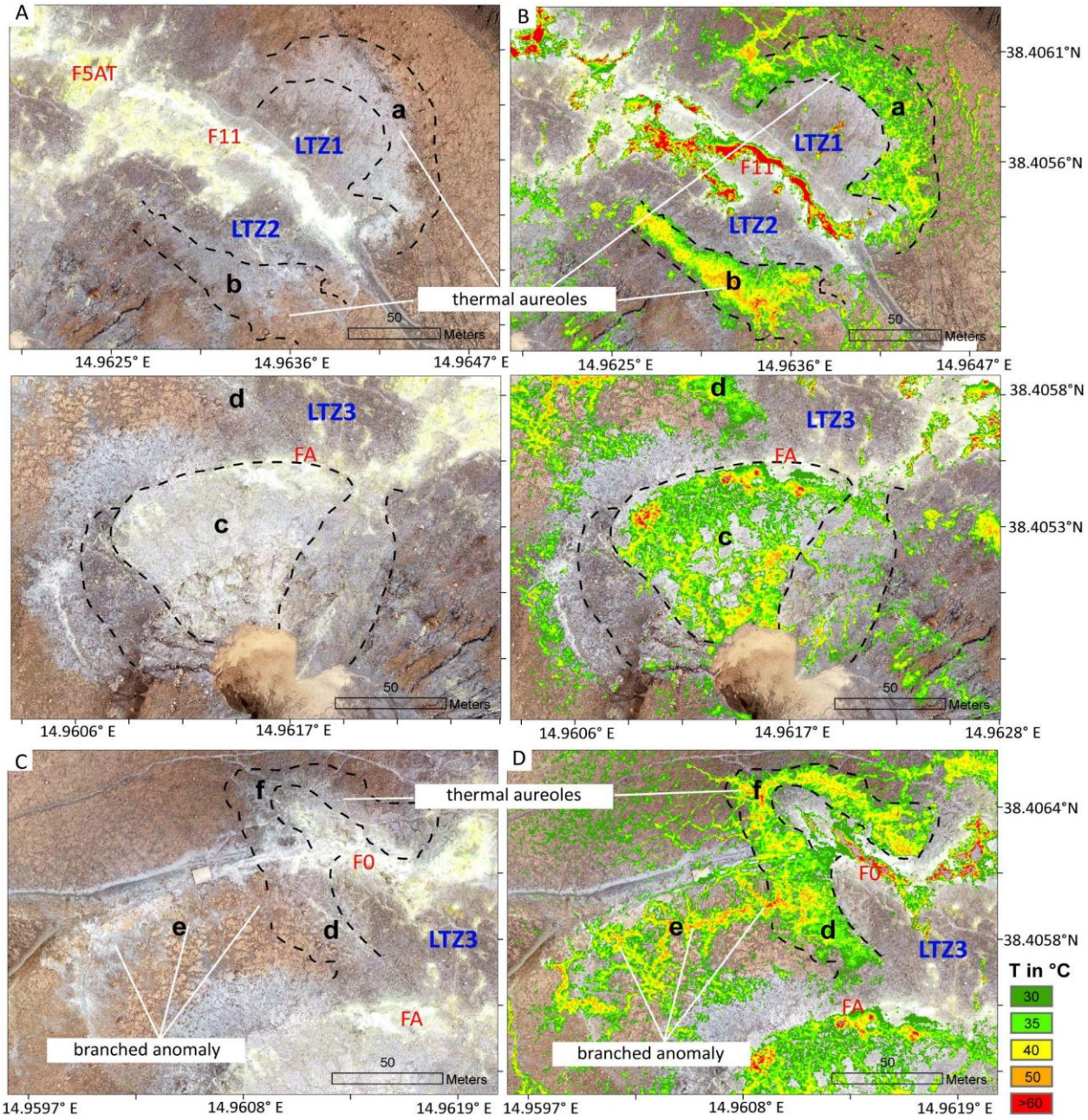

A4.3 Detail views of distinct units a-f and LTZ1-3 in a true color representation as seen from our 2019 orthomosaic data and an overlay by the thermal data with T>30 °C. A/B) Shown are units 1 and b and respective LTZ1 and 2. Note the outward spatial offset of both thermal units with respect to the surface coloration. C/D) Unit c is characterized by a network of thermal anomalies embedded in colder surroundings. E/F) Thermal aureole d and f branched anomaly e. Also here an outward shift of the thermal feature with respect to the surface coloration os observed, which could indicate gradual sealing processes with proximity to the main vents.

Appendix A4.4 Spearman correlation test for non-normal distributed variables

The test for correlation between optical and thermal anomalies was performed using the ggpubr package (Kassambara, 2019) in the statistical software environment R. The method used was Spearman's rank correlation which is suggested to be used for non-normal distributed data. The correlation test is based on the vectorized classification raster data set (classp_fumclip) with 8,890,830 data points with the analyzed variables pixel class (0-32) and pixel temperature (20-150 °C). The results show a correlation factor of 0.3485299, which is considered a mean positive correlation, and a p-value of 2.2e-16 proves statistical significance.

Spearman's rank correlation rho

data: x and y
S = 7.6277e+19, p-value < 2.2e-16
alternative hypothesis: true rho is not equal to 0
sample estimates:
   rho
0.3485299

Appendix A4.5 Thermal aureoles and low-temperature zones depicted in field photographs

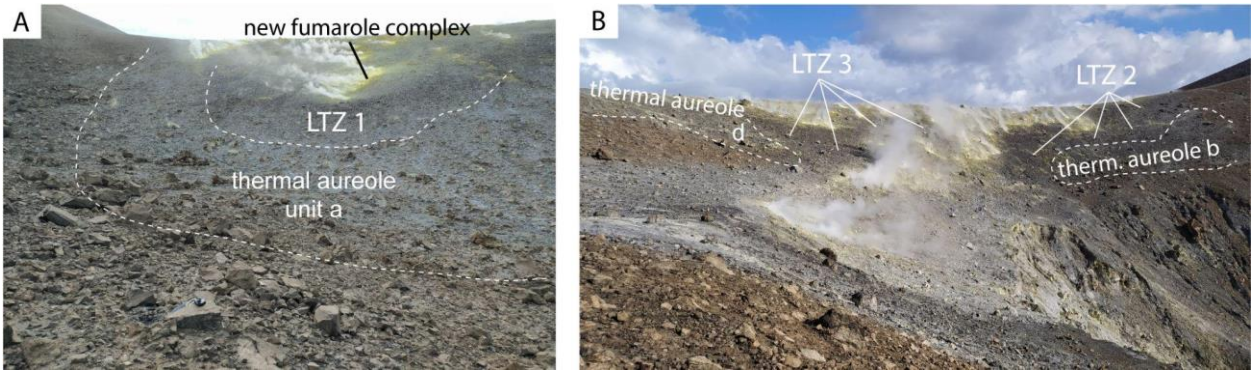

A4.5 Thermal aureoles and low-temperature zones depicted on field photographs. A) Thermal aureole a and LTZ1. B) Thermal aureole b and d with LTZ2 and LTZ3.

Appendix A4.6 XRD results / bulk chemical composition (%) of samples taken along transect A and B

Sample ID	A1	A2	A3	A4	A5	A6	B1	B2	B3
Sanidine	86.7	85.7	87.4	61.5	72.2	60.3	68.2	49.2	0
Cristobalite	13.3	14.3	12.6	18.2	0	0	0	0	0
Coesite	0	0	0	0	0.7	0	0	0	0
Sulfur	0	0	0	20.3	25.1	39.7	31.8	50.8	100
amorphous	50	0	0	0	0	50	50	0	0

Appendix A4.7 XRF results of samples taken along transects A-C.

Note that samples with s>10% were not analyzed by XRF.

S-ID	SiO_2 (%)	TiO_2 (%)	Al_2O_3 (%)	Fe_2O_3 (%)	MnO (%)	MgO (%)	CaO (%)	Na_2O (%)	K_2O (%)	P_2O_5 (%)	LOI (%)	S Eltra (%)
A1	76.0	0.2	10.7	1.6	0.1	0.1	1.1	1.8	4.8	0.1	3.8	0.1
A2	76.2	0.4	10.6	1.5	0.1	0	0.8	1.5	5.0	0.1	3.9	0.3
A3	77.0	0.3	10.2	1.4	0.1	0	0.7	1.6	4.8	0.1	4.3	0.2
A4	x	x	x	x	x	x	x	x	x	x	x	11.7
A5	67.3	2.2	0.4	0.3	11.9	0.1	1.2	3.1	5.0	0.1	2.0	6.0
A6	71.0	1.2	0.3	0.3	6.7	0.0	0.4	1.3	2.7	0.0	9.8	6.3
B1	73.0	1.2	0.3	0.3	7.0	0.0	0.5	1.3	3.0	0.0	4.3	9.0
B2	x	x	x	x	x	x	x	x	x	x	x	31.9
B3	x	x	x	x	x	x	x	x	x	x	x	60.5
C1	69.7	0.4	8.4	2.0	0	0.3	1.0	2.4	4.2	0.1	11.3	0.1
C2	81.3	0.3	6.1	1.1	0	0.1	0.4	1.1	2.5	0	6.1	0.5
C3	77.4	0.4	7.6	1.8	0	0.2	0.9	2.0	4.0	0.1	5.1	0.4
C4	x	x	x	x	x	x	x	x	x	x	x	40.3
C5	x	x	x	x	x	x	x	x	x	x	x	26.2
C6	x	x	x	x	x	x	x	x	x	x	x	12.5
C7	x	x	x	x	x	x	x	x	x	x	x	17.5
C8	63.8	0.4	12.0	3.2	0.1	0.4	1.7	5.0	8.0	0.1	3.2	1.2
C9	68.9	0.4	11.4	1.5	0	0.4	1.3	3.0	4.7	0.1	8.1	0.2

9 Further contributions

9.1 Eruptive cycle and bubble trap of Strokkur geyser, Iceland (Eibl et al., 2021)

Abstract

The eruption frequency of geysers can be studied easily on the surface. However, details of the internal structure including possible water and gas filled chambers feeding eruptions and the driving mechanisms often remain elusive. We used a multidisciplinary network of seismometers, video cameras, water pressure sensors and one tiltmeter to study the eruptive cycle, internal structure, and mechanisms driving the eruptive cycle of Strokkur geyser in June 2018. An eruptive cycle at Strokkur always consists of four phases: (1) Eruption, (2) post-eruptive conduit refilling, (3) gas filling of the bubble trap, and (4) regular bubble collapse at shallow depth in the conduit. For a typical single eruption 19 ± 4 bubble collapses occur in Phase 3 and 8 ± 2 collapses in Phase 4 at a mean spacing of 1.52 ± 0.29 and 24.5 ± 5.9 s, respectively. These collapses release latent heat to the fluid in the bubble trap (Phase 3) and later to the fluid in the conduit (Phase 4). The latter eventually reaches thermodynamic conditions for an eruption. Single to sextuple eruptions have similar spacings between bubble collapses and are likely fed from the same bubble trap at 23.7 ± 4.4 m depth, 13–23 m west of the conduit. However, the duration of the eruption and recharging phase linearly increases likely due to a larger water, gas and heat loss from the system. Our tremor data provides documented evidence for a bubble trap beneath a pool geyser.

Summary and Contribution

In this work we explored the physics of geyser eruptions at Strokkur geyser in Iceland by a combination of instruments. Especially the use of a pressure-temperature sensor and analysis of the resulting data (Figure 9.1), turned out beneficial for the explanation and creation of conceptual ideas about the general physics associated with eruptive cycles. Water as a medium transports pressure signals particularly well. By emplacing pressure sensors into the Strokkur basin, we could record short- and long-term changes generated at depth and transferred over the conduit into the basin. The general oscillation of the pressure pattern allowed to explain the general physics within the Strokkur system. A continuous basin level rise after an eruption indicates a constant inflow of hot water at depth (Fig. 9.1 A/B). Small positive pressure peaks indicate the formation and starting migration of bubbles at depth, followed by a pressure drop

indicating the bubble burst (Fig. 9.1 B/C). Towards an eruption these peaks become stronger, indicating either an increasing pressurization of the system with time or the formation of larger bubbles or longer travel distances before the burst. Bubble collapses occur at relatively equal intervals, once the first bubble collapse after an eruption occurred. The timing between an eruption and the first bubble collapse, in turn, is highly variable and may be an equivalent measure of discharge and heat loss. These general insights into the geyser plumbing system were then used to interpret a long seismic time series which was then statistically analyzed by the first author. My contribution to this work was the acquisition of drone and pressure-temperature data used for this study, as well as the analysis of the pressure data. Conceptualization of the physics of the geyser cycles was done in discussion with all authors. The bulk of the work for this study, the writing of the largest parts of the manuscript as well as handling of the submission and review process were done by Eva Eibl. I contributed mainly to the pressure chapter and supported the writing and review process.

Published in Solid Earth - Journal of Geophysical Research:
Eibl, E. P., Müller, D., Walter, T. R., Allahbakhshi, M., Jousset, P., Hersir, G. P., & Dahm, T. (2021). Eruptive cycle and bubble trap of Strokkur geyser, Iceland. Journal of Geophysical Research: Solid Earth, 126(4), e2020JB020769. https://doi.org/10.1029/2020JB020769

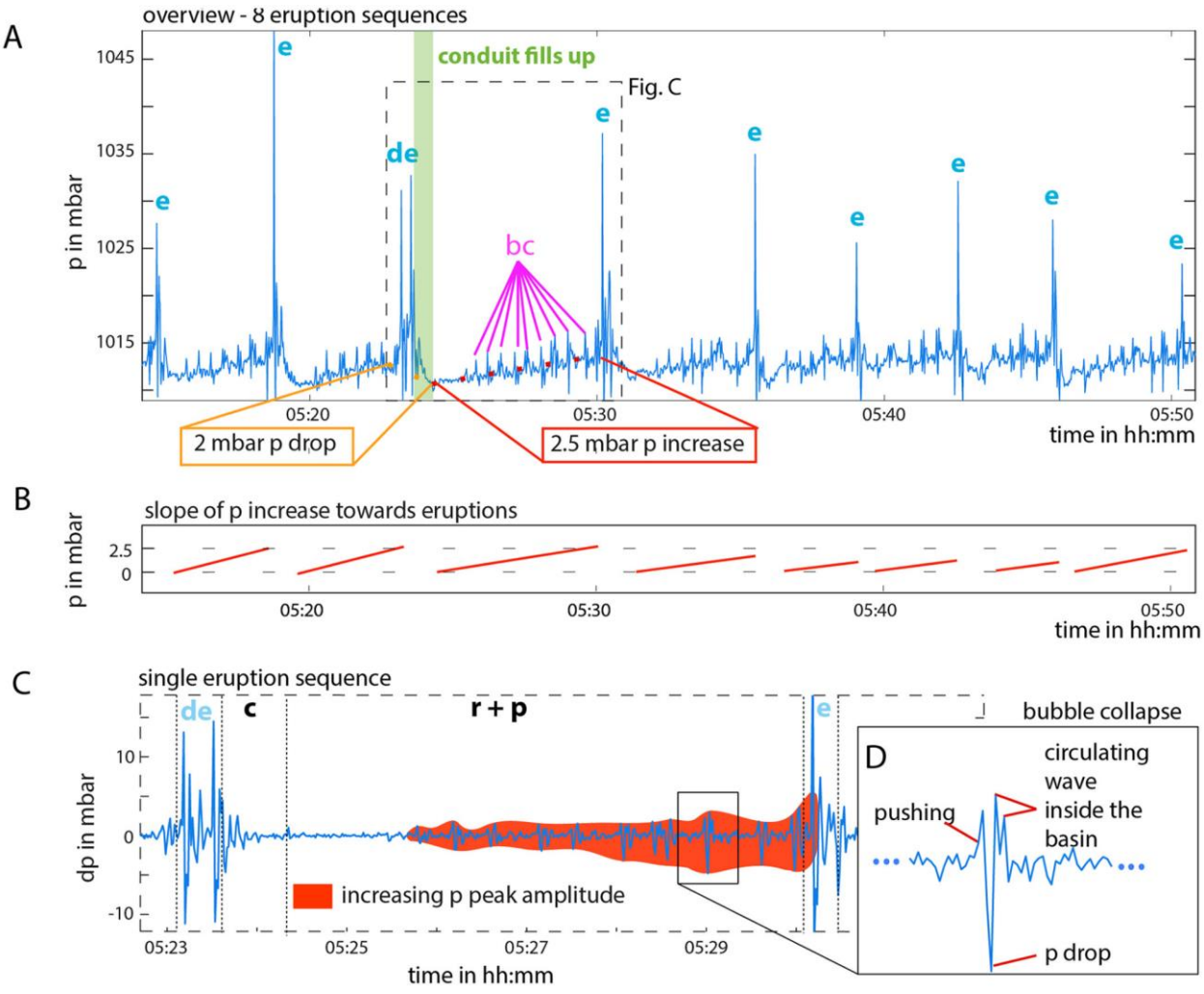

Figure 9.1 Typical pressure sensor recording inside the geyser pool. (a) Sequence of eight eruptions where eruptions (e), double eruptions (de), peaks in pressure (bc) are marked. The pressure data revealed a certain range of pressure conditions in the pool, that are affected by the eruptive behavior, like pressure drop during and increase after eruptions. (b) Pressure increase at the sensor caused by water level changes vary slightly in amplitude and frequency from cycle to cycle. (c) The first deviation of pressure shown in subfigure a for a single eruption sequence. The intensity of bubble collapses toward an eruption seems to increase. (d) shows a typical sequence of a bubble collapse, starting with a slight positive peak, followed by a larger pressure drop and following positive peaks, that are likely caused by traveling waves inside the pool.

9.2 Hidden mechanical weaknesses within lava domes provided by buried high-porosity hydrothermal alteration zones (Darmawan et al., 2022)

Abstract

Catastrophic lava dome collapse is considered an unpredictable volcanic hazard because the physical properties, stress conditions, and internal structure of lava domes are not well understood and can change rapidly through time. To explain the locations of dome instabilities at Merapi volcano, Indonesia, we combined geochemical and mineralogical analyses, rock physical property measurements, drone-based photogrammetry, and geoinformatics. We show that a horseshoe-shaped alteration zone that formed in 2014 was subsequently buried by renewed lava extrusion in 2018. Drone data, as well as geomechanical, mineralogical, and oxygen isotope data suggest that this zone is characterized by high-porosity hydrothermally altered materials that are mechanically weak. We additionally show that the new lava dome is currently collapsing along this now-hidden weak alteration zone, highlighting that a detailed understanding of dome architecture, made possible using the monitoring techniques employed here, is essential for assessing hazards associated with dome and edifice failure at volcanoes worldwide.

Contribution

This work provides a comprehensive approach to analyze hydrothermal alteration and mechanical weakening of lava domes. One aspect of this work, a remote sensing study, uses a similar approach as proposed in Müller et al. (2021), showing the evolution of alteration pattern at the lava dome. I contributed to this work in a subordinate position by conducting preliminary data analysis and supporting the remote sensing chapter and reviewing related chapters in this work. The bulk of the work has been done by Herlan Darmawan and associated other authors.

Published in Nature - Scientific Reports:
Darmawan, H., Troll, V. R., Walter, T. R., Deegan, F. M., Geiger, H., Heap, M. J., ... & Müller, D. (2022). Hidden mechanical weaknesses within lava domes provided by buried high-porosity hydrothermal alteration zones. Scientific Reports, 12(1), 3202. https://doi.org/10.1038/s41598-022-06765-9

9.3 Hydrothermally altered deposits of 2014 Askja landslide, Iceland, identified by remote sensing imaging (Marzban et al., 2023)

Abstract

Volcanic flanks subject to hydrothermal alteration become mechanically weak and gravitationally unstable, which may collapse and develop far-reaching landslides. The dynamics and trajectories of volcanic landslides are hardly preserved and challenging to determine, which is due to the steep slopes and the inherent instability. Here we analyze the proximal deposits of the 21 July 2014, landslide at Askja (Iceland), by combining high-resolution imagery from satellites and Unoccupied Aircraft Systems. We performed a Principal Component Analysis in combination with supervised classification to identify different material classes and altered rocks. We trained a maximum-likelihood classifier and were able to distinguish 7 different material classes and compare these to ground-based hyperspectral measurements that we conducted on different rock types found in the field. Results underline that the Northern part of the landslide source region is a hydrothermally altered material class, which bifurcates halfway downslope and then extends to the lake. We find that a large portion of this material is originating from a lava body at the landslide headwall, which is the persistent site of intense hydrothermal activity. By comparing the classification result to *in-situ* hyperspectral measurements, we were able to further identify the involved types of rocks and the degree of hydrothermal alteration. We further discuss associated effects of mechanical weakening and the relevance of the heterogeneous materials for the dynamics and processes of the landslide. As the study demonstrates the success of our approach for identification of altered and less altered materials, important implications for hazard assessment in the Askja caldera and elsewhere can be drawn.

Contribution

I contributed to this work through pre-site surveys, the organization of the fieldwork, the writing of the research proposal, and the acquisition of all necessary permissions from the relevant authorities in Iceland. I acquired some of the drone data in the field, supported the principal component analysis chapter, and the writing of the manuscript in a subordinate position. The bulk of the work has been done by Pouria Marzban.

Published in Frontiers in Earth Science:
Marzban, P., Bredemeyer, S., Walter, T. R., Kästner, F., Müller, D., & Chabrillat, S. (2023).

Hydrothermally altered deposits of 2014 Askja landslide, Iceland, identified by remote sensing imaging. Frontiers in Earth Science, 11, 1083043. https://doi.org/10.3389/feart.2023.1083043

9.4 Water in clinopyroxene from the 2021 Geldingadalir eruption of the Fagradalsfjall Fires, SW-Iceland (Radu et al., 2023)

Abstract

Water content plays a significant role in magma genesis, ascent rate, and, ultimately, in the style and intensity of volcanic eruptions, due to its control on the density, viscosity and melting behavior of silicate melts. A reliable method for determining the pre-eruptive magmatic water content is to use phenocrysts of nominally anhydrous minerals (NAMs) which can preserve water as hydrogen configurations in structural defects. The advantage of this method is that eruptive changes such as water loss during magma degassing may be experimentally reconstructed and analyzed by infrared spectroscopy. Applying this to clinopyroxene crystals (n=17) from lava samples (n=7) from April 2021 of the Geldingadalir eruption, SW-Iceland, reveals parental water contents of 0.69 ± 0.07 to 0.86 ± 0.09 wt. % H2O. These values are higher than those expected for typical mid-ocean ridge basalts (MORB 0.3–0.5 wt. % on average) indicating a significant plume (OIB) contribution to the magma source. Moreover, such water concentrations would imply that water saturation in the ascending Geldingadalir magmas was attained only at very shallow levels within the plumbing system. This could explain the at times pulsating behavior within the uppermost conduit system as being the result of shallow episodic water vapor exsolution in addition to the deep-sourced CO2 flux.

Contribution

My contribution to this work reduces on providing image and video data that shows conduit dynamics of the Fagradalsfjall eruption, acquired during a period characterized by periodic lava lake overflows, and on the creation of Figure 9.4 of the manuscript (see below).

Published in Bulletin of Volcanology:
Radu, I. B., Skogby, H., Troll, V. R., Deegan, F. M., Geiger, H., Müller, D., & Thordarson, T. (2023). Water in clinopyroxene from the 2021 Geldingadalir eruption of the Fagradalsfjall Fires, SW-Iceland. Bulletin of Volcanology, 85(5), 31.
https://doi.org/10.1007/s00445-023-01641-4

Acquisition date: June 8th 2021, time stamps in UCT

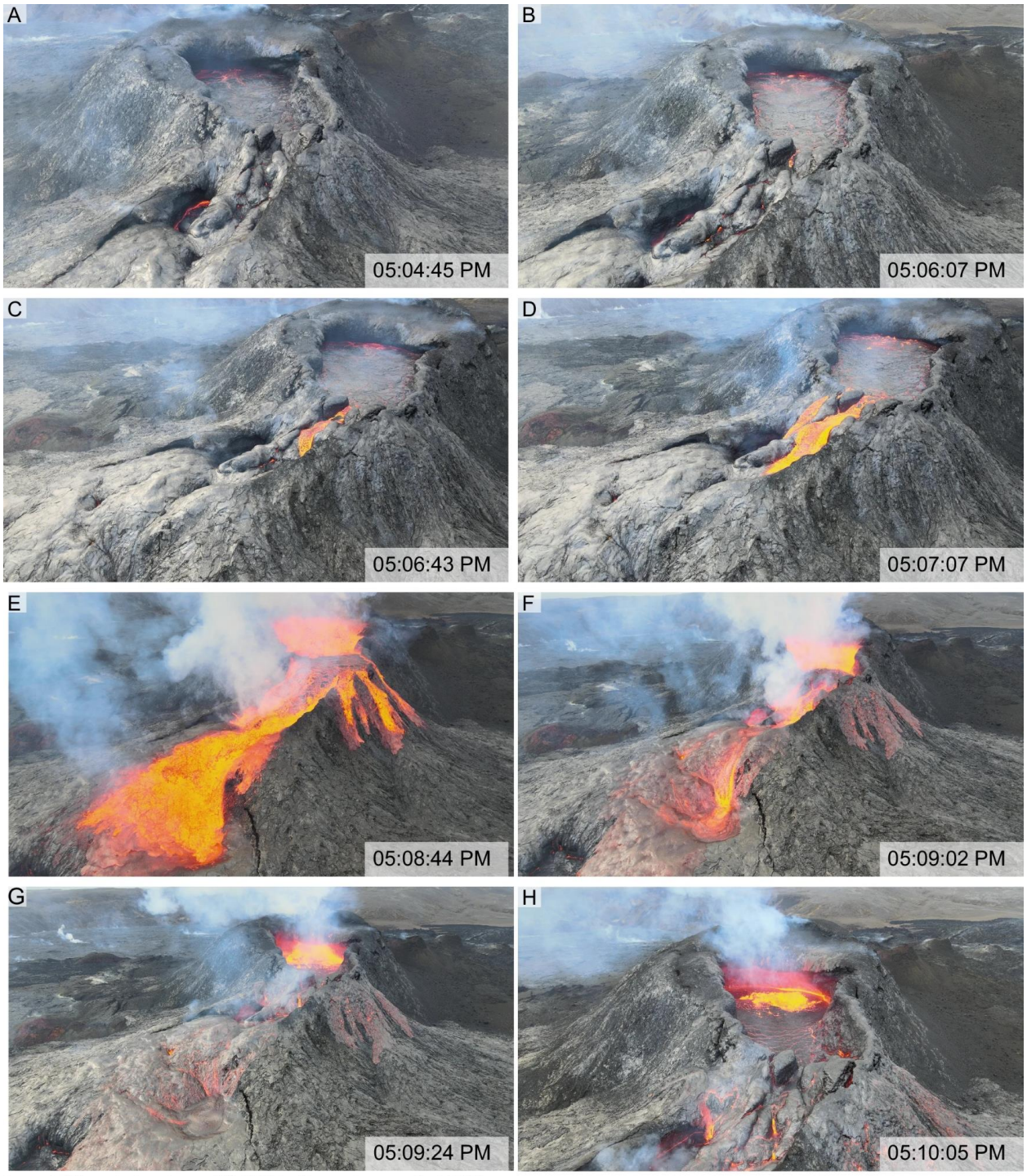

Acquisition date: June 8th 2021, time stamps in UCT

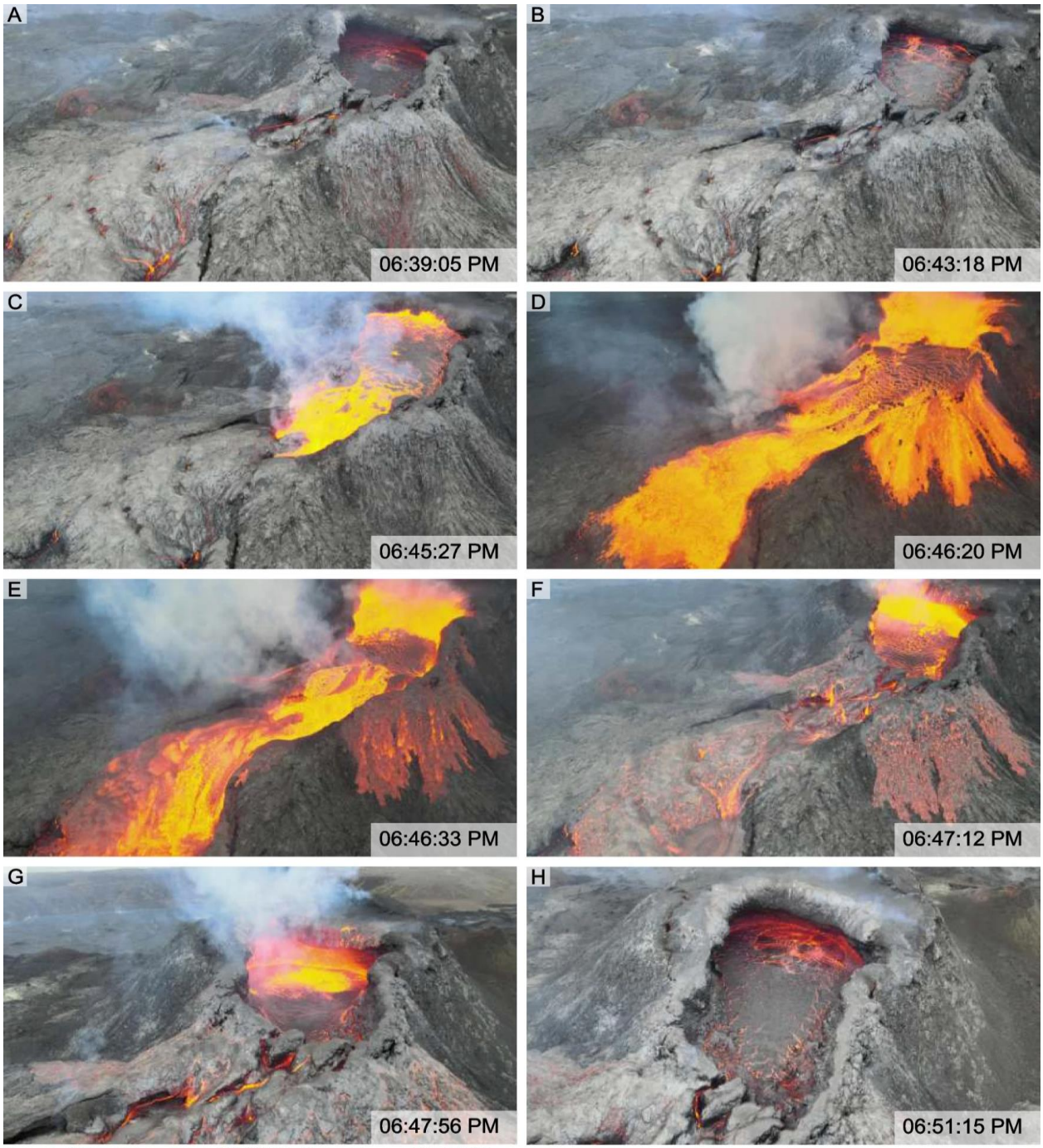

Figure 9.4 Aerial images of the main active crater at Geldingadalir. Extracted frames from video recording of the erupting crater on the 8th of June 2021. The lava flow was roughly towards the south, and the images were acquired from south of the crater, at ~50m altitude, with the camera oriented northward, facing the main discharge direction. On the day of acquisition, the eruption was stable, with pulsating flows at regular intervals of 8–10 min on average.